Creation of a strontium microtrap: Towards a spin-squeezed atomic clock

RYAN KEITH HANLEY

HANLEY, RYAN KEITH (2018) Creation of a strontium microtrap: Towards a spin-squeezed atomic clock. Doctoral thesis, Durham University.

Creation of a strontium microtrap: Towards a spin-squeezed atomic clock

Ryan Keith Hanley

A thesis submitted in partial fulfillment
of the requirements for the degree of
Doctor of Philosophy

Joint Quantum Centre (JQC) Durham
Department of Physics
Durham University
United Kingdom
October 3$^{\text{rd}}$, 2018

Creation of a strontium microtrap: Towards a spin-squeezed atomic clock

Ryan Keith Hanley

This thesis details the development of the pre-requisite experimental tools to create a proof-of-principle spin-squeezed atomic clock based upon an array of individual strontium atoms using Rydberg-dressed interactions. We experimentally and theoretically study Rydberg-dressing in a strontium narrow-line MOT, demonstrating that it is possible to coherently admix a Rydberg state into the narrow intercombination transitions of strontium. This work is based upon a quantitative semi-classical Monte-Carlo model of a strontium narrow-line MOT, where the combination of a quantum treatment of the light scattering process with a Monte-Carlo simulation of the atomic motion leads to a quantitative description of the spatial, thermal and temporal dynamics of the narrow-line MOT. By performing calculations of the dynamic polarisability of all the states relevant to laser cooling strontium, we have designed and constructed a new experimental apparatus to facilitate the creation of a microtrap of strontium. We observe and characterise the first known microtrap of strontium and outline the next steps towards the creation of an array of single atoms.

Due to the creation of Rydberg atoms in the strontium microtrap, understanding ionisation and interaction mechanisms may be of significant importance. We therefore study Rydberg ionisation mechanisms in a thermal beam of strontium atoms using simultaneous measurements of Rydberg EIT and spontaneously created ions or electrons. By connecting the optical and electrical signals using the optical Bloch equations, we are able to determine the dominant ionisation mechanisms of Rydberg atoms in the thermal beam. We also report the first observations of optical and electrical bistability, which may shed further light onto the origin of bistability in atom vapours.

Declaration

The work in this thesis is based on research carried out at the JQC Durham, Department of Physics, United Kingdom. No part of this thesis has been submitted elsewhere for any other degree or qualification and it is all my own work unless referenced to the contrary in the text.

Acknowledgements

During the course of my PhD, I have had the privilege of working alongside many people, without whom this thesis would be significantly shorter. First and foremost, I must thank my supervisor Matt Jones. I couldn’t have hoped for a better supervisor, and I wouldn’t be half the scientist I am today without his guidance. ‘Team Strontium’ has seen many personnel changes over my time, however this has given me the opportunity to work with a variety of students and postdocs. I thank Liz Bridge for kindly showing me the ropes when I first stepped foot in the lab. Paul Huillery was a source of endless optimism and taught me how to develop both my theoretical and experimental skills. Alistair Bounds showed me the variety of idiosyncrasies of the experiment, and was a great help for debugging electronic circuits. Niamh Jackson is one the hardest working people I have met, and the experiment is in good hands with her at the helm.

I have also learnt so much from people outside of Team Strontium. In particular, Dani Pizzey has been a brilliant strontium consultant, especially with ultra-stable cavities and laser systems. James Keaveney and Daniel Whiting have been my ’go-to’ python and optical Bloch equation experts and I have had many a conversation with Hannes Busche about dipole traps and high NA aspheric lenses. I must also thank Teodora Ilieva for allowing us to borrow equipment in times of need. I would like to thanks Josh Rogers, Hannes Busche and Niamh Jackson for reading significant parts of this thesis.

My time in AtMol has been one of the best experiences, which is due to the people with whom I have spent many a day. I must thank in particular the morning office morning team of Francisco Ponciano-Ojeda and Dani Pizzey for putting up with my constant moaning about how hot/cold it was on my morning runs whilst training for the great north run. Ifan Hughes has been an endless source of enthusiasm every morning, and has doubled my Welsh vocabulary to a total of two words! I thank Oliver Wales and William Hamlyn for constant laughs, and keeping me sane whilst writing this thesis.

I must give thanks to the technical staff in the department. Duncan Kennedy from the electronics workshop has always taken the time to show and teach me a variety of electronics, for which I am very grateful. The new experimental innards were painstakingly constructed by Kevin Ring, whose skill has made this project possible. Stephen Lishman and the rest of the mechanical workshop team have provided me with many tools, skills and most importantly laughs.

Finally, I am incredibly lucky to have such a supportive family. My parents have always supported me in the choices I have made, and have allowed me to follow a path I love. I must also thank my partner Miranda, who followed me to the north of England without a single doubt, and has shown me unwavering love, support and friendship.

Contents

List of Figures

List of Tables

Chapter 1

Introduction

Advances in the precision of atomic clocks has recently opened the door to ‘table-top’ test of fundamental physics [1], such as measurements of fundamental constants [2,3] and searches for physics beyond the standard model [4–6]. The pursuit of increased precision in atomic clocks is ongoing. However, with technological advances, the fundamental limit of precision is readily approaching. Therefore, new methods to reach beyond this fundamental limit are of current interest. The goal of this thesis is to develop the pre-requisite experimental tools to create a proof-of-principle spin-squeezed atomic clock based upon an array of individual strontium atoms using Rydberg-dressed interactions [7], which will lead to quantum-enhanced precision measurements. The experimental overview is illustrated in figure 1.1.

In recent times, the frontier of clock technology has moved to atomic clocks operating on electric-dipole transitions in the optical regime, where the transition frequencies are of the order of hundreds of THz. These optical atomic clocks typically use ions (Al^+, Sr^+, Hg^+ etc.) trapped in radio-frequency traps or divalent atoms (Sr, Yb, Ca, Mg etc.) trapped in optical lattices, where there are atomic transitions in the optical domain which are spectrally narrow. The current state of the art is a strontium optical lattice clock with a precision of 2.5×10^{-19} after an averaging time of six hours [8], three orders of magnitude more precise than the current definition of the SI second.

The increasing precision of atomic clock technology is fundamentally limited by

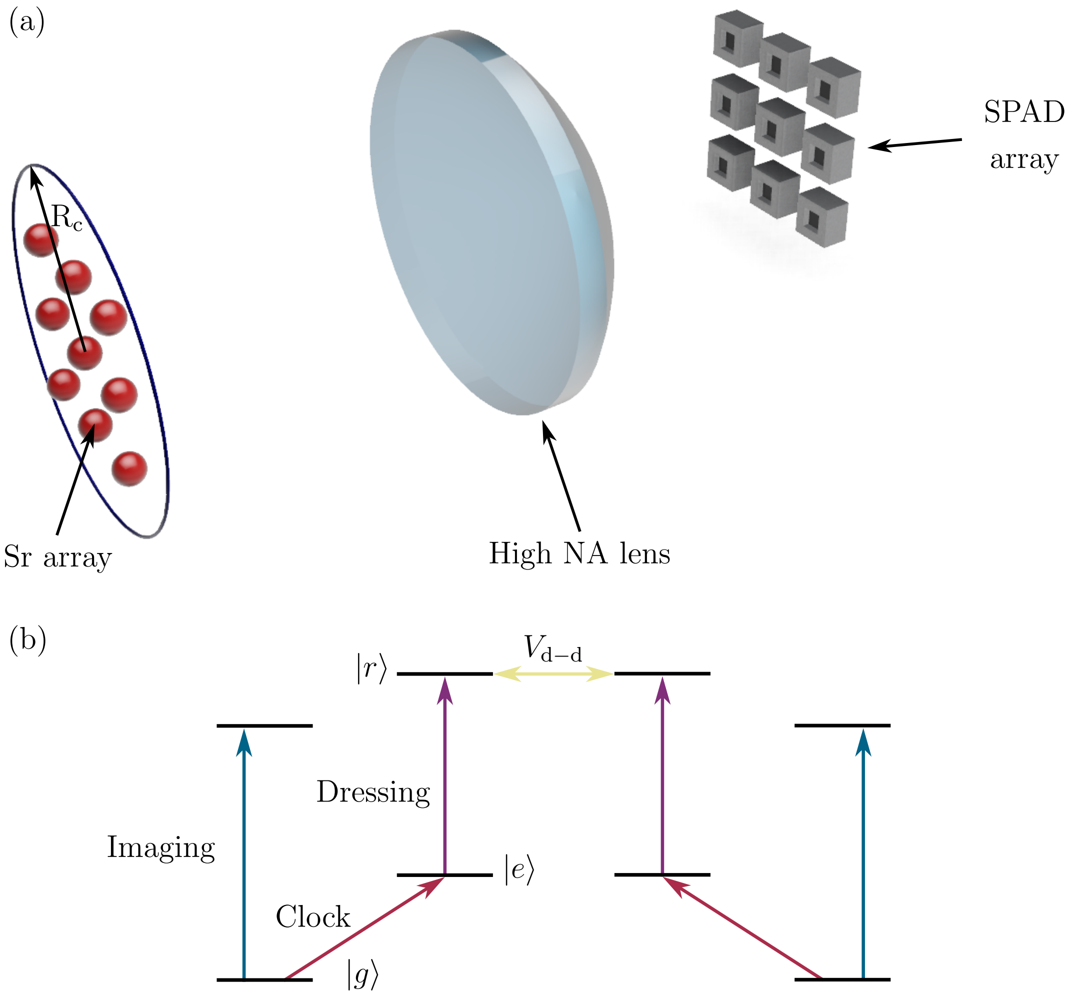

Figure 1.1: (a) A high numerical aperture lens is used to create an array of strontium atoms, and enables site resolved readout of the array using an array of single photon avalanche detectors (SPAD). (b) Single atoms are loaded into the array and imaged on a broad dipole-allowed transition. The clock state $|e\rangle$ is coupled to a Rydberg state $|r\rangle$ with long range dipole-dipole interactions $V_{\mathrm{d-d}}$ which induces an effective interaction between atoms in $|e\rangle$ (Rydberg dressing). The length scale of the interactions is R_{c}.

quantum projection noise (QPN) [9]. QPN is the fundamental source of noise for population measurements of a fixed number of uncorrelated atoms. By introducing quantum correlations between atoms however, it is possible to beat the QPN limit [10, 11]. The uncertainty relationship between orthogonal measurements of a spin system obeying the cyclic commutation relation $[S_i, S_j] = i\hbar\epsilon_{ijk}S_k$ is given by [12]

$$\left\langle \Delta S_i^2 \right\rangle \left\langle \Delta S_j^2 \right\rangle \geq \frac{\hbar^2}{4} \left|\langle S_k \rangle\right|^2 \ , \tag{1.0.1}$$

where ϵ_{ijk} is the Levi-Cevita symbol and the suffixes i, j, k denote the components in any three orthogonal directions. The introduction of quantum correlations facilitates the redistribution of quantum fluctuations between two orthogonal observables. This allows one to reduce or 'squeeze' the uncertainty in one observable, at the expense of increasing the uncertainty in the other. The correct use of a squeezed state in an atomic clock would improve the precision of the clock beyond the fundamental QPN limit. This has been previously demonstrated on microwave transitions [13, 14].

The extension of spin squeezing into optical clocks is an ongoing challenge. The creation of correlations from initially uncorrelated atoms relies upon a suitable and controllable inter-atomic interaction. There are a variety of proposals which typically fall into one of two categories [15]. The first relies upon elastic collisions in Bose-Einstein condensates. The second is based upon quantum nondemolition measurements by coupling atoms into an optical resonator. Applying these techniques to optical lattice clocks presents many challenges. The majority of optical lattice clocks operate using fermionic isotopes where Bose-Einstein condensation is not possible. Bosonic isotopes can be used, however significant losses from the clock state have been previously observed [16]. Quantum nondemolition measurements typically require the atoms to be placed into an optical resonator. The introduction of an optical resonator into the atomic clock raises the risk of uncontrollable electric fields, which would limit the ultimate precision of the atomic clock.

An ideal squeezing scheme is one in which the preparation of the atomic squeezed state is reasonably simple and does not alter the 'standard' clock sequence or experimental apparatus. A proposal of such a scheme has been outlined by Gil *et al.* [7]. They propose to use an additional laser to make use of strong Rydberg-Rydberg interactions (see figure 1.1(b)). By off-resonantly coupling the clock state to a high-lying Rydberg state, it has been shown that it is possible to utilise Rydberg-dressed interactions to create a squeezed state. An advantage of this scheme is that it only requires one additional laser, which is switched off after the squeezing is performed, enabling the atomic clock to operate in its standard form. The use of an additional laser coupling atoms to a Rydberg state has previously been shown to be compatible with a strontium optical lattice clock [17].

The verification and optimisation of such a squeezing scheme requires low-noise measurements of the spin-state of each atom in the atomic clock. This is technically very challenging in optical lattice clocks as the spacing between adjacent lattice sites is typically of the order of 400 nm. We therefore propose a novel approach where the optical lattice is replaced with a controllable array of optical tweezers, with each tweezer loaded with a single atom. This has been realised in the alkali-metal atoms [18–21], where it is now possible to create arbitrary three-dimensional arrays of individual atoms. A pre-requisite of the project is therefore the extension of this technique to divalent atoms.

The extension of configurable single atom arrays to divalent atoms also creates opportunities in the field of quantum simulation. The ability to trap both ground and Rydberg state atoms in a common optical trap is a pre-requisite for many quantum state manipulations without significant loss or heating involving Rydberg states [22, 23]. Due to the single valence electron of alkali-metal atoms, the number of methods available to simultaneously trap both ground and Rydberg state atoms is limited to the use of static electric [24] and magnetic fields [25], and the ponderomotive force [26]. Divalent atoms such as strontium offer a novel approach to this problem as the remaining valence electron of a singly-excited Rydberg state provides an additional degree of freedom to probe and manipulate the atom. It has been shown by Mukherjee *et al.* [27] that there exists regimes where the dynamic polarisability of both the ground and singly-excited Rydberg state have the same sign as well as similar magnitude, due to the core transitions of the remaining valence electron. It is therefore possible to create an all optical trap where the sign and magnitude of the force experienced by both ground and Rydberg state atoms is similar, opening avenues to improving quantum logic gates using ultracold atoms.

1.1 Thesis outline

This thesis is separated into three parts. Part I focusses on the study of Rydberg dressing in an ultracold sample of strontium, as well as the design, construction and characterisation of a strontium microtrap. We experimentally and theoretically study Rydberg-dressing in a strontium narrow-line MOT, demonstrating that it is possible to coherently admix a Rydberg state into the narrow intercombination transitions. We then design and construct a new experimental apparatus to facilitate the creation of a microtrap of strontium. We observe and characterise the first known microtrap of strontium and outline the next steps towards the creation of an array of single atoms.

Part II explores ionisation mechanisms of Rydberg atoms in a thermal beam of strontium. Due to the creation of Rydberg atoms in the strontium microtrap, understanding these ionisation and interaction mechanisms [28–31] may be of significant importance in future work. In this part, we demonstrate a novel method for probing interaction effects in a thermal beam of strontium atoms using simultaneous measurements of Rydberg EIT and spontaneously created ions or electrons.

Finally, part III draws these results together and discusses the next steps towards the creation of a squeezed state using Rydberg-dressed. The outline of this thesis is as follows:

Part I: Towards a spin-squeezed atomic clock

- Chapter 2 details the theoretical basis upon which this thesis rests.

- Chapter 3 details the Monte-Carlo simulation of the cooling dynamics of a strontium narrow-line MOT. This model is then extended to model Rydberg-dressed interactions in a strontium narrow-line MOT, as well as the loading of ultracold strontium into a far-off-resonance dipole trap.

- Chapter 4 describes the design and construction of a new experimental apparatus used to create a strontium microtrap.

- Chapter 5 describes the first observation of a strontium microtrap. The microtrap is characterised and progress towards single atom detection is discussed.

Part II: Probing interactions of thermal Sr Rydberg atoms using simultaneous optical and ion detection

- Chapter 6 shows a novel method for probing Rydberg ionisation mechanisms in a thermal beam of strontium.

Part III: Conclusions and Outlook

- Finally, chapter 7 summarises the main results of this thesis and discusses the next steps towards the creation of a squeezed state using Rydberg-dressed interactions.

1.2 Publications

Below are the publications arising from this work:

R. K. Hanley, A. D. Bounds, P. Huillery, N. C. Keegan, R. Faoro, E. M. Bridge, K. J. Weatherill and M. P. A. Jones (2017). *Probing interactions of thermal Sr Rydberg atoms using simultaneous optical and ion detection*, Journal of Physics B: Atomic, Molecular and Optical Physics, **50** 115002, DOI:10.1088/1361-6455/aa6e79.

R. K. Hanley, P. Huillery, N. C. Keegan, A. D. Bounds, D. Boddy, R. Faoro and M. P. A. Jones (2018). *Quantitative simulation of a magneto-optical trap operating near the photon recoil limit*, Journal of Modern Optics, **65**:5-6, 667-676, DOI:10.1080/09500340.2017.1401679.

A. D. Bounds, N. C. Jackson, R. K. Hanley, R. Faoro, E. M. Bridge, P. Huillery, and M. P. A. Jones (2018). *Rydberg-Dressed Magneto-optical Trap*, Physical Review Letters **120**, 183401, DOI:10.1103/PhysRevLett.120.183401.

Chapter 2

Atom-Light Interactions

The results presented in this thesis are based upon the interaction of strontium atoms with coherent laser radiation. These interactions lead to a variety of physical phenomena. Here we detail the theoretical background upon which this thesis rests. We initially detail the properties and energy level diagram of ^{88}Sr which is used throughout this thesis. We discuss laser cooling, trapping, and Rydberg-dressing which are three crucial pre-requisites to creating a spin-squeezed atomic clock. We also present electromagnetic-induced transparency (EIT) which is used in chapter 6 to characterise Rydberg ionisation mechanisms.

2.1 Sr energy level structure

Strontium is a divalent atom with two distinct series of atomic transitions, namely spin-singlet and spin-triplet transitions (see figure 2.1). These series of transitions give rise to spectrally-narrow intercombination transitions, between spin-singlet and spin-triplet states, ranging from $2\pi \times 7.4\,\mathrm{kHz}$ to $\sim 2\pi \times 1\,\mathrm{mHz}$. Due to the divalent nature of strontium there are two relevant cooling transitions; the $5\mathrm{s}^2\ ^1\mathrm{S}_0 \rightarrow 5\mathrm{s}5\mathrm{p}\ ^1\mathrm{P}_1$ and $5\mathrm{s}^2\ ^1\mathrm{S}_0 \rightarrow 5\mathrm{s}5\mathrm{p}\ ^3\mathrm{P}_1$ transitions. These are shown in figure 2.1. Due to dipole selection rules, the $5\mathrm{s}^2\ ^1\mathrm{S}_0 \rightarrow 5\mathrm{s}5\mathrm{p}\ ^1\mathrm{P}_1$ singlet transition is dipole allowed which results in a broad transition. The transitions to the triplet manifold however ($5\mathrm{s}^2\ ^1\mathrm{S}_0 \rightarrow 5\mathrm{s}5\mathrm{p}\ ^3\mathrm{P}_\mathrm{J}$) are spin forbidden. Nevertheless, due to state mixing [32], the

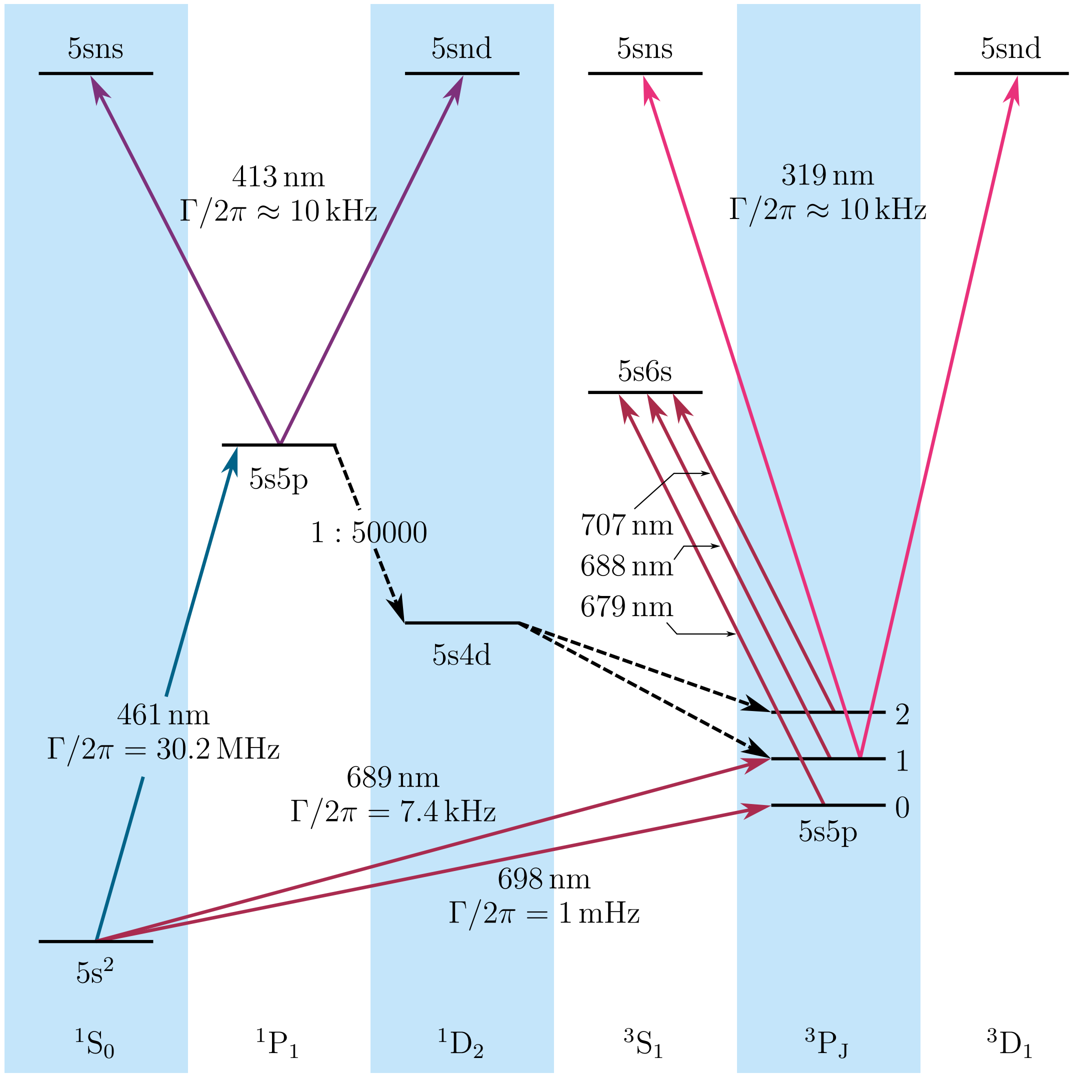

Figure 2.1: Energy levels and transition rates in strontium. Figure modified from [33].

5s^2 ^{1}S$_0$ → 5s5p ^{3}P$_1$ is weakly allowed, resulting in a narrow transition with linewidth $\Gamma/2\pi = 7.4\,\mathrm{kHz}$.

The singlet transition is not completely closed as there is a decay path to the 5s4d ^{1}D$_2$ state, with a branching ratio of 1:50000. The 5s4d ^{1}D$_2$ state decays to the triplet manifold with a branching ratio of 1:2 to the 5s5p ^{3}P$_2$ and 5s5p ^{3}P$_1$ states respectively. Atoms in the 5s5p ^{3}P$_1$ state decay back to the ground state at at rate of $\Gamma/2\pi = 7.4\,\mathrm{kHz}$. As the 5s5p ^{3}P$_2$ is metastable, atoms do not decay from this state in a time comparable to experiments. This 'leak' can be closed by pumping atoms to the 5s6s ^{3}S$_1$ state at 707 nm, from which they can decay to the 5s5p ^{3}P$_1$

state and finally back to the 5s^2 ^{1}S$_0$ state. It is also possible for atoms to decay from the 5s6s ^{3}S$_1$ state to the 5s5p ^{3}P$_0$ state. The 5s5p ^{3}P$_0$ is also metastable, and therefore an additional repumping laser at 679 nm is required to drive population back to the ground state.

The existence of both singlet and triplet Rydberg states gives rise to both isotropic attractive and repulsive interactions [34], a degree of freedom which is not accessible in the alkali-metal atoms. This degree of freedom enables one to arbitrarily choose the type of interactions required for a particular experiment. The divalent nature also creates an alternative detection method of singly-excited Rydberg atoms. The 'spare' inner-electron can be excited to form a doubly excited state where the total energy of the state is greater than the ionisation threshold, leading to rapid ionisation. This method is typically labelled 'auto-ionisation' and has been shown to be a formidable tool in detecting Rydberg atoms with spatial, temporal and atomic-state resolution [35, 36].

2.2 The two-level atom

In terms of atom-light interactions, the simplest system to consider is that of a two-level atom interacting with a coherent light field with Rabi frequency Ω and detuning from resonance $\Delta \equiv \omega_{\mathrm{L}} - \omega_0$, where ω_{L} is the angular frequency of the light field and ω_0 is the transition frequency. This is depicted in figure 2.2.

The upper state $|e\rangle$ can decay back to the ground state $|g\rangle$ with a rate Γ. One can describe the state of the atoms using the density matrix formalism [37]. The density matrix $\hat{\rho}$ of the two-level atom is given by

$$\hat{\rho} = \begin{pmatrix} \rho_{gg} & \rho_{ge} \\ \rho_{eg} & \rho_{ee} \end{pmatrix}, \tag{2.2.1}$$

where ρ_{ii} is the population of state i, and ρ_{ij} is the coherence between states i and j. The dynamics of the density matrix are governed by the von Neumann equation,

$$\dot{\hat{\rho}} = \frac{i}{\hbar}[\hat{\rho}, \hat{H}] + \hat{\mathcal{L}}(\hat{\rho}), \tag{2.2.2}$$

where $\dot{\hat{\rho}}$ is the derivative of the density matrix with respect to time. $\hat{H}$ is the

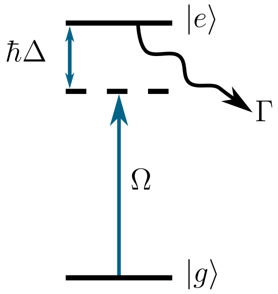

Figure 2.2: Energy level of a two-level atom interacting with light with detuning Δ and Rabi frequency Ω. Γ is the decay rate between $|e\rangle \rightarrow |g\rangle$.

Hamiltonian describing the system and $\hat{\mathcal{L}}(\rho)$ is the Lindblad operator

$$\hat{\mathcal{L}}(\rho) = \begin{pmatrix} \Gamma\rho_{ee} & -\frac{1}{2}\Gamma\rho_{ge} \\ -\frac{1}{2}\Gamma\rho_{eg} & -\Gamma\rho_{ee} \end{pmatrix} . \tag{2.2.3}$$

The Lindblad term describes the interaction of the system with the environment, leading to spontaneous decay and decoherence mechanisms. The appropriate Hamiltonian, in the rotating wave-approximation [37], to describe the atom-light system shown in figure 2.2 is given by

$$\hat{H} = \frac{\hbar}{2} \begin{pmatrix} 0 & \Omega \\ \Omega^* & -2\Delta \end{pmatrix} , \tag{2.2.4}$$

and the resulting equations are named the optical Bloch equations. In the following sub-sections, we will explore different regimes of this Hamiltonian and how this leads to a variety of physical phenomena; namely laser cooling, dipole trapping and Rydberg-dressed interactions.

2.2.1 Laser cooling

When $|\Delta| \lessapprox \Omega$, the laser field leads to significant excitation of the upper state $|e\rangle$. This significant excitation can be used to laser cool atoms to sub-millikelvin temperatures. The principle behind laser cooling arises from the idea that radiation carries momentum. It therefore follows that when an atom absorbs radiation, the momentum of the atom must change to obey conservation laws. A monochromatic

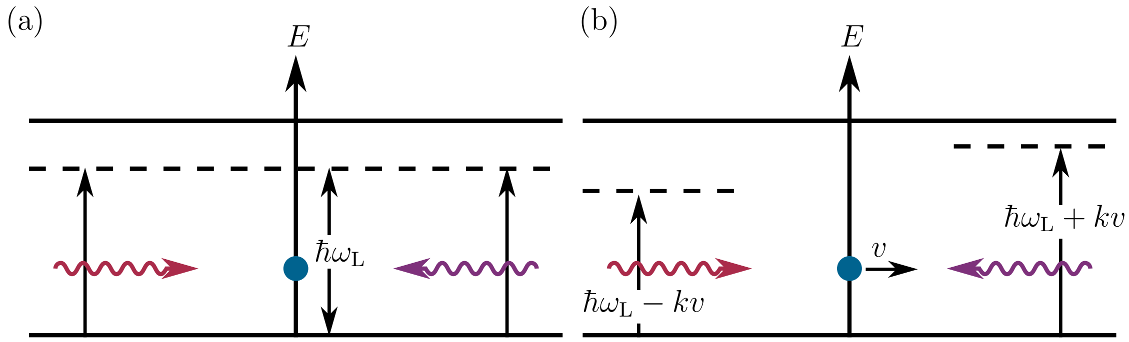

Figure 2.3: Energy levels and laser frequencies in the atomic frame of a (a) stationary and (b) moving atom interacting with counter-propagating laser beams.

laser incident on an atom exerts a scattering force given by

$$F = \hbar k R \ , \tag{2.2.5}$$

where $\hbar k$ is the momentum of a single photon and R is the atomic scattering rate. The scattering rate can be calculated using the density matrix ($R = \Gamma\rho_{\mathrm{ee}}$), as

$$F = \hbar k \frac{\Gamma}{2} \frac{S}{1 + S + 4\left(\Delta + \boldsymbol{k}\cdot\boldsymbol{v}\right)^2/\Gamma^2} \ , \tag{2.2.6}$$

where $S = I/I_{\mathrm{Sat}}$ is the intensity of the cooling light I normalised by the saturation intensity I_{Sat} [38], and $\boldsymbol{k}\cdot\boldsymbol{v}$ is the Doppler shift an atom experiences when travelling at a velocity $\boldsymbol{v}$. To cool an atomic sample in all three dimensions, three orthogonal counter-propagating laser beams are required. This is the so called 'Optical Molasses'. Figure 2.3 shows an energy level diagram along an axis of one pair of cooling laser beams. At first glance, one may expect that due to the symmetry of the system there is no effect on the atom as there are equal and opposite forces in all directions (figure 2.3(a)). However, this is only the case for a stationary atom. Due to the Doppler shift of a moving atom, if one chooses the frequency of the cooling laser to be lower than the atomic transition frequency (red-detuned) then atoms moving towards a laser beam experience a Doppler shift closer to resonance and therefore a larger scattering rate, as shown in figure 2.3(b). This effect leads to cooling in that dimension [39]. This technique does not lead to an atomic trap however as when the atoms are sufficiently cold, the Doppler shift of the cooling laser is too small and the atomic scattering rate decreases.

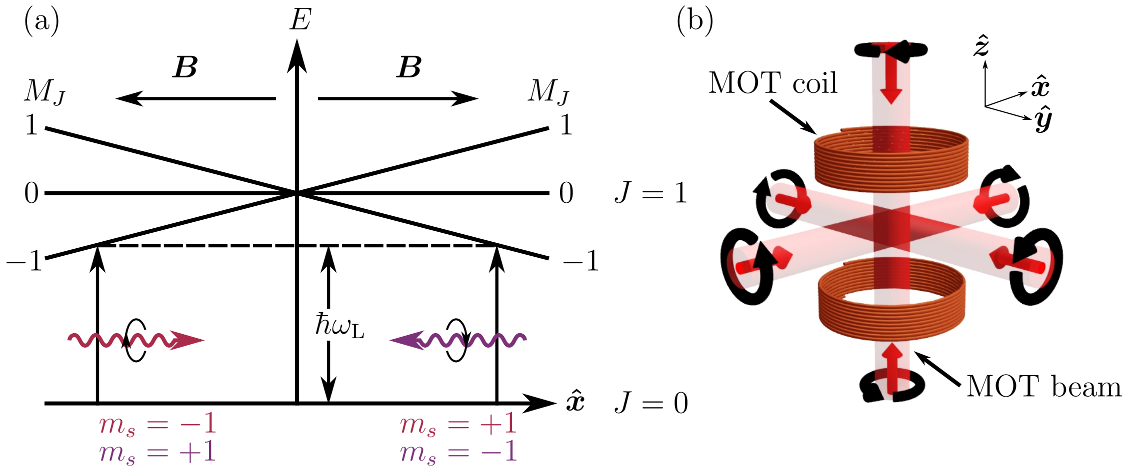

Figure 2.4: (a) Diagram showing the atomic energy levels along the one axis of the quadrupole field, along with the laser helicity and spin projections. (b) Three-dimensional diagram detailing the conventions used in this thesis.

Addition of a quadrupole field

An ingenious solution to this problem was discovered by Raab *et al.* [40] by introducing a quadrupole magnetic field and using circularly polarised laser light. The role of the quadrupole magnetic field is to use the Zeeman effect to create spatially varying atomic energy levels, leading to a scattering force which is not only velocity dependent but also spatially dependent.

Here we consider a simple $J = 0 \rightarrow J = 1$ transition, as shown in figure 2.4(a). The magnetic field $\boldsymbol{B}$ splits the upper state into three Zeeman levels with splitting $\Delta\omega_z = g\mu_{\mathrm{B}} \left|\boldsymbol{B}\right| / \hbar$ where g is the g-factor and μ_{B} is the Bohr magneton. The handedness of the laser beams is chosen such that atoms travelling away from the quadrupole centre are pushed back. This is because the spin projection of photons propagating in the same direction as the local magnetic field for left-hand (right-hand) circularly polarized light is $+\hbar$ ($-\hbar$) onto the axis, and drives σ^+ (σ^-) transitions. The combination of the quadrupole magnetic field and the helicity of the orthogonal laser beams, leads to a situation where atoms are both laser cooled and trapped.

2.2.2 Far-off resonance dipole trap (FORT)

When $|\Delta| \gg \Omega$, the laser field does not lead to significant excitation, but acts as a perturbation of the bare energy levels. By direct diagonalisation of the Hamiltonian shown in 2.2.4 in the limit of $|\Delta| \gg \Omega$, the perturbation of the energy levels from that of the bare states is given by

$$U = \frac{\hbar\Omega^2}{4\Delta} = \frac{1}{4}\left|\boldsymbol{E}\right|^2 \frac{\left|\boldsymbol{d_{eg}}\right|^2}{\hbar\left(\omega_\mathrm{L} - \omega_0\right)} \ . \tag{2.2.7}$$

Here we have used the definition of Rabi frequency $\Omega = \boldsymbol{d_{eg}} \cdot \boldsymbol{E}/\hbar$ and $\boldsymbol{d_{eg}}$ is the transition dipole moment. Up until now, we have used the rotating wave approximation. This is valid when $\omega_\mathrm{L} \approx \omega_0$. However, this is not the case for a FORT. We must therefore include the co-rotating term [41], leading to

$$U = \frac{1}{4}\left|\boldsymbol{E}\right|^2 \frac{\left|\boldsymbol{d_{eg}}\right|^2}{\hbar}\left(\frac{1}{\omega_\mathrm{L} - \omega_0} + \frac{1}{\omega_\mathrm{L} + \omega_0}\right) \ . \tag{2.2.8}$$

Experimentally, one normally measures the intensity I of an applied laser field. Therefore, using the definition $\left|\boldsymbol{E}\right|^2 = 2I/\epsilon_0 c$, we write the perturbation of the energy levels as

$$U = -\frac{\left|\boldsymbol{E}\right|^2\left|\boldsymbol{d_{eg}}\right|^2}{2\hbar}\frac{\omega_0}{\omega_0^2 - \omega_\mathrm{L}^2} = -\frac{1}{2\epsilon_0 c}\alpha I \ , \tag{2.2.9}$$

where ϵ_0 is the permittivity of free space, c is the speed of light and α is the dynamic polarisability. From this, the definition of α is

$$\alpha = \frac{2\left|\boldsymbol{d_{eg}}\right|^2}{\hbar}\frac{\omega_0}{\omega_0^2 - \omega_\mathrm{L}^2} \ . \tag{2.2.10}$$

In reality, an atom cannot be treated as a simple two-level atom and a multitude of atomic states must be included. The definition of the polarisability α_i for a state i is therefore[1]

$$\alpha_i = \frac{2}{\hbar}\sum_k \left|\boldsymbol{d_{ik}}\right|^2 \frac{\omega_{ik}}{\omega_{ik}^2 - \omega_\mathrm{L}^2} \ , \tag{2.2.11}$$

where ω_{ik} is the angular transition frequency between state i and state k. To calculate the polarisability in equation 2.2.11, one requires the transition dipole moments

---

[1] Note that this is a perturbative treatment and that a full diagonalisation of all atomic states and couplings is required for an exact solution.

$\boldsymbol{d_{ik}}$. In practice, one usually measures the transition decay rate A_{ik} as this is linked to the transition dipole moment via [38]

$$A_{ik} = \frac{\omega_{ik}^3}{3\pi\epsilon_0 \hbar c^3} \left|\boldsymbol{d_{ik}}\right|^2 \ . \tag{2.2.12}$$

We finally arrive at the expression

$$\alpha_i = 6\pi\epsilon_0 c^3 \sum_k \frac{A_{ik}}{\omega_{ik}^2 \left(\omega_{ik}^2 - \omega_{\mathrm{L}}^2\right)} \ , \tag{2.2.13}$$

which is dependent only on experimental measurables. From hereon, the derivation is relevant to ^{88}Sr in particular. Equation 2.2.13 relies on the measured values of A_{ik}. However, as each excited state has Zeeman degeneracy, one must take into consideration the trap polarisation and the relative coupling strength to each Zeeman level. This is a standard problem in angular momentum theory and there are a range of mathematical tools to solve this [42]. The relevant value of A_{ik} for an initial state with quantum numbers J_i and m_i, and a final state with quantum numbers J_k and m_k is

$$A_{ik} \rightarrow A_{ik} \sum_{m_k=-J_k}^{J_k} (2J_k+1) \begin{pmatrix} J_i & 1 & J_k \\ m_i & q & -m_k \end{pmatrix}^2 \ , \tag{2.2.14}$$

where q represents the polarisation of the FORT in the spherical basis [42, 43] and the matrix in the round brackets is the Wigner 3-j symbol. Equation 2.2.14 is only valid for the singlet states where $S = 0$, as there is no fine or hyperfine structure. The correction to A_{ik} is more complicated for the triplet states where $S = 1$, as the literature typically reports the total decay rate from an excited state to a fine-structure manifold below, or a lifetime of an excited state $\tau = 1/A_T$. For an excited state with quantum numbers S, L_k, J_k and lifetime τ, the value of A_{ik} used in the calculation is given by [32, 44]

$$A_{ik} \rightarrow \xi_{ik} A_T \frac{(2J_i+1) \sum\limits_{m_k=-J_k}^{J_k} \begin{Bmatrix} J_i & J_k & 1 \\ L_k & L_i & S \end{Bmatrix}^2}{\sum\limits_{J=|L_i-S|}^{|L_i+S|} (2J+1) \begin{Bmatrix} J_i & J_k & 1 \\ L_k & L_i & S \end{Bmatrix}^2} \sum_{m_k=-J_k}^{J_k} (2J_k+1) \begin{pmatrix} J_i & 1 & J_k \\ m_i & q & -m_k \end{pmatrix}^2 \ , \tag{2.2.15}$$

where the matrices in the curly brackets are the Wigner 6-j symbol, and ξ_{ik} is a correction factor [32] which takes into account the fact that the fine structure manifold is not degenerate in energy. To calculate the polarisability, we simply combine equations 2.2.14 and 2.2.15 with 2.2.13.

Experimental Realisation

In order to create a trap for ultra-cold atoms, one requires a spatially varying perturbation of the energy levels. The simplest experimental method of creating such a perturbation is to tightly focus a laser beam with a Gaussian intensity profile. The intensity of a Gaussian laser beam is given by

$$I\left(r,z\right) = I_0 \left(\frac{w_0}{w\left(z\right)}\right)^2 \mathrm{e}^{-2r^2/w(z)^2} \ , \tag{2.2.16}$$

where r and z are the radial and axial co-ordinates respectively, I_0 is the peak intensity, w_0 and $w\left(z\right)$ are the $1/\mathrm{e}^2$ radius of the beam at the focus and at a distance z respectively. This is given by

$$w\left(z\right) = w_0 \left(1 + \left(\frac{z}{z_\mathrm{R}}\right)^2\right)^{1/2} \ , \tag{2.2.17}$$

where z_R is the Rayleigh length, defined as $z_\mathrm{R} = \pi w_0^2/\lambda$ where λ is the wavelength of the laser beam. As the gradient of the laser intensity with respect to position is non-zero, the atoms feel an associated dipole force F_d given by

$$F_\mathrm{d}\left(r,z\right) = -\frac{1}{2\epsilon_0 c}\alpha \nabla I\left(r,z\right) \ . \tag{2.2.18}$$

If $\alpha > 0$, the atoms feel a force which pushes them towards regions of high intensity, leading to confinement of the atoms. For an atom to be trapped in the FORT, the kinetic energy of the atom must be less than the potential energy. However, as the dipole potential is conservative, the atom must lose its initial kinetic energy whilst in the FORT. This dissipation is typically induced by laser cooling techniques.

2.2.3 Rydberg Dressing

Rydberg dressing has been proposed as a way to introduce controllable long-range interactions into low-lying atomic states. Here we will briefly explore the physics of

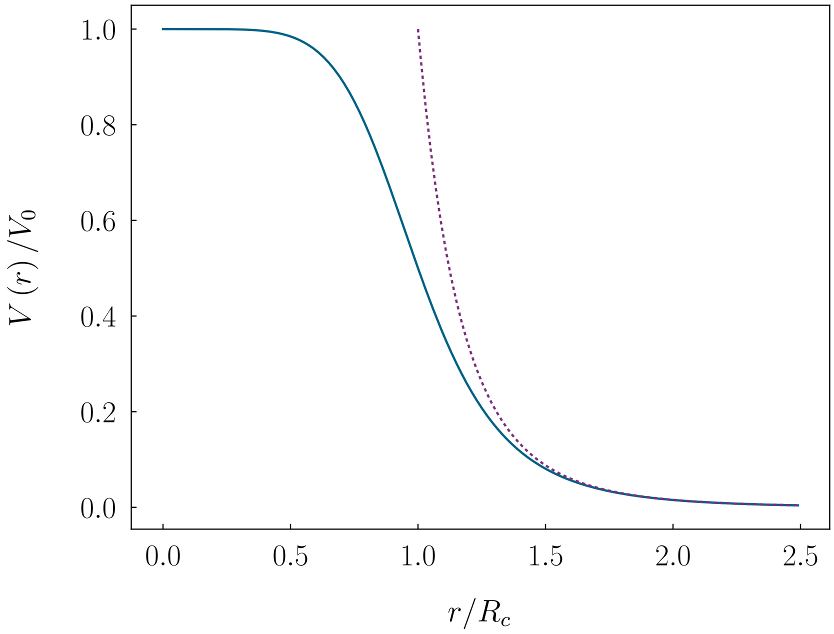

Figure 2.5: Dressed potential (blue-solid line) as a function of separation between two Rydberg-dressed atoms. The purple-dotted line shows the Van der Waals $1/r^6$ potential.

Rydberg dressing, however for a more detailed explanation see the theses of A. D. Bounds [45] and N. C. Jackson [46]

We will consider the atom-light interaction of the two-level atom shown in figure 2.2. However, we consider coupling to a high-lying Rydberg $|r\rangle$ instead of a low-lying excited state $|e\rangle$. In the limit of $\Delta \gg \Omega$, the dressed ground state $|g'\rangle$ can be approximated by

$$|g'\rangle \approx |g\rangle - \frac{\Omega}{2\Delta} |r\rangle \ . \tag{2.2.19}$$

The ground state of the system now contains a small, tunable fraction of the state $|r\rangle$, given by $\epsilon^2 = \Omega^2/4\Delta^2$.

Due to the Rydberg character of the dressed state, there exists a distance dependent interaction between two dressed-state atoms. The interaction energy between two Rydberg-dressed atoms $V(r)$ is given by [47–49]

$$V(r) = V_0 \left[1 + \left(\frac{r}{R_c} \right)^6 \right]^{-1} , \tag{2.2.20}$$

where the peak magnitude $V_0 = \hbar\Omega^4/8\left|\Delta\right|^3$ and length scale $R_c = \left|C_6/2\hbar\Delta\right|^{1/6}$. Here, C_6 is the van der Waals coefficient of the Rydberg state $|r\rangle$. This interaction has the form of a long-range potential with a soft core, as shown in figure 2.5. If one however considers an ensemble of Rydberg-dressed atoms, there is a collective enhancement to this interaction. The collective energy shift experienced by N_c atoms within a range $r < R_c$ to first order approximation is given by

$$V_c = \frac{N_c\left(N_c - 1\right)}{2} V_0 \ , \tag{2.2.21}$$

where $N_c = \rho 4\pi R_c^3/3$ and ρ is the atomic density of the ensemble.

2.3 Three-level atom

The addition of a third energy level gives rise to coherent phenomena such as EIT [50–52], where a medium becomes transparent to an incident light-field, only in the presence of another light-field. Figure 2.6(b) shows the case of an additional coupling beam with Rabi frequency Ω_c which couples the state $|e\rangle$ to the state $|r\rangle$ which is detuned from the transition resonance by a frequency Δ_c. The density matrix for the three level system shown in figure 2.6(b) is given by

$$\hat{\rho} = \begin{pmatrix} \rho_{gg} & \rho_{ge} & \rho_{gr} \\ \rho_{eg} & \rho_{ee} & \rho_{er} \\ \rho_{rg} & \rho_{re} & \rho_{rr} \end{pmatrix} \ , \tag{2.3.22}$$

and the appropriate Hamiltonian for this system in the rotating wave approximation is

$$\hat{H} = \frac{\hbar}{2} \begin{pmatrix} 0 & \Omega_\mathrm{p} & 0 \\ \Omega_\mathrm{p}^* & -2\Delta_\mathrm{p} & \Omega_\mathrm{c} \\ 0 & \Omega_\mathrm{c}^* & -2\left(\Delta_\mathrm{p} - \Delta_\mathrm{c}\right) \end{pmatrix} \ . \tag{2.3.23}$$

If one first considers the Hamiltonian in (2.3.23) and neglects the Lindblad terms, the effect of EIT can be readily seen [52]. The eigenstates of this Hamiltonian for the case of resonance ($\Delta_\mathrm{p} = \Delta_\mathrm{c} = 0$) are given by

$$|+\rangle = \frac{\Omega_\mathrm{p}}{\Omega_\mathrm{c}} |g\rangle + \frac{\sqrt{\Omega_\mathrm{p}^2 + \Omega_\mathrm{c}^2}}{\Omega_\mathrm{c}} |e\rangle + |r\rangle \ , \tag{2.3.24}$$

$$|0\rangle = \frac{\Omega_\mathrm{c}}{\Omega_\mathrm{p}} |g\rangle - |r\rangle \ , \tag{2.3.25}$$

$$|-\rangle = \frac{\Omega_\mathrm{p}}{\Omega_\mathrm{c}} |g\rangle - \frac{\sqrt{\Omega_\mathrm{p}^2 + \Omega_\mathrm{c}^2}}{\Omega_\mathrm{c}} |e\rangle + |r\rangle \ . \tag{2.3.26}$$

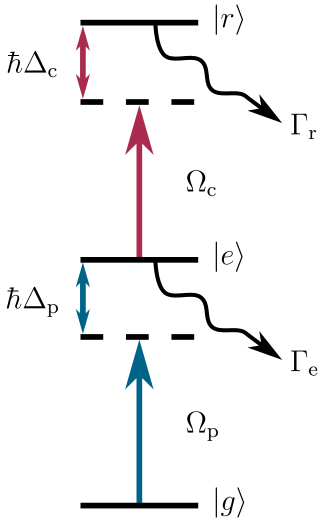

Figure 2.6: Energy level of a three-level atom interacting with two light fields with detunings Δ_p and Δ_c, and Rabi frequencies Ω_p and Ω_c. Γ_e and Γ_r are the decay rates between $|e\rangle \rightarrow |g\rangle$ and $|r\rangle \rightarrow |e\rangle$ respectively.

In the EIT regime, where $\Omega_\mathrm{c} \gg \Omega_\mathrm{p}$, the eigenstates reduce to $|\pm\rangle = \frac{1}{\sqrt{2}}(|r\rangle \pm |e\rangle)$ and $|0\rangle = |g\rangle$. As the probe laser only couples to $|e\rangle$, neither the probe nor the coupling fields interact with $|0\rangle$ and this is named the dark state. The probe laser couples to the $|e\rangle$ component of $|\pm\rangle$, however, these components for the two eigenstates are π out of phase with each other and the transition probability amplitudes interfere destructively. This results in a transparency window on resonance where the probe beam is not absorbed. This is demonstrated in figure 2.7 which shows that $\rho_{eg} \rightarrow 0$ as $\Delta_\mathrm{p} \rightarrow 0$ when $\Delta_\mathrm{c} = 0$.

One must however consider decay and decoherence in this system. This has the effect of reducing the resonant transmission of the probe from unity. The Lindblad term has two contributions, the first is due to spontaneous emission and the second is due to the finite laser linewdiths of the probe and coupling beams. The Lindblad term due to spontaneous emission is given by

$$\hat{\mathcal{L}}_\mathrm{spon} = \begin{pmatrix} \Gamma_\mathrm{e}\rho_{ee} & -\frac{1}{2}\Gamma_\mathrm{e}\rho_{ge} & -\frac{1}{2}\Gamma_\mathrm{r}\rho_{gr} \\ -\frac{1}{2}\Gamma_\mathrm{e}\rho_{eg} & -\Gamma_\mathrm{e}\rho_{ee} + \Gamma_\mathrm{r}\rho_{rr} & -\frac{1}{2}\left(\Gamma_\mathrm{e}+\Gamma_\mathrm{r}\right)\rho_{er} \\ -\frac{1}{2}\Gamma_\mathrm{r}\rho_{rg} & -\frac{1}{2}\left(\Gamma_\mathrm{e}+\Gamma_\mathrm{r}\right)\rho_{re} & -\Gamma_\mathrm{r}\rho_{rr} \end{pmatrix}, \tag{2.3.27}$$

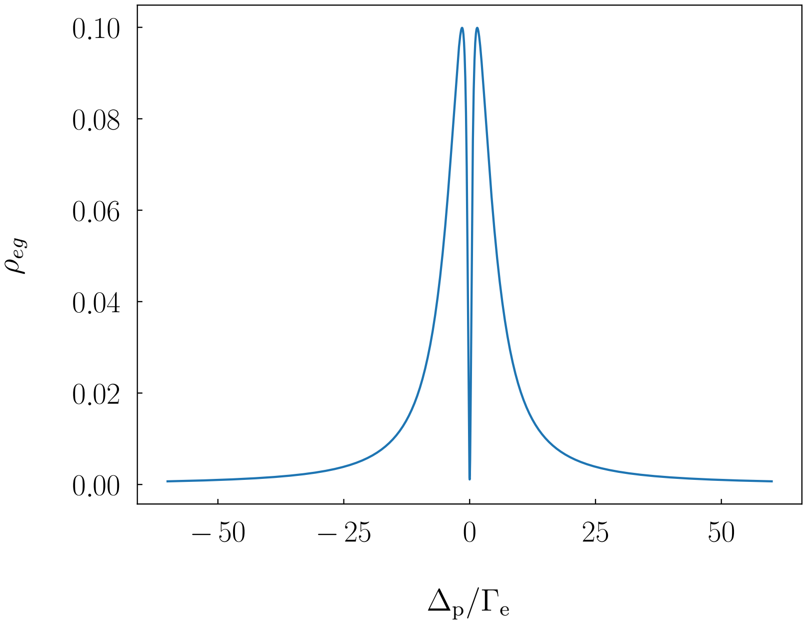

Figure 2.7: Example probe transition coherence as a function of probe detuning for the case when $\Delta_c = 0$. Here $\Gamma_\mathrm{e} = 10^3\Gamma_\mathrm{r}$ and $\Omega_\mathrm{c}^2/\Gamma_\mathrm{e}\Gamma_\mathrm{r} = 90$.

and the Lindblad term due to the finite laser linewidths is given by

$$\hat{\mathcal{L}}_\mathrm{laser} = \begin{pmatrix} 0 & -\Gamma_\mathrm{p}\rho_{ge} & -\Gamma_\mathrm{rel}\rho_{gr} \\ -\Gamma_\mathrm{p}\rho_{eg} & 0 & -\Gamma_\mathrm{c}\rho_{er} \\ -\Gamma_\mathrm{rel}\rho_{rg} & -\Gamma_\mathrm{c}\rho_{re} & 0 \end{pmatrix}, \tag{2.3.28}$$

where Γ_p and Γ_c are the linewidths of the probe and coupling laser respectively and Γ_rel is the relative linewidths between the lasers which is a convolution of the two lineshapes. Therefore, $\Gamma_\mathrm{rel} = \Gamma_\mathrm{p} + \Gamma_\mathrm{c}$ due to the properties of the convolution operation for Lorentzian lineshapes.

2.3.1 Macroscopic dynamics

The above formalism deals with the microscopic dynamics. However, one can link these microscopic dynamics to the macroscopic dynamics of a thermal vapour containing many atoms. With the full solution to the OBE's, one can calculate the complex electric susceptibility χ of a medium which contains N two-level atoms. This allows one to calculate the absorptive and dispersive properties of the medium.

The absorption coefficient μ is simply given by[2]

$$\mu = k_{\mathrm{p}} \chi_{\mathrm{Im}} \ , \tag{2.3.29}$$

where k_{p} is the wavenumber of the probe beam and χ_{Im} is the imaginary part of χ [53]. χ is given by

$$\chi = -\frac{2\left|\boldsymbol{d_{eg}}\right|^2 n}{\hbar \epsilon_0 \Omega_{\mathrm{p}}^*} \rho_{eg} \ , \tag{2.3.30}$$

where $\boldsymbol{d_{eg}}$ is the transition dipole moment and n is the atomic number density [54]. This equation shows that the absorption coefficient is directly proportional to ρ_{eg}.

Up to now, we have neglected the fact that a thermal ensemble of atoms has a velocity distribution. This results in a measured optical response which is averaged over all atomic velocity classes. Doppler averaging can be included in this formalism by calculating the density matrix for altered probe and coupling beam detunings $\Delta_{\mathrm{p}} \rightarrow \Delta_{\mathrm{p}} + \boldsymbol{k_{\mathrm{p}}} \cdot \boldsymbol{v}$ and $\Delta_{\mathrm{c}} \rightarrow \Delta_{\mathrm{c}} + \boldsymbol{k_{\mathrm{c}}} \cdot \boldsymbol{v}$ where the range of velocities $\boldsymbol{v}$ is taken from a Boltzmann distribution with a temperature T. The density matrices for all values of Δ_{p} and Δ_{c} are then integrated over a Maxwell Boltzmann distribution of velocities.

2.4 Summary

We have introduced the properties of ^{88}Sr, in particular the two distinct laser cooling schemes on the broad dipole-allowed and the narrow dipole-forbidden transitions. We have discussed the physics of laser cooling and the operation of a magneto-optical trap, both of which are required for chapter 3. We have shown how strong Rydberg-Rydberg interactions can be mapped onto a lower lying state, which is a technique which will employed for engineering interactions between atoms. We have detailed how to perform calculations of the dynamic polarisability, a tool which is needed in chapter 4 for the design of the new experimental apparatus. We finally discussed how the coupling between three atomic energy levels can lead to coherent phenomena such as EIT. This formalism is critical in coupling both optical and electrical signals in chapter 6.

---

[2] Only true in a dilute regime where dipole-dipole interactions are negligible.

Part I

Towards a spin-squeezed atomic clock

Chapter 3

Quantitative simulation of a narrow-line MOT

In order to implement the spin-squeezing protocol outlined by [7], it is imperative to be able to load atoms into a FORT and coherently admix a Rydberg state into the narrow intercombination transitions. Recent experiments have explored Rydberg dressing in a variety of ordered settings. Rydberg-dressed interactions have been measured between two atoms in optical tweezers [55] and in an array of atoms confined in an optical lattice [56, 57]. The observation of Rydberg-dressed interactions in disordered systems however seems to be more challenging due to uncontrolled loss mechanisms [58–61].

The current experimental apparatus facilitates the creation of a strontium MOT on the ^{88}Sr 5s^2 ^{1}S$_0$ → 5s5p ^{3}P$_1$ transition (nMOT), as well as the excitation from the 5s5p ^{3}P$_1$ state to both the 5sns and 5snd Rydberg series. Here we explore Rydberg dressing in a nMOT, where the interactions between Rydberg-dressed atoms are large compared to both the kinetic energy and transition linewidth. The laser cooling and Rydberg dressing scheme is shown in figure 3.1. The upper state of the nMOT cooling transition is coupled to a Rydberg state with Rabi frequency Ω and detuning Δ_{D} using a home-built UV laser system [62]. This results in a dressed excited state of the cooling transition.

Before one can study Rydberg dressing in a nMOT however, one must fully

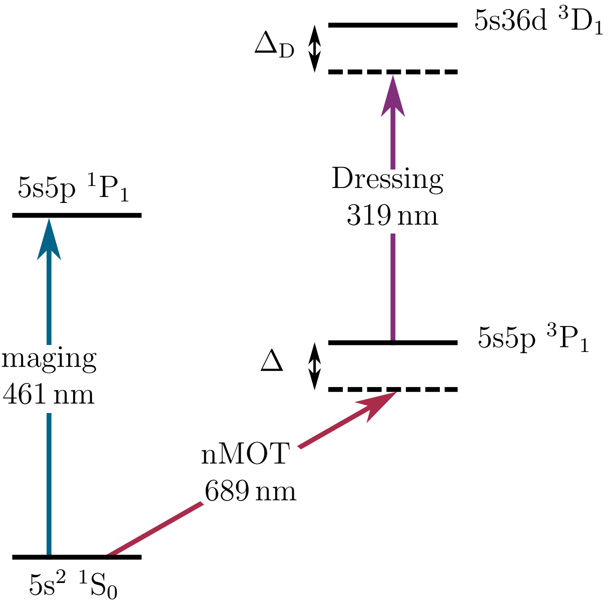

Figure 3.1: Energy level diagram showing the dressing scheme used in the experiment.

understand the dynamics of a nMOT in the absence of Rydberg dressing. To address this, we create a quantitative model of a nMOT operating on the narrow 5s^2 ^{1}S$_0$ → 5s5p ^{3}P$_1$ transition, by combining a quantum treatment of the light scattering process with a Monte-Carlo simulation of the atomic motion. By comparing this model to experimental measurements, we are able to quantitatively reproduce the spatial, thermal and temporal dynamics of the nMOT. This quantitative agreement creates a solid theoretical foundation upon which we are able to study a Rydberg-dressed nMOT.

The work in this chapter is based upon the publications:

R. K. Hanley, P. Huillery, N. C. Keegan, A. D. Bounds, D. Boddy, R. Faoro and M. P. A. Jones (2018). *Quantitative simulation of a magneto-optical trap operating near the photon recoil limit*, Journal of Modern Optics, **65**:5-6, 667-676, DOI:10.1080/09500340.2017.1401679.

A. D. Bounds, N. C. Jackson, R. K. Hanley, R. Faoro, E. M. Bridge, P. Huillery, and M. P. A. Jones (2018). *Rydberg-Dressed Magneto-optical Trap*, Physical Review Letters **120**, 183401, DOI:10.1103/PhysRevLett.120.183401.

3.1 Narrow-line MOT (nMOT)

The experimental configuration for a nMOT is the same as that for a conventional MOT [40] (see section 2.2.1), with atoms cooled and confined by a combination of a quadrupole magnetic field and laser beams with the appropriate helicity. What makes nMOTs distinctive is the ratio $\eta = \Gamma/\omega_{\mathrm{R}}$, where Γ is the natural linewidth of the cooling transition, and $\omega_{\mathrm{R}} = (4\hbar\pi^2)/(2m\lambda^2)$ is the frequency shift due to the atomic recoil following the absorption or emission of a photon. In a conventional MOT $\eta \gg 1$, whereas $\eta \approx 1$ in a nMOT. In this limit, individual scattering events significantly alter the subsequent probability of absorption, and the ultimate limit of laser cooling is set by the recoil temperature rather than the Doppler temperature [63].

Loftus *et al.* [64] showed that the behaviour of atoms in a nMOT is governed by the scaled detuning $\delta = |\Delta|/\Gamma'(S)$, where $\Gamma'(S) = \Gamma\sqrt{1+S}$ is the power-broadened linewidth. Three regimes can be identified.

The regime that is closest to a conventional MOT occurs when $\delta \approx 1$ and $S >> 1$. This is illustrated in figures 3.2(a) and (b). Here the power-broadened linewidth dominates and the cloud forms close to the quadrupole centre as atoms are resonant with all three pairs of laser beams. In this “Doppler” regime (I) the power-broadened linewidth determines the temperature, and the atoms are comparatively hot.

If Δ is increased such that $\delta \gg 1$ but $S > 1$, the trap no longer forms at the quadrupole centre, but is displaced to where the Zeeman shift $\Delta\omega_z = \Delta$. The resulting resonance condition forms an elliptical ‘shell’ around the quadrupole centre. Since gravity is strong compared to the light-induced forces, the atoms fall under gravity until the resonance condition is met, forming an elliptically-shaped nMOT (shown in figure 3.2(c)) where the atoms predominantly interact with the beam that directly opposes gravity. This is seen by the clearly separated force peaks displaced from the quadrupole zero in figure 3.2(d). We refer to this as the “power-broadened” regime (II).

Finally, the recoil dominated “quantum” regime (III) occurs when $\delta \gg 1$, and $S \leq 1$. As in the power-broadened regime, the MOT position is determined by

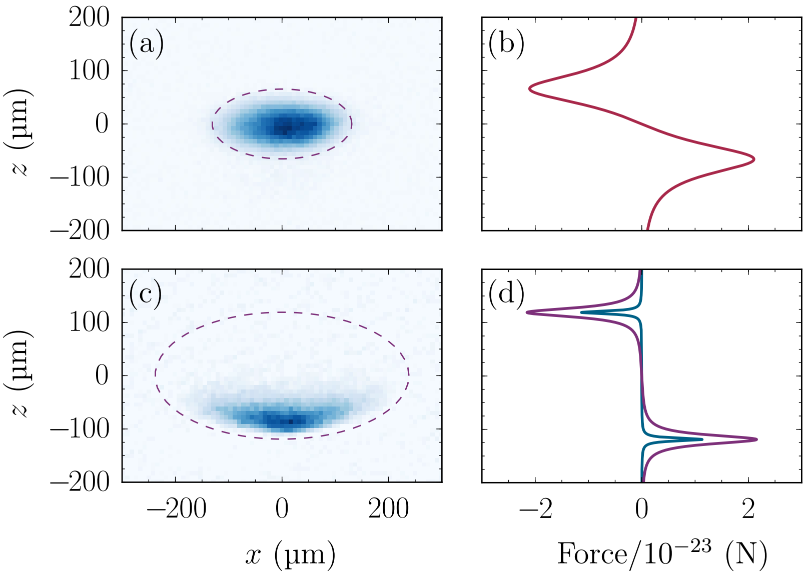

Figure 3.2: Absorption images of the nMOT along with their associated force curves. (a) and (b) correspond to $S = 250$ and $\Delta = -2\pi \times 110\,\text{kHz}$ whilst (c) and (d) correspond to $S = 20$ and $\Delta = -2\pi \times 200\,\text{kHz}$. The force curve associated with $S = 1$ is also shown in (d) for comparison. The dashed ellipse in (a) and (c) shows where $\Delta\omega_z = \Delta$ in the quadrupole field with a gradient of 8 G/cm.

Δ and the magnetic field gradient. However since a photon recoil is sufficient to tune an atom out of resonance with the nMOT beams, recoil effects dominate the scattering behaviour of the atoms. This regime enables the lowest temperatures, ultimately reaching half the photon recoil limit, which for ^{88}Sr is 460 nK [64].

3.2 Numerical models

One approach typically used to simulate MOT dynamics is to make simplifying assumptions about the atomic system and perform a Monte-Carlo [65] integration of the classical equations of motion. This assumes that the atoms experience an average force from the laser beams. Wohlleben [66] and Chaudhuri [67] have used this method to accurately simulate the atomic trajectories of rubidium atoms in a 2D^{+} MOT. This method has also been used to simulate loading into optical traps [68, 69]. For more complex systems where optical pumping must be included, such as molecular MOTs, this model breaks down. A more accurate model is produced using the optical Bloch equations [37]. By performing an adiabatic elimination of the density matrix coherences, one is left with a series of rate equations. Atutov [70] has shown this model to be accurate at modelling a sodium MOT involving optical pumping whilst both Comparat [71] and Tarbutt [72] have utilised this method to study the formation of molecular MOTs. However, as the transition linewidth in a nMOT is so small, the transition is often power broadened, which precludes the conventional adiabatic elimination of the density matrix coherences [71, 72].

To circumvent this problem, we develop a Monte-Carlo model which is based upon the steady-state solution of the optical Bloch equations. This model is applicable not only to the ^{88}Sr 5s^2 ^{1}S$_0$ $\rightarrow$ 5s5p ^{3}P$_1$ transition, but also to the lowest-lying intercombination lines in other divalent atoms. These $J = 0 \rightarrow J = 1$ transitions are completely closed[1], and there is no optical pumping or dark states, as shown in figure 3.3(a). Despite this apparent simplicity, it is still very challenging to fully model the interaction of this four-level system with the spatially varying quadrupole field and laser polarisation, since one must keep track of complex spatially varying phases between the laser beams that appear in the off-diagonal terms in the atomic density matrix. Therefore, we make a significant simplification and treat each Zeeman transition as an independent two-level system, as shown in figure 3.3(b). This amounts to non-conservation of population in the limit of $S \gg 1$ and also neglects absorption and stimulated emission events from laser beams with differing $\boldsymbol{k}$ vectors, which is related to coherences between Zeeman sub-levels. We expect that this is a good approximation in regimes (II) and (III). In these regimes, the atoms fall under gravity until the resonance condition is met and predominantly interact with the laser beam that opposes gravity. The Zeeman splitting between the m_j sublevels is much greater than the transition linewidth, effectively isolating the three Zeeman sublevels, of which the $m_j = -1$ state is most strongly driven due to the helicity of the laser beams. However we expect the model to fail in the "Doppler" regime (I), and we show that this is indeed the case.

---

[1] This is only true for the bosonic isotopes.

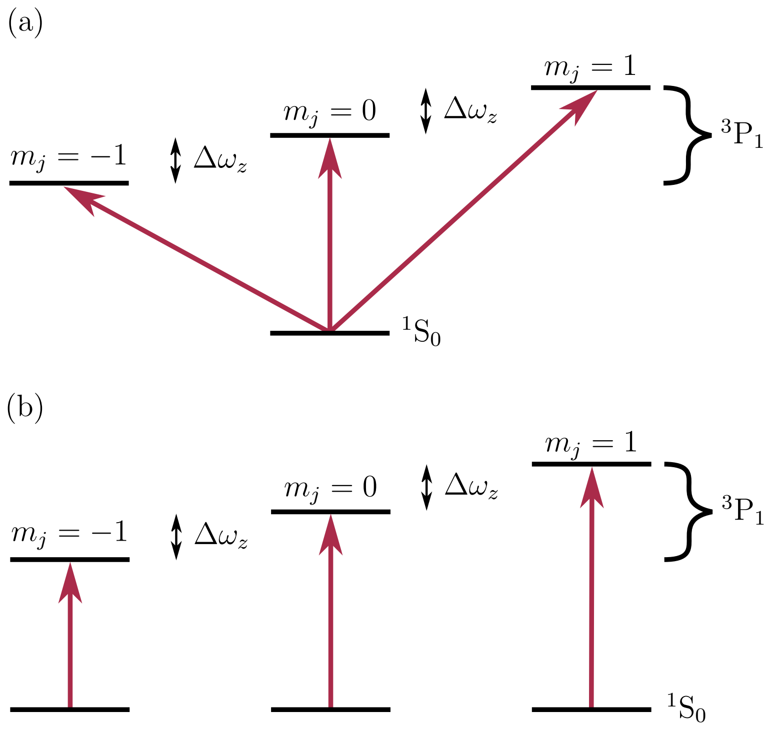

Figure 3.3: (a) Energy level structure of the nMOT. $\Delta\omega_z$ is the Zeeman splitting due to the quadrupole field. (b) Simplified energy level structure used in the simulation.

3.2.1 Mathematical Formalism

We simulate the ^{88}Sr 5s^2 $^1\mathrm{S}_0 \rightarrow$ 5s5p $^3\mathrm{P}_1$ nMOT using the conventions and definitions shown in figure 2.4(b). The nMOT is constructed from three retro-reflected orthogonal laser beams in the laboratory co-ordinate system $\boldsymbol{r} = (x, y, z)$ where the unit vector directions $\hat{\boldsymbol{x}}$, $\hat{\boldsymbol{y}}$ and $\hat{\boldsymbol{z}}$ are shown in figure 2.4(b), and the origin of the coordinate system is taken to be the zero of the quadrupole magnetic field. Each circularly-polarised laser beam i has angular frequency ω_i and wave-vector $\boldsymbol{k_i}$. The helicity of each beam is illustrated in figure 2.4(b). The nMOT quadrupole field $\boldsymbol{B}$ is defined as $\boldsymbol{B} = \gamma\left(x\hat{\boldsymbol{x}} + y\hat{\boldsymbol{y}} - 2z\hat{\boldsymbol{z}}\right)$ where γ is the gradient of the magnetic field along the radial $(\hat{\boldsymbol{x}}, \hat{\boldsymbol{y}})$ directions. The magnetic field splits the 5s5p $^3\mathrm{P}_1$ state into three Zeeman levels j with splittings $\Delta\omega_z = g\mu_\mathrm{B}\left|\boldsymbol{B}\right|/\hbar$ where $g = 3/2$ is the g-factor and μ_B is the Bohr magneton.

To reproduce the macroscopic dynamics of the nMOT, the simulation is performed for $\sim$ 5000 atoms. Initially, the atoms are uniformly, randomly placed into a user-defined ellipsoid in the laboratory frame with position $\boldsymbol{r}$. The atoms are also assigned random velocity vectors $\boldsymbol{v}$ taken from a 3D-Boltzmann distribution with a user defined initial temperature. These initial conditions are chosen to be similar to the final nMOT to reduce the processing time[2]. Typically, an initial temperature of $T = 1\,\mu\mathrm{K}$ is used.

The total simulation time t_{tot} is broken into time-steps of length δt. At each time-step, the probability that each atom scatters a photon from laser i via a transition j is given by

$$\begin{aligned} P_{ij} &= \Gamma_e \rho_{ee}^{ij} \delta t && (3.2.1) \\ &= \frac{\Gamma_e}{2} \frac{W_j S \delta t}{1 + W_j S + 4\left(\Delta_i - \boldsymbol{k_i} \cdot \boldsymbol{v} - \Delta\omega_z^j\right)^2 / \Gamma_e^2} , && (3.2.2) \end{aligned}$$

where ρ_{ee}^{ij} is the steady state excited state population derived from standard two-level optical Bloch equations [37], W_j is a dimensionless coupling strength and $\delta t = 0.1/\Gamma_e$ such that $P_{ij} \ll 1$.

The coupling strength W_j is dependent on the local magnetic field and the polarisation of the nMOT laser beam. Due to the spatial inhomogeneity of the magnetic field, W_j must be calculated as a function of position for each laser beam. This is most easily performed by entering a local atomic frame for the calculation. This frame is defined such that the local z-axis $\boldsymbol{\hat{z}'}$ is directed along the local magnetic field vector. Firstly, the total electric field for each laser beam $\boldsymbol{\mathcal{E}}$ is defined in the laboratory frame in the spherical basis $\boldsymbol{\hat{\epsilon}_q}$ [42, 43] as

$$\boldsymbol{\mathcal{E}} = \sum_q \mathcal{E}^q \boldsymbol{\hat{\epsilon}_q} , \tag{3.2.3}$$

where $\boldsymbol{\mathcal{E}} = (\mathcal{E}^1, \mathcal{E}^0, \mathcal{E}^{-1})$ and

$$\begin{aligned} \mathcal{E}^1 &= -\frac{1}{\sqrt{2}} (\mathcal{E}_x + i\mathcal{E}_y) , && (3.2.4) \\ \mathcal{E}^0 &= \mathcal{E}_z , && (3.2.5) \\ \mathcal{E}^{-1} &= \frac{1}{\sqrt{2}} (\mathcal{E}_x - i\mathcal{E}_y) , && (3.2.6) \end{aligned}$$

---

[2] The simulation is written in Python and makes use of parallelisation packages (psutil) in order to reduce the computation time. A typical running time using a standard desktop computer with an Intel Core i5-4690 Processor with 5000 atoms up to a time of 15 ms is ≈ 1 hour.

where $\mathcal{E}_{x,y,z}$ is the electric field defined in Cartesian coordinates in the laboratory frame. A rotation is then performed to enter the local co-ordinate system of each atom to determine which transitions can be driven along with the associated transition coupling strengths. The rotation matrix is given by

$$\begin{aligned} M_q(\theta) &= UR(\theta)U^\dagger \,, && (3.2.7)\\ &= \frac{1}{2}\begin{pmatrix} 1+\cos(\theta) & -\sqrt{2}\sin(\theta) & 1-\cos(\theta) \\ \sqrt{2}\sin(\theta) & 2\cos(\theta) & -\sqrt{2}\sin(\theta) \\ 1-\cos(\theta) & \sqrt{2}\sin(\theta) & 1+\cos(\theta) \end{pmatrix} \,, && (3.2.8)\end{aligned}$$

where $R(\theta)$ is the rotation matrix which maps $\hat{\boldsymbol{k}}_{\boldsymbol{i}}$ onto $\boldsymbol{B}$ by an angle θ, and U is the transformation from the Cartesian basis to the spherical basis and is given by

$$U = \frac{1}{\sqrt{2}}\begin{pmatrix} -1 & i & 0 \\ 0 & 0 & \sqrt{2} \\ 1 & -i & 0 \end{pmatrix} \,. \tag{3.2.9}$$

This leads to a new polarisation vector $\boldsymbol{\mathcal{E}}' = M_q\boldsymbol{\mathcal{E}}$ where $W_j = |\mathcal{E}^{j\prime}|^2$.

Once P_{ij} is known, random sampling from an uniform distribution is used to determine whether a scattering event occurs or not. If no scattering event occurs, the atom follows its initial trajectory defined in the laboratory frame as

$$\begin{aligned} \boldsymbol{v}' &= \boldsymbol{v} + \boldsymbol{g}\delta t && (3.2.10)\\ \boldsymbol{r}' &= \boldsymbol{r} + \boldsymbol{v}'\delta t + \frac{1}{2}\boldsymbol{g}\delta t^2 \,, && (3.2.11)\end{aligned}$$

where $\boldsymbol{g} = g(0,0,-1)$ is the acceleration due to gravity and the prime notation represents the final atom position or velocity after a time step δt. If a scattering event does occur, the atom evolves as

$$\boldsymbol{v}' = \boldsymbol{v} + \frac{\hbar|\boldsymbol{k}_{\boldsymbol{i}}|}{M}\left(\hat{\boldsymbol{k}}_{\boldsymbol{i}} + \hat{\boldsymbol{k}}_{\boldsymbol{s}}\right) + \boldsymbol{g}\delta t \,, \tag{3.2.12}$$

where $\boldsymbol{k}_{\boldsymbol{i}}$ is the wavevector of the laser from which the atom initially absorbed a photon with $\hat{\boldsymbol{k}}_{\boldsymbol{i}}$ its associated unit vector, and $\hat{\boldsymbol{k}}_{\boldsymbol{s}}$ is a random unit vector representing the direction of spontaneous emission.

During each time step, the atomic positions and velocities are recorded, yielding a complete trajectory of each atom. A simulated absorption image of the nMOT is constructed by histogramming the atomic positions in the $\hat{\boldsymbol{x}}-\hat{\boldsymbol{z}}$ plane and calculating the column density along $\hat{\boldsymbol{y}}$. This is then normalised such that comparisons between theory and experiment can be made. A vertical and horizontal temperature (T_z and T_x) is associated with the motion in the z and x directions by fitting a Maxwell-Boltzmann distribution to the vertical and horizontal components of $\boldsymbol{v}$. This allows us to obtain the spatial, thermal and temporal dynamics of the atom cloud.

3.3 Comparisons to experiment

The experimental apparatus used in this section is described in detail elsewhere [33, 73–75] and later on in this thesis (see chapter 4), so it is not discussed here. Comparisons to experiment are performed with a strontium nMOT formed on the $5s^2\ ^1S_0 \rightarrow 5s5p\ ^3P_1$ transition.

3.3.1 Spatial distribution

As discussed in section 3.1, the properties of a nMOT are significantly dependent on Δ and S. This strong parameter dependence allows us to test the accuracy of

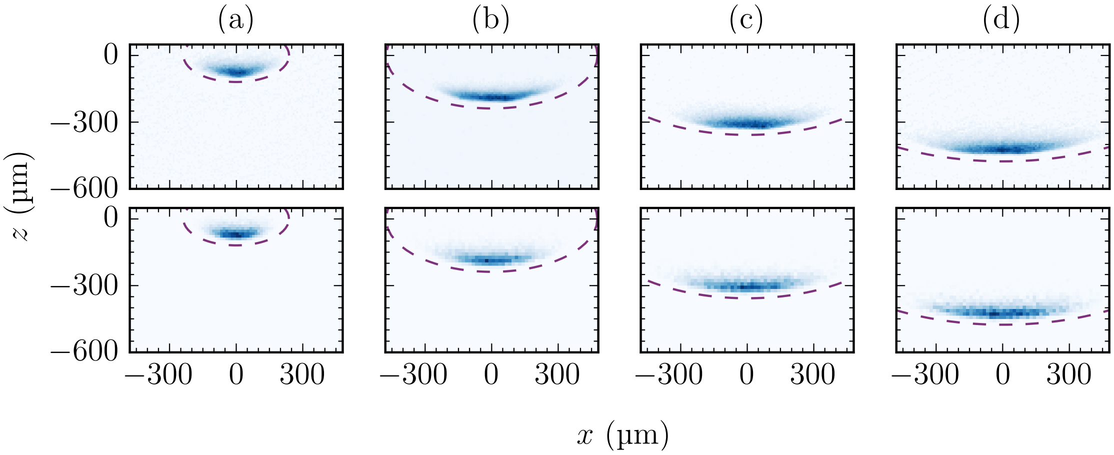

Figure 3.4: Experimental (top row) and theoretical (bottom row) absorption image as a function of nMOT beam detuning with $S = 9$, where $\Delta/2\pi =$ (a) $-200\,\mathrm{kHz}$, (b) $-400\,\mathrm{kHz}$, (c) $-600\,\mathrm{kHz}$ and (d) $-800\,\mathrm{kHz}$. The dashed purple line shows the resonance condition where $\Delta = \Delta\omega_z$.

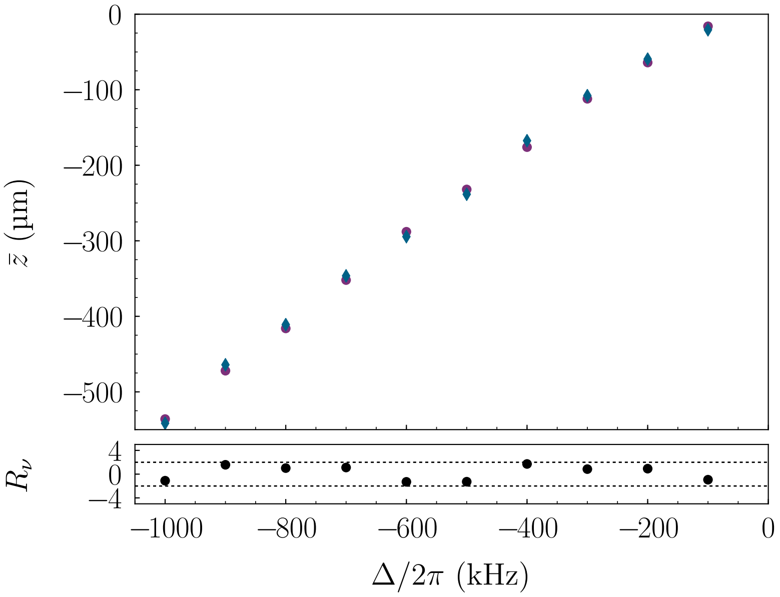

Figure 3.5: Experimental (purple circles) and theoretical (blue diamonds) vertical position of the nMOT as a function of nMOT beam detuning. The dashed black lines show the residuals normalised to their estimated uncertainties $R_\nu = \pm 2$.

the model in a wide variety of nMOT regimes. Firstly, we test the model operating in regime (II) where the width and position of the nMOT are strongly dependent on Δ. The top row of figure 3.4 shows experimental absorption images of the nMOT at four different values of Δ. It is clear that the MOT 'sags' under gravity and forms at lower positions as Δ is decreased. The lower row of figure 3.4 shows the theoretical absorption images obtained from the simulation. We qualitatively observe excellent agreement in position and shape of the nMOT in the absence of fitting parameters.

In order to quantitatively compare the model to the experimental data, the mean vertical position $\bar{z}$ and full width at half maximum (FWHM) of the nMOT were extracted numerically from the experimental and theoretical data. The results are plotted as a function of Δ in figures 3.5 and 3.6 respectively. The residuals normalised to their estimated uncertainties R_ν [76], are shown below each figure. The vertical FWHM saturates as a function of Δ as the width is determined by the temperature of the atoms. The horizontal FWHM however continually increases as the radius of the resonant ellipse is proportional to Δ. We observe excellent agreement between experiment and theory with no adjustable parameters.

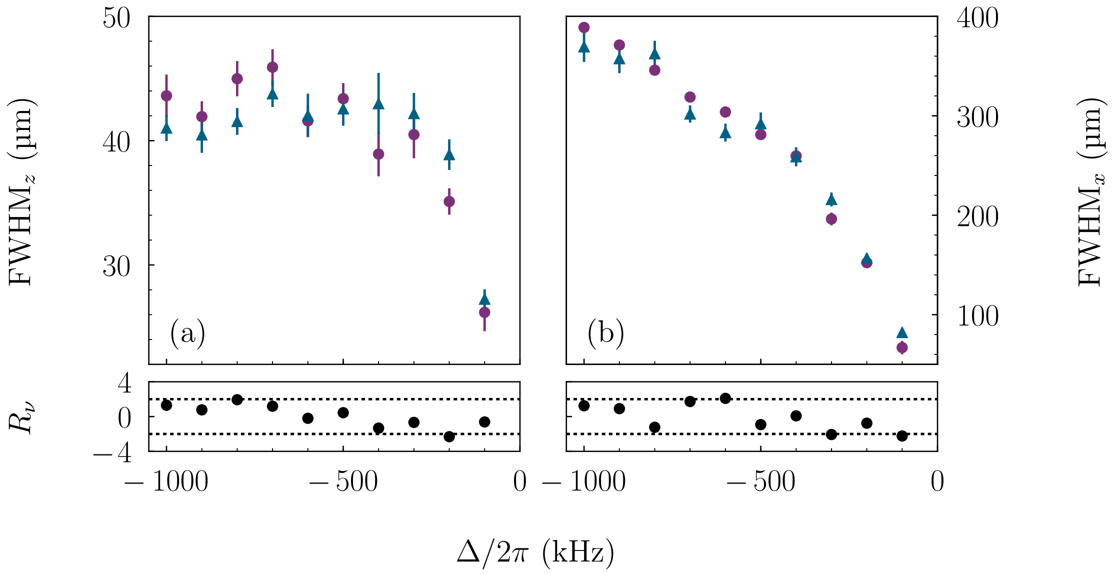

Figure 3.6: Experimental (purple circles) and theoretical (blue diamonds) vertical (a) and horizontal (b) FWHM of the nMOT as a function of nMOT beam detuning. The dashed black lines show the normalised residuals $R_\nu = \pm 2$.

3.3.2 Thermal properties

A more stringent test of the model is provided by the atomic temperature. Unlike the position, which is largely determined by the resonance condition, the nMOT temperature is strongly dependent on the intensity of the cooling beams. As S varies, the nMOT crosses between the different regimes identified in section 3.1. The dependence of the nMOT temperature on Δ for two different values of S is shown in figure 3.7(a). Firstly we consider a nMOT operating close to the quantum regime with $S = 1.9$. The temperature is essentially independent of Δ, since the position of the nMOT just tracks the resonance condition. In this regime, our model is again in excellent agreement with the measurements.

At higher intensity ($S = 60$) the nMOT operates in the power-broadened regime (II). As expected the cloud is hotter, and the temperature is once again largely independent of detuning. The model is in excellent agreement for $|\Delta|/2\pi > 140\,\mathrm{kHz}$, but begins to deviate significantly from experiment close to resonance. Here, the power-broadened linewidth approaches the Zeeman splitting in the excited state. Thus the nMOT crosses over into the conventional "Doppler" regime (I) where the

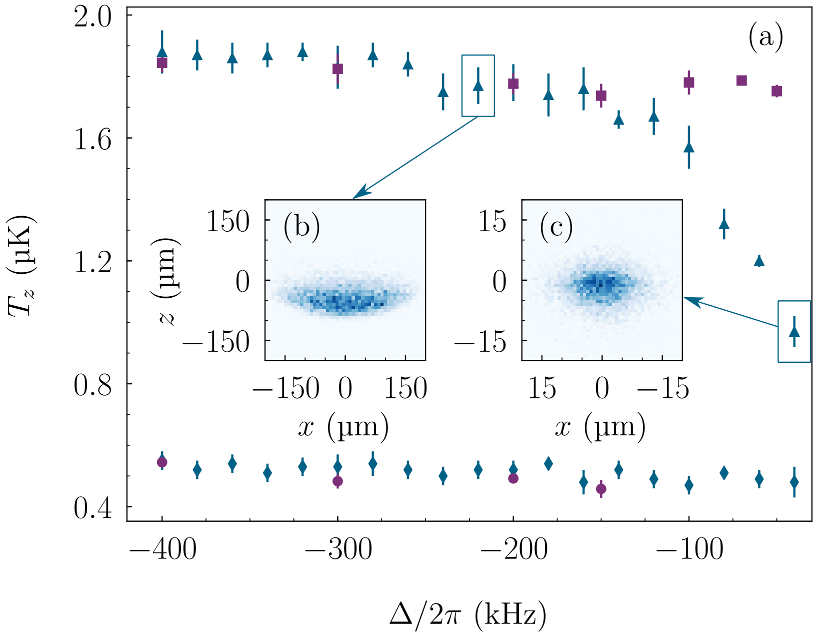

Figure 3.7: (a) The purple circles(squares) and blue diamonds(triangles) represent the measured and simulated nMOT temperatures for $S = 1.9(60)$. (b) and (c) are the theoretical absorption images for nMOT beam detunings of $-2\pi \times 220\,\text{kHz}$ and $-2\pi \times 40\,\text{kHz}$ respectively.

linewidth is dominant, forming near the quadrupole zero, as shown in figure 3.7(c). Our key assumption that the atoms scatter independently on each of the three Zeeman transitions no longer holds, and the model breaks down.

3.3.3 Temporal dynamics

As well as the equilibrium properties, we have also considered whether the model can reproduce the out-of-equilibrium dynamics of the nMOT. To do this, we looked at the response of the temperature to a sudden increase or decrease in the power of the nMOT beams. Initially, the nMOT was allowed to reach equilibrium at $S = S_0$. At $t = 0$, S was suddenly decreased (increased). Experimental measurements of the subsequent cooling (heating) are shown in figure 3.8, along with the results of the simulation. The reduced chi-squared statistics [76] were $\chi^2_\nu = 0.7$ and 1.8 respectively, illustrating that our technique quantitatively reproduces both the steady state and dynamic properties of the nMOT.

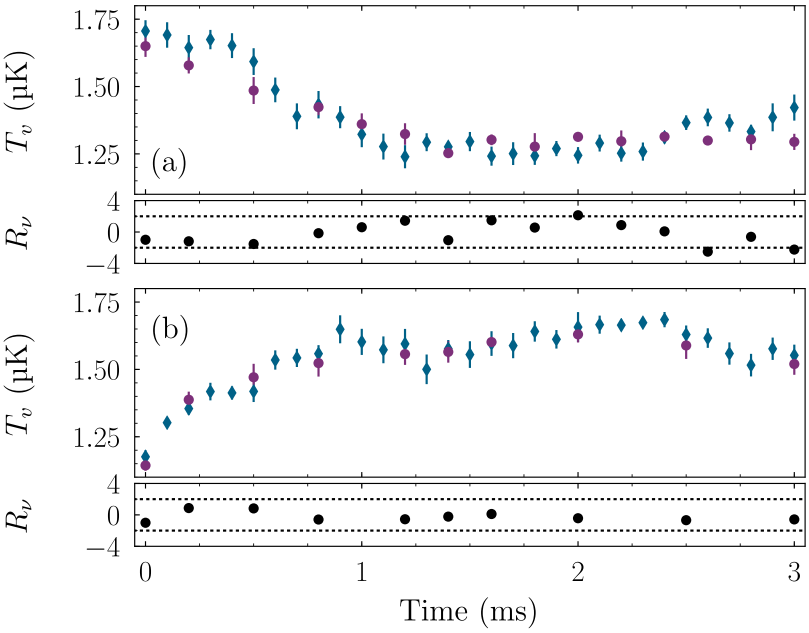

Figure 3.8: Experimental (purple circles) and theoretical (blue diamonds) nMOT temperatures as a function of time after a decrease (a) or increase (b) in nMOT laser beam power. The two nMOT beam powers used here were $S = 14$ and 31. The dashed lines show $R_\nu = \pm 2$.

3.4 A Rydberg dressed nMOT

The work detailed above shows that we are able to quantitatively reproduce the spatial, thermal and temporal dynamics of a nMOT. This therefore creates a solid theoretical understanding upon which we are able to study more complicated physical systems, relevant to the goal of this work. The addition of the dressing laser gives rise to two distinct effects. The first is an AC Stark shift associated with the application of the dressing laser, and the second is the effect of the strong dipole-dipole interactions between the Rydberg states. We initially neglect the dipole-dipole interactions between the Rydberg states and focus on the AC Stark shift induced by the dressing laser.

We extend the Monte-Carlo model presented earlier to include the Rydberg series. Each m_j Zeeman level is connected independently to a Rydberg series, resulting in three, three-level systems. The three-level optical Bloch equations, detailed in

2.3.23, are solved in the steady state using Mathematica. This gives rise to the AC Stark shift of the nMOT transition as well as facilitating the inclusion of an atomic loss rate. The probability of loss due to direct excitation to the Rydberg state $|r_i\rangle$ is given by

$$P = \Gamma_{\mathrm{r}}\rho^i_{rr}\delta t \ , \tag{3.4.13}$$

where Γ_{r} is the Rydberg state decay rate, ρ^i_{rr} is the Rydberg state population for a given transition i and δt is the simulation time-step. This simulates the event that the direct excitation of a Rydberg atom leads to the loss of that atom from the nMOT.

To test the accuracy of the model in the absence of interactions, we compared the simulation to a Rydberg-dressed nMOT coupled to the 5s36d $^3\mathrm{D}_1$ state, in a low density nMOT where the Rydberg-dressed interactions are negligible. The experiments began with the formation of a nMOT. The 5s5p $^3\mathrm{P}_1$ was coupled to the Rydberg state $|r\rangle$ = 5s36d $^3\mathrm{D}_1$, for which the interactions are weakly attractive [34], using a horizontally propagating dressing laser. This was linearly polarized in the $\hat{\boldsymbol{z}}$ direction. The 1/e^2 beam radius was 120 µm (160 µm) in the horizontal (vertical) direction, and the Rabi frequency Ω was measured using Autler-Townes splitting [45]. After dressing for a time t_{d}, the cloud was imaged at an angle of 30° to the coupling beam via absorption on the 5s^2 $^1\mathrm{S}_0 \rightarrow$ 5s5p $^1\mathrm{P}_1$ transition.

3.4.1 AC-Stark Shift of the nMOT

As discussed in 3.1, the force on the atoms due to the nMOT beams are weak compared to gravity. Therefore the atoms in the nMOT fall under gravity until the Zeeman shift, induced by the nMOT quadrupole field, matches the nMOT beam detuning. The resulting resonance condition forms an elliptical 'shell' around the quadrupole centre. The addition of the dressing beam causes a spatially-dependent AC Stark shift (with a maximum shift of Δ_{AC}) of the nMOT cooling transition, due to its Gaussian intensity profile. This causes a distortion of the energy contours and therefore a distortion of the nMOT shape. An example of the distortion of the contours of constant energy are shown in figure 3.9(a). The distortion is strikingly dependent on the sign of Δ_{D}. For the case of $\Delta_{\mathrm{D}} < 0$, the resonance condition

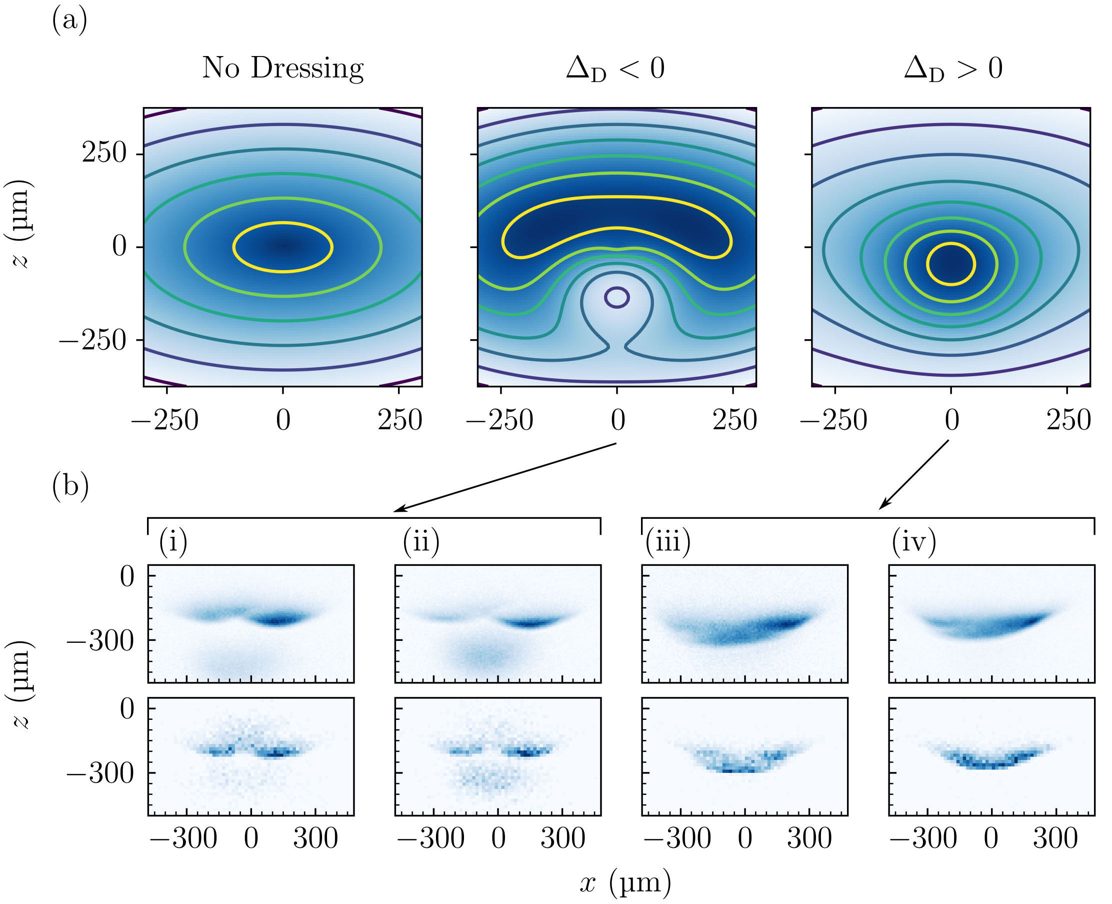

Figure 3.9: (a) Contours of constant energy of the $m_j = -1$ state in the presence of the magnetic quadrupole field, with a vertical gradient of $8\,\mathrm{G cm^{-1}}$, for the case of no dressing and dressing with $\Omega/2\pi = 4\,\mathrm{MHz}$ for $\Delta_\mathrm{D}/2\pi = -12\,\mathrm{MHz}$ or $\Delta_\mathrm{D}/2\pi = 12\,\mathrm{MHz}$. (b) The top (experimental) and bottom (theoretical) rows show absorption images of the nMOT coupled to the 5s36d $^3\mathrm{D}_1$ Rydberg state with detunings and Rabi frequencies of $\Omega/2\pi = 2.1\,\mathrm{MHz}$, $\Delta/2\pi = -400\,\mathrm{kHz}$ and $\Delta_\mathrm{D}/2\pi =$ (i) $-12\,\mathrm{MHz}$, (ii) $-6\,\mathrm{MHz}$, (iii) $6\,\mathrm{MHz}$ and (iv) $12\,\mathrm{MHz}$.

becomes shallower and ‘double-welled’, leading to a spreading of the nMOT and a weakening of the confinement. Conversely, for $\Delta_\mathrm{D} > 0$, the resonance condition becomes more deeply furrowed, resulting in an increased confinement of the nMOT.

A comparison between experimental images and the adapted Monte-Carlo model is shown in figure 3.9(b). The top row shows experimental images of the nMOT in the presence of the dressing beam. For $\Delta_\mathrm{D} < 0$, the nMOT forms in two separate locations, in agreement with the ‘double-welled’ distortion of figure 3.9(a). For

$\Delta_\mathrm{D} > 0$, the nMOT forms in lower positions, creating a vertically elongated nMOT. This is once again in qualitative agreement with figure 3.9(a). The bottom row of figure 3.9 shows the results of the adapted Monte-Carlo nMOT model. Here the only fit parameter is the position of the dressing beam with respect to the nMOT, in this case 185 µm below and 45 µm left of the quadrupole centre. We observe qualitative agreement between the experimental and theoretical absorption images, demonstrating that the adapted Monte-Carlo model is able to accurately predict the nMOT dynamics in the presence of the dressing beam. It is critical to understand this effect in the non-interacting regime before one can look for Rydberg-dressed interactions.

3.4.2 Compensated nMOT

As illustrated in figure 3.9, a consequence of applying the dressing beam is a position shift of the nMOT. When the nMOT is smaller than the dressing beam, this tends to drive atoms out of the region of highest intensity of the dressing beam. This limits the magnitude of the Rydberg-dressed interaction effect one is able to observe. This effect is shown in figure 3.10(a) and (b). Figure 3.10(a) shows the nMOT in the absence of the dressing beam and figure 3.10(b) shows the nMOT in the presence of the dressing beam. The dashed line indicates the vertical position of the undressed nMOT and clearly shows that the nMOT has moved. A solution to this problem is to compensate the AC Stark shift of the cooling transition so that the atoms in the nMOT remain in their initial position. By adjusting the detuning of the nMOT beams when the dressing beam is applied to $\Delta \rightarrow \Delta - \Delta_\mathrm{AC}$, the AC Stark shift of the cooling transition induced by the dressing beam is compensated, and the nMOT remains at its original position (figure 3.10(c)). The vertical shift shown in figure 3.10(b) is eliminated for a detuning compensation of +300 kHz, close to the calculated peak AC Stark shift of $\Delta_\mathrm{AC}/2\pi = +325\,\mathrm{kHz}$. Note, that the nMOT cooling beams are now blue-detuned with respect to the bare transition. Therefore the compensated nMOT only traps Rydberg-dressed atoms. Atoms which are not at the centre of the dressing beam do not experience the correct detuning of the cooling light and are observed falling away under gravity (figure 3.10(c)).

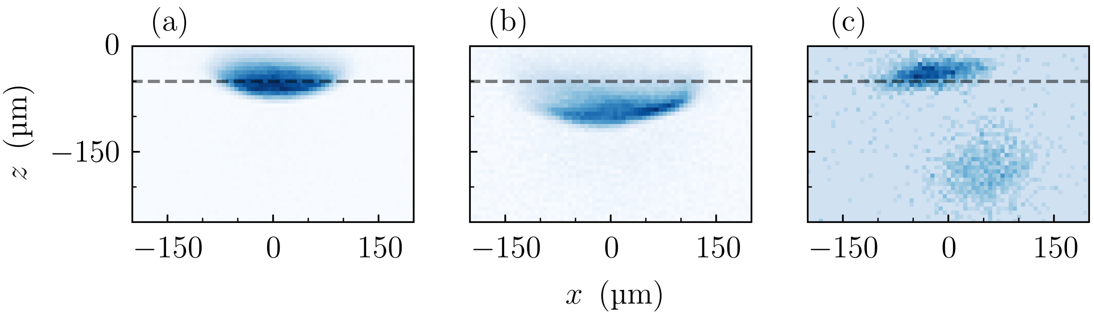

Figure 3.10: Images of (a) the undressed nMOT with $\Delta/2\pi = -110\,\mathrm{kHz}$, (b) after 5 ms of dressing with $\Delta/2\pi = -110\,\mathrm{kHz}$ (c) after 5 ms of dressing with the detuning altered to $\Delta/2\pi = +190\,\mathrm{kHz}$. The nMOT is coupled to the 5s36d $^3\mathrm{D}_1$ Rydberg state with $\Omega/2\pi = 4\,\mathrm{MHz}$ and $\Delta_\mathrm{D}/2\pi = 12\,\mathrm{MHz}$. The dashed line indicates the position of the undressed nMOT.

An important question is whether the Rydberg-dressed atoms in the compensated nMOT are undergoing continuous laser cooling. To test this, the temperature of the atoms was measured as a function of dressing time using the ballistic expansion technique. This is shown by the blue diamonds in figure 3.11. We initially observe heating in the first millisecond, however the temperature returns to that of the initial undressed nMOT after a period of $\sim 3\,\mathrm{ms}$. This is direct evidence that Rydberg-dressed atoms are being actively cooled. These temporal dynamics can be simulated using the adapted Monte-Carlo model above. This is shown by the purple circles in figure 3.11. We observe excellent quantitative agreement between theory and experiment, where the only fit parameter is the position of the dressing beam relative to the centre of the quadrupole magnetic field, in this case 20 µm below and 60 µm right of the quadrupole centre. The simulation suggests that the initial heating is caused by the spatial dependence of the AC Stark shift induced by the dressing beam, which causes an increased scattering rate in particular regions of the cloud as the atoms find themselves at a non-equilibrium position. Subsequent cooling then occurs as the cloud shape adapts to match the new spatially-dependent resonance condition.

We have shown in this section that we are able to accurately model the spatial distribution of atoms in the Rydberg-dressed nMOT. This now allows us to incor-

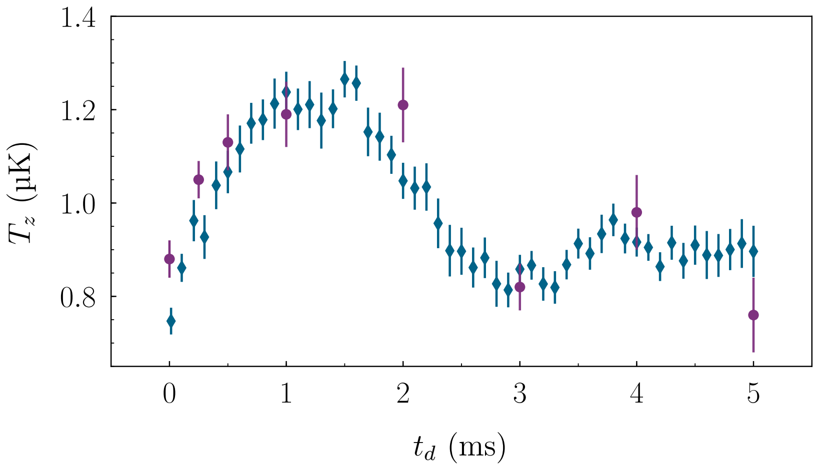

Figure 3.11: Measured (purple circles) and simulated (blue diamonds) temperature in the vertical (z) direction T_z versus dressing time t_d for the nMOT coupled to the 5s36d ^{3}D$_1$ Rydberg state with $\Omega/2\pi = 4\,\text{MHz}$, $\Delta_\text{D}/2\pi = 12\,\text{MHz}$ and $\Delta_\text{MOT}/2\pi = 190\,\text{kHz}$. Errorbars are the standard error on the mean.

porate density dependent interactions into the model. However, as the Rydberg-dressed interactions only occur between atoms in the dressed state, we must first estimate the fraction of atoms in the dressed-state η_d. Naively, one may expect that the steady-state of the three-level Bloch equations would lead to an accurate value of ρ_{ee}. However, due to the motion of the atoms in the quadrupole field, this is not the case. We estimate η_d by taking the average value of ρ_{ee} calculated from the simulation. Fig. 3.12 shows η_d as a function of S for two experimental configurations. The first (blue diamonds) is where the power in all MOT beam directions is equal. The second (purple circles) is where the power of the MOT beam in the vertical direction is three times that of the other MOT beams. One would expect that as S is increased, the population in the excited should saturate to $\rho_{ee} = 0.5$. The model suggests however that this regime is not immediately achievable. This is due to the frequency shift due to the atomic recoil following the absorption or emission of a photon, and the fact that the atoms mainly interact with the nMOT beam which opposes gravity.

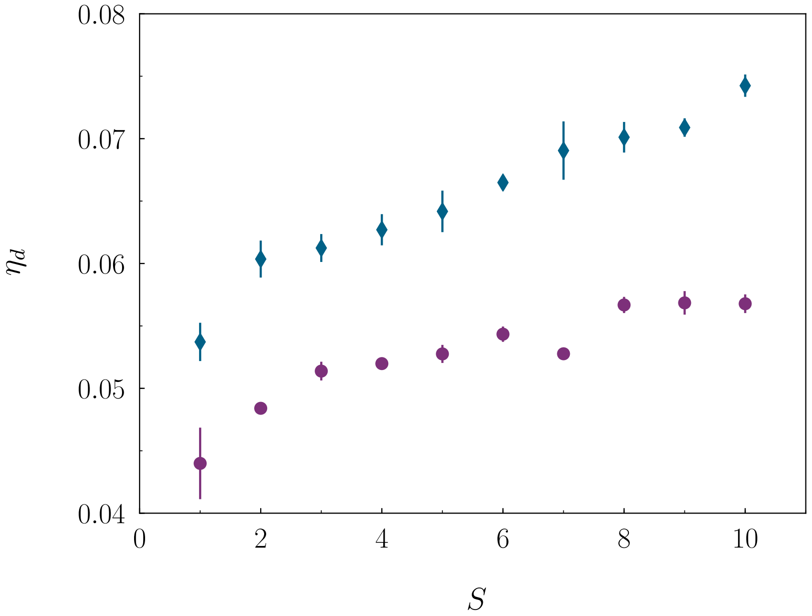

Figure 3.12: The average $^3\mathrm{P}_1$ population as a function of nMOT beam power for beam powers in a ratio of 1:1:1 (blue diamonds) and 1:1:3 (red circles) where the ratio is between $\hat{\boldsymbol{x}} : \hat{\boldsymbol{y}} : \hat{\boldsymbol{z}}$ laser beam axes. The error bar shows the standard error on the mean.

3.4.3 Inclusion of a mean-field interaction

Common approximations used in simulating interacting many-body systems [77–82] are not able to be fully utilised in the simulation of a Rydberg-dressed nMOT, as it operates in a complex regime where the interaction strength, dissipation and kinetic energy are all comparable in scale. A full theoretical model must include correlations between atoms as the Rydberg-dressed interactions correlates the scattering dynamics of neighbouring atoms. The coupling of these scattering correlations to atomic motion is a formidable theoretical challenge and beyond the scope of this work. For this reason, we consider a first-order mean-field approximation to the Rydberg-dressed potential. The collective energy shift V_c of N_c atoms within a range $r < R_c$ is given by 2.2.21. We therefore define an average energy shift per atom as $\bar{V} = V_c/N_c$, which is the mean-field interaction. We also approximate the

Rydberg-dressed potential to that of a step-function, given by

$$\bar{V}\left(N\left(\boldsymbol{r'}\right),\boldsymbol{r}\right)=\frac{N\left(\boldsymbol{r'}\right)-1}{2}\eta_d V_0 \qquad \text{for } \left|\boldsymbol{r}-\boldsymbol{r'}\right|<R_C\ , \tag{3.4.14}$$

$$\bar{V}\left(N\left(\boldsymbol{r'}\right),\boldsymbol{r}\right)=0 \qquad \text{for } \left|\boldsymbol{r}-\boldsymbol{r'}\right|>R_C\ , \tag{3.4.15}$$

where $N\left(\boldsymbol{r'}\right)=\pi R_c^2\rho_{2\mathrm{D}}\left(\boldsymbol{r'}\right)$ [83, 84]. Here the two dimensional density $\rho_{2\mathrm{D}}\left(\boldsymbol{r'}\right)$ is used as the simulation is reduced to two-dimensions to reduce the computation time. The consequence of 3.4.14 is an additional energy shift $\bar{V}\left(N\left(\boldsymbol{r'}\right)\right)/\hbar$ of the cooling transition that depends on the local atomic density $\rho_{2\mathrm{D}}\left(\boldsymbol{r'}\right)$.

This density-dependent interaction is added in to the model as follows. At each time-step, the atomic positions are histogrammed in both dimensions using a bin width of $2R_c$. This creates a grid of the local density distribution, with a characteristic length-scale R_c. The local atomic density is then used to calculate $\bar{V}$ for each atom at a given spatial co-ordinate. At each time-step, the local mean-field interaction $\bar{V}$ is added to the local detuning of each atom. This process is repeated, resulting in a density distribution in the presence of interactions and one-body loss from the Rydberg state.

The achievable interaction strength of Rydberg-dressed interactions in the nMOT is currently limited by the non-uniform spatial profile of the dressing beam causing a reduction in atomic density [46,85]. This is because it is only possible to compensate a small fraction of the nMOT due to the non-uniform AC Stark shift of the cooling transition. However, this can be overcome by creating a flat-top beam. With a flat-top beam, it should be possible compensate the whole nMOT, and therefore retain sufficient atomic density to observe interaction effects. In this section, we discuss the possible observables of Rydberg-dressed interactions. We also add a mean-field interaction to the Monte-Carlo model above as an attempt to simulate a Rydberg-dressed nMOT in the presence of strong interactions.

We simulate the effect of Rydberg-dressed interactions on a nMOT using achievable experimental parameters outlined in [85]. The results are shown in figure 3.13(a) and (c) for a uniform intensity $300\times100\,\mu\mathrm{m}$ dressing beam with power 1 W, coupling the upper state of the nMOT cooling transition to the 5s36d $^3\mathrm{D}_2$ state. The upper plot shows a vertical slice through the centre of the simulated nMOT for a

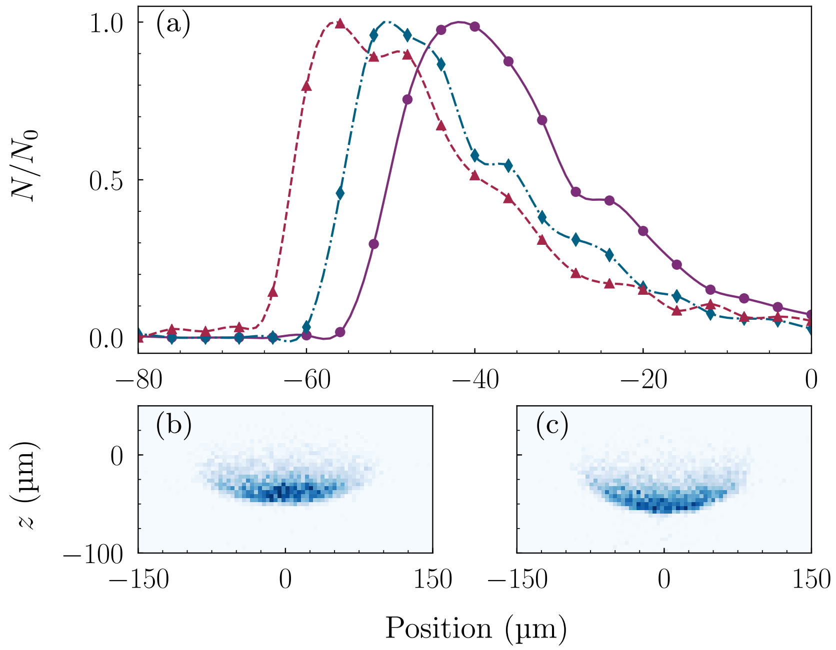

Figure 3.13: (a) Vertical slices through the centre ($x = 0$) of the simulated density distribution for parameters: non-interacting ($\bar{V}_c = 0$ (purple circles)), $\epsilon^2 = 0.007$, $\bar{V}_c = 2.3$ (blue diamonds) and $\epsilon^2 = 0.014$, $\bar{V}_c = 3.4$ (red triangles). The lines are a guide to the eye. Images show the full 2D density distribution for the (b) non-interacting ($\bar{V}/\hbar\Gamma = 0$) (c) interacting ($\bar{V}/\hbar\Gamma = 3.4$) clouds.

non-interacting nMOT (purple circles), an interacting nMOT with dressed Rydberg fraction $\epsilon^2 = 0.007$ (blue diamonds) and an interacting nMOT with dressed Rydberg fraction $\epsilon^2 = 0.014$ (red triangles). The interaction causes a density-dependent shift in the vertical position of the cloud. As the Rydberg-dressed interactions are dependent on the local atomic density, the nMOT seems to 'bend', since the interaction effect is larger in the dense central region than in the wings of the nMOT. These changes in the atomic distribution are comparable to those used to study strong interactions in superfluid systems [86,87].

3.4.4 Outlook

Since the mean field interaction is greater than the transition linewidth $\left(\bar{V}/\hbar\Gamma > 1\right)$, one would expect to observe beyond mean-field effects. The Rydberg-dressed interaction leads to strong correlations in the scattering dynamics of neighbouring atoms.

These are are mapped to and from the motional state of the atoms by the atomic recoil shift, which exceeds the linewidth Γ. These correlations may lead to novel spatial and dynamical effects not captured by our model. There are a variety of possible beyond mean-field signatures of Rydberg-dressed interactions. One possible consequence could be the semi-crystallisation of the nMOT, where the suppression of scattering in dense regions induces a spatially correlated system. Another possible example could be Sisyphus-like cooling [46] induced by the Rydberg-dressed potential.

3.5 Loading into a FORT

Having shown the success of extending the Monte-Carlo model to simulating a Rydberg-dressed nMOT, we now turn our attention to the loading of a FORT. We include the effect of FORT beams in our model by considering the conservative optical dipole force experienced by atoms in the ground state. We therefore include an additional acceleration in the Newtonian dynamics part of the model, given by

$$\boldsymbol{a}_{\mathrm{DT}} = -\frac{1}{M}\nabla U\left(x, y, z\right) \ . \tag{3.5.16}$$

This assumption is valid when the time-scale for the atom to experience a significant change in potential is comparable to $1/\Gamma$. To ensure the validity of this assumption, we simulate the loading of a FORT where $w > 15\,\mu\mathrm{m}$.

In order to compare this adaptation to experimental results, we simulated the experiment performed by Ido *et al.* [88]. Their FORT consisted of two crossed laser beams with $1/\mathrm{e}^2$ radius of 28 µm, operating at 800 nm. The differential AC Stark shift between the ground and excited states at this wavelength is negligible, which allows the simultaneous use of trapping and Doppler cooling. The FORT was loaded by first forming a single-frequency nMOT operating at $\Delta = -200\,\mathrm{kHz}$ with a total beam intensity of $S = 18$. While the nMOT was running, the FORT beams were overlapped with the nMOT for a total time of 35 ms before the nMOT beams were switched off. The temperature of the atoms in the FORT was subsequently measured using time-of-flight expansion.

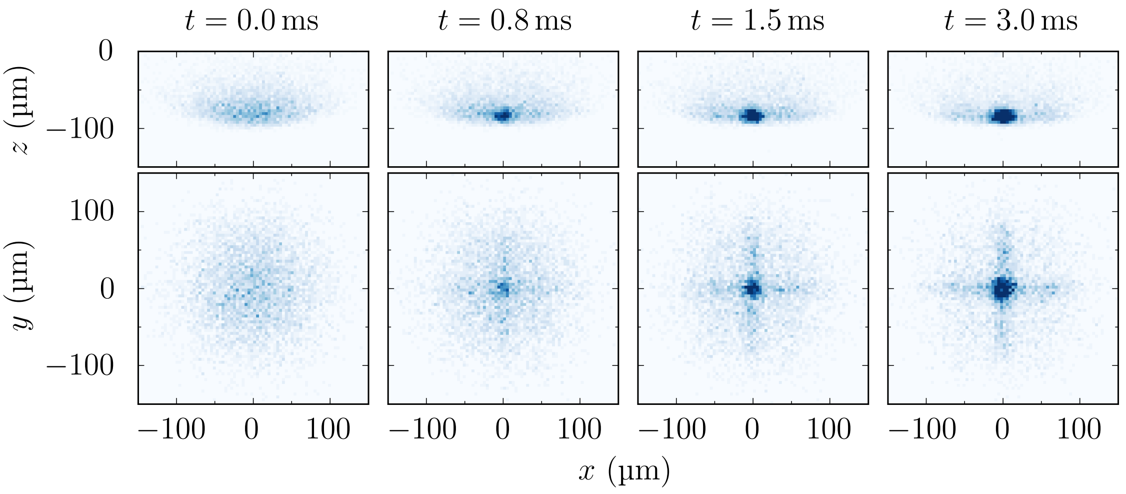

Figure 3.14: Theoretical nMOT dynamics of the simulated crossed FORT with a trap depth of 5 µK. The top and bottom row shows a theoretical absorption image in the $\hat{\boldsymbol{x}} - \hat{\boldsymbol{z}}$ and $\hat{\boldsymbol{x}} - \hat{\boldsymbol{y}}$ plane respectively. All images in each row have the same colour-scale in order to show particle dynamics.

The geometry of the dipole-trapping beams used in the experiment results in a dipole potential of

$$U\left(x, y, z\right) = U_0 \left(\mathrm{e}^{-2\left[(\mathrm{x}-\mathrm{x}_0)^2 + (\mathrm{z}-\mathrm{z}_0)^2\right]/\mathrm{w}^2} + \mathrm{e}^{-2\left[(\mathrm{y}-\mathrm{y}_0)^2 + (\mathrm{z}-\mathrm{z}_0)^2\right]/\mathrm{w}^2} \right) \,, \tag{3.5.17}$$

where U_0 is the trap depth, x_0, y_0 and z_0 are linear offsets in the $\hat{\boldsymbol{x}}$, $\hat{\boldsymbol{y}}$ and $\hat{\boldsymbol{z}}$ directions respectively and w is the $1/e^2$ radius of the FORT beams. Figure 3.14 shows the simulated effect of applying the crossed FORT beams to the nMOT as a function of time. The atoms clearly move into the high intensity region where the FORT beams intersect. We also observe a small number of atoms leaking into each individual FORT beam which is in qualitative agreement with experimental observations. Ido *et al.* typically capture ≈ 20 % of the atoms from the nMOT into the FORT. However, the model predicts a value of approximately double this. We attribute this difference to the lack of collisional losses in the model.

To make a quantitative comparison with experiment, we simulate the temperature of atoms trapped in the FORT as a function of U_0, assuming the only cooling mechanism is laser cooling. The experimental measurements shown in figure 3.15 exhibit a linear dependence, with the temperature varying in the range $0.1 - 0.2\;U_0$. Also shown is the simulated temperature of the atoms captured in the FORT. The

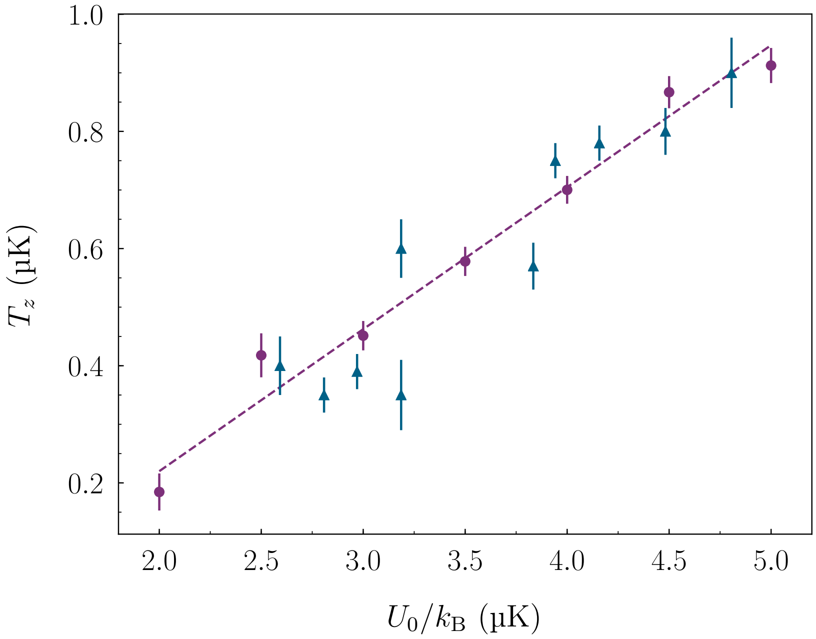

Figure 3.15: Experimental (blue triangles) and theoretical (purple circles) temperatures of the atoms in the crossed FORT as a function of trap depth. The dashed line is a linear fit to the simulated atom temperature. Experimental data taken from [88].

error bars on the simulated temperature are estimated from the statistical error in the fit of the Maxwell-Boltzmann distribution to the velocity distribution. We clearly observe excellent agreement between theory and experiment, once again in the absence of any adjustable fitting parameters.

Unfortunately, we are not able to use this model to gain further insight into the loading of microtraps, as our approximation to the dynamics of the system break down. This is because $1/\Gamma \approx t_{\mathrm{dip}}$, where t_{dip} is the time required for an atom to travel a distance $2w_0$. This simulation does however demonstrate that it is the interplay between the optical dipole force and laser cooling that sets the atomic temperature in the FORT

3.6 Summary

In this chapter, we have shown that it is possible to quantitatively simulate the spatial, thermal and temporal dynamics of a nMOT. This has allowed us to study a Rydberg-dressed nMOT, where we have shown that is is possible to coherently admix a Rydberg state into the narrow intercombination transitions, a vital tool for the engineering of Rydberg-dressed interactions. We have also briefly discussed the loading dynamics of a FORT, and are now in a position to develop the technology to create a strontium microtrap.

Chapter 4

Designing a microtrap for ultracold Sr

Having demonstrated the coherent admixture of a Rydberg state into the 5s5p $^3P_1$ state, we are now faced with the challenge of trapping a single strontium atom in an optical microtrap. The pioneering work by Schlosser *et al.* [89] demonstrated that if the trapping volume of a microtrap is small enough, then two-body collisions dominate the loading process and one can enter a 'Collisional Blockade' regime where it is only possible to load one atom into the microtrap. This experiment utilised a nine-element in-vacuo objective made from spherical lenses to focus the dipole trap light to approximately 0.7 µm. It should be possible to enter this collisional blockade regime in strontium as the two-body light-assisted collision loss rate $\beta \approx 1 \times 10^{-9}\,\mathrm{cm^3 s^{-1}}$ [90] is comparable to that of rubidium $\beta = (3.1 \pm 0.2) \times 10^{-8}\,\mathrm{cm^3 s^{-1}}$ [91]. Although the experiment produced groundbreaking results, the objective was expensive and technically challenging to construct. More recently, due to advances in manufacture, it has been possible to replace cumbersome multi-lens objectives with single aspheric lenses [92].

The previous experimental apparatus was designed and constructed by J. Millen and M. P. A. Jones [73], and is shown schematically in figure 4.1. The experiment is constructed from three main sections. The first section is a strontium oven which is filled with strontium metal and heated to ∼ 700 K. Inside the oven is an array of

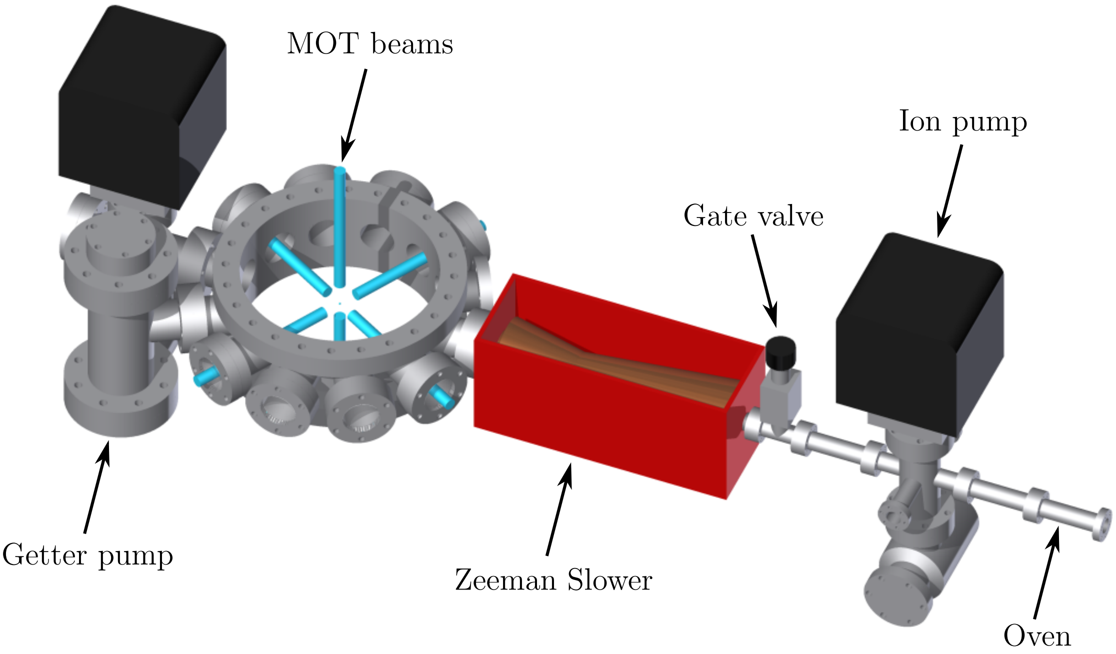

Figure 4.1: Sketch of the current experimental vacuum chamber showing the main constituents. Diagram adapted from [74].

capillary tubes which produces a tightly collimated jet of strontium atoms. The jet of strontium atoms pass through a gate valve and into a Zeeman slower. The cooled atoms then enter the main chamber which is a DN200 pancake chamber with twelve horizontal DN40 flanges and two vertical flanges. The 'innards' of the main chamber consists of a pair of MOT coils and four pairs of electrodes in a split-ring geometry which are mounted onto the top flange of the main chamber. A micro-channel plate (MCP) is also mounted on a horizontal flange of the main chamber.

The previous apparatus was not capable of creating a microtrap as a high numerical objective is required. Due to the diameter of the main chamber, it is not possible to create a microtrap with the objective placed outside vacuum. We therefore require a new experimental innards which facilitates the production of microtraps of the order of 1 µm. Here we focus on the creation of microtraps at three wavelengths; 813 nm, 914 nm, and 532 nm. The reason for this is two-fold. The magic wavelength of the 5s5p $^3P_0$ and 5s5p $^3P_1$ states are at 813 nm [93] and 914 nm [94] respectively. We therefore wish to work towards microtraps at these wavelengths as the reduction in differential AC Stark shift is critical for the spin squeezing protocol [7]. Secondly, it is predicted that it is possible to optically trap Rydberg atoms for trapping wavelengths less than 580 nm [27]. We consider microtraps operating at 532 nm as lasers operating at this wavelength are readily available and offer large power outputs.

In this chapter, we will calculate the polarisability of all the relevant states of strontium, after which we detail the design and construction of the experimental innards. We also detail improvement to the rest of the experimental apparatus, which have made the experiment significantly more reliable.

4.1 Strontium polarisability calculations

In order to create a suitable microtrap for the manipulation of single atoms, the wavelength of the trap must be such that the direct excitation from the microtrap light is minimised as well as providing deep enough potentials for reasonable amounts of laser power. One must also take into consideration the differential shift between cooling transitions as this is what limits the loading of atoms into the microtrap. To analyse what wavelengths are best for trapping strontium, we have calculated the polarisability of the four most relevant states ($5s^2\ {}^1S_0$, $5s5p\ {}^1P_1$, $5s4d\ {}^1D_2$, and $5s5p\ {}^3P_1$) using the formalism detailed in 2.2.2. The first state is the ground state of strontium, the next two are relevant to laser cooling of strontium on the broad dipole-allowed transition and the last state is relevant to laser cooling strontium on the narrow inter-combination line. The transitions which couple most strongly to these four states are summarised in figure 4.2.

To calculate the polarisability, we simply combine equations 2.2.14 and 2.2.15 with 2.2.13. We are therefore left with the task of finding all the relevant energies and transition rates. The transitions from the $5s^2\ {}^1S_0$ and $5s5p\ {}^3P_1$ states have been studied in detail and are well documented [32, 44], due to the study of strontium lattice clocks. For the $5s5p\ {}^1P_1$ and $5s4d\ {}^1D_2$ states however, there is no compilation of relevant transitions. We therefore tabulate the available transitions and rates from both the $5s5p\ {}^1P_1$ and $5s4d\ {}^1D_2$ states. These are shown in table 4.1. The asterisk denotes where the only available information is a theoretical prediction.

With the full set of state energies and transition rates, we can now calculate the

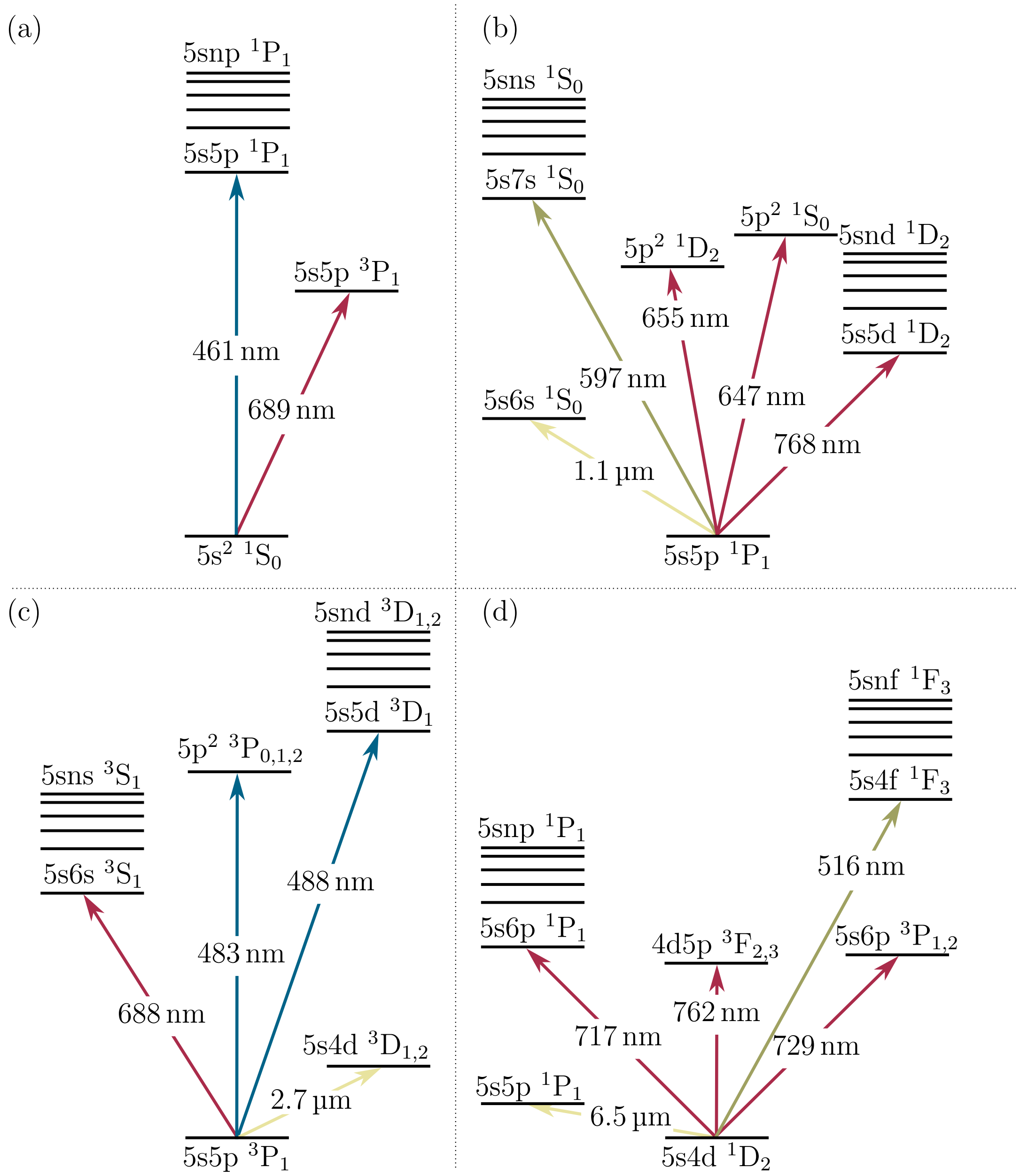

Figure 4.2: Transitions from the relevant states in this experiment. (a) the ground state; (b) upper-state of the broad cooling transition; (c) upper-state of the narrow cooling transition; (d) intermediate state to which the upper-state of the broad cooling transition decays. The stacked lines in the diagram represent a series of energy levels with the same orbital angular momentum but different principal quantum number. Data taken from [32, 44, 95–97].

State	**Energy**	**A_T**
5s5p ^{1}P$_1$	**(cm^{-1})**	**(10^6 s^{-1})**
5s5p ^{1}P$_1$	21698.482(4)	-
5s^2 ^{1}S$_0$	0	190.01(1)
5s6s ^{1}S$_0$	30591.83(2)	19(2)*
5s7s ^{1}S$_0$	38444.022(7)	47(4)*
5s8s ^{1}S$_0$	41052.33(2)	7.4(7)*
5s9s ^{1}S$_0$	42596.57(2)	3.3(3)*
5s10s ^{1}S$_0$	43512.166(1)	1.9(2)*
5s11s ^{1}S$_0$	44097.122(1)	1.2(1)*
5s4d ^{1}D$_2$	20149.685(3)	0.017(7)*
5s5d ^{1}D$_2$	34727.447(5)	7(3)
5s6d ^{1}D$_2$	39733.067(9)	22(2)*
5s7d ^{1}D$_2$	41831.45(2)	6.6(7)*
5s8d ^{1}D$_2$	43021.06(2)	2.1(2)*
5s9d ^{1}D$_2$	43755.76(3)	0.56(6)*
5p^2 ^{1}D$_2$	36960.842(5)	89(2)
5p^2 ^{1}S$_0$	37160.234(5)	29(3)*

State	**Energy**	**A_T**
5s4d ^{1}D$_2$	**(cm^{-1})**	**(10^6 s^{-1})**
5s4d ^{1}D$_2$	20149.685(3)	-
5s5p ^{1}P$_1$	21698.482(4)	0.017(7)*
5s6p ^{1}P$_1$	34098.404(6)	9.4(2)
5s7p ^{1}P$_1$	38906.86(1)	17(3)
5s8p ^{1}P$_1$	42462.14(1)	19(4)
5s9p ^{1}P$_1$	43328.04(7)	13(4)
4d5p ^{3}F$_2$	33266.851(3)	7.8(5)
4d5p ^{3}F$_3$	33589.709(7)	0.5(3)
4d5p ^{1}D$_2$	33826.899(3)	39(8)
4d5p ^{3}P$_2$	37336.591(4)	0.30(2)
4d5p ^{1}F$_3$	38007.74(2)	0.30(8)
4d5p ^{1}P$_1$	41172.05(1)	21(4)
5s6p ^{3}P$_1$	33868.317(6)	1.6(3)
5s6p ^{3}P$_2$	33973.065(4)	6(1)
5s4f ^{1}F$_3$	39539.013(7)	27(9)
5s5f ^{1}F$_3$	41519.0(2)	19(5)
5s6f ^{1}F$_3$	42839.59(3)	12(3)
5s7f ^{1}F$_3$	43656.22(3)	7.7(2)

Table 4.1: The tables show the energy of the each state, as well as the transition rate between the state of interest shown in bold in the table title, and the state in a particular row. The left and right tables show the transitions from the 5s5p ^{1}P$_1$ and 5s4d ^{1}D$_2$ states respectively. The asterisk denotes where the only available information is a theoretical prediction. Data taken from [32, 44, 95–98]

polarisability for the four different states. Figure 4.3 shows the polarisability of both the $5s^2\ ^1S_0$ (purple-dashed line) and $5s5p\ ^3P_1$ $|m_j| = 1$ (blue-solid line) states, for a linearly polarised trapping beam, in atomic units. The sub-plots in figure 4.3 show zooms over the regions 490 nm → 550 nm and 800 nm → 950 nm.

Plotting the polarisability of both the ground state and excited state on the same graph enables us to predict the position of the magic wavelengths. The well-studied $5s^2\ ^1S_0 \rightarrow 5s5p\ ^3P_1$ is a good tool to check for computational errors. The measured magic wavelength on the $5s^2\ ^1S_0 \rightarrow 5s5p\ ^3P_1$ transition is at 914 ± 1 nm [94]. The predicted magic wavelength from our calculations is 914.4 nm, in excellent agreement with the measured value. This gives us confidence in our calculation method, and limits us to the accuracy of transition energies and rates.

There is also a predicted magic wavelength at 499.7 nm, however this has not been experimentally measured. This magic wavelength occurs at a point where the gradient of the polarisability for the $5s^2\ ^1S_0$ and $5s5p\ ^3P_1$ states is drastically different, resulting in a very steep crossing (unlike the crossing at 914 nm) and is dominated by the transitions near 475 nm. Any inaccuracy in these transition energies or strengths will therefore have a large impact on the position of the magic wavelength.

The polarisability of the $5s5p\ ^1P_1$ state is critical as the $5s^2\ ^1S_0 \rightarrow 5s5p\ ^1P_1$ transition is the transition on which the atoms would be imaged[1]. Figure 4.4 shows the polarisability of both the $5s^2\ ^1S_0$ (purple-dashed line), $5s5p\ ^1P_1$ $m_j = 0$ (green-dashed-dotted line) and $|m_j| = 1$ (blue-solid line) states as a function of wavelength, for a linearly polarised trapping beam, in atomic units. The polarisabilities for the different trapping wavelengths are summarised in table 4.2, along with the shift in the $5s^2\ ^1S_0 \rightarrow 5s5p\ ^1P_1$ transition frequency. The polarisability of the $5s^2\ ^1S_0$ and $5s5p\ ^1P_1$ states have opposing signs at 532 nm. This not only causes atoms in the $5s5p\ ^1P_1$ state to be anti-trapped, but also results in a very large frequency shift of the transition. The fact that the excited state is anti-trapped is not a limiting factor however, as other microtrap experiments using ^{87}Rb where the polarisability

---

[1] It is possible to image on the $5s^2\ ^1S_0 \rightarrow 5s5p\ ^3P_1$, however due to the much lower scattering rate, this is experimentally challenging.

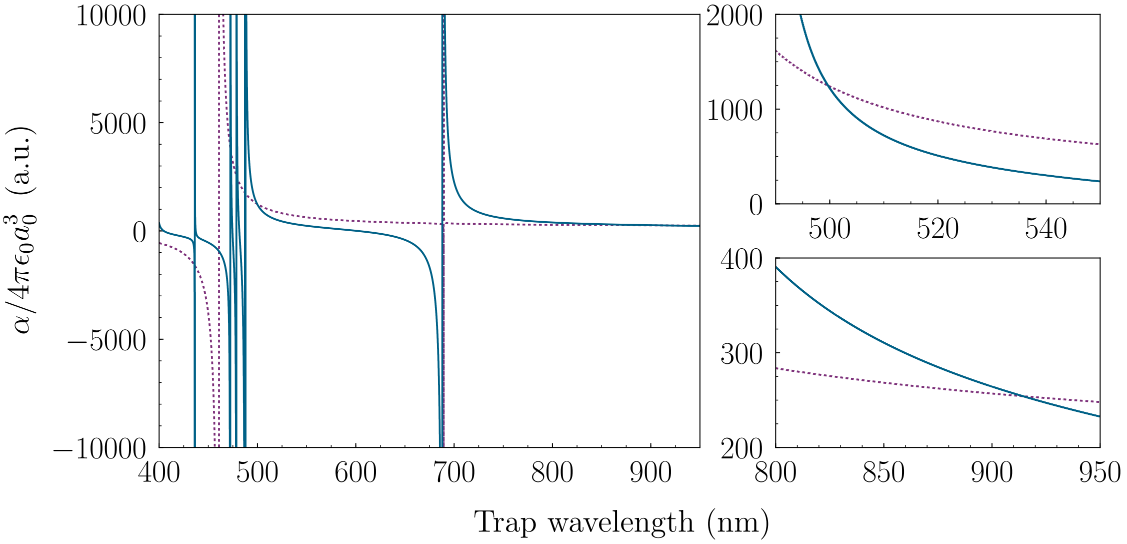

Figure 4.3: Polarisability of the 5s^2 ^{1}S$_0$ (purple-dashed line) and 5s5p ^{3}P$_1$ $m_j = -1$ (blue-solid line) states as a function of wavelength, for a linearly polarised trapping beam, in atomic units.

of the upper state results in anti-trapping are able to simultaneously image and trap their atoms [89]. The polarisability of the 5s^2 ^{1}S$_0$ and 5s5p ^{1}P$_1$ states at 813 nm and 914 nm have the same sign of polarisability and therefore both the ground and excited states are trapped. The large transition shifts at all trapping wavelengths must be considered however, as off-resonant light may lead to heating of the atomic sample.

Another state to consider when imaging the atoms on the 5s^2 ^{1}S$_0$ $\rightarrow$ 5s5p ^{1}P$_1$ transition is the 5s4d ^{1}D$_2$ state, as atoms decay to this state with a branching ratio of $\sim 1 : 50000$ (see figure 2.1). If this state is anti-trapped, then the number of imaging scattering events one could perform would be limited to ~ 50000 before the atom is lost. Figure 4.5 shows the polarisability of the 5s4d ^{1}D$_2$ $m_j = 0$ (green-dashed-dotted line), $|m_j| = 1$ (blue-solid line) and $|m_j| = 2$ (red-dashed line) states as a function of wavelength, for a linearly polarised trapping beam, in atomic units. Interestingly, there is a transition from 5s4d ^{1}D$_2$ $\rightarrow$ 5s7p ^{1}P$_1$ at 533 nm for atoms in the $|m_j| = 0, 1$ states. Therefore, the system may be self-repumping, as the most likely decay from the 5s7p ^{1}P$_1$ is back to the ground state. The $|m_j| = 2$ state is very weakly trapped with a polarisability of $\alpha = 23$ a.u., and therefore atoms which

	532 nm	**813 nm**	**914 nm**
$\alpha_{^1\mathrm{S}_0\ \mathrm{m_j=0}}$ (a.u)	749	279	254
$\alpha_{^1\mathrm{P}_1\ \mathrm{m_j=0}}$ (a.u)	-1254	933	319
$\alpha_{^1\mathrm{P}_1\ \mathrm{m_j=-1}}$ (a.u)	-583	791	498
$^1\mathrm{P}_1 - ^1\mathrm{S}_0\ \mathrm{m_j} = 0$ (MHz/mK)	57	-49	-5
$^1\mathrm{P}_1 - ^1\mathrm{S}_0\ \mathrm{m_j} = -1$ (MHz/mK)	37	-38	-20

Table 4.2: Polarisabilities and differential shifts of the 5s^2 ^{1}S$_0$ → 5s5p ^{1}P$_1$ transition at a variety of trapping wavelengths. The unit of MHz/mK refers to the transition shift as a function of microtrap depth.

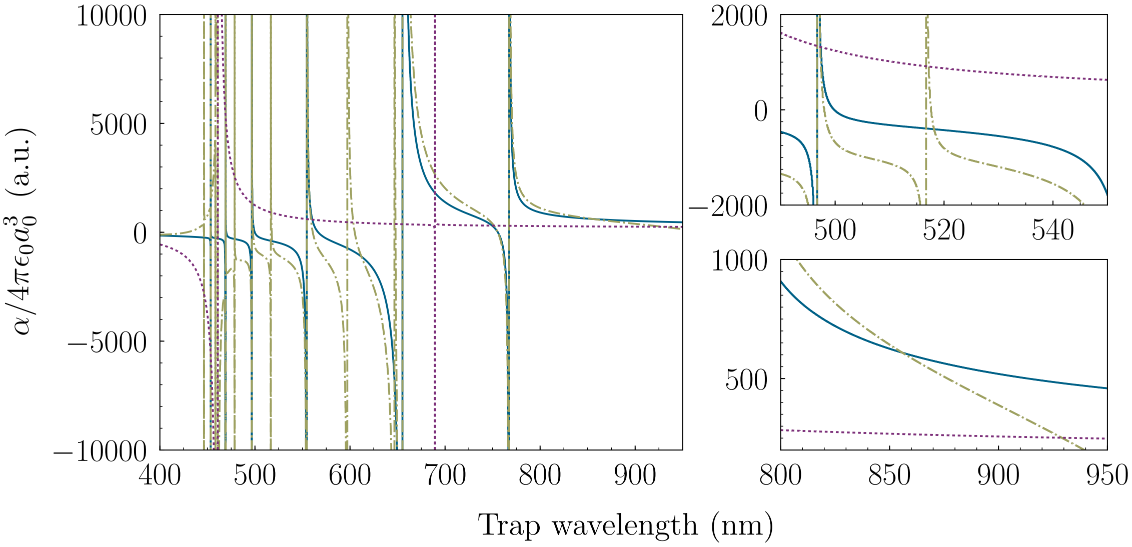

Figure 4.4: Polarisability of the 5s^2 ^{1}S$_0$ (purple-dashed line), 5s5p ^{1}P$_1$ $m_j = 0$ (green-dashed-dotted line) and $|m_j| = 1$ (blue-solid line) states as a function of wavelength, for a linearly polarised trapping beam, in atomic units.

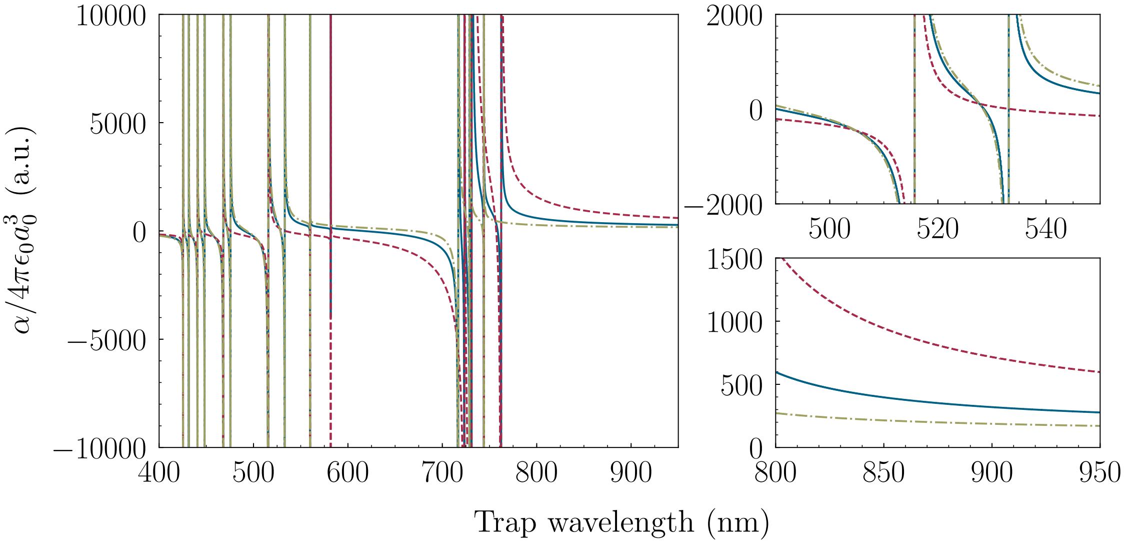

Figure 4.5: Polarisability of the 5s4d $^1\mathrm{D}_2$ $m_j = 0$ (green-dashed-dotted line), $|m_j| = 1$ (blue-solid line) and $|m_j| = 2$ (red-dashed line) states as a function of wavelength, for a linearly polarised trapping beam, in atomic units.

arrive in this state may or may not be lost, depending on the ratio of the trap depth to the atomic temperature. At 813 nm and 914 nm, the polarisability of all the m_j states is greater than the polarisability of the 5s^2 $^1\mathrm{S}_0$ state. Therefore, at these wavelengths, atoms which decay to the 5s4d $^1\mathrm{D}_2$ should not be spatially lost. Atoms in this state can either decay back to the ground state via the 5s5p $^3\mathrm{P}_1$ state, or decay to the metastable 5s5p $^3\mathrm{P}_2$ state. If atoms decay 5s5p $^3\mathrm{P}_2$ state, a repump laser is required to pump the atoms back to the ground state. However, as all these states are trapped, the atoms should not be spatially lost, but only remain dark for a time which it takes to pump the atoms back to the ground state.

In summary, it should be possible to create and image a strontium microtrap at the wavelengths of 813 nm, 914 nm and 532 nm. Microtraps at 813 nm are the optimal solution for experiments working with the 5s5p $^3\mathrm{P}_0$ state, and the calculations suggest that the differential AC Stark shift of the other relevant transitions are compatible.

4.2 UHV compatible experimental apparatus design

The false colour CAD drawing shown in figure 4.6 gives an overview of the changes to the innards of the main chamber. There are four major changes compared to that designed by J. Millen [75]. The first is the addition of a pair of in-vacuo aspheric lenses. These are mounted in a large stainless steel lens mount with a separation of 2WD = 74.86 mm where WD is the working distance. This provides the ability to focus light to a size of approximately 1 µm. The second change is an increase in the diameter of the wire used to create the MOT coils to increase the magnitude of the magnetic quadrupole field gradient which can be generated from the MOT coils.

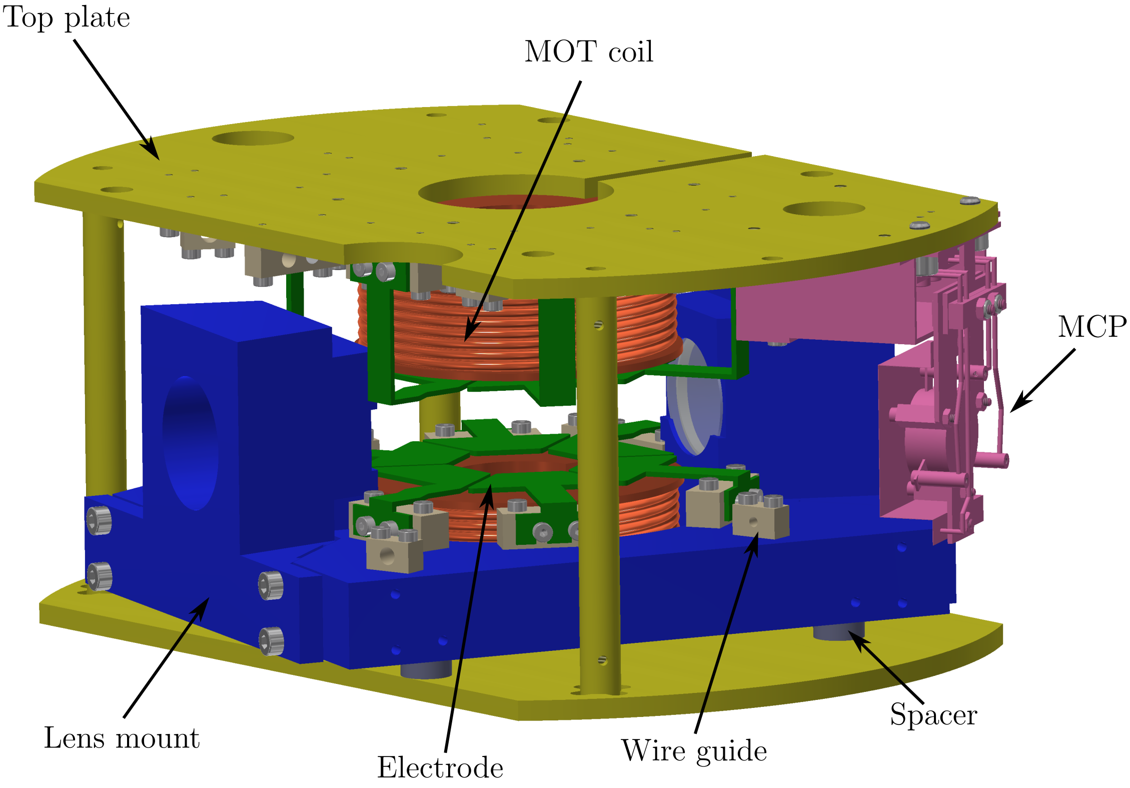

Figure 4.6: Flase colour CAD drawing showing the new experimental innards. This is bolted to the top flange of the main chamber via the top plate. Note that the wires connecting the electrodes and the vacuum feed-throughs are not shown for clarity.

This is to make it possible to produce deep magnetic traps for atoms in the 5s5p $^3P_2$ state [99]. Thirdly, the MCP position has been moved from the flange on the main chamber and has been mounted between two flanges. This increases optical access into the main chamber. The final change is the electrode configuration. As shown in the CAD drawing, the electrodes are in a hexagonal split-ring geometry. This not only improves our ability to reduce stray fields due to the increased degrees of freedom, but also improves our ability to create a quantisation axis along any optical axis, which was previously limited. We will now explore in more detail each of the changes to the experimental apparatus.

4.2.1 Custom lenses and holders

Following the success of microtrap experiments using single aspheric lenses [92], we have designed our microtrap system based upon two single aspheric lenses separated by a distance of twice the focal length. The lenses focus the trapping light as well as collect the fluorescence from the atoms.

Aspheric Lenses

There are a variety of experimental constraints which must be considered when designing such a system. Typically, experiments of this kind work with small aspheric lenses ($\sim$ 10 mm diameter) and a short working distance ($\sim$ 6 mm diameter) [92,100]. This is in order to produce a high numerical aperture (NA) lens which is small enough to fit inside the vacuum chamber. One of the challenges of such a short working distance is the ability to pass orthogonal MOT beams through the centre of the experimental chamber. An additional challenge which is considered in our experimental apparatus is the detection of charges. In order to detect charges from ionised Rydberg atoms, there must be a clear line of sight between the trapping region and the MCP[2]. This drastically increases the minimum permissible distance between the two lenses. Increasing the working distance however reduces the numerical aperture. Therefore, the lens diameter must also be increased. The geometrical

---

[2] It is possible to use guiding electrodes, however this becomes significantly more challenging.

constraints associated with this are illustrated in figure 4.7. To maintain orthogonal MOT beams with a diameter of 15 mm, the minimum lens separation for lenses with diameter 25 mm is ∼ 75 mm[3]. Based upon this geometrical constraint, we now analyse the achievable microtrap parameters.

For a clear aperture of 20 mm and a working distance of 37 mm, the NA of the lens is 0.26 which leads to an associated collection efficiency of 1.7 %. This collection efficiency is approximately four times smaller than the typical collection efficiency of lenses used in rubidium microtrap experiments (6.7 %) [101]. Although a reduction in NA may seem catastrophic for the detection of single atoms, the ^{88}Sr 5s^2 ^{1}S$_0$ → 5s5p ^{1}P$_1$ transition which will initially be used for imaging, has a scattering rate which is approximately five times larger than the imaging transition used in rubidium. It is therefore possible to increase the working distance of our lenses and maintain a count rate on our detector which is comparable to other single-atom experiments.

One of the challenges of using a single aspheric lens is the ability to focus a variety of different wavelengths. As discussed in the previous section, the wavelengths

---

[3] This is the tightest crossing angle.

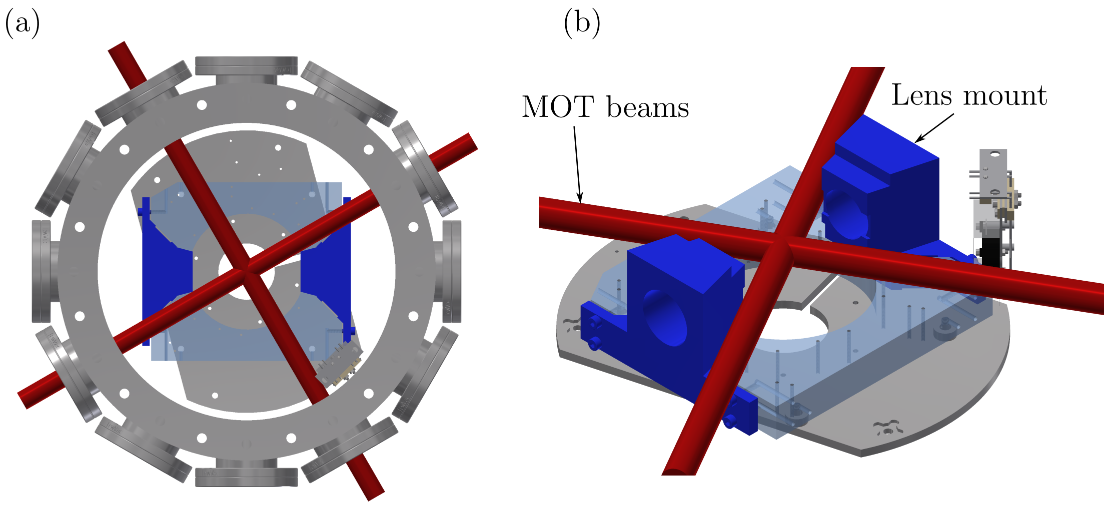

Figure 4.7: Diagram showing the crossing of orthogonal MOT beams (red) of diameter 15 mm for a lens separation of ∼ 80 mm and a lens diameter 25 mm. (a) and (b) show a top and isometric view respectively.

Wavelength (nm)	Focal distance (mm)	w_0 (µm)	z_R (µm)
461	37.029	-	-
532	37.402	1.1	5.9
813	38.106	1.57	9.4
914	38.247	1.73	10.6

Table 4.3: Predicted focal distance, 1/e^2 radii and Rayleigh ranges for the possible trapping wavelengths.

of interest for the microtrap are 532 nm, 813 nm and 914 nm, and 461 nm for imaging. The lens must therefore perform well at all of these wavelengths. The physical optics package in Zemax was used to optimise the surface of the aspheric lens to produce a diffraction limited focus for a Gaussian input beam at all wavelengths. The optimised predicted focal shifts, 1/e^2 radii and Rayleigh ranges for the different wavelengths are summarised in table 4.3. The predicted waists of all trapping wavelengths are small enough to facilitate a two-dimensional array with a lattice spacing of $\sim 3\,\mu\text{m}$, a length scale over which Rydberg-dressed interactions can be achieved [46]. The relatively long Rayleigh length at 813 nm and 914 nm however does limit the applicability of this lens design to three dimensional arrays operating at the clock magic wavelength, but given that we are striving for a proof-of-principle experiment, this is acceptable.

The suitability of the proposed lens is dependent on the number of microtraps we are able to generate with the available laser power. The microtrap light is provided by a titanium-sapphire laser[4] (Ti:Sa). The Ti:Sa laser is pumped using a diode-pumped solid-state laser at 532 nm[5]. A pick-off unit is installed before the Ti:Sa cavity which facilitates the simultaneous production of ~ 2.7 W at 813 nm or ~ 1.8 W at 914 nm and 5 W at 532 nm. Assuming an efficiency from the laser to the atoms of 70 % and that the temperature of the atoms in the microtrap can be cooled to the Doppler temperature on the $5s^2\ ^1S_0 \rightarrow 5s5p\ ^1P_1$ transition of $T = 0.7$ mK,

---

[4] M2 Squared SolsTiS

[5] Lighthouse Photonics, Sprout-G 15W

Wavelength (nm)	**Available traps**
532	89
813	9
914	5

Table 4.4: Number of available microtraps for the possible trapping wavelengths, assuming an efficiency from the laser to the atoms of 70 %.

table 4.4 shows the number of microtraps which can be created using a trap depth U_0 of $U_0/k_\mathrm{B}T = 5$. This indicates that we are able to create a two-dimensional array at all wavelengths, and therefore the lens design is suitable for the proof-of-principle experiment.

The lenses were manufactured by Thorlabs from NBK-7 glass. Diffraction limited performance was guaranteed using magnetorheological finishing (MRF). To test the quality of manufacture of the aspheric lenses, an interferometric measurement of the lens surface was performed using a Zygo Verifire, to measure the surface deviation of the lenses from their designed shape. All lenses had an rms deviation of $< 12\,\mathrm{nm}$ across the clear aperture of the lens. The lenses were coated with an anti-reflection coating on the aspheric side to minimise Fresnel reflections. The reflection losses from this surface are $< 1\,\%$ at wavelengths of 408, 461, 532, 689, 813 and 914 nm. The planar side of the aspheric lens is coated with a 15 nm thick layer of conductive indium-tin-oxide (ITO)[6] with a sheet resistance of $160\,\Omega/\Box$. This is to minimise the risk of patch charge build-up on the lenses [101]. Due to the high refractive index of the ITO layer, there are significant losses from this surface. The calculated transmission through the lenses are summarised in table 4.2.1.

Upon further analysis of the lens performance using Zemax post lens production, the optimisation of the aspheric surface for the trapping light led to a less than optimal performance of the lens when imaging a point source at 461 nm, resulting in a diffraction limited performance for a clear aperture of 17 mm. In future experiments, it may be required to re-design the aspheric surface to optimise the

---

[6] Diamond coatings: https://www.diamondcoatings.co.uk/

Wavelength (nm)	**Transmission (%)**
408	91.0
461	91.5
532	92.5
689	93.0
813	94.0
914	95.0

Table 4.5: Calculated transmission of the aspheric lenses at relevant wavelengths.

diffraction-limited performance at 461 nm and improve the imaging resolution of the experiment.

Having manufactured the aspheric lenses, we now design the rest of the experimental innards around them.

Lens Holders

The two main requirements of the lens holders are alignment and stability. The lens holder must be constructed in such a way that the two aspheric lenses share

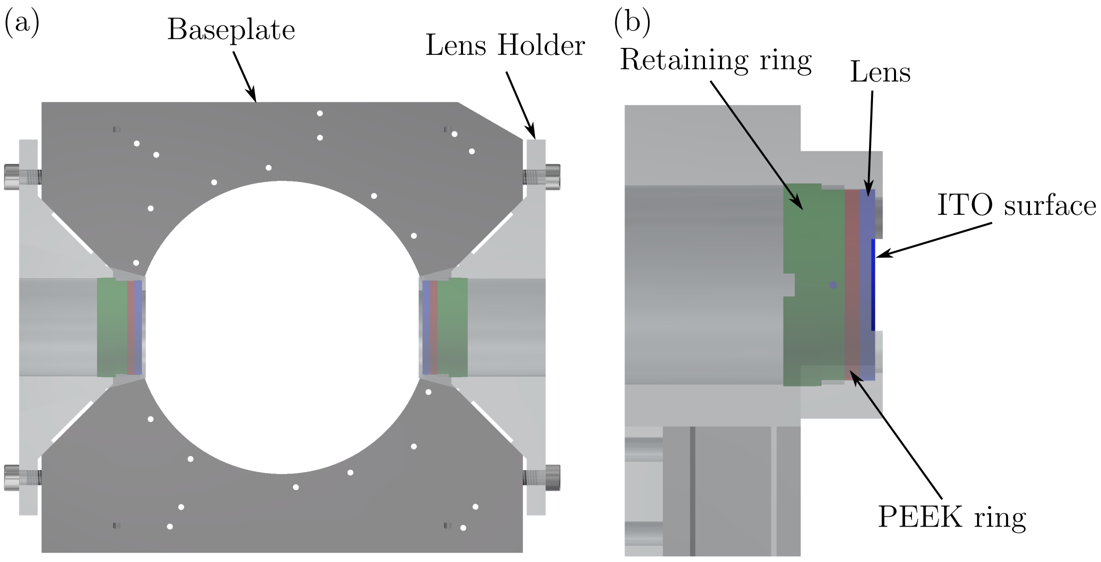

Figure 4.8: CAD drawing of the lens holders used in the experiment. (a) shows a top view of the whole lens mount. (b) shows a side view of the lens holder.

a common focal point and that under baking of the vacuum system and general day-to-day use, the lenses are unlikely to move. To achieve this, the lens holder is based on a locating trapezoid design whereby each lens is mounted in a holder which is then located and affixed into a trapezoid cut section base plate. The purpose of using a trapezoid cut section is to ensure the precise centration of the lens pair.

An overview of the lens holder is shown in figure 4.8. The lens holder is constructed of 316LN stainless steel, for its strong mechanical and low magnetic properties. It consists of three sections, as shown in figure 4.8. Each lens (blue) sits inside a holder which has a bore that is 0.2 mm wider than the outer lens diameter. The planar side of the aspheric lens makes contact with a lip at the front of the lens holder, creating an electrical contact with the ITO layer. A 1 mm thick ring (red) of polyether-ether-ketone (PEEK)[7] is placed on top of the aspheric side of the lens before a stainless steel threaded retaining ring (green) is used to secure the lens in place. The PEEK ring acts as a malleable material to absorb any potential strain on the lenses under baking. The two lens holders are aligned via the base plate with respect to a trapezoid cut section (figure 4.8(b)). The small face plates of the lens holders locate the holder into the trapezoid cut section. The holders are then fixed to the base plate via four M4 screws. The precision grinding[8] of the trapezoid cut section and the small face plates ensures that the two lenses share a common focal point. The separation of the lenses is such that collimated 532 nm light entering from one lens is re-collimated by the other lens.

Before mounting the lens holder into the vacuum chamber, the centration of the lens pair was tested. The test configuration is shown in figure 4.9. Initially, a ‘pencil’ beam parallel to the table was aligned onto the centre of the first lens by overlapping all reflections from the lens. Then the second lens was added such that the retro-reflected beam from the far mirror passed through both irises. We initially aligned the system such that the back reflection from the first lens and the retro-reflected beam passed through the first iris. The back reflection from the second lens passed through the first iris also, and therefore indicated that the lenses were co-axial.

---

[7] PEEK is a UHV compatible plastic.

[8] This has a tolerance of ±5 µm.

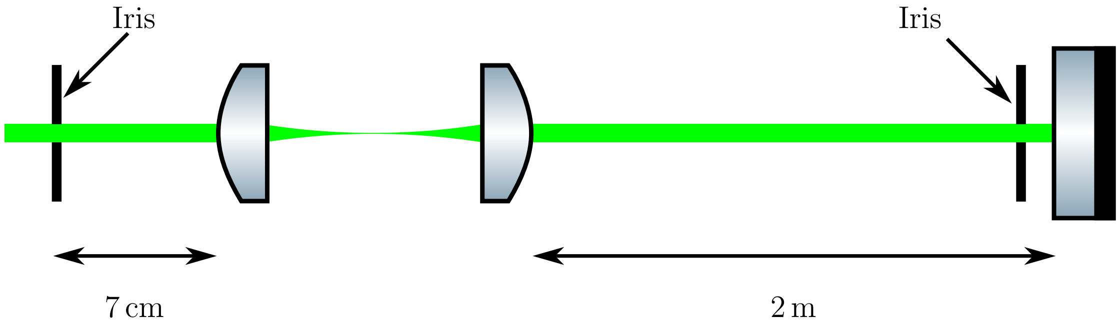

Figure 4.9: Schematic of the experimental configuration used for testing the alignment of the aspheric lens pair. Note that this diagram is not to scale.

The collimation of the beam was also measured to test the separation of the lens pair. One must take note however, that the refractive index difference between air and vacuum is sufficient to change the collimation of the lens pair. We therefore used a combination of divergence predictions from Zemax and divergence measurements to estimate the separation of the lens pair. Initially, the input beam with $1/e^2$ radius 10.35 ± 0.02 mm was collimated using a shear plate interferometer and aligned onto the lens pair. The output beam was measured as a function of distance from the second lens. If the lens separation is correct, one would expect the output beam to be slightly diverging as the refractive index of vacuum is smaller than that of air. The beam was measured to be converging with a convergence of 8.6 mRad. Using calculations from Zemax, this indicates that the lens separation was 220 µm longer than the optimal position. The trapezoid cut section was re-ground to reduce the separation of the lenses to the correct distance.

4.2.2 MOT coils under vacuum

To produce a quadrupole field at the centre of the chamber, we mount a pair of coils, made from Kapton-dipped single-strand copper wire[9], on OFHC (Oxygen-free high thermal conductivity) copper formers. A CAD drawing of the MOT coils and former are shown in figure 4.10. The copper formers have a centre bore to allow the vertical MOT beams to pass into the chamber, and have a slot cut to minimise

---

[9] Allectra 311-KAP-180-5M

the production of eddy currents in the former. There are also small pedestals at the base of the former to minimise the contact area of the former with the base plate which reduces the likelihood of trapped gases. The wire has a core diameter of 1.8 mm and total thickness $d = 2.0\,\mathrm{mm}$. This is a much larger core size than the previous generation of the experiment and should allow larger currents to pass through the coils at a similar heating rate[10]. We calculate the number of turns required to produce the quadrupole field by assuming the field produced by the coil is a linear summation of multiple single turns of wire at varying distances and radii. The on axis magnetic field B_z produced at a distance z is given by

$$B_z = \frac{\mu_0}{2} \sum_{z_i}^{z_f} \sum_{R_i}^{R_f} \frac{IR^2}{\left[(z - z_0)^2 + R^2\right]^{3/2}} - \frac{IR^2}{\left[(z + z_0)^2 + R^2\right]^{3/2}}, \tag{4.2.1}$$

where $z_f = z_i + (\nu_{\mathrm{ax}} - 1)\,d$ where ν_{ax} is the number of turns axially and z_i is half the distance between the top turn of the two MOT coils, R_i is the radius of the inner most turn and $R_f = R_i + (\nu_{\mathrm{rad}} - 1)\,d$ where ν_{rad} is the number of turns radially. We optimise the number of turns both axially and radially, along with the coil separation to produce a field gradient greater than 50 G/cm, but also at a total power dissipation similar to the old MOT coils. The final parameters are $\nu_{\mathrm{rad}} = 7$, $\nu_{\mathrm{ax}} = 9$, $R_i = 14.5\,\mathrm{mm}$ and $z_i = 13.5\,\mathrm{mm}$ which produces a theoretical quadrupole gradient along $\hat{\boldsymbol{z}}$ of $\kappa_q = 9.2\,\mathrm{Gcm^{-1}A^{-1}}$.

The current through the MOT coils is controlled via a servo circuit which stabilises the current through the coils using a $0.7\,\Omega$ sense resistor and a MOSFET [45]. In the previous experiment, a quantisation axis was provided by a single external coil. There are several limitations of this system; the single coil does not produce a uniform field and the application of a field externally induces eddy currents in the main chamber. A solution to this problem is to use the internal MOT coils. The MOT coils are wired in an anti-Helmholtz configuration. However, by implementing a relay circuit (see Appendix B), we are able to change the polarity of one of the

---

[10] We observe a negligible pressure increase in the vacuum chamber when running successive experiments with a power of 1.4 W (corresponding current of 3.2 A) through the MOT coils. Note that there is no active cooling of the MOT coils.

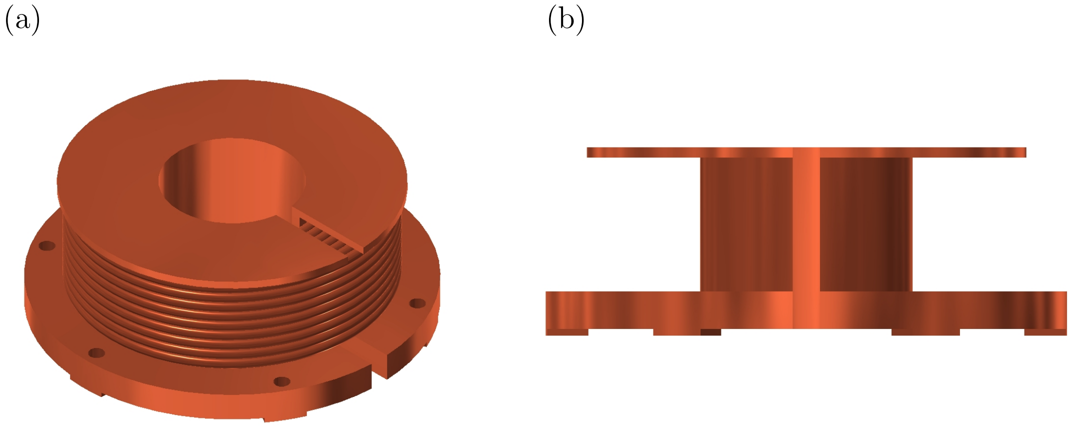

Figure 4.10: CAD drawing of the MOT coils used in the experiment. (a) shows an orthographic projection of the MOT coils wrapped onto the former. (b) shows a side view of the former.

coils to change to a Helmholtz configuration, producing a uniform magnetic field in the centre of the main chamber. This typically takes 8 ms to switch.

4.2.3 MCP charge detector

The previous MCP was mounted onto one of the horizontal flanges of the main chamber. To improve optical access, we have mounted the MCP on the new innards. The MCP is mounted such that it is located as close to the main chamber housing as possible, and in between two of the horizontal flanges. This reduces the obscuration of the optical access from adjacent viewports.

One of the main technical challenges of moving the MCP is shielding the atoms from high voltages. The final design of the MCP mount is shown in 4.11. The MCP[11] (blue) is mounted on a 1 mm thick stainless steel substrate (green) via three M1.6 screws. This substrate is connected to a stainless steel bracket (red) which is connected to the top plate of the innards (see figure 4.6). The substrate is electrically isolated from the main chamber by a Macor spacer (beige). The MCP is a covered with a wire mesh[12] (orange) which shields the atoms from the high voltage on

---

[11] Hamamatsu F4655-14

[12] Goodfellow FE228710

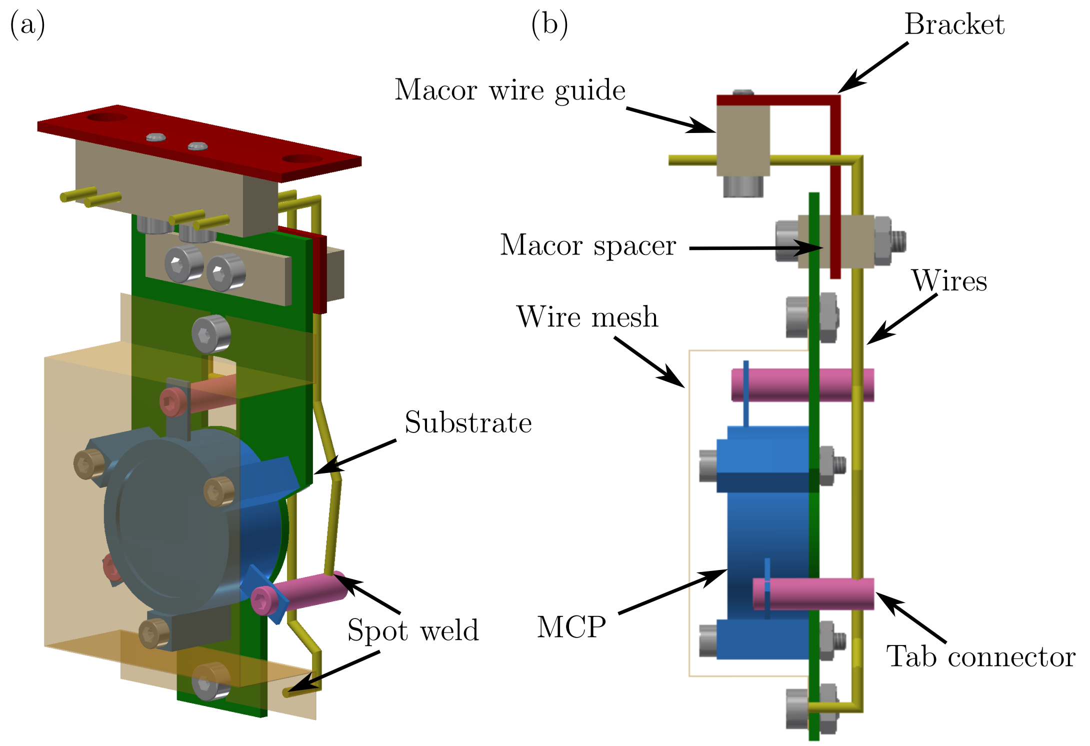

Figure 4.11: CAD drawing showing the mounting configuration of the MCP from the front, side and back.

the MCP, as well as increasing the collection efficiency. The MCP is mounted approximately 3 mm from the main chamber wall to maximise the optical access. Due to this close proximity to the walls of the main chamber, it is not possible to use insulated wire as dielectric breakdown is likely to occur. Therefore, the electrical connections to the MCP are made via 1 mm thick stainless wire (yellow), which are spot welded into a cylindrical, threaded tab connector (pink). M1.6 screws are used to create a strong electrical contact between the tabs of the MCP and the connector. The mesh is connected to the wires via spot-welding. The wires are guided through Macor wire guides (beige) to ensure that there is a minimal risk of electrical shorts during baking. The wires are guided behind the MCP mount and up to the top plate of the innards to protect the atoms from voltages supplied to the MCP. As shown in figure 4.6, the MCP wires are shielded by a grounded plate once they emerge in-front of the MCP. The wires are then connected to a feedthrough to the outside of the vacuum chamber. The connections are shown in appendix A.1.

4.2.4 Control electrodes

The electrodes in the experiment have two purposes; to push charges towards the MCP and to apply electric fields in arbitrary directions. The previous electrodes were in a four-quadrant split-ring geometry. A limitation of this system is that it is not possible to apply a homogenous electric fields along all optical axes. To improve upon this design, we have created a hexagonal split-ring geometry, as shown in figure 4.12(a). As this configuration has the same symmetry as the main chamber, it is possible to apply electric fields along each optical axis. The MCP is placed in between two flanges and hence offset by an angle of 15° from the symmetry of the main chamber flanges. To simplify the electrode pulses required to send charges to the MCP, the electrodes are also rotated by an angle of 15° so that only two-pairs of electrodes are required to push charges towards the MCP. A consequence of this is that it requires four pairs of electrodes to produce an electric field along an optical axis.

In the previous generation of the experiment, the electrodes were glued to a Macor spacer which was glued to the copper MOT coil former. During baking, the differential expansion of the material caused the electrodes to detach from the former [102]. To avoid this, the electrodes were designed to be situated 1.5 mm above the MOT coil formers. The electrodes are made from 1 mm thick stainless steel sheet,

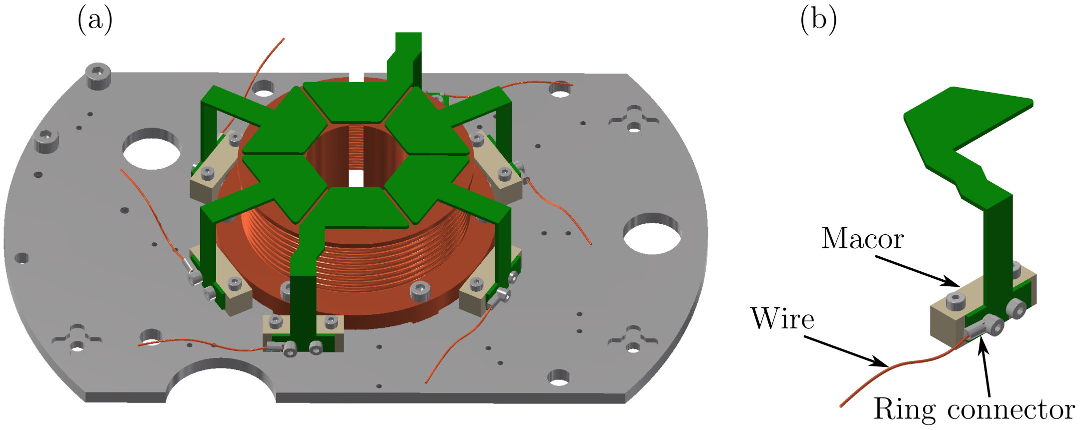

Figure 4.12: CAD drawing showing the mounting configuration of the (a) electrodes on the baseplate and (b) a single electrode.

.

machined and hand polished to a good finish. The electrodes are mounted onto a Macor block (figure 4.12(b)), which provides electrical isolation from the rest of the chamber. Electrical contact to the electrodes is made via a crimped ring connector[13] and Kapton-coated wire[14]. The wires are fed through wire guides and into a multi-pin UHV connector[15]. The electrical connections to each electrode are detailed in appendix A.2.

4.2.5 Viewports and pumping

Viewports

Due to the multitude of wavelengths used in an ultracold strontium experiment, it is not feasible to have anti-reflection coatings on all viewports for all wavelengths. We therefore have particular anti-reflection coatings on each viewport. The viewports and their respective coatings which are placed on each flange of the main chamber are shown in A.3. There are four uncoated fused silica viewports on the chamber. This is to allow ultraviolet light into the chamber as NBK-7 glass absorbs strongly in the ultraviolet range.

Reaching UHV conditions

Before placing the experimental chamber under vacuum, each component was cleaned to UHV standard (see figure 4.13). To reach UHV conditions, the experiment was attached to a turbo pump with all other pumps switched off. The experiment was baked using resistive heaters for approximately one week at a temperature of 130 °C. The limiting component for the maximum baking temperature was the MCP which is limited to a temperature of 150 °C. Towards the end of the baking procedure, a current of 5 A was passed through the MOT coils for one day to locally heat the coils and help clear contaminants. Upon cooling and activation of both the ion pumps and the getter pump, the main chamber was at a pressure of $\sim 5 \times 10^{-11}$ mbar.

---

[13] Allectra 360-RING-1.0-M2

[14] LewVac KAPW1X061, Kapton wire, 0.6 mm, 2 kV DC, 7 A.

[15] LewVac FH-MSC19-40CF, MS circular feedthrough, 1 kV, 3 A, 19 pin DN40CF ASC/VSC.

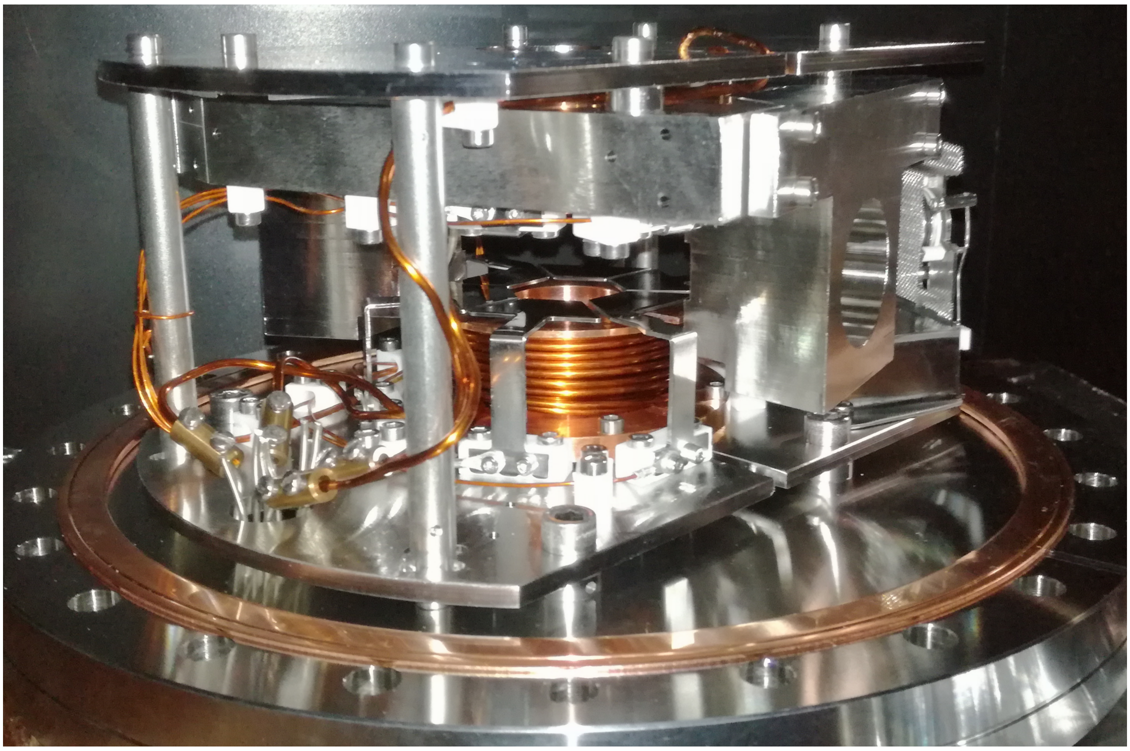

Figure 4.13: Picture showing the final constructed innards before being placed under vacuum.

.

4.3 Laser systems

Strontium can be laser cooled on both the broad $5s^2\ {}^1S_0 \rightarrow 5s5p\ {}^1P_1$ and narrow $5s^2\ {}^1S_0 \rightarrow 5s5p\ {}^3P_1$ transitions (see figure 2.1). The laser systems involved in laser cooling on these transitions are vastly different from one another due to the drastically different linewidths of the transitions. In this section we discuss changes to the laser systems detailed in the thesis of N. Jackson [46], which are used to create an ultracold sample of strontium atoms on both transitions. We also detail the optical configuration for the creation of a strontium microtrap.

4.3.1 461 nm laser system

The 461 nm light is produced using a frequency-doubled diode-laser system[16]. This laser system uses a non-linear crystal inside a ring cavity to frequency-double 922 nm light, producing up to 280 mW of 461 nm light. The full laser system is shown in figure 4.14. The output of the laser passes through two cylindrical telescopes to reshape the laser beam. This is then coupled into a single-mode polarisation-maintaining (SM/PM) fibre, with a coupling efficiency of $\sim 70\,\%$ to remove the astigmatism of the laser beam. Approximately 1.2 mW of the light is picked-off using a glass-plate and sent through AOM 2 to lock the laser 240 MHz below resonance using modulation transfer spectroscopy. Approximately 80 mW is doubled passed through AOM 1 to produce the Zeeman beam which is ~ -500 MHz from resonance. The zeroth-order light is picked-off using a small prism, and coupled down a SM/PM fibre. This light is sent to another optical table where it is used to beat lock an additional 461 nm laser[17]. AOM 3 produces a resonant probe beam which is used for imaging, with a power of ~ 4 mW. The rest of the light is single-passed through AOM 4 and into a SM/PM fibre to produce the MOT beams with a linear detuning of -40 MHz from resonance. The AOM frequencies and diffracted orders are summarised in table 4.3.1.

---

[16] Toptica Photonics DL-SHG frequency-doubled system.

[17] MOGLabs ECDL. This won't be used during the rest of this thesis.

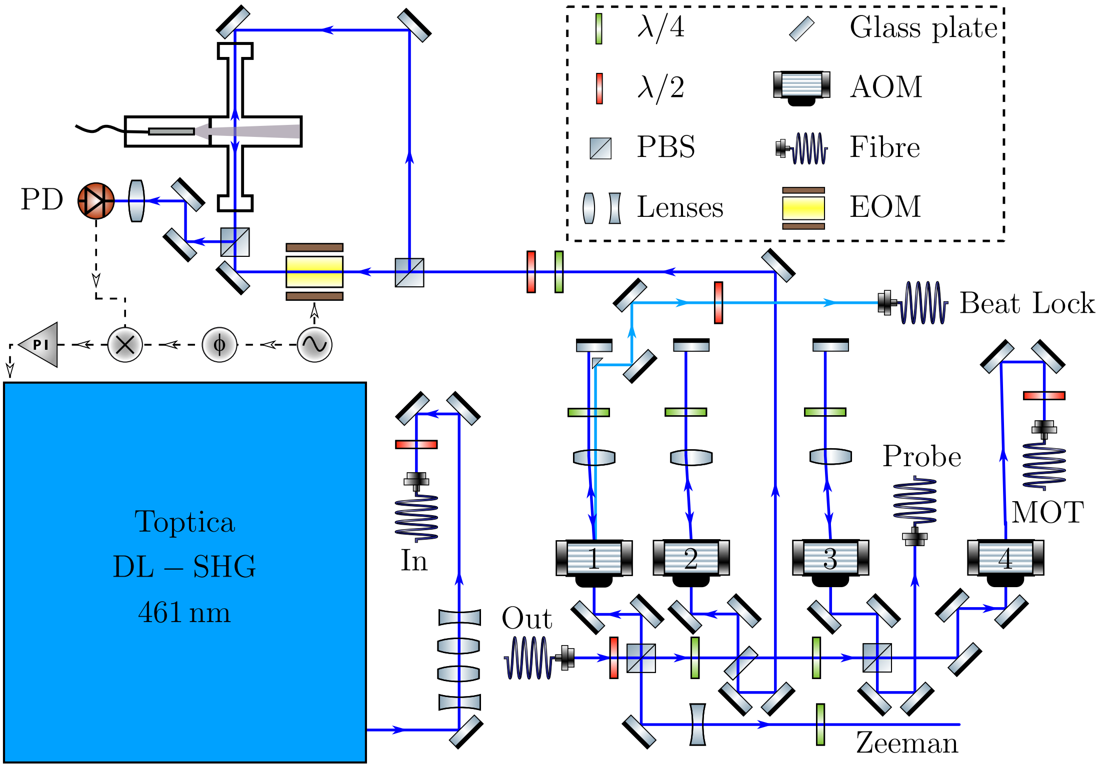

Figure 4.14: Full optical layout of the blue laser system used in the experiment. The dotted box shows a key to the diagram.

AOM Number	Drive Frequency (MHz)	Diffracted Order	Pass Number
1	130.5	-1	2
2	120	+1	2
3	120	+1	2
4	200	+1	1

Table 4.6: AOM settings used in the 461 nm optical set-up. The AOM number refers to the labelling shown in figure 4.14.

Observation of a ‘Blue’ MOT

Strontium atoms are slowed in the Zeeman slower and caught in a MOT operating on the $5s^2\ ^1S_0 \rightarrow 5s5p^1P_1$ transition. A picture of the first ‘Blue’ MOT using the new innards is shown in figure 4.15(a). This MOT contains $\sim 5 \times 10^7$ atoms at a density of $\sim 4 \times 10^9\,\mathrm{cm}^{-3}$, measured by absorption imaging on the cooling transition at a predicted field gradient of $\sim 33\,\mathrm{G/cm}$. The power in the MOT and Zeeman beams were 12 mW and 60 mW respectively, and the current supplied to the strontium oven was 1.5 A. The temperature of the atoms in the horizontal and vertical directions was measured using a ballistic expansion method. Figure 4.15(b) and (c) show the width of the cloud as a function of ballistic expansion time. From the gradient, we derive a temperature of $T_x = 4.2 \pm 0.1\,\mathrm{mK}$ and $T_z = 2.9 \pm 0.1\,\mathrm{mK}$ in the horizontal and vertical directions respectively. This is much hotter than the Doppler limited temperature one would expect for the blue MOT. This result is similar to other experiments however [103], where it seems that the heating rate in the blue MOT is approximately 20 times larger than one would expect.

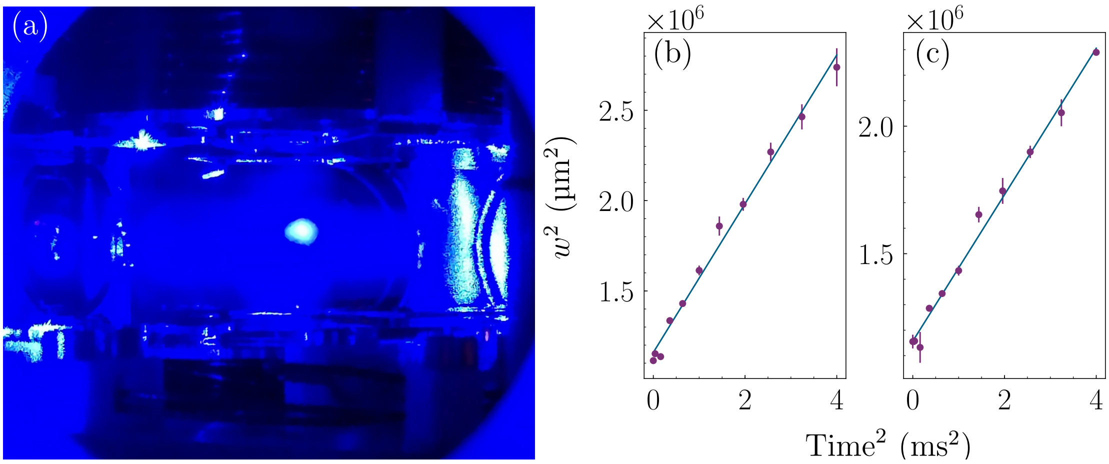

Figure 4.15: (a) Photograph of the first ‘Blue’ MOT using the new innards. (b) and (c) show the width of the cloud as a function of ballistic expansion time for the horizontal and vertical directions respectively. The calculated horizontal and vertical temperatures are $T_x = 4.2 \pm 0.1\,\mathrm{mK}$ and $T_z = 2.9 \pm 0.1\,\mathrm{mK}$.

4.3.2 689 nm laser system: A narrow linewidth laser for cooling

It is not possible to load directly into a nMOT due to the narrow linewidth of the transition. Typically, atoms from a blue MOT are transferred into a nMOT. After initial cooling, the blue-MOT light is removed and cooling light at 689 nm, which addresses the $5s^2\ ^1S_0 \rightarrow 5s5p\ ^3P_1$ transition, is applied. This light is artificially broadened to match the Doppler-broadened profile of the atoms in the blue-MOT. After sufficient cooling, the broadening of the 689 nm light is removed, leaving single-frequency light, and a cold, dense nMOT. This transference process is discussed in more detail in [33].

As with the formation of a blue MOT, the cooling laser frequency has to be stabilised. This becomes a technical challenge when working with such a narrow transition as typically, diode lasers have a frequency spectrum of several hundred kHz, which is much broader than the transition linewidth. To solve this problem, the laser frequency is locked to a high-finesse optical cavity using the Pound-Drever-Hall (PDH) locking technique [104, 105], which narrows the laser linewidth to the order of a few tens of Hz. We will now explore the changes made to this laser system compared with previous work [33, 45, 46, 102].

Ultra-stable ECDL laser

One of the limitations of the previous 689 nm laser system was the stability of the laser. Due to stability issues, the mode-hop free range of the laser would drift too far for the laser to stay locked to the high-finesse cavity, limiting the laser lock to several hours. To solve this problem, we have built an ultra-stable ECDL laser based upon the design of Cook *et al.* [106]. The entire laser is machined from a single aluminium block which lowers the susceptibility of the laser to temperature changes and mechanical vibrations. The diffraction-grating arm is stiff and light, and has its pivot point in an optimum position for tuning a laser diode at 689 nm. The laser is surrounded by fibre-glass insulation to improve the temperature stability and reduce acoustic noise. Another improvement to the laser system is the use of

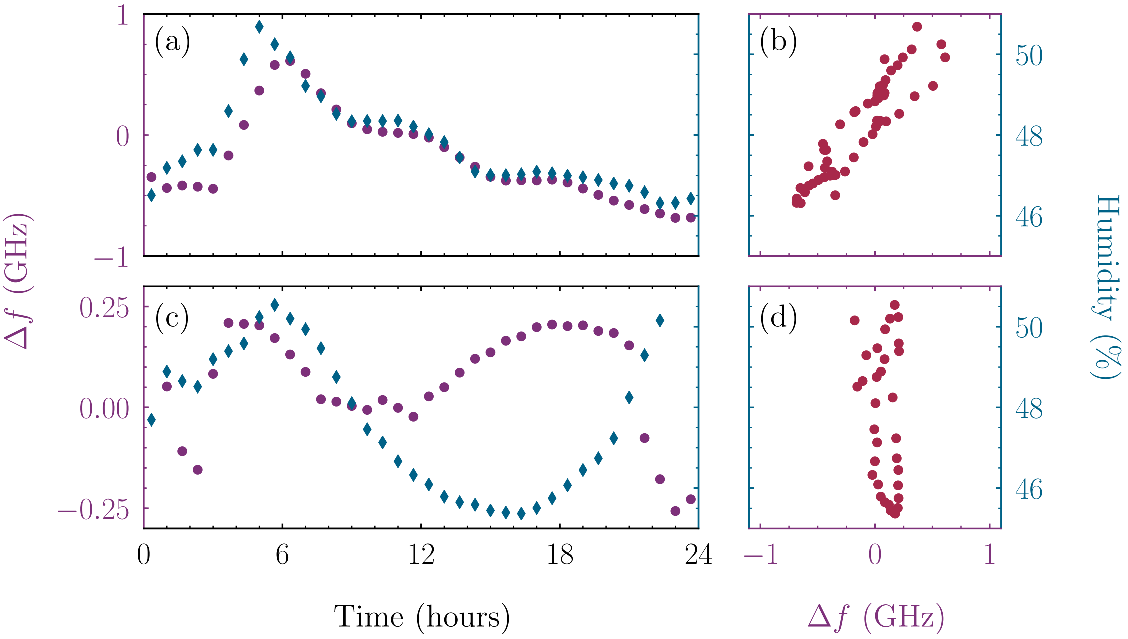

Figure 4.16: (a) and (c) show the laser frequency (purple circles) and humidity (blue diamonds) as a function of time for the laser with and without the addition of silica beads in the laser cavity. (b) and (d) is a plot of laser frequency against humidity for the two cases.

.

an AR coated laser diode[18]. Although this makes it more challenging to initially align the feedback into the diode, it improves the mode-hop-free range of the laser, which in turn should increase the length of time the laser remains locked to the high-finesse cavity. When optimised, the threshold of the laser is 70 mA and has a mode-hop-free range of ±1.1 GHz when scanning the laser current, and > 8 GHz when scanning the angle of the diffraction grating.

The frequency drift of the laser in the absence of feedback has a range of $\sim \pm 0.65$ GHz over a time-scale of 24 hours, which is much smaller than the previous current limited mode-hop-free range. To investigate the cause of the laser frequency drift, a miniature weather station was installed next to the laser to measure temperature, humidity and pressure changes. The most striking correlation is shown in figure 4.16(a) where the laser frequency (purple circles) and humidity

---

[18] Eagleyard, 675-692 nm, EYP-RWE-0690-00703-1000-SOT02-0000

(blue diamonds) are plotted as a function of time. To evaluate the strength of the correlation, the laser frequency is plotted against humidity (figure 4.16(b)), and the Pearson correlation coefficient R [107] is calculated. Here, $R = 0.91$ indicating that the laser frequency is strongly correlated with the local humidity. This is most likely due to a change in refractive index of the air in the laser cavity and hence the effective cavity length. To reduce the effect of the humidity on the laser cavity, the laser was sealed with an epoxy resin and a bag of silica beads was inserted into the laser cavity. Figure 4.16(c) shows the laser drift as a function of time after these changes were made. There is a clear reduction in the range of laser frequency drift over the same time period. Figure 4.16(d) shows that the correlation between humidity and laser frequency has been removed, resulting in $R = -0.01$.

High-finesse cavity

The high-finesse cavity used previously in the experiment was a home-built system with a finesse of $\mathcal{F} = (41.3 \pm 0.6) \times 10^3$. The cavity length was actively stabilised to the transition frequency of the $5s^2\ ^1S_0 \rightarrow 5s5p\ ^3P_1$ transition using piezoelectric actuators [33]. A technical problem with this configuration was the stability of piezoelectric actuators. Typically, the drift rate of the cavity was too high for the laser to remain locked for more than a few hours. Also, the shot-to-shot frequency fluctuations of the laser were of the order of $\sim 20\,\mathrm{kHz}$. To improve upon this system, we have replaced it by a commercial ultra-stable passive cavity[19]. The cavity has a free spectral range $\Delta\nu_{\mathrm{FSR}} = 1.5\,\mathrm{GHz}$ and is made from two high-reflectivity mirrors with an expected finesse of $\mathcal{F} = 250 \times 10^3$. The cavity is machined from ultra-low expansion glass (ULE), a material with an extremely low thermal expansion coefficient. The cavity is housed in a vacuum chamber at $7 \times 10^{-8}\,\mathrm{mbar}$, which is then housed in an aluminium can which is thermally stabilised[20] using thermoelectric heaters. The expected laser linewidth is of the order of $\sim 50\,\mathrm{Hz}$ with a specified absolute drift rate of $< 15\,\mathrm{kHz/day}$. The absolute frequency drift is caused by the creep of the cavity length.

---

[19] Stable Laser Systems, Fabry-Perot Cavity

[20] Stanford Research Systems, PTC10 Programmable Temperature Controller

An important characteristic of the cavity is the finesse, as this sets the linewidth of the cavity resonances and hence the achievable laser linewidth. For a cavity where the cavity resonance is broader than the linewidth of the laser, the simplest way to measure this is to scan the laser frequency and measure the width of the transmitted light as a function of frequency. However, when the cavity resonance is narrower than the laser linewidth, this method is not possible as the transmission becomes unstable. A way to measure the finesse of a such a cavity is via a ring-down measurement. This measures the lifetime of the photons inside the cavity. To perform this measurement, the laser is locked to the cavity TEM_{00} mode (described later) and the transmitted light measured on a fast-photodiode[21]. When the light into the cavity is suddenly turned off, the exponential decay of the light inside the cavity is measured. The ring-down measurement for the ultra-stable cavity is shown in figure 4.17, along with an exponential decay fit. The fitted 1/e decay rate τ is measured to be $\tau = 25.05 \pm 0.05\,\mu\mathrm{s}$. From this, we calculate the finesse using the relation [108]

$$\mathcal{F} = 2\pi \Delta\nu_{\mathrm{FSR}} \tau \ , \tag{4.3.2}$$

to be $\mathcal{F} = (236.0 \pm 0.5) \times 10^3$ and a full-width at half-maximum resonance width of $\Delta\nu_{\mathrm{c}} = 6.35 \pm 0.01\,\mathrm{kHz}$. This is slightly below specification, most likely due to the estimation of scattering and absorption losses of the mirrors. This is still however, much greater than the previous home-built cavity.

The 689 nm laser frequency is locked to the cavity using the PDH technique [104, 105] and is shown schematically in figure 4.18(a). The 689 nm light is passed through an optical isolator and phase modulated at 10.11 MHz using an EOM. The light is then sent through a polarising beamsplitter cube to create clean linear polarisation. Approximately 100 µW of light is then focussed into the cavity using a $f = 400\,\mathrm{mm}$ lens to improve the mode matching into the cavity. The mode matching is measured to be $\sim 12\,\%$ by measuring the transmission of the light when locked to the cavity. The reflected component of the light is detected on a fast-photodiode and sent to a frequency mixer. The signal sent to the EOM is also sent to the mixer with a

---

[21] Thorlabs PDA10A-EC

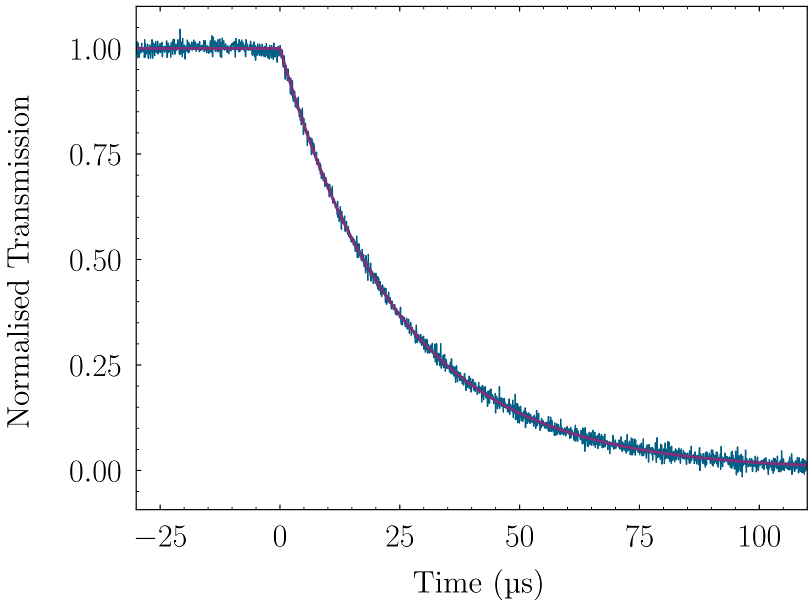

Figure 4.17: Normalised transmission of the light inside the cavity after a sudden turn off of the input light. The solid line is an exponential fit to the data.

phase shift set by a length of SMA cable. The demodulated signal is then used to frequency lock[22] the laser to the cavity.

The in-loop error signal was used to optimise the lock performance, following the procedure detailed in [33]. Whilst the laser was locked to the cavity, a directional coupler was attached to the fast-photodiode and the signal sent to a spectrum analyser. The goal is to reduce the frequency components near to the origin and maximise the bandwidth of the signal. Figure 4.18(b) shows the optimised in-loop error signal as a function of detuning Δf from the EOM drive frequency, 10.11 MHz. Here, the bandwidth of the lock is ~ 1.4 MHz.

To truly evaluate the lock performance and measure the laser frequency spectrum, one needs to perform an Allan deviation [46]. However, this requires another laser system of similar linewidth to the laser of interest, which we currently do not have available. Another method to infer the quality of the laser lock is to use the cold gas of strontium. As described in chapter 3, the atomic spatial and thermal distribution are extremely sensitive to the frequency of the laser light. Therefore,

---

[22] Vescent Photonics D2-125 Laser Servo

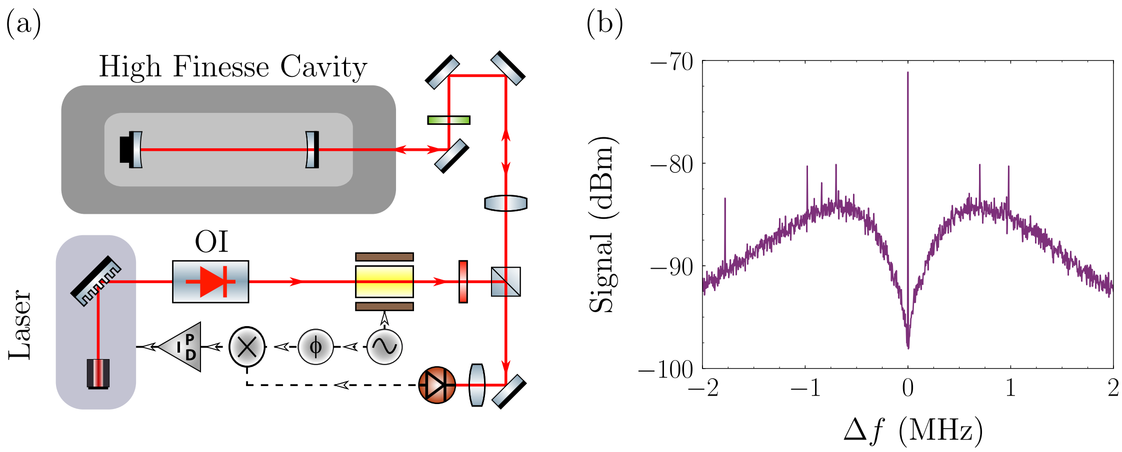

Figure 4.18: (a) Schematic of the optical configuration to lock the frequency of the laser to the high finesse cavity. OI refers to an optical isolator and all other components follow the key shown in figure 4.14. (b) In loop error signal as a function of detuning, centred at 10.11 MHz.

the spatial stability and temperature of the atoms in a nMOT is a good measure of the stability of the laser system. This is explored in section 4.3.4.

Optical layout

The frequency of the $5s^2\ {}^1S_0 \rightarrow 5s5p\ {}^3P_1$ transition is in the middle of two cavity modes. This means that the locked laser must be frequency shifted by almost 750 MHz in order to form a nMOT. To accomplish this large frequency shift, we employ a series of AOMs. The optical layout is shown in figure 4.19. The ultra-stable laser discussed earlier (Master) is double-passed through AOM 1 where it is frequency shifted by 560 MHz. This light is then sent to the ultra-stable cavity and the laser locked to a TEM_{00} mode. The master light is then split between two SM/PM fibers to a wavemeter[23] and the optical frequency comb. A flipper mirror in the wavemeter beam path allows the creation of a resonant probe beam. This light is double passed through AOM 3 and coupled into a SM/PM fibre. The amount of power produced by the master laser is not sufficient to create a nMOT. We therefore inject an additional laser diode (slave) with 1 mW of light from the

---

[23] HighFinesse WS7

master, to produce laser light with a narrow linewidth and a power of ∼ 50 mW. To monitor the injection of the slave, ∼ 1.5 mW are coupled into a scanning Fabry-Perot etalon[24] and 1 mW are sent to the HighFinesse wavemeter. The rest of the light from the slave is double passed through AOM 2 and coupled into a SM/PM fibre for delivery to the experimental chamber.

4.3.3 Creation of a nMOT

The previous laser system used to create a nMOT was locked to an atomic reference on the $5s^2\ {}^1S_0 \rightarrow 5s5p\ {}^3P_1$ transition. However, the new laser system is not referenced to the atomic transition and therefore the transition frequency must be found. To find the transition frequency, a 'shelving' experiment was performed. The 689 nm MOT beams were shone onto a blue MOT and the frequency of AOM 2 was

---

[24] Coherent laser spectrum analyzer

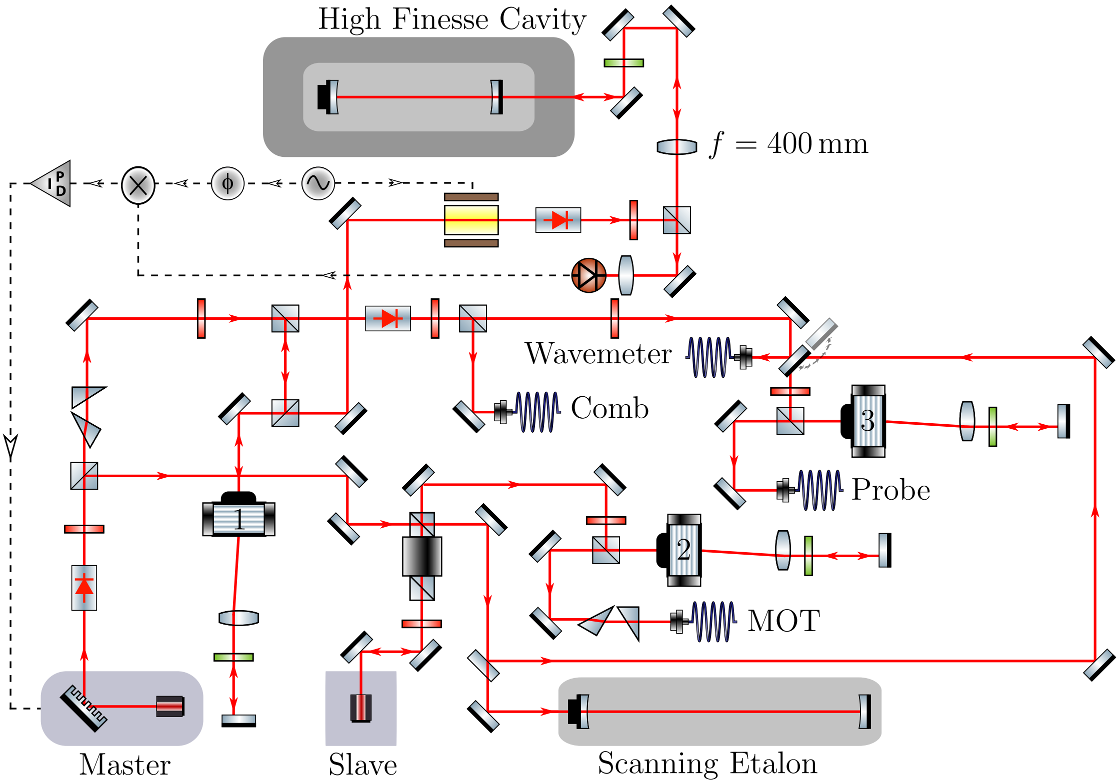

Figure 4.19: Schematic of the optical layout of the full narrow-linewidth 689 nm laser system.

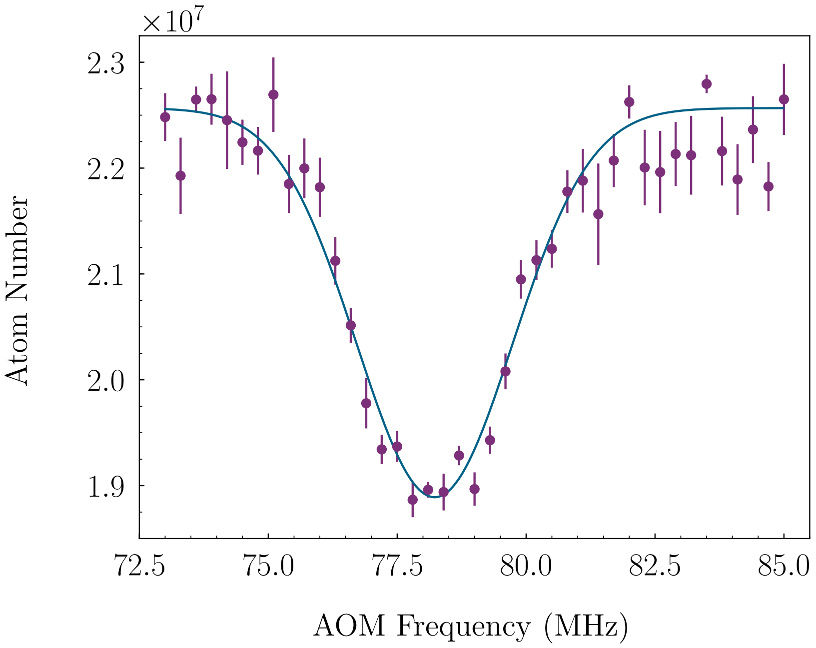

Figure 4.20: Blue MOT atom number as a function of 689 nm MOT beam AOM frequency.

varied. When the 689 nm MOT beams are on resonance with the $5s^2\ ^1S_0 \rightarrow 5s5p\ ^3P_1$ transition, atomic population becomes 'shelved' in the $5s5p\ ^3P_1$ state and one observes a reduction in fluorescence on the $5s^2\ ^1S_0 \rightarrow 5s5p\ ^1P_1$ transition. An example of the observed depletion is shown in figure 4.20. The blue line is a Gaussian fit to the data and the centre frequency is 78.23 ± 0.05 MHz[25].

From this, we are able to set the correct frequency of the 689 nm MOT beams. Naively, one may expect that it is trivial to transfer the atoms from the blue MOT to a nMOT by simply overlapping both of the MOT beams. This is not the case however. The temperature of the atoms in the blue MOT induces a Doppler shift which is too large and the 689 nm MOT beams do not provide a sufficient capture efficiency. To circumvent this problem, the 689 nm MOT beams are initially frequency modulated at 50 kHz, with a deviation of 2 MHz. This creates a comb of frequencies, which enables the 689 nm MOT beams to interact with the vast majority of velocity classes [33]. A MOT formed using the artificially broadened light is

---

[25] Note that the actual frequency shift is double this as the light performs a double-pass through the AOM.

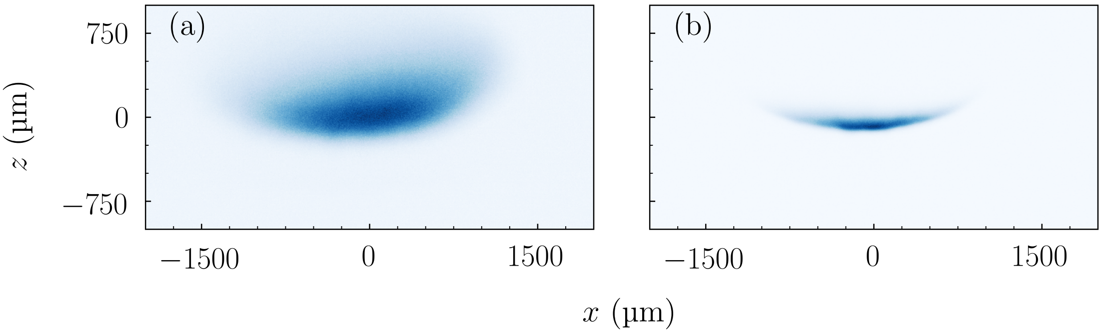

Figure 4.21: Fluorescence images of the first (a) broadband MOT and (b) nMOT in the new experimental chamber.

called a ‘Broadband MOT’. Additionally, the g-factor of the 5s5p ^{3}P$_1$ state is larger than the 5s5p ^{1}P$_1$ state, and therefore a smaller field gradient must be used.

First sighting of a nMOT

The initial attempt to load into the broadband MOT involved using $\sim$ 10 mW of 689 nm MOT light and a frequency modulation of 50 kHz and a deviation of 2 MHz. The centre frequency of the nMOT was $\Delta/2\pi = -3.6$ MHz. The current through the MOT coils was dropped to 0.36 A, one tenth of the current used for the blue MOT, to increase the capture volume. Figure 4.21(a) shows a fluorescence image of the first broadband MOT, imaged on the 5s^2 ^{1}S$_0$ $\rightarrow$ 5s5p ^{1}P$_1$ transition. Even in the broadband MOT, we are able to see the atoms forming a more elliptical shape, similar to that shown in 3.1. The temperature of the atoms in the broadband MOT was measured using the ballistic expansion technique to be $T_z = 11.5 \pm 0.4$ µK and $T_x = 19.5 \pm 0.5$ µK. The difference between the vertical and horizontal temperatures is due to power imbalances in the MOT beams. With no optimisation however, we still observe a reduction in temperature of almost three orders of magnitude compared to the blue MOT.

Once the atoms are cooled in the broadband MOT, they interact most strongly with the sideband on the 689 nm light which is closest to resonance. To transfer atoms from the broadband MOT to the nMOT, we suddenly switch off the frequency modulation and jump the 689 nm light frequency to that of the highest frequency sideband. We also reduce the total power in the MOT beams to 250 µW. This is not the most efficient way to transfer atoms from a broadband MOT to a nMOT; a discussion of this can be found in [45]. Nevertheless, we are able to transfer atoms from the broadband MOT into the nMOT. Figure 4.21(b) shows a fluorescence image of the first nMOT, imaged on the $5s^2\ {}^1S_0 \rightarrow 5s5p\ {}^1P_1$ transition. The nMOT clearly takes the form of the elliptical resonance condition described in 3.1. We once again measured the temperature of the atoms using the ballistic expansion technique, and measured $T_z = 0.85 \pm 0.03\,\mu\mathrm{K}$ and $T_x = 1.04 \pm 0.04\,\mu\mathrm{K}$. This is another order of magnitude colder than the broadband MOT.

4.3.4 Ultracold atoms as an experimental diagnostic

The extreme sensitivity of the nMOT with respect to detuning makes it an ideal tool for characterising the new experimental chamber. Here we use the nMOT to characterise both the magnetic quadrupole field and the 689 nm laser stability.

Calibration of the magnetic quadrupole gradient

As discussed in 3.1, the atoms in the nMOT fall under gravity until the Zeeman shift induced by the magnetic quadrupole field is equal in magnitude to the detuning of the nMOT beams. This makes the position of the nMOT extremely sensitive to the Zeeman shift and hence the local magnetic field. By measuring the change in vertical centroid of the nMOT as a function of nMOT beam detuning, we are able to calibrate the magnetic field gradient. This is shown in figure 4.22 where the current passing through the MOT coils was 0.65 A and the solid blue line is a linear fit to the data, giving a fitted gradient of $\kappa = 0.822 \pm 0.004\,\mu\mathrm{m\,kHz^{-1}}$. The splitting of the Zeeman levels is given by

$$\Delta\omega_z = \frac{g\mu_{\mathrm{B}}\,|\boldsymbol{B}|}{\hbar}\ . \tag{4.3.3}$$

Assuming that the change in vertical centroid of the nMOT is equal to the change in Zeeman shift and hence $|\boldsymbol{B}| = \gamma z$, then

$$\gamma = \frac{\hbar\kappa}{g\mu_{\mathrm{B}}}\ . \tag{4.3.4}$$

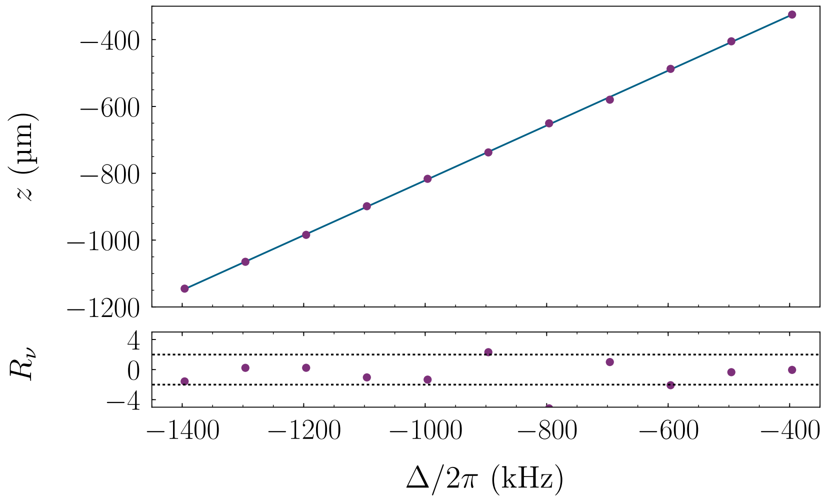

Figure 4.22: The upper plot shows the nMOT vertical centroid as a function of Δ. The lower plot shows the residuals between the data and the fit, normalised to the error bars. The dashed lines show $R_\nu = \pm 2$.

From this, the quadrupole gradient measured in figure 4.22 is $5.80 \pm 0.02\,\mathrm{Gcm^{-1}}$ and $\kappa_q = 8.92 \pm 0.03\,\mathrm{Gcm^{-1}A^{-1}}$. The predicted gradient is $\kappa_q = 9.2\,\mathrm{Gcm^{-1}A^{-1}}$. The discrepancy is most likely due to imperfections in the winding of the coils[26].

Laser Stability

The nMOT can be used to infer the quality of the laser lock to the ultra-stable cavity. If the linewidth of the nMOT beams is larger than the linewidth of the cooling transition, then it is not possible to cool atoms in the nMOT to the fundamental limit of the photon recoil temperature [33]. By reducing the total nMOT beam power to 50 µW where power-broadening become negligible, we are able to create a nMOT with temperatures $T_z = 0.49 \pm 0.03\,\mu\mathrm{K}$ and $T_x = 0.57 \pm 0.03\,\mu\mathrm{K}$ which is very close to the fundamental photon recoil limit of 460 nK, indicating that the linewidth of the laser is less than the transition linewidth.

Another diagnostic is to observe the shot-to-shot variations in the vertical centroid of the nMOT. As the position is very sensitive to the detuning of the nMOT beams, any changes in frequency should appear as a vertical position shift. Figure

---

[26] The magnification of the imaging systems is measured using gravitational free-fall.

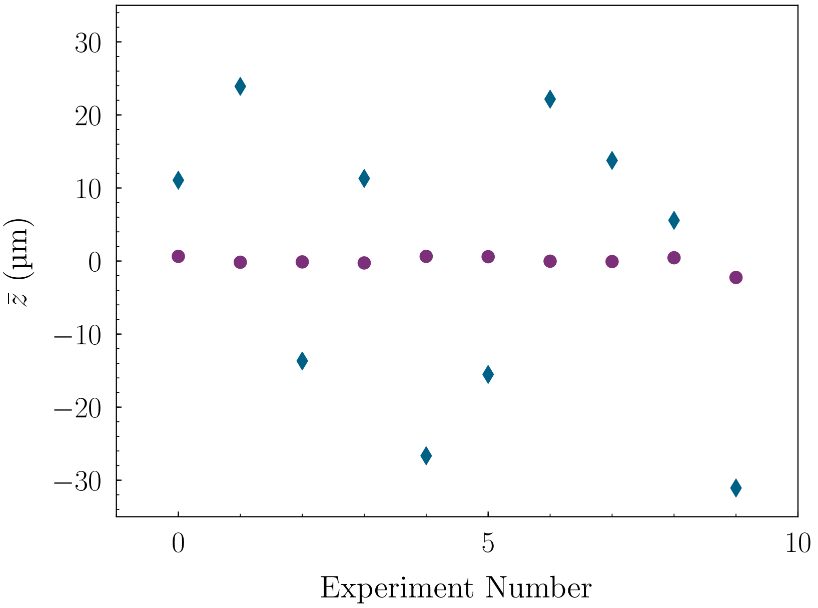

Figure 4.23: The mean position of the nMOT using the new (purple circles) and old (blue diamonds) 689 nm laser systems. The dotted lines are guides to the eye.

4.23 shows the vertical centroid of the nMOT for both the previous (blue diamonds) and new ULE (purpler circles) cavities when forming a nMOT with a detuning of $\Delta/2\pi = -100$ kHz. The shot-to-shot fluctuations in position for the previous cavity have a standard deviation of 19.1 µm, whilst the standard deviation for the new cavity is 0.8 µm. This is a vast improvement on the shot-to-shot fluctuations of the laser an indicate an improved linewidth of the laser system.

4.4 Microtrap configuration

An overview of the main experimental configuration for the creation and detection of atoms in the microtrap is shown in figure 4.24. From hereon, the wavelength of the microtrap used is 532 nm.

4.4.1 Laser system

The microtrap light is provided by a Ti:Sa laser. The microtrap light is focused through an AOM and the first diffracted order is aligned into a SM/PM optical fibre to enable quick switching (typically ∼ 200 ns) of the microtrap. The light

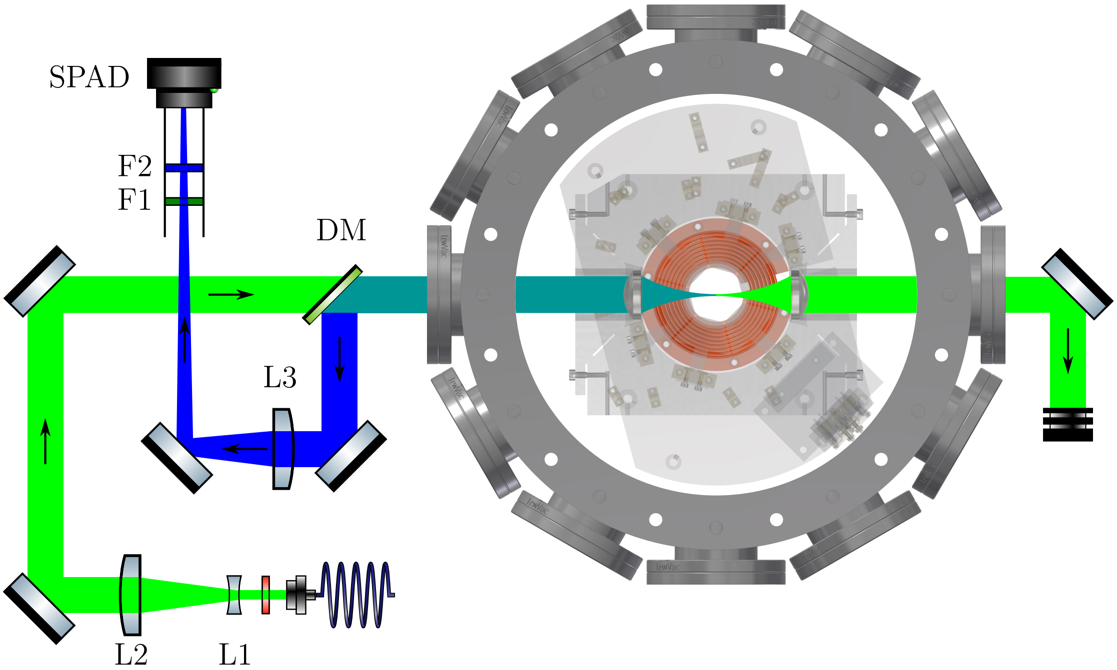

Figure 4.24: Optical schematic for the microtrap. The elements labelling are as follows: L1 - $f = -50\,\text{mm}$; L2 - $f = 200\,\text{mm}$; L3 - $f = 400\,\text{mm}$; DM - dichroic mirror; F1 - 532 nm notch filter; F2 - 461 nm bandpass filter.

is linearly polarised and a half-waveplate is used to align the polarisation of the microtrap parallel to gravity. To create a microtrap of the order of 1 µm, the whole aperture of the in-vacuo high NA lens must be used. We therefore expand the beam out of the fibre to a $1/e^2$ radius of $\sim 12\,\text{mm}$. The beam expander is a cage mounted system comprising of $f = -50\,\text{mm}$ and $f = 200\,\text{mm}$ achromatic doublets. Achromatic doublets are used to minimize aberrations. The expanded beam is sent through both in-vacuo lenses and impinges on a beam dump on the other side of the chamber.

4.4.2 Imaging

Atoms trapped in the microtrap will scatter light on the broad $5s^2\ {}^1S_0 \rightarrow 5s5p\ {}^1P_1$ transition at 461 nm. This scattered light is separated from the microtrap light using a dichroic mirror[27]. The microtrap light is transmitted through and the scattered

---

[27] Semrock DI03-R473-T3-50.8-D

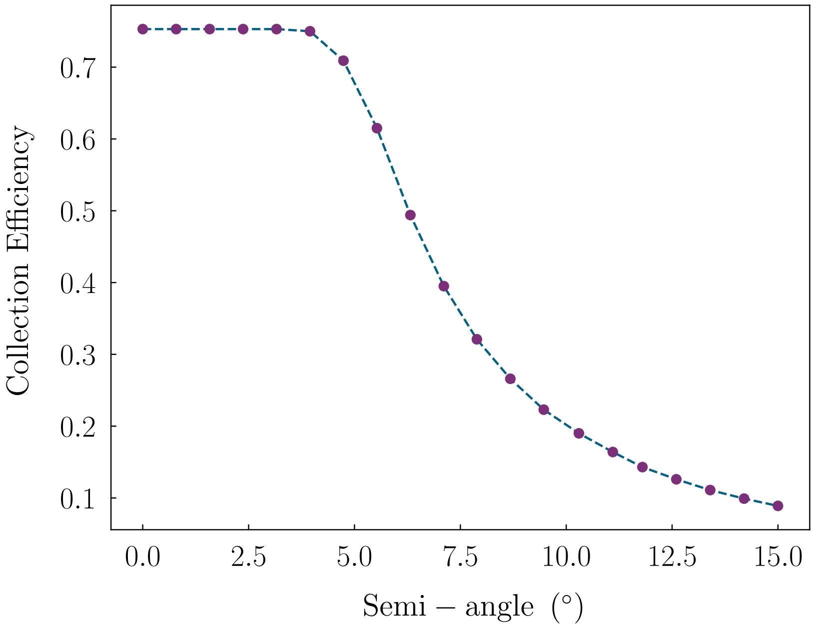

Figure 4.25: Collection efficiency of the SPAD camera as a function of the semi-angle of the input beam. Simulated data provided by Micro Photon Devices.

light is reflected off the dichroic mirror. This configuration was chosen as the transmitted wavefront error is significantly less than the reflected wavefront error due to mechanical stress between the multiple layers of the dichroic mirror [109]. The 461 nm light is focused using a $f = 400$ mm achromatic doublet onto a SPAD array camera[28]. The camera is an array of 64×32 individual single-photon avalanche detectors (SPAD) with integrated counting electronics. The quantum efficiency is optimised for 'blue' wavelengths with a peak of 50% at 420 nm. One of the downsides of this product is that each pixel has a size of 150 µm × 150 µm but the active area is only 30 µm × 30 µm, limiting the detection efficiency. However, the camera used in the experiment is a research-grade product which has an integrated micro-lens array in front of the SPAD's. The collection efficiency as a function of the incident beam angle is shown in figure 4.25. For incident beam angles of $< 4°$, the collection efficiency increases to ~ 75 %, much greater than the 4 % which one would expect without the micro-lens array.

---

[28] MPD-SPC3, a commercially available SPAD array camera (Micro Photon Devices), whose SPAD imager is described here [110].

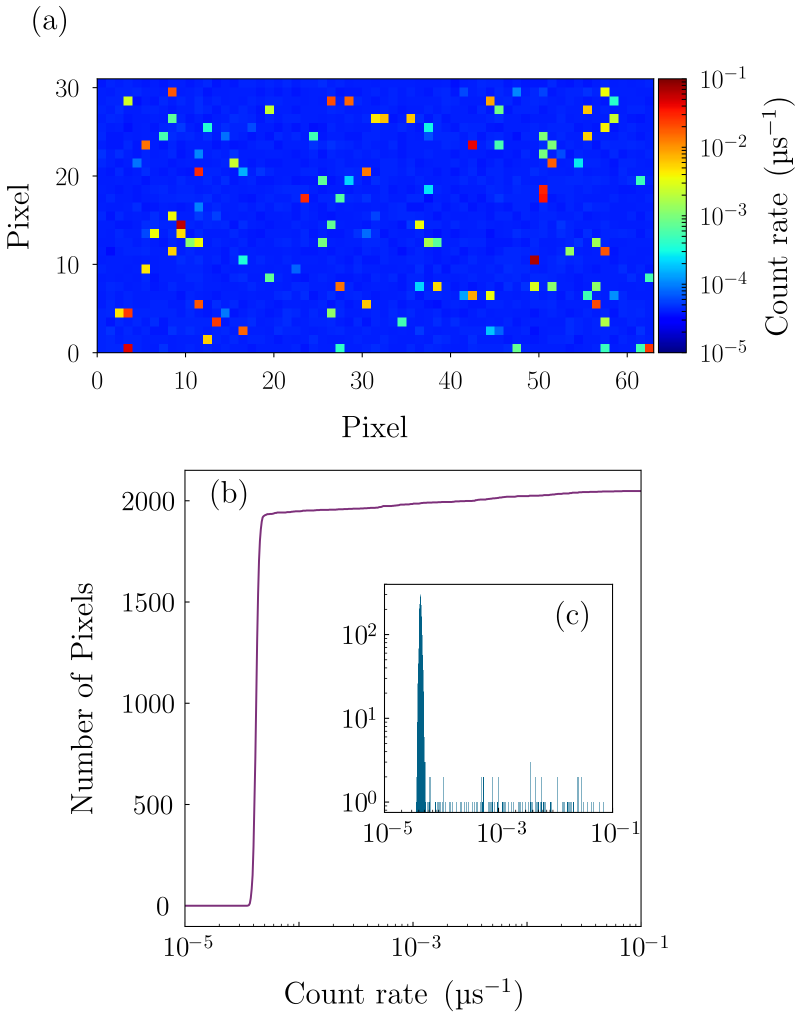

Figure 4.26: Count rate of the SPAD in the presence of 50 mW of microtrap light and the absence of atoms. (a-c) show the individual pixel count rates, the cumulative distribution function of count rate, and the histogram of count rates respectively.

The front of the SPAD camera is enclosed with a 100 mm lens tube, containing a 532 nm notch filter[29] and a 461 nm bandpass filter[30]. The notch filter has an optical depth > 6 at 532 nm and a spectral width of 17 nm. This attenuates any microtrap photons which are incorrectly reflected into the imaging path. The band-pass filter has a transmission of 98 % at 461 nm with a FWHM of 10 nm, and an optical depth > 4 for the wavelength range 270 nm → 1200 nm. This reduces the collection of unwanted photons. Figure 4.26 shows the count rate across the SPAD camera in

---

[29] Thorlabs NF533-17

[30] Edmund 88-010

Component	**Efficiency (%)**
In-vacuo lens collection	1.7
In-vacuo lens transmission	92
Viewport transmission	99.5
Dichroic reflectance	99.8
$f = 400\,\mathrm{mm}$ lens transmission	99.6
Mirrors ×3	99.6
Notch filter transmission	96.7
Band-pass filter transmission	98
SPAD camera detection	38.0 ± 0.2
Total	$\mathbf{0.55 \pm 0.04}$

Table 4.7: Collection efficiency of the imaging system.

the presence of 50 mW of microtrap light and the absence of atoms. There are a few 'hot' pixels, but the count rate for the majority of the pixels is limited by the dark count rate of the camera.

Based on the description of the imaging system above, we are able to estimate the total detection efficiency of the imaging system at 461 nm. The collection efficiency of the in-vacuo lens is 1.7 %, based on a working distance of 37 mm and a clear aperture of 20 mm. The transmission through the lenses is limited by the absorbency of the ITO coating on the lens. This limits the transmission of the lenses to 92 %. The dichroic mirror has a high reflectance of 99.8 %. The rest of the standard optics contribute little to the loss of 461 nm photons. The final limiting factor is the detection efficiency of the SPAD camera. With the microlens array, the detection efficiency of the camera is approximately 38 %. The total detection efficiency of the imaging system is estimated to be 0.55 ± 0.04 %, where the dominant error is the detection efficiency of the SPAD array. The total detection efficiency of the imaging system is summarised in table 4.7.

4.5 Summary

In this chapter, we have calculated the polarisability of the relevant states of strontium at a variety of wavelengths, and shown that it should be possible to create a microtrap at wavelengths of 813 nm, 914 nm and 532 nm. We have discussed and detailed upgrades to the experimental innards which will facilitate the creation of a strontium microtrap, as well as upgrades to the laser systems.

Chapter 5

Loading and imaging a microtrap of Sr atoms

In the previous chapter, we discussed the new experimental innards and laser systems which will facilitate the creation of a strontium microtrap. At the time of submission, to the best of our knowledge the smallest FORT of strontium was approximately 15 µm [111]. Therefore, an initial goal was the loading and characterisation of a single strontium microtrap. However, more recently arrays of single strontium atoms in FORT's have been demonstrated by Cooper *et al.* [112] and Norcia *et al.* [113] in a FORT of $w_0 \sim 0.5$ µm.

5.1 Loading the microtrap

As discussed in section 2.2.2, for an atom to be trapped in the microtrap, its kinetic energy must be less than the potential energy. We therefore require a situation where the scattering rate of the atoms in the microtrap is high enough and the transit time is long enough, such that the atoms lose their initial kinetic energy whilst in the microtrap.

There are a multitude of loading schemes available to load atoms into the microtrap. The simplest option is to load the microtrap directly from a MOT as this is a sample of trapped, cold atoms which are undergoing laser cooling. However, due to the existence of multiple laser cooling transitions in strontium, there are a range of loading possibilities. These options are summarised below:

- Direct loading from a blue MOT with a deep trap,
- Direct loading from a broadband red MOT (bMOT),
- Direct loading from a nMOT.

To test the feasibility of these loading schemes, we compare the time it takes for an atom to cross the microtrap t_{dip} against the time taken for atoms to scatter enough photons from the cooling light to remove the initial kinetic energy $E_{\mathrm{k}}^{\mathrm{i}}$. We analyse the loading mechanisms for a microtrap operating at 532 nm, as this has the largest transition shifts (see table 4.2).

By making some simple assumptions, we are able to qualitatively analyse the different loading schemes. For a given atomic temperature, we calculate the cumulative Maxwell-Boltzmann distribution (CDF) and the time it takes for an atom to travel a distance of $2w_0 = 2\,\mu\mathrm{m}$. If we assume that the cooling light directly opposes the atomic velocity, then the number of scattering events N_{s} required for an atom to be trapped is given by

$$N_{\mathrm{s}} = \frac{E_{\mathrm{k}}^{\mathrm{i}}}{E_{\mathrm{r}}} \,, \tag{5.1.1}$$

where $E_{\mathrm{r}} = \hbar^2 k^2 / 2m$ is the recoil energy of the absorbed photon with wavenumber k. The time t_{s} required to scatter N_{s} photons for a given scattering rate R is then calculated by

$$t_{\mathrm{s}} = \frac{N_{\mathrm{s}}}{R} \,. \tag{5.1.2}$$

We calculate this for two scattering rates. The first is where there is no light shift of the atomic states and the detuning from resonance is the MOT beam detuning. The second is the maximal light shift one would expect for a given trap depth, in addition to the MOT beam detuning. By comparing the velocities at which $t_{\mathrm{dip}} = t_{\mathrm{s}}$, we are able to estimate the fraction of atoms which can be trapped in the microtrap.

Figure 5.1 illustrates the above calculations for loading the microtrap from a blue, bMOT and nMOT. Naively, one may expect that loading from the blue MOT is the best option due to the large transition scattering rate. However the calculations

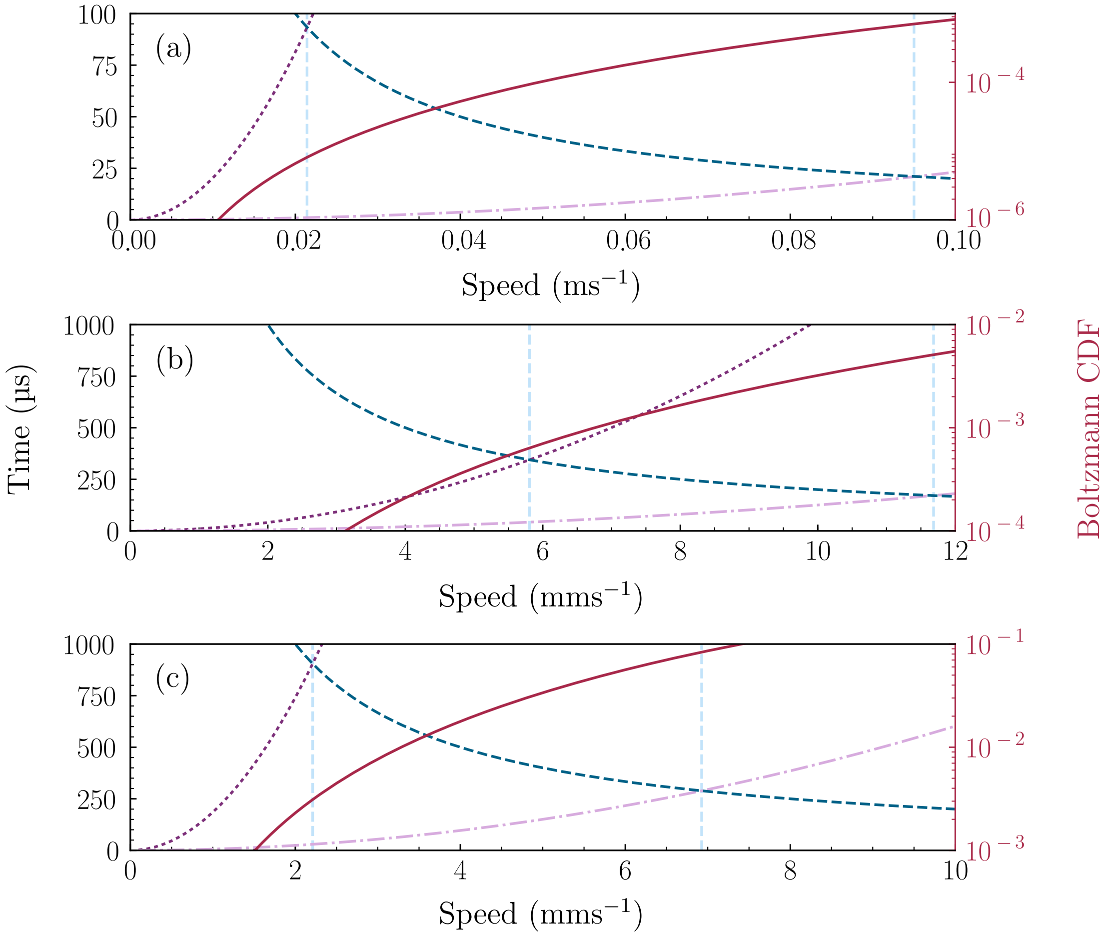

Figure 5.1: 532 nm microtrap loading possibilities from a blue (a), bMOT (b) and nMOT (c). The red (solid) curve shows the cumulative Maxwell-Boltzmann distribution for a temperature of (a) 5 mK, (b) 20 µK, (c) 1 µK. The microtrap trap depths are (a) 10 mK, (b) 100 µK, (c) 10 µK. The dark purple (dotted) curve shows the scattering time required for $\Delta/2\pi =$ (a) 410 MHz, (b) 50 kHz, (c) 50 kHz. The light purple (dot-dashed) curve shows the scattering time required for $\Delta/2\pi =$ (a) 40 MHz, (b) 7.4 kHz, (c) 7.4 kHz. The power of the cooling light is $S =$ (a) 0.4, (b) 20, (c) 1. The blue curve (dashed) shows the time taken for an atom to travel 2 µm. The light blue (vertical-dashed) lines show the maximum velocity which can be captured into the microtrap for a given scattering rate.

MOT Type	**CDF Range**	**Typical MOT Density ($\mathbf{cm^{-3}}$)**
Blue	$8 \times 10^{-6} \to 7 \times 10^{-4}$	1×10^{9}
bMOT	$1 \times 10^{-3} \to 8 \times 10^{-3}$	1×10^{10}
nMOT	$3 \times 10^{-3} \to 7 \times 10^{-1}$	1×10^{12}

Table 5.1: Maxwell-Boltzmann CDF range for loading from a blue, bMOT or nMOT. The typical MOT densities are also tabulated.

suggest that for an initial MOT temperature of $T = 5\,\mathrm{mK}$, only $8 \times 10^{-6} \to 7 \times 10^{-4}$ of the number of atoms in the MOT can be trapped in the microtrap. This makes it very challenging to load the microtrap from a blue MOT. If we consider loading the microtrap from a red MOT, one may expect the scattering rate to be too low to load atoms into the microtrap, given that $t_{\mathrm{dip}} \approx 1/\Gamma$. However, plots (b) and (c) suggest that it should be possible to load directly from both the bMOT and nMOT, due to the 'slow tail' of the Maxwell-Boltzmann distribution. One factor which isn't taken into consideration in this figure is the atomic density. The density of the nMOT is almost three orders of magnitude larger than that of the blue MOT, making the loading from a nMOT the best option by far. This is summarised in table 5.1.

5.2 First sighting of the microtrap

The loading scheme with the highest propensity for success is direct loading from a nMOT. One of the challenges of this method however is the initial alignment of the microtrap beam onto the nMOT, due to a typical nMOT size of 100 µm. Here we detail the initial alignment procedure of the microtrap beam onto the nMOT.

Initially the microtrap beam was apertured using an iris to create a 'pencil beam', and aligned onto the centre of the in-vacuo lens using the back reflections from the lens surfaces. Once the microtrap was centred on the first lens, a 461 nm resonant probe beam was counter-propagated and overlapped with the microtrap beam by sending it through the second in-vacuo lens. By filling the main chamber with ultracold atoms, we were able to observe the the profile of the resonant probe beam. Figure 5.2 shows a false colour fluorescence image of the probe beam, using the PixelFly QE camera with a long-exposure time of 10 ms. We are able to clearly observe the focussing of the probe beam through the chamber. Although this doesn't provide the axial location of the microtrap waist due to the imaging angle, it does facilitate the vertical alignment of the nMOT with respect to the microtrap. The nMOT was positioned to the same vertical position as the observed focus by applying a shim magnetic field using an additional set of orthogonal coils [33]. The x and y positions of the nMOT were also varied using the shim coils, such that we could observe the probe beam destroying the nMOT.

The 461 nm probe was also used to align the imaging system. The SPAD camera was set to a distance of 365 mm from the $f = 400$ mm lens used for imaging, based upon calculations performed in Zemax. An iris was placed in front of the SPAD camera and the camera was positioned so that the probe light hit the centre of the iris, ensuring that the SPAD camera was centred on the imaging focus. To position the nMOT at the correct axial location, the y-shim coil was varied such that the nMOT image was at the optimum focus on the SPAD camera.

Initially, we created a larger microtrap by aperturing the microtrap beam to a diameter of 3 mm. From Zemax calculations, this produced a microtrap with $w_0 \sim 6.2$ µm which increased the ease of detection of the microtrap. The power of

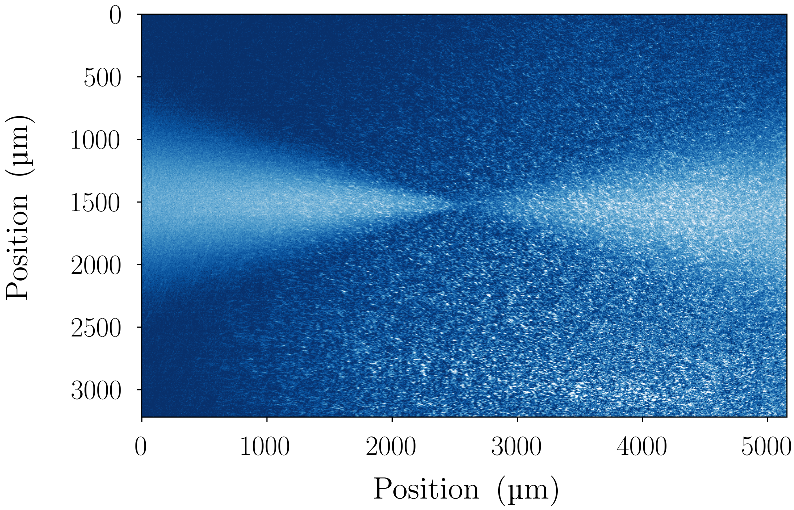

Figure 5.2: Fluorescence image of the probe beam with the PixelFly QE camera, from the side.

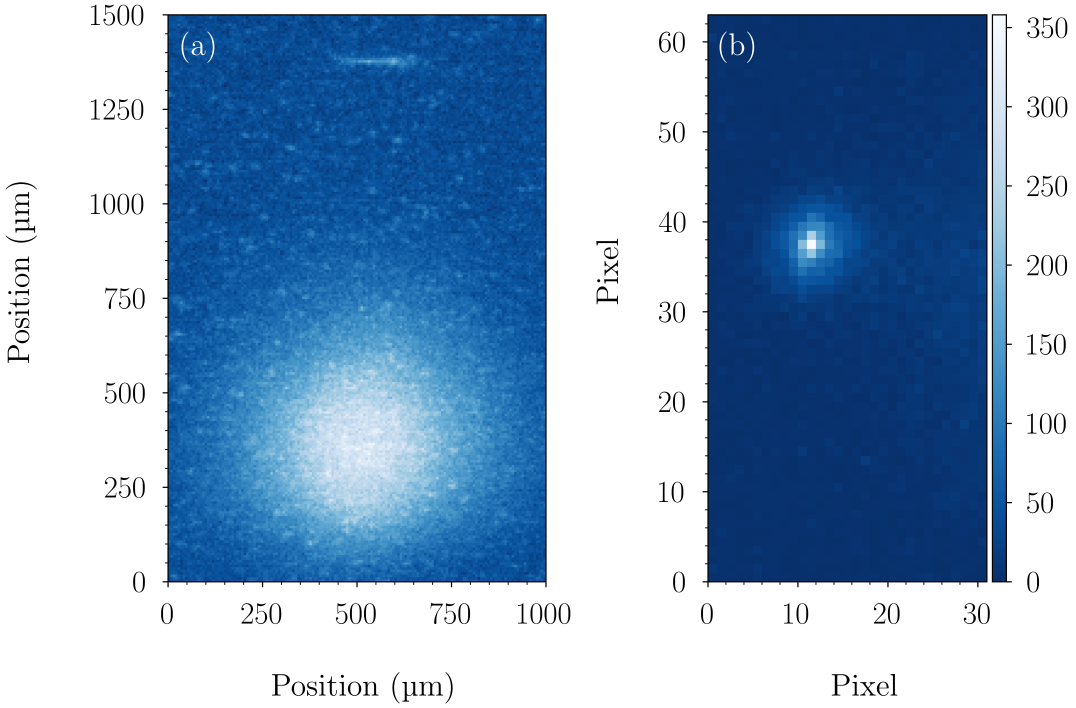

Figure 5.3: Fluorescence image of the first sighting of the microtrap imaging with the (a) PixelFly QE camera and the (b) SPAD camera.

the microtrap beam after the aperture was 5 mW, with an estimated trap depth of 14 µK. We attempted to load the microtrap by shining the microtrap light into an actively cooled nMOT for 100 ms. To distinguish atoms trapped in the microtrap from those in the nMOT, the nMOT light and the quadrupole field were turned off, whilst the microtrap light remained on. This allowed the nMOT atoms to fall away under gravity but allowed the trapped atoms to remain. After a time of 15 ms, the blue MOT light was used to image the atoms on both the PixelFly QE and SPAD cameras. Figure 5.3(a) shows the first sighting of the microtrap loaded with atoms, imaged from the side with the PixelFly QE camera with an exposure time of 100 µs. The trapped atoms are clearly visible above the un-trapped falling nMOT atoms. Figure 5.3(b) shows the microtrap imaged using the SPAD camera and an exposure time of 10 µs. Due to the large waist of the microtrap, the Rayleigh length of the microtrap is much larger than the depth of field of the in-vacuo lens and therefore the image of the microtrap spreads over a larger number of pixels.

5.3 In situ imaging

Removing the aperture from the microtrap allows the in-vacuo lens to be fully illuminated, creating the smallest possible microtrap. The imaging system detailed in section 4.4.2 has a magnification of 10. Therefore a microtrap of size $\sim 1\,\mu\mathrm{m}$ is mapped onto one pixel of the SPAD camera. By lowering the atomic density, we are able to enter a regime where the microtrap is loaded with few atoms. We now analyse the distribution of counts one would expect when operating in this regime, the optimum experimental parameters for imaging single atoms and the current limit of detection.

5.3.1 Composite Poisson distribution

This is based upon the work of [20]. The distribution of counts detected by the SPAD camera is a composite of three Poisson distributions ($\Pi(\mu, n)$); the atomic distribution, the distribution of scattered photons and the distribution of background counts. The probability to detect n_{b} background counts is given by

$$P_{\mathrm{b}}(n_{\mathrm{b}}) = \Pi(\bar{n}_{\mathrm{b}}, n_{\mathrm{b}}) \quad , \tag{5.3.3}$$

where $\bar{n}_{\mathrm{b}}$ is the mean number of background counts. The probability to trap N_{at} atoms in the microtrap is given by

$$P_{\mathrm{at}}(N_{\mathrm{at}}) = \Pi\left(\bar{N}_{\mathrm{at}}, N_{\mathrm{at}}\right) \quad , \tag{5.3.4}$$

where $\bar{N}_{\mathrm{at}}$ is the mean number of atoms in the microtrap. The probability to detect n counts due to scattered photons from a fixed number of atoms in the microtrap is given by

$$P_{\mathrm{s}}(n)\,|_{N_{\mathrm{at}}} = \Pi(\epsilon_{\mathrm{s}} N_{\mathrm{at}}, n) \quad , \tag{5.3.5}$$

where ϵ_{s} is a constant of proportionality which is dependent on the experimental imaging parameters. However, as there is a distribution of atoms in the microtrap, one must perform a sum over all possibilities. This results in a distribution for the number of counts n_s due to scattered photons from the atoms of

$$\begin{aligned} P_\mathrm{s}\left(n_\mathrm{s}\right)|_{N_\mathrm{at}} &= \sum_{N_\mathrm{at}=0}^{\infty} P_\mathrm{at}\left(N_\mathrm{at}\right) \times P_\mathrm{s}\left(n_\mathrm{s}\right)|_{N_\mathrm{at}} && (5.3.6)\\ &= \sum_{N_\mathrm{at}=0}^{\infty} \Pi\left(\bar{N}_\mathrm{at}, N_\mathrm{at}\right) \Pi\left(\epsilon_\mathrm{s} N_\mathrm{at}, n_\mathrm{s}\right) \ . && (5.3.7) \end{aligned}$$

Equation 5.3.6 in its current form does not include the detection of background counts n_b. The probability of the SPAD camera to detect n_tot counts is given by $n_\mathrm{tot} = n_\mathrm{b} + n_\mathrm{s}$. Therefore, for a given number of detected counts, the number of those which are due to scattered photons and due to background counts range from

$$\begin{aligned} n_\mathrm{s} &= 0 \rightarrow n_\mathrm{tot} && (5.3.8)\\ n_\mathrm{b} &= n_\mathrm{tot} - n_\mathrm{s} = n_\mathrm{tot} \rightarrow 0 \ . && (5.3.9) \end{aligned}$$

The total probability $P_\mathrm{tot}\left(n_\mathrm{tot}\right)$ to detect n_tot counts on the SPAD camera, given that we detect both background counts and counts from atom fluorescence, is given by

$$P_\mathrm{tot}\left(n_\mathrm{tot}\right) = \sum_{k=0}^{n} P_\mathrm{b}\left(k\right) P_\mathrm{s}\left(n_\mathrm{tot} - k\right) \ . \qquad (5.3.10)$$

This probability distribution includes terms which involve an infinite sum. In reality, performing an infinite sum is not possible. We therefore calculate the probability distribution until convergence at the 0.1% level. Based upon this composite Poisson distribution, we require ~ 80 counts per atom per imaging frame to enter the regime of single atom distinguishability (see figure 5.4).

5.3.2 Imaging with MOT beams

Typically in single atom experiments involving the alkali-metal atoms, the microtrap is loaded continuously from an optical molasses and the fluorescence of atoms in the microtrap caused by the MOT beams is used to detect single atoms [89]. As the strontium microtrap is loaded on the narrow $5\mathrm{s}^2\ ^1\mathrm{S}_0 \rightarrow 5\mathrm{s}5\mathrm{p}\ ^3\mathrm{P}_1$ inter-combination transition, this method is not experimentally feasible due to the low scattering rate. We therefore propose to load the microtrap from a nMOT using a shallow microtrap of the order of a few µK, then linearly increase the microtrap depth to $> 5\,\mathrm{mK}$

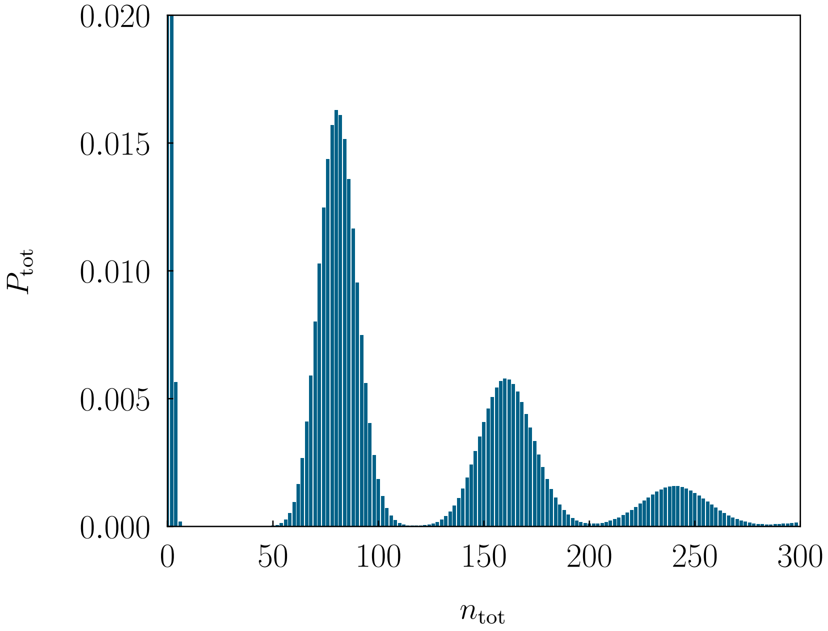

Figure 5.4: Simulated probability mass function as a function of detected counts for a microtrap with a mean atom number of $\bar{N}_{\text{at}} = 1$, $\bar{n}_{\text{b}} = 1$ and $\epsilon_{\text{s}} = 80$. Note that the y-scale is truncated to clarify the peaks associated with atomic scattering.

and image the microtrap using the 461 nm MOT beams. The two most important parameters to consider are the ratio of the atomic temperature to the trap depth $k_{\text{B}}T/U_0$, and ϵ_{s} which is an interplay between atomic scattering rate, exposure time, and detection efficiency.

Naively, the final microtrap depth should be sufficiently deep given that it is nearly an order of magnitude greater than than the Doppler temperature. In reality however, the AC Stark shift of the imaging transition must be taken into consideration. Due to the lack of hyperfine structure in ^{88}Sr, sub-Doppler cooling doesn't apply and the atomic temperature is limited by Doppler theory. The temperature is dependent on the detuning of the light as [114, 115]

$$k_{\text{B}}T = \frac{\hbar\Gamma}{2}\frac{1 + S + (2\Delta/\Gamma)^2}{4\,|\Delta|\,/\Gamma}\ . \tag{5.3.11}$$

This is shown by the blue-solid line in figure 5.5. The differential AC Stark shift is not detrimental in the alkali-metal atoms as sub-Doppler cooling largely removes the detuning dependence. The purple-dashed line shows a sketch of the expected behaviour if sub-Doppler cooling were to exist.

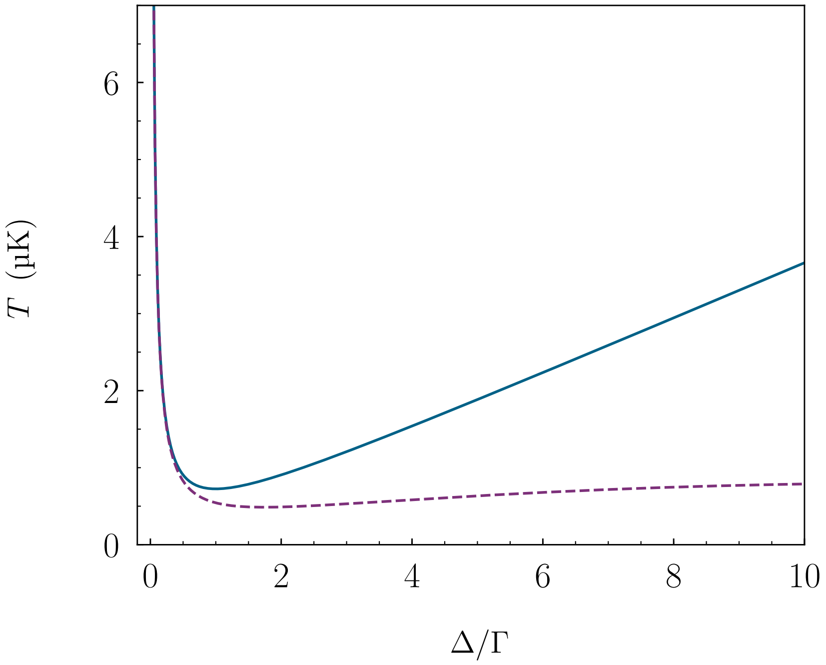

Figure 5.5: Doppler limited atomic temperature (blue-solid line) and sub-Doppler temperature (purple-dashed line) as a function of imaging beam detuning. Note that the sub-Doppler temperature is a sketch of the expected behaviour if sub-Doppler cooling were to exist.

The differential frequency shift of the $5\mathrm{s}^2\ {}^1\mathrm{S}_0 \rightarrow 5\mathrm{s}5\mathrm{p}\ {}^1\mathrm{P}_1$ transition for the $m_j = -1$ state (see table 4.2) is 37 MHz/mK. Figure 5.6(a) shows the Doppler limited temperature of the atoms (solid purple line) in the microtrap as a function of the microtrap depth, given that they are scattering photons from the blue MOT beams with intensity $S = 0.4$. The dashed blue line shows where the temperature of the atoms is equal to the microtrap depth. This figure indicates that a microtrap depth of the order of 1 K is required to enter a regime where the microtrap depth is approximately an order of magnitude greater than the Doppler temperature, which is practically infeasible. This is because the gradients of both of the lines are similar. To explore this parameter space further, figure 5.6(b) shows a two-dimensional plane of the Doppler limited temperature of the atoms in the microtrap as a function of both microtrap depth and power of the MOT beams. The dashed line shows where $U_0/k_\mathrm{B}T = 1$, which indicates that even for a large parameter space, there is not a regime where $U_0 \gg k_\mathrm{B}T$.

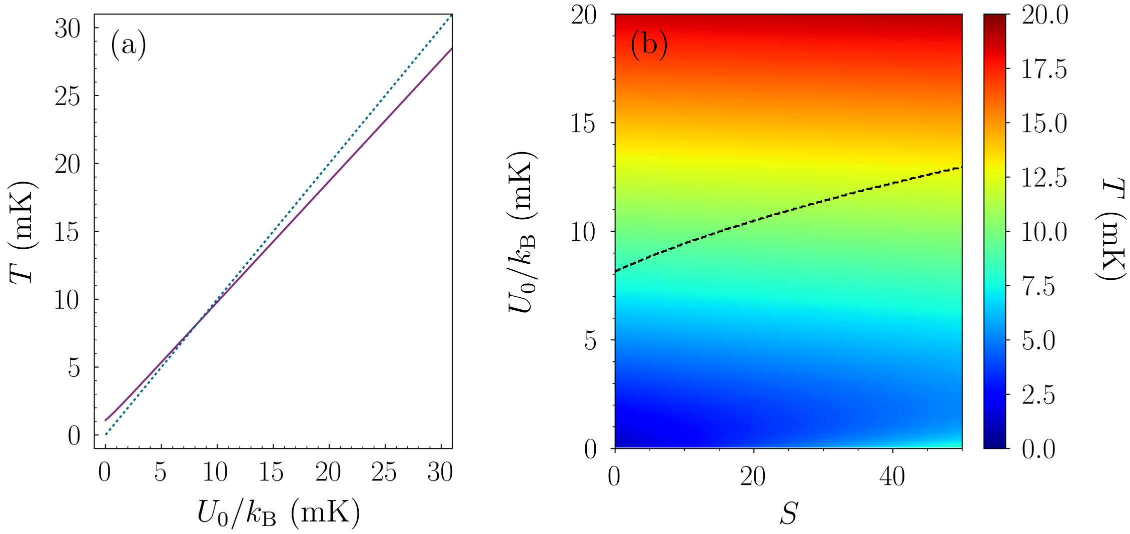

Figure 5.6: (a) The solid purple line shows the Doppler limited temperature of the atoms (solid purple line) in the microtrap. The dashed blue line shows where the temperature of the atoms is equal to the microtrap depth. (b) Doppler limited temperature of the atoms in the microtrap as a function of microtrap depth and MOT beam intensity. The dashed black line shows where $U_0/k_\mathrm{B}T = 1$.

The differential frequency shift of the $5\mathrm{s}^2\ {}^1\mathrm{S}_0 \rightarrow 5\mathrm{s}5\mathrm{p}\ {}^1\mathrm{P}_1$ transition also has a significant impact on ϵ_s. Figure 5.7 shows the expected number of counts per atom per microsecond, as a function of microtrap depth and imaging beam power. The white dashed line also shows where the trap depth is equal to the Doppler limited temperature. The background count rate ϵ_b when using the MOT beams is $\epsilon_\mathrm{b} \sim 1 \times 10^{-2}\,\mathrm{cts}\,\mu\mathrm{s}^{-1}$. This is much larger than the dark count rate of the SPAD camera and is caused by diffusive scatter from the viewports and from inside the chamber. Given that the maximum intensity of the MOT beams is $S = 0.4$, it is impossible to enter a regime where $\epsilon_\mathrm{s} > \epsilon_\mathrm{b}$. We can enter a regime where $\epsilon_\mathrm{s} > \epsilon_\mathrm{b}$ however by using a focused imaging beam. When using a focused imaging beam, we are able to reduce the background count rate to $\epsilon_\mathrm{b} \sim 1 \times 10^{-4}\,\mathrm{cts}\,\mu\mathrm{s}^{-1}$.

One would assume that it is not possible to continually image atoms in a microtrap when the atomic temperature is approximately equal to the microtrap depth. To test this conjecture, we imaged the atoms in a microtrap of depth $\sim 10\,\mathrm{mK}$ as a function of time using a probe beam with $S = 15$ and $\Delta = -\Gamma$ from the unperturbed

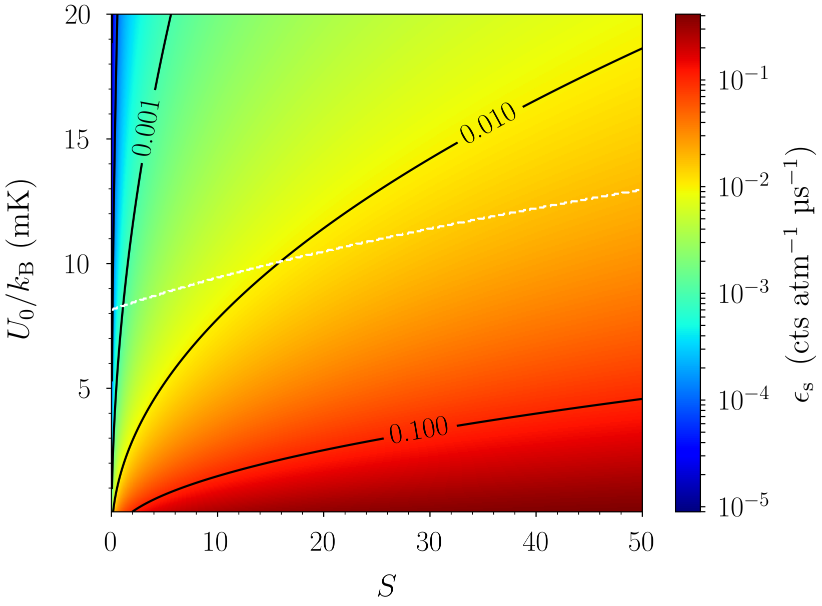

Figure 5.7: Expected number of counts per atom per microsecond, as a function of microtrap depth and imaging beam power. The dashed white line shows where $U_0/k_\mathrm{B}T = 1$.

$5s^2\ ^1S_0 \rightarrow 5s5p\ ^1P_1$ transition. Figure 5.8 shows the estimated[1] mean atom number after an exposure time of 1 ms (a), and the statistics of the detected counts (b) in the low atom number regime, over 500 realisations of the experiment. The density was controlled by varying the load time of the blue MOT. A loading time of 150 ms was used here. We clearly observe a rapid loss in the mean number of detected atoms as a function of time. This rapid loss reduces the total number of photons we are able to detect per atom and therefore prevents us from distinguishing between single atoms, as shown in the statistics of (b-d). It is also not possible to combine the data shown in (b-d) as the mean of the distributions vary significantly as a function of time. If we assume that the heating rate of the imaging beam is given by $E_\mathrm{r}R$ where E_r is the recoil energy of the emission of a 461 nm photon, then one would expect a heating rate of $\sim 2\,\mathrm{mK/ms}$, which is compatible with the loss rate observed.

---

[1] The atom number is estimated from the detected count rate, given the calculated atomic scattering rate and the detection efficiency of the imaging system.

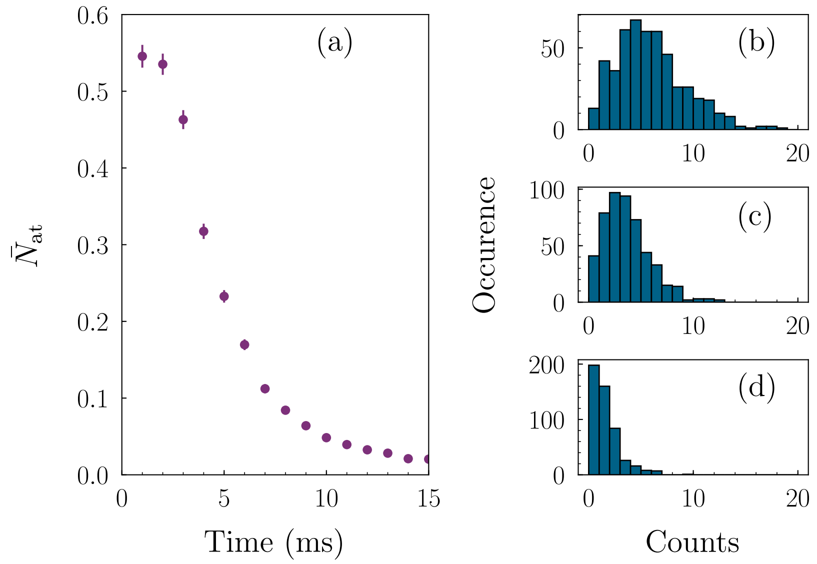

Figure 5.8: (a) Mean number of atoms, estimated from the number of counts, as a function of time when imaging with a probe beam with $S = 15$ and $\Delta = -\Gamma$ from the unperturbed $5s^2\ {}^1S_0 \rightarrow 5s5p\ {}^1P_1$ transition. (b-d) Histogram of the detected counts after 1 ms, 3 ms, and 5 ms respectively.

5.3.3 Stroboscopic Imaging

A possible solution to this problem has been demonstrated by Hutzler *et al.* [116]. They showed that by stroboscopically pulsing on and off the MOT and trapping light, they were able to mitigate the effect of detrimental light shifts. We implemented this solution with a retro-reflected one dimensional imaging beam with $1/e^2$ radius of 3 mm, detuned from the bare resonance by $\Delta = -\Gamma$. Initially, the effect of pulsing the microtrap light at a frequency of 500 kHz in the absence of any other light on the atoms in the microtrap was measured. We were able to perform 5×10^4 cycles with no detriment to the atom number in the microtrap. The microtrap pulses were then interleaved with the imaging beam, as shown in the inset of figure 5.9. Figure 5.9 shows the lifetime of the atoms in the microtrap as a function of imaging power for a modulation frequency of 500 kHz (purple circles) and 1 MHz (blue diamonds). To enter a regime where $\epsilon_s \approx 80$, we would require a lifetime of ~ 10 ms for a probe power of approximately 1 mW. The data clearly suggests that this is not possible.

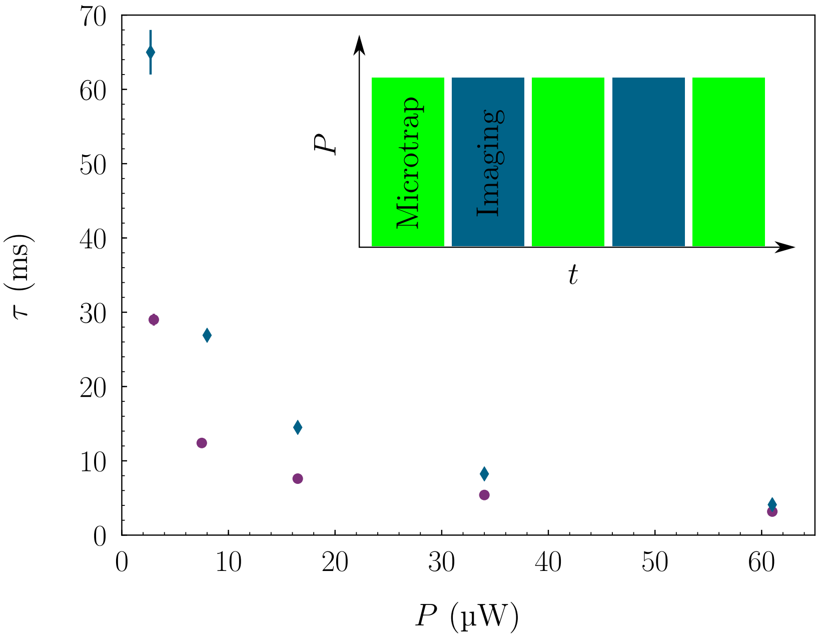

Figure 5.9: The main figure shows the lifetime of the atoms in the microtrap as a function of the power used for imaging. The purple circles and blue diamonds correspond to a stroboscopic frequency of 500 kHz and 1 MHz respectively. The inset shows the timing sequence between the microtrap and imaging light.

We believe the reason for this short lifetime is due to the one-dimensional nature of the probe beam and the modulation rate. The method demonstrated by Hutzler *et al.* [116] relies on the fact that during the time when the trapping light is switched off, the atoms do not move sufficiently far outside of the trapping region that they are lost. Hutzler *et al.* used the MOT beams for imaging and a modulation rate of 3 MHz. Although the probe beam used in our experiments was red-detuned from the bare-resonance, and therefore provided Doppler cooling in one dimension, the atoms experienced heating in the other two dimensions due to spontaneous emission and the lack of laser cooling. This could cause the atoms to gradually move away from the trapping region and be lost. Strontium also has a larger decay rate than that of Na and Cs, which are used in [116], meaning that a modulation rate of ~ 10 MHz is required to enter a similar experimental regime. This interpretation is supported by the data as we are able to observe a longer lifetime when using an increased modulation cycle. Increasing the modulation frequency further is not possible with an AOM however, and therefore an alternative solution to this problem is required.

5.3.4 Alternative imaging techniques

There are a variety of possible solutions to the problem of imaging the atoms in the microtrap. Here we detail several proposals which should alleviate the problem.

Tunable imaging

The Doppler induced heating of the atoms in the microtrap could be solved by using a tunable imaging laser. This would allow us to spectroscopically determine the 5s^2 ^{1}S$_0$ → 5s5p ^{1}P$_1$ transition frequency in the microtrap. Once the transition frequency in the microtrap is known, it is possible to lock the laser $\Gamma/2$ below the AC Stark shifted resonance. This would not only improve the scattering rate of atoms in the microtrap, but would also allow the atoms to be cooled to the Doppler limit of 0.7 mK in the microtrap, whilst arbitrarily increasing the microtrap depth. There are several possible locking tunable locking schemes, such as a beat-lock [117, 118] or a wavemeter lock to name but a few.

Imaging on the 5s5p ^{3}P$_1$ → 5s6s ^{3}S$_1$ transition

A limitation of the large scattering rate of the 5s^2 ^{1}S$_0$ → 5s5p ^{1}P$_1$ transition is the comparatively large Doppler temperature due to the large differential polarisability. Although the 5s^2 ^{1}S$_0$ → 5s5p ^{3}P$_1$ transition facilitates significantly colder temperatures and magic wavelengths, the reduction in scattering rate makes it experimentally infeasible to image single atoms on this transition. An alternative possibility is to image atoms on the 5s5p ^{3}P$_1$ → 5s6s ^{3}S$_1$ transition at 688 nm (see figure 2.1), where the transition rate of $\Gamma = 2\pi \times 4.3 \pm 0.3\,\mathrm{MHz}$ [95] leads to a Doppler temperature of $T \sim 100\,\mu\mathrm{K}$, which is comparable to the alkali-metal atoms. Imaging on this transition would also facilitate the production of approximately five time more microtraps.

The imaging scheme would work as follows. Both the 689 nm and 688 nm light would simultaneously illuminate the atoms. When population is shelved into the 5s5p ^{3}P$_1$ state, it can then undergo many scattering events on the 5s5p ^{3}P$_1$ → 5s6s ^{3}S$_1$ transition before decaying back to the ground state. The differential polarisability of the 5s5p ^{3}P$_1$ → 5s6s ^{3}S$_1$ transition is likely to be smaller than the 5s^2 ^{1}S$_0$ → 5s5p ^{1}P$_1$ transition as the sign of the polarisability of both the upper and lower states is the same, however this is yet to be fully calculated. This may therefore lead to a situation where the Doppler limited temperature is significantly less than the microtrap depth.

Using ^{87}Sr

In alkali-metal single atom experiments, sub-Doppler cooling maintains a low atomic temperature even for large detunings from resonance. Throughout this work, we have only considered working with ^{88}Sr. However the ^{87}Sr fermionic isotope has hyperfine structure, and therefore sub-Doppler cooling is achievable [103]. Temperatures as low as 300 µK have been experimentally measured, and it has been shown that the temperature of the atoms is vastly independent of the detuning of the laser beams from resonance. This would therefore solve the problem of a large atomic temperature when imaging in the microtrap concomitant with ^{88}Sr. One point to note however is that an additional 'stirring' laser is required when working with ^{87}Sr, operating between the ^{1}S$_0\,|F = 9/2\rangle \rightarrow {}^3P_1\,|F = 9/2\rangle$ states [119] to re-distribute atoms among the many Zeeman levels to achieve efficient cooling.

5.4 Microtrap characterisation

Having discussed the limit of detection of the microtrap, we now move on to its characterisation. Here we use many atoms in the microtrap to improve the signal-to-noise ratio. Three quantities of particular interest here are the microtrap size, atomic temperature and lifetime. These were measured via a variety of methods and are explained below, along with measurement pitfalls. There are several idiosyncrasies related to these characterisation measurements. In particular, it is only possible to load into shallow microtraps ($\sim 30\,\mu$K, $\sim 1\,$mW). Unless stated otherwise in this section, to perform measurements in deep microtraps the atoms were first loaded into shallow traps and then the microtrap depth was linearly increased. The reason for this is explored in detail in section 5.5.

5.4.1 Microtrap waist measurement

The atoms trapped in the microtrap oscillate due to the conservative nature of the dipole potential. If one is able to measure the frequency of the oscillations, it is possible to infer the microtrap size. Near the bottom of the microtrap, one can approximate the Gaussian profile to that of a parabola by performing a Maclaurin expansion of the Gaussian trapping potential. By equating this expansion to the energy of a particle in a harmonic oscillator potential, we are able to derive a radial ω_{r} and an axial ω_{a} microtrap frequency. To lowest order, these are given by

$$\omega_{\mathrm{r}} = \sqrt{\frac{4U_0}{mw_0^2}}\,, \tag{5.4.12}$$

$$\omega_{\mathrm{a}} = \sqrt{\frac{2U_0}{mz_{\mathrm{R}}^2}}\,. \tag{5.4.13}$$

A common technique to measure these frequencies in larger dipole traps is to induce parametric excitations in the atoms, and detect resonances in either heating or loss of the atoms. One typically observes resonances at ω and 2ω, the stronger being at 2ω. The parametric excitations are normally induced by modulating either the intensity or the position of the dipole trap beam [120].

In more recent times, another method for measuring oscillation frequencies in a microtrap [121, 122] has come to the fore. The experimental sequence is a series of release and recapture events, and is shown in figure 5.10(i). The rationale behind this sequence is best illustrated in phase-space. Figure 5.10(a) shows the initial Gaussian distribution of atoms in the microtrap. The microtrap is turned off for a very short amount of time Δt_{i}, which allows the atoms to expand ballistically which results in an elliptical distribution in phase-space (figure 5.10(b)). The microtrap is turned back on for a time Δt, during which the ellipse in phase-space rotates at a frequency ω. During the second turn off period of length Δt_{f}, atoms are lost. The probability of loss from the microtrap is dependent on the position of the atom in phase-space. If the phase-space distribution is elongated along x (figure 5.10(c)), the atoms have minimal velocity and therefore are less likely to move from the trapping centre during the second release-recapture period. However, if the phase-space distribution is elongated along v (figure 5.10(d)), the atoms have maximal

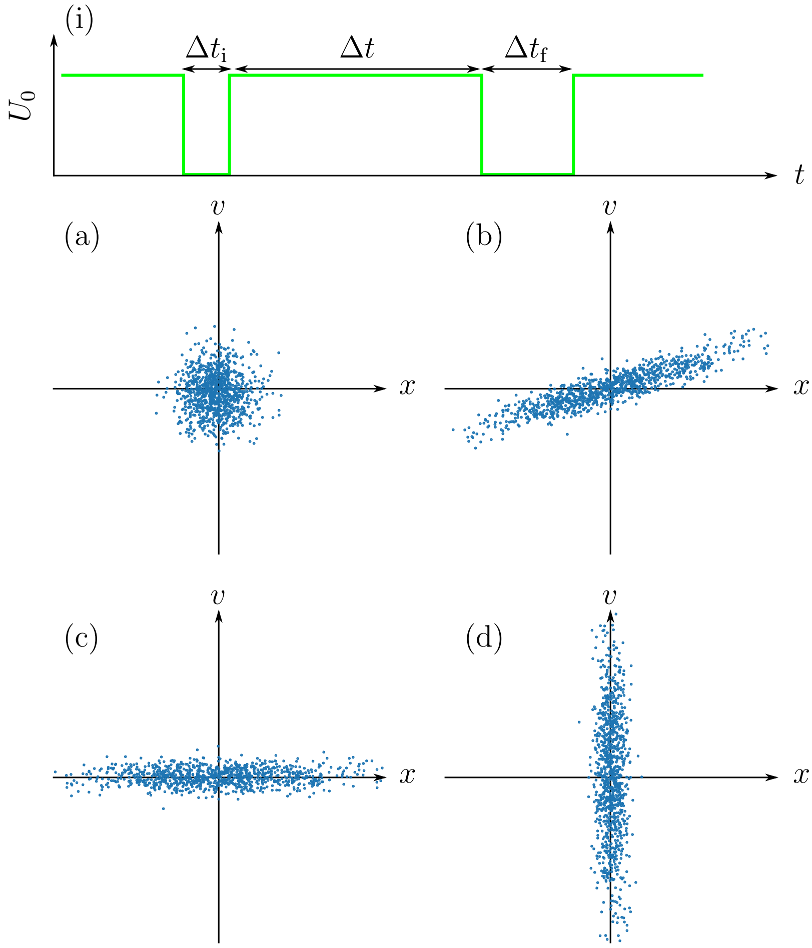

Figure 5.10: (i) Depth of the microtrap as a function of time. One-dimensional phase-space atomic distribution in the microtrap: (a) initially, (b) after first release, (c) minimal loss for second release-recapture, (d) maximal loss for second release-recapture.

velocity and are likely to be lost from the microtrap. The result is an oscillating recapture probability as a function of Δt. Note, that due to the symmetry of the system, the recapture probability oscillates at 2ω. It is typically only possible to observe the radial frequency oscillations ω_r as $\omega_\mathrm{r} > \omega_\mathrm{a}$.

Typical experimental parameters for experiments in rubidium are $\Delta t_\mathrm{i} = 4\,\mu\mathrm{s}$ and $\Delta t_\mathrm{f} = 12\,\mu\mathrm{s}$ [101]. However, as the strontium microtrap is loaded from a nMOT with a temperature of $\sim 1\,\mu\mathrm{K}$, the atoms in the microtrap are approximately 50 times colder than those loaded from a rubidium optical molasses. We therefore find empirically that the best contrast in oscillations are observed for $\Delta t_\mathrm{i} = 25\,\mu\mathrm{s}$ and

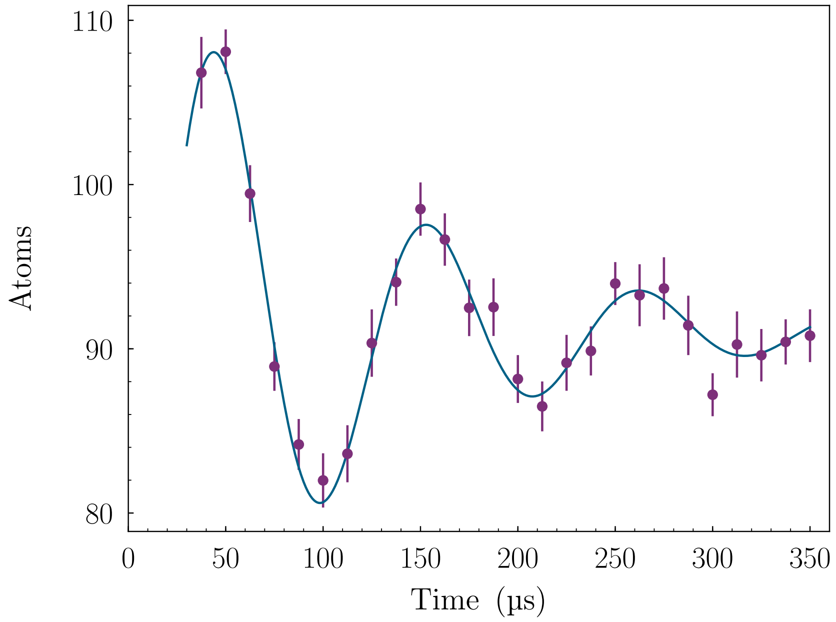

Figure 5.11: Number of atoms as a function of delay Δt for a trap power of 0.3 mW. The solid line is a fit to the data using the function $P = y_0 + A \exp\left(2\omega_{\mathrm{r}}' t + \phi\right)$.

$\Delta t_{\mathrm{f}} = 60\,\mu\mathrm{s}$. An example of these oscillations are shown in figure 5.11. The observed oscillations are severely damped. This is because the simplified picture above assumes that the atoms are experiencing a harmonic potential. In reality, the trapping potential is not harmonic and therefore atoms at different spatial co-ordinates in the microtrap oscillate at different frequencies. This leads to a de-phasing of the atomic oscillations in the microtrap and a damping of the measured recapture probability oscillation [122]. In this damped regime, the measured frequency ω_{r}' differs from the actual frequency ω_{r} by

$$\omega_{\mathrm{r}}' = \sqrt{\omega_{\mathrm{r}}^2 - \iota^2}\ , \tag{5.4.14}$$

where ι is the damping rate. This result can be derived by solving the equations of motion for a classical damped harmonic oscillator. By re-arranging equation 5.4.12 and substituting the definition of U_0, it can be shown that

$$\omega_{\mathrm{r}}'^2 = \omega_{\mathrm{r}}^2 - \iota^2 = \frac{4\alpha P}{m\pi\epsilon_0 c w_0^4}\ . \tag{5.4.15}$$

Figure 5.12 shows a graph of ω_{r}^2 as a function of P. It is possible to extract the microtrap waist from the gradient κ, which is independent of the damping rate ι.

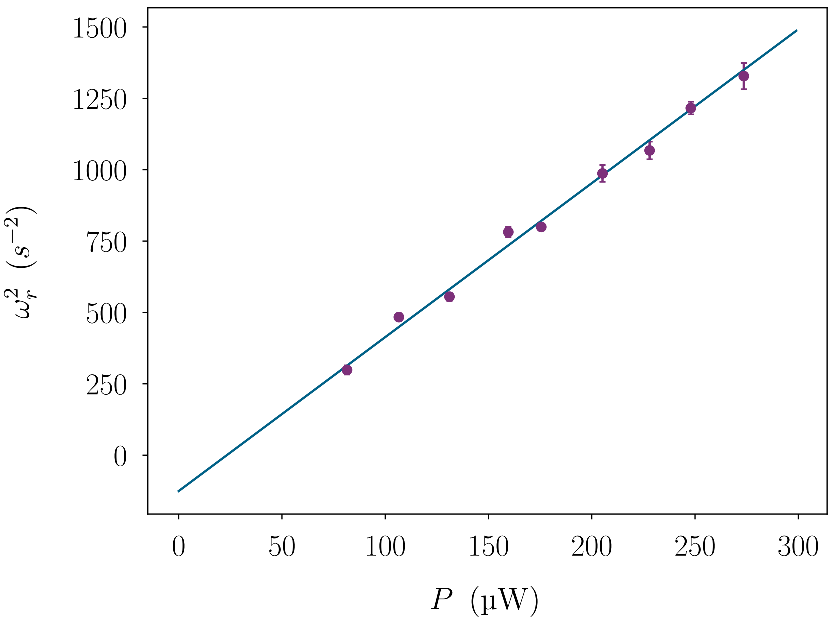

Figure 5.12: Fitted microtrap frequency as a function of microtrap power. The error bars are statistical errors from the fit to the oscillations. The line is a best fit of the form $y = mx + c$. Note that the y-offset is due to the damping of the oscillations, and therefore $c = \iota^2$.

This is simply given by

$$w_0 = \left(\frac{4\alpha}{m\pi\epsilon_0 c\kappa}\right)^{1/4} . \tag{5.4.16}$$

The fitted waist from this data is $w_0 = (1.65 \pm 0.002_{\mathrm{stat}} \pm 0.01_{\mathrm{syst}})$ µm, where σ_{stat} is the statistical error from the fit to the data, and σ_{syst} is the systematic error caused by the 3 % error in the measurement of the microtrap power.

This is much larger than the predicted waist from Zemax of $w_0 = 1.1$ µm. There may be several causes of this large microtrap waist, such as

- Incorrect polarisability or power measurements,
- System aberrations,
- Poor alignment onto the lens,
- Accuracy of the microtrap frequency measurement method,

We will explore each of these possibilities in succession.

Polarisability and power

The trap frequency measurements rely upon accurate measurements of both the ground state polarisability and the microtrap power. The ground state polarisability is strongly dominated by the broad 5s^2 ^{1}S$_0$ → 5s5p ^{1}P$_1$ transition which is well known [98]. Due to the study of optical lattice clocks in strontium, the ground state polarisability is of significant importance and has also received significant attention. The polarisability calculated in section 4.1 is in agreement with the available literature, and therefore we believe that this is not the cause of the large measured microtrap waist.

An additional source of error is the measurement of the microtrap power which the atoms perceive. The microtrap power was measured using a Thorlabs PM100D power meter, taking into account measured power losses at each optical surface. The power meter was recently calibrated and therefore systematic uncertainties are minimised to ±3 %. The systematic uncertainty of the microtrap power is significantly smaller than the systematic shift required to explain the large microtrap waist.

Aberration measurements

It is unlikely that there is a problem with the manufacture of the lens given that an interferometric measurement of the lens surface was performed using a Zygo Verifire, indicating that the RMS deviation from the calculated surface was $< 12\,\mathrm{nm}$. However, by measuring the wavefront of the microtrap beam which has passed through the chamber and both in-vacuo lenses, it is possible to infer some information about the lens performance.

In order to measure the beam quality entering and exiting the chamber, we measured the beam aberrations using a Shack-Hartmann interferometer[2] (SH) [123]. The active area of the SH is approximately 3 mm. Therefore, the microtrap beam was focussed onto the SH using a 2 inch, $f = 200\,\mathrm{mm}$ achromatic doublet lens. A limitation of focussing onto the SH is that the measured wavefront is dominated by the curvature induced by the focussing lens. However, by measuring the wavefront in

---

[2] Thorlabs WFS150C

terms of Zernike polynomials [124,125], a set of orthogonal basis polynomials defined on a unit disk, it is possible to extract the important aberrations of the system, such as coma, astigmatism and spherical aberration. All Zernike coefficients for the input beam were $< 0.015\,\lambda$, indicating that there wasn't significant aberration on the input beam. The significant Zernike coefficients of the beam exiting the chamber were vertical coma $Z_3^1 = 0.04\lambda$ and spherical aberration $Z_4^0 = 0.02\lambda$. The large coma aberration could be caused by either poor alignment onto the first lens or bad centration of the two in-vacuo lenses. The spherical aberration must be caused by the in-vacuo lenses themselves, or an undesired curvature of the viewports.

Lens alignment

As discussed, there was a significant amount of coma on the microtrap beam exiting the chamber. To improve the alignment onto the lens, the microtrap frequency was measured as a function of angle of the input beam. Figure 5.13 shows the measured microtrap frequency as a function of fractions of full turns of the fine adjustment screw of the mirror directly before the in-vacuo lens. The thread of the mirror adjustment screw is 170 threads per inch, from which we also calculate the change in angle of the incident beam. The origin of these graphs are the original positions of the mirror adjustments screws.

We clearly see that the microtrap frequency, and hence the microtrap waist, is very sensitive to the incident angle of the microtrap beam. We were not able to increase the microtrap frequency by changing the horizontal angle. However, a significant increase was measured when varying the vertical angle of the incident beam. This supports our interpretation of the coma aberration measured using the SH. The re-aligned microtrap waist was measured to be $w = (1.42 \pm 0.004_{\mathrm{stat}} \pm 0.01_{\mathrm{syst}})\,\mu\mathrm{m}$ using the same measurement procedure as that shown in figure 5.12. This is significantly smaller than the waist measured previously, however it is still much larger than the expected waist size.

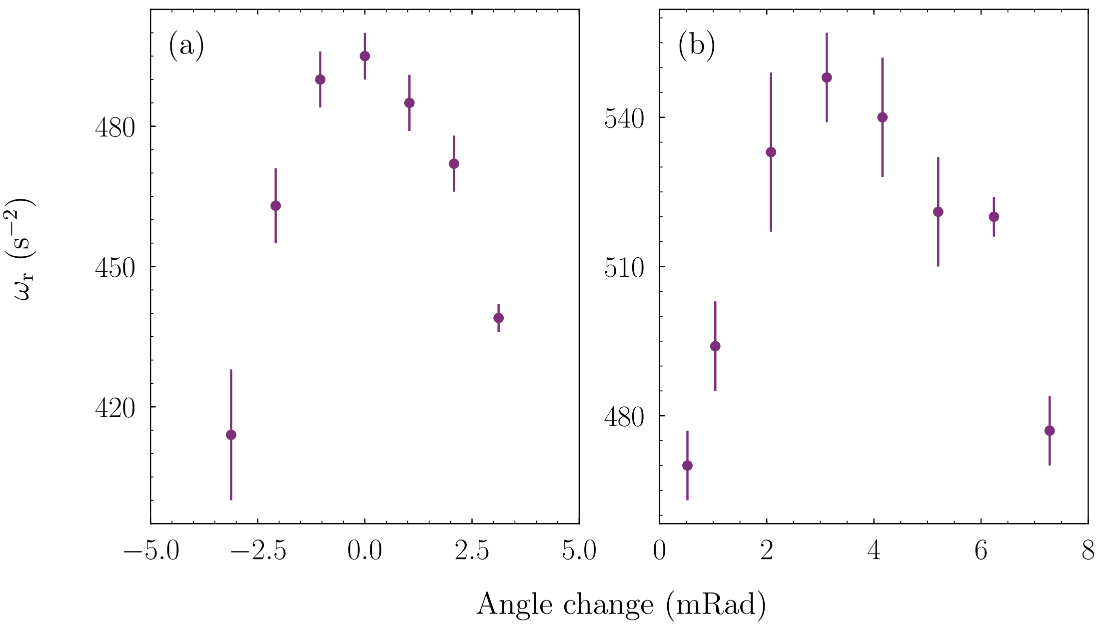

Figure 5.13: Trap frequency as a function of incident beam angle for the (a) horizontal and (b) vertical directions. The origin of the graphs are the original positions of the mirrors before adjustment.

Accuracy of the microtrap frequency measurement method

The approximation made when deriving the expressions for microtrap frequencies in equation 5.4.12 is only valid when the amplitude of the atomic oscillations are small compared to the microtrap depth, such that the harmonic approximation to the trapping potential is valid. The data shown in figure 5.12 is strongly damped, indicating that the validity of this regime is put into question. To investigate the effect of microtrap depth on the measured microtrap waist, we measured the microtrap frequency at a variety of different powers. It is only possible to load into shallow microtraps ($\sim 30\,\mu$K), with powers up to ~ 1 mW (this is explained later in section 5.5). Therefore, after the initial load of atoms in the microtrap at $10\,\mu$K, the power of the microtrap was linearly increased over a time of 300 ms. Figure 5.14(a) shows an example microtrap frequency measurement at a final microtrap depth of ~ 1.2 mK, using the technique outlined in 5.4. However, as the atomic temperature increases whilst increasing the microtrap depth, the optimum release times in the experimental sequence were $\Delta t_\mathrm{i} = 5\,\mu$s and $\Delta t_\mathrm{f} = 20\,\mu$s. The microtrap frequency

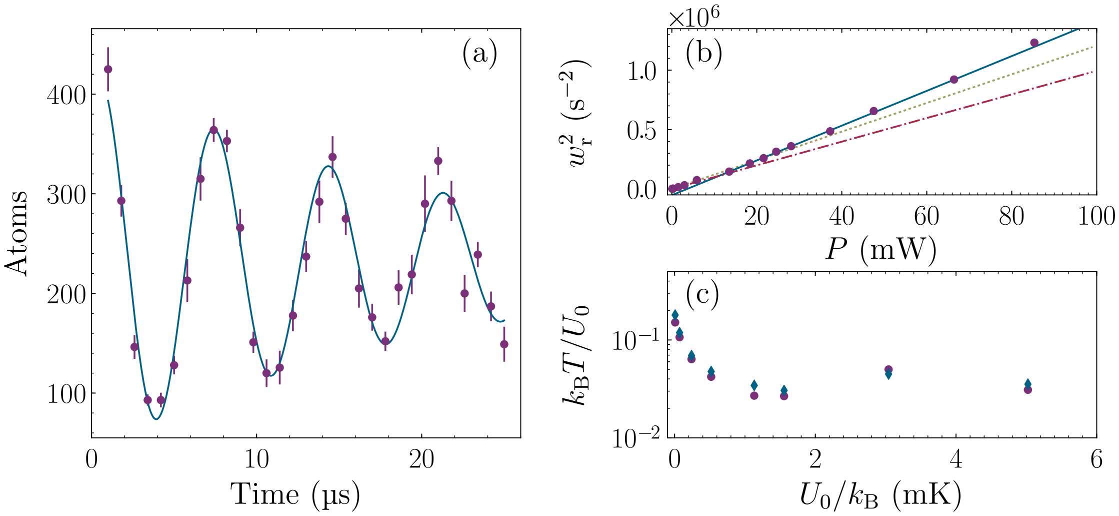

Figure 5.14: (a) Detected atoms as a function of delay Δt. The solid line is a fit to the data using the function $P = y_0 + A\exp(2\omega_{\mathrm{r}}' t + \phi)$. (b) Fitted microtrap frequency as a function of microtrap depth. The green dotted line is a linear fit to all data points. The red dashed-dotted line is a linear fit to the first six data points and the solid blue line is a linear fit to the data, neglecting the first six data points. (c) Horizontal (blue diamonds) and vertical (purple circles) temperatures as a function of final microtrap depth, measured using the ballistic expansion technique.

oscillations are significantly less damped than the oscillations shown in figure 5.11, indicating that the atoms are oscillating in a more harmonic manner.

Figure 5.14(b) shows the fitted microtrap frequency as a function of final microtrap power. The green dotted line is a linear fit to all data points. The reduced Chi-squared statistic [76] is $\chi^2_\nu = 22$, indicating that this is a poor fit to the data. A linear fit to the first six data points is shown by the red dashed-dotted line. This is a fit to data taken in the regime of significant damping, similar to that of figure 5.11. Here, $\chi^2_\nu = 2.2$ which is indicative of a reasonable fit. However, this fit clearly does not agree with data taken at much higher powers. The solid blue line is a linear fit to the data, neglecting the first six data points. Here $\chi^2_\nu = 0.97$ which indicates an excellent fit, however this line does not pass through the measurements measured at lower microtrap powers. We hypothesize that at lower microtrap powers, the ratio of the atomic temperature to the microtrap depth is too small, which invalidates the harmonic approximation and returns an inaccurate result of the microtrap waist.

The microtrap frequency measurements at higher powers are less critically damped, and the linear fit is in agreement with the data over a larger range of microtrap powers, providing more confidence in these measurements than those taken at low microtrap powers.

Figure 5.14(c) shows the ratio of the microtrap depth to the atomic temperature as a function of final microtrap power. Here the atomic temperature was measured using the ballistic expansion technique (see section 5.4.3). For the range of measurements where we believe the harmonic approximation to the microtrap potential is valid, $k_{\mathrm{B}}T/U_0$ is approximately an order of magnitude smaller than at the lower microtrap power measurements. This data would indicate that a ratio of $k_{\mathrm{B}}T/U_0 \approx 0.01$ is required for accurate measurements of the microtrap frequency and hence the microtrap waist. The microtrap waist size extracted from these measurements is $(1.28 \pm 0.004_{\mathrm{stat}} \pm 0.01_{\mathrm{syst}})\,\mu\mathrm{m}$. This is significantly smaller than the previous measurement, however it is still larger than the predicted microtrap waist using Zemax ‘Physical Optics’ calculations.

Lens testing

To test the quality of the in-vacuo lens, we measured the microtrap waist as a function of apodisation, as the waist size is critically dependent on the aperture of the lens. Figure 5.15 shows the measured microtrap waist (purple circles) as a function of the aperture size. The solid blue line is the prediction from Zemax. The measured microtrap waist is systematically larger than the predicted size. The theoretical prediction is obtained by fitting a Gaussian profile to the centre of the predicted intensity profile. The systematic shift may indicate that this method of predicting the waist is inaccurate, and that the measured waist is what one would truly expect.

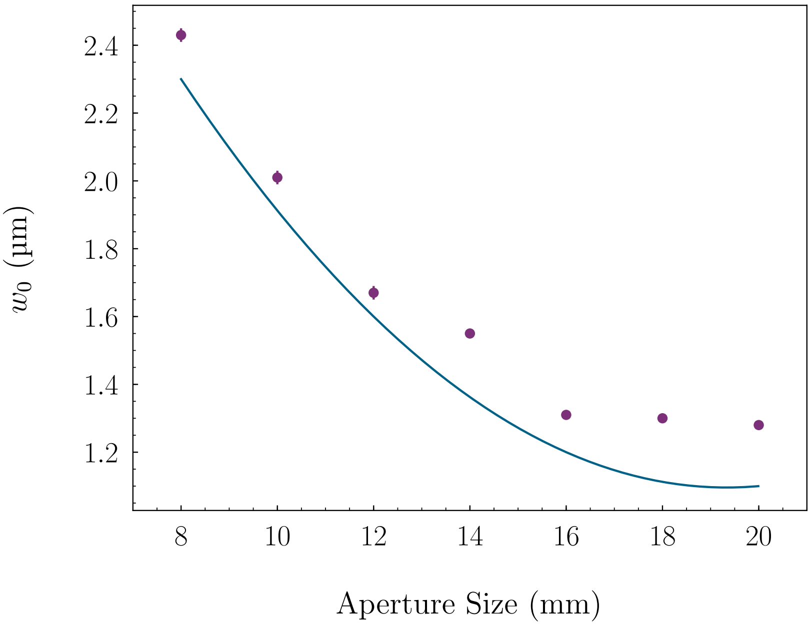

Figure 5.15: Measured microtrap waist (purple circles) as a function of lens clear aperture. The solid line is the predicted waist size using Zemax.

5.4.2 Microtrap Lifetime

An important microtrap statistic is the atomic lifetime, as this determines how long on average one can manipulate the atoms in the microtrap before losing them. For a typical experiment time of 50 ms, a lifetime of 5 s is required to limit loss rates to the 1 % level. To measure the lifetime of the atoms in the microtrap, atoms were loaded into a microtrap of depth $8.5 \pm 0.5\,\mathrm{mK}$, after which all laser beams were switched off for a time Δt. The number of atoms in the microtrap was then measured using fluorescence imaging on the $5\mathrm{s}^2\ {}^1\mathrm{S}_0 \rightarrow 5\mathrm{s}5\mathrm{p}\ {}^1\mathrm{P}_1$ transition. The number of counts as a function of time are shown in figure 5.16. The fitted lifetime of the atoms in the microtrap is $\tau = 5.2 \pm 0.6\,\mathrm{s}$, and is comparable to the observed nMOT lifetime.

The two main possible reasons for this lifetime are heating due to scattering photons from the microtrap light, or due to collisions with strontium atoms produced by the strontium oven. For the parameters above, one would expect a scattering rate from the microtrap of $\Gamma_\mathrm{s} = 330\,\mathrm{s}^{-1}$. Assuming the heating rate is given by $\Gamma_\mathrm{s} E_\mathrm{r}/3$, one would expect a temperature increase of $\sim 46\,\mathrm{\mu K s}^{-1}$. This heating rate is not compatible with the lifetime of the atoms in the trap and therefore we believe

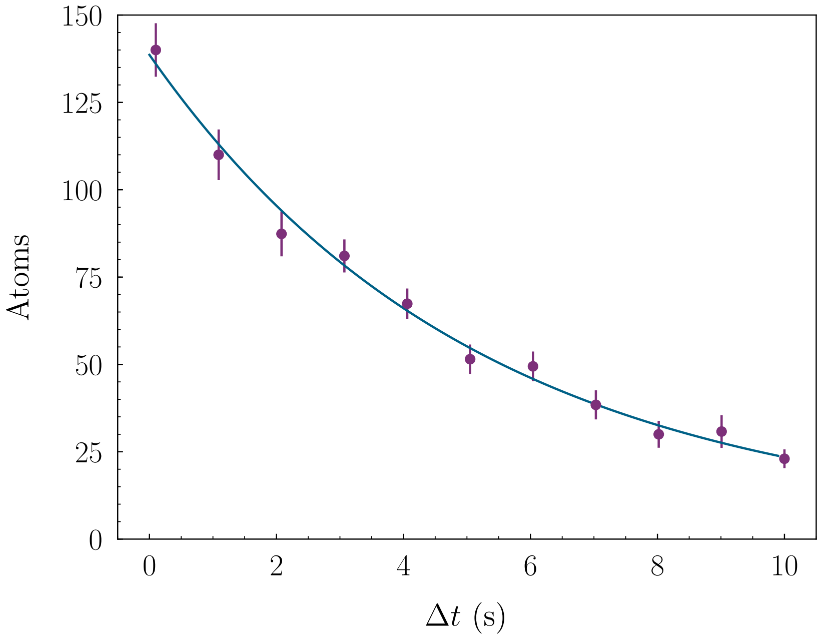

Figure 5.16: The purple circles show the number of counts as a function of time for atoms trapped in a microtrap of depth $8.5 \pm 0.5\,\mathrm{mK}$ in the absence of any laser beams. The solid blue line is an exponential fit to the data.

the lifetime of the trap to be limited by collisions with strontium atoms produced by the strontium oven. However, this lifetime is sufficiently long to perform microtrap experiments, and is indicative of a low background pressure.

5.4.3 Temperature measurements

There are two possible ways of measuring the temperature of the atoms in the microtrap. The first is the ballistic expansion method which is typically used when the atom number is $\gg 1$. The temperature of the atoms is inferred from the width of the atomic distribution as a function of time. Figure 5.14(c) shows the temperature of the atoms in the microtrap as a function of microtrap depth, measured using the ballistic expansion method. At low microtrap depths ($\sim 10\,\mu\mathrm{K}$), the atom temperature is approximately $\sim 1\,\mu\mathrm{K}$, similar to that of the nMOT temperature. As the microtrap depth is increased, we see an increase in the atomic temperature as one would expect.

When the atom number is small however, the term temperature refers to the

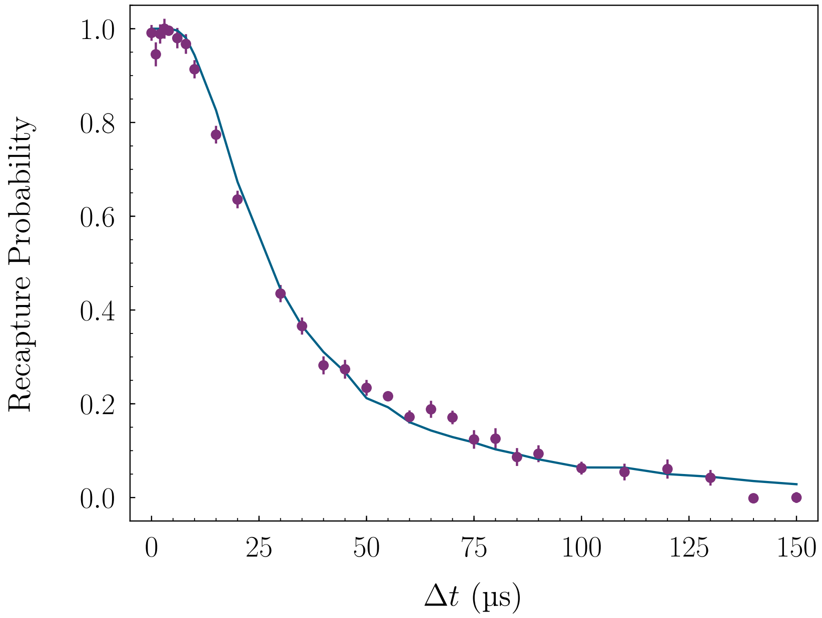

Figure 5.17: Recapture probability as a function of release time (purple circles). The blue solid line is the Monte Carlo fit to the data with a temeprature of $24.0 \pm 1.0\,\mu\mathrm{K}$, assuming a microtrap waist of $w_0 = 1.28\,\mu\mathrm{m}$.

distribution of energies of many realisations of the same experiment. Tuchendler *et al.* [126] demonstrated a method for inferring the temperature of a single atom using a release-recapture method. The premise of this method is that the energy of the atoms can be inferred by switching off the microtrap for a time Δt, after which the microtrap light is switched back on. If the atom has moved sufficiently far such that its kinetic energy is greater than the potential energy, the atom is lost; otherwise the atom remains trapped. By measuring the recapture probability as a function of Δt, a temperature is extracted by fitting a Monte-Carlo simulation to the data, where the only free parameter is the atomic temperature. A full description of the simulation is detailed in [126].

To confirm the accuracy of the ballistic expansion method, we also measured the atomic temperature using the release-recapture method described above. Figure 5.17 shows the recapture probability as a function of release time for atoms in a $(5.2 \pm 0.2) \times 10^2\,\mu\mathrm{K}$ microtrap. The solid blue line is the result of the Monte-Carlo simulation. The fitted temperature is $24.0 \pm 1.0\,\mu\mathrm{K}$, in agreement with the measurement of $T = 24.8 \pm 0.4\,\mu\mathrm{K}$ measured using the ballistic expansion technique, giving confidence in the accuracy of both measurement methods.

5.4.4 Shelving spectroscopy

To the best of our knowledge, the polarisability of the 5s5p ^{3}P$_1$ state at 532 nm has never been measured. This wavelength is of interest due to the close vicinity to the predicted magic wavelength point (see figure 4.3), as well as the possibility of performing Rydberg trapping experiments. The predicted magic wavelength crossing point is strongly dominated by transitions at approximately 480 nm to the 5s7s ^{3}S$_1$, 5p^2 ^{3}P$_{1,2,3}$ and 5s5d ^{3}D$_{1,2}$ states. Therefore, a measurement of the polarisability at 532 nm allows us to assess the accuracy of the predicted polarisability in this region.

The differential polarisability was inferred by measuring the differential AC Stark shift of the 5s^2 ^{1}S$_0$ → 5s5p ^{3}P$_1$ transition as a function of microtrap power. This was measured for both the $m_j = 0$ and $m_j = -1$ states. The AC Stark shift was measured using the shelving technique described earlier in 4.3.3. Initially, the 532 nm light was shone onto the nMOT to load the microtrap. The microtrap was linearly polarised along $\hat{\boldsymbol{z}}$, along which the quantisation axis was also defined. The cooling light and magnetic field were switched off for 50 ms in order for the un-trapped nMOT atoms to fall away under gravity. During this time, the MOT coil relay was switched to set the coils into a Helmholtz configuration. A current of 0.28 A was passed through the MOT coils, producing a uniform field of 3.3 G along $\hat{\boldsymbol{z}}$, to define a quantisation axis and to separate the m_j-sublevels of the 5s5p ^{3}P$_1$ state. A linearly-polarised, tunable 689 nm probe beam with 1/e^2 radius of 1 mm was aligned onto the microtrap. Approximately 1 µW was shone onto the microtrap for a period of 1 ms to ‘shelve’ atoms in the 5s5p ^{3}P$_1$ state. Following this, the 461 nm MOT beams were shone onto the microtrap for 31.2 µs to measure the population difference.

A typical shelving spectrum is shown in figure 5.18. The resonance width is of the order of 60 kHz and is limited by the Doppler temperature of the atoms. The solid blue line is a Gaussian fit to the data, and is used to extract the centre frequency of the resonance. A similar resonance curve was measured in the absence of the microtrap light before and after the measurement in the microtrap to minimise the effect of systematic errors caused by the drift of the ultra-stable cavity to which the

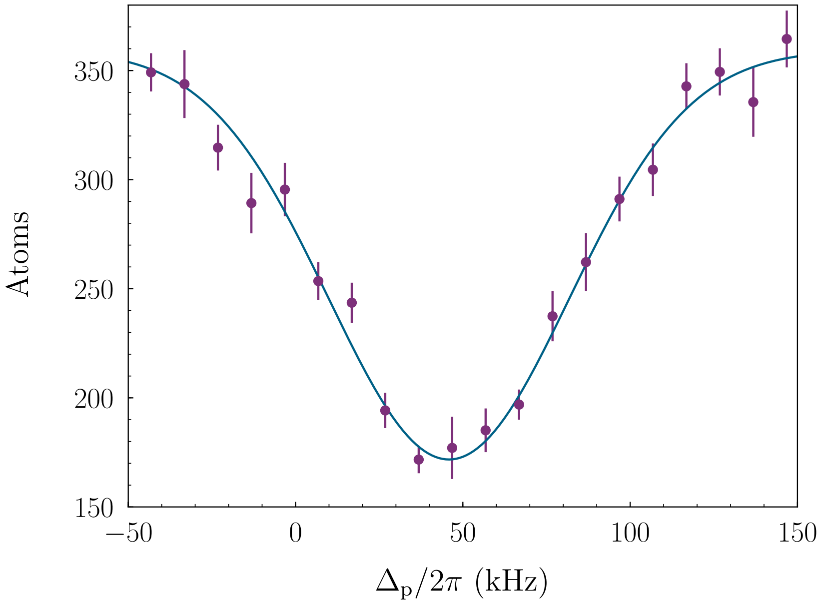

Figure 5.18: Counts (purple circles) as a function of detuning of the 689 nm probe beam with respect to the $m_j = 0$ bare resonance. The error bars are the standard error on the mean of 15 repeated experiments. The solid blue line is a Gaussian fit to the data.

laser is locked. Figure 5.19 shows the differential AC Stark shift of the 5s^2 ^{1}S$_0$ → 5s5p ^{3}P$_1$ as a function of microtrap power, along with a linear fit, for the (a) $m_j = 0$ and (b) $m_j = -1$ states. The data shown in figure 5.19(b) is more scattered than that in (a). This is due to the magnetic field sensitivity of the $m_j = -1$ state. For reference, a transition frequency shift of 1 kHz is induced by a magnetic field of magnitude 0.5 mG. It can be shown that the gradient κ is related to the differential polarisability by

$$\kappa = \frac{\alpha\left({}^1\mathrm{S}_0\right) - \alpha\left({}^3\mathrm{P}_1\right)}{\epsilon_0 c \pi h w_0^2} \ , \tag{5.4.17}$$

where $\alpha\left({}^1\mathrm{S}_0\right)$ and $\alpha\left({}^3\mathrm{P}_1\right)$ are the polarisability of the 5s5p ^{3}P$_1$ and 5s^2 ^{1}S$_0$ states at 532 nm respectively. We define the quantity

$$\xi = \frac{\alpha\left({}^1\mathrm{S}_0\right) - \alpha\left({}^3\mathrm{P}_1\right)}{\alpha\left({}^1\mathrm{S}_0\right)} \ , \tag{5.4.18}$$

as a measure of the 'magicity' of the transition. Table 5.4.4 details the theoretical and experimental values. There is clearly a large discrepancy between the theoretical and experimental values, especially for the $m_j = -1$ state. This discrepancy is

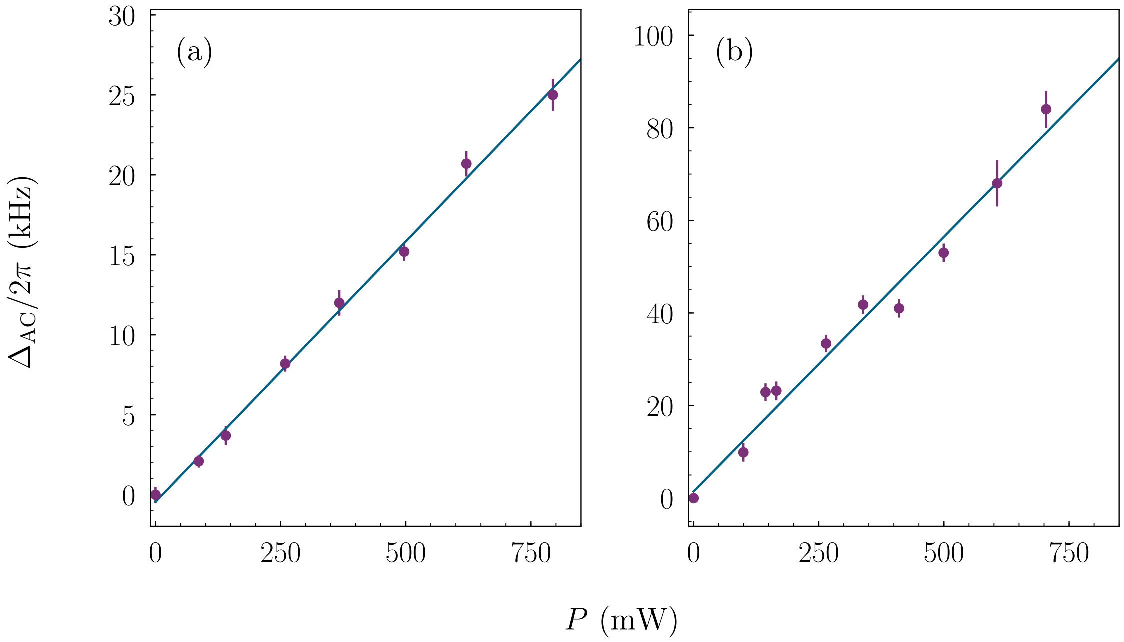

Figure 5.19: Centre frequency of the shelving resonance (purple circles) as a function of microtrap power of the (a) $m_j = 0$ and (b) $m_j = -1$ states. The error bars are the standard error on the mean of 15 repeated experiments. The solid blue line is a linear fit to the data.

either caused by systematic uncertainties in the experimental measurements, or inaccuracies in the measurement of the transition strengths to the 5s7s $^3\mathrm{S}_1$, 5p^2 $^3\mathrm{P}_{1,2,3}$ and 5s5d $^3\mathrm{D}_{1,2}$ states. Errors is the microtrap power and waist could lead to discrepancies between the theoretical and experimental differential polarisability. However, one would require scaling factors of ~ 4 and ~ 2 respectively to explain this discrepancy. Given the calibration of the power meter and the analysis of the trap frequency measurements performed earlier, these large scaling factors are unlikely to be the source of the discrepancy. Using the polarisability calculations detailed in section 4.1, one would require a $\sim 10\,\%$ increase in the transition rate from the 5p^2 $^3\mathrm{P}_{1,2,3}$ and 5s5d $^3\mathrm{D}_{1,2}$ states, and therefore we believe this to be the source of the discrepancy between the experimental and theoretical values.

The larger than predicted value of the polarisability of the $m_j = -1$ state increases the capture velocity of microtrap, improving the predicted loading ability detailed in section 5.1. Although the transition to the $m_j = 0$ state is almost magic,

$\mathbf{m_j}$	$\alpha\,(^3\mathrm{P}_1)$ (a.u.), Th.	$\alpha\,(^3\mathrm{P}_1)$ (a.u.), Exp.	ξ, Th.	ξ, Exp.
0	625	$(7.2 \pm 0.2) \times 10^2$	0.17	0.035 ± 0.002
-1	366	$(6.6 \pm 0.2) \times 10^2$	0.51	0.118 ± 0.004

Table 5.2: Theoretical and experimental polarisabilities of the 5s5p $^3\mathrm{P}_1$ $m_j = 0$ and $m_j = -1$ states. The error bar here is the dominant systematic uncertainty of the measurement of the microtrap power.

this does not help with loading as the nMOT beams interact atoms most strongly with the $m_j = -1$ state. From this measurement, we are not able to directly infer deviations to the full polarisability spectrum. In order to do this, polarisability measurements at a variety of wavelengths are required. This data does however suggest that the magic wavelength, predicted at 500 nm, is at a higher wavelength than predicted.

5.5 Loading into deep microtraps

The Doppler temperature on the 5s^2 $^1\mathrm{S}_0 \rightarrow$ 5s5p $^1\mathrm{P}_1$ transition is ~ 0.7 mK. Therefore, we must be able to load atoms into a microtrap with depth $U_0/k_\mathrm{B} \gg 1$ mK to continually image atoms in the microtrap. In section 5.4.1, we stated that it is not possible to load directly into a microtrap where the microtrap depth is larger than ~ 30 µK. This statement is based upon both spectroscopic and temperature measurements, which are detailed in this section.

5.5.1 Temperature measurements

In section 5.4.3, we showed that the atoms are in thermal equilibrium by measuring their temperature by both ballistic expansion and release-recapture techniques. When loading directly into a deep microtrap, the ballistic expansion is not consistent with a single thermal temperature distribution. An example ballistic expansion of atoms loaded directly into a microtrap of depth $(5.2 \pm 0.2) \times 10^2$ µK is shown in figure 5.20(a). There are two distinct regions to the data. At short times we observe

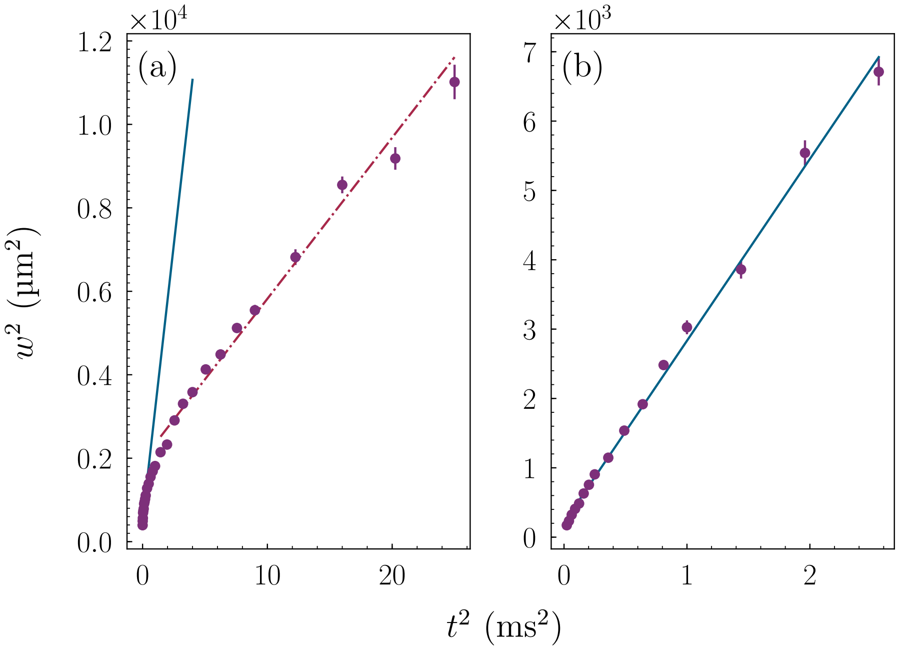

Figure 5.20: Width of the atomic cloud as a function of ballistic expansion time for the (a) directly loaded deep microtrap and (b) the ramped microtrap. In (a), the blue solid line and red dashed-dotted lines are linear fits to the first 10 and last 10 data points respectively. In (b) the blue solid line is a linear fir to all data.

a rapid expansion of the cloud, which then curtails to a much slower expansion at longer times. This data is consistent with two temperature distributions, as shown by the linear fits to short (solid blue) and long (red dashed-dotted) times. These fits correspond to a fitted temperature of $27 \pm 3\,\mu\mathrm{K}$ and $3.9 \pm 0.2\,\mu\mathrm{K}$ respectively.

The intensity profile of the microtrap at the focus is not a Guassian, but a sinc function, which has a series of intensity maxima. When using large microtrap powers, the intensity in the subsidiary maxima is sufficient to create regions where the potential depth is of the order of a few µK. We therefore believe that the different thermal distributions originate from atoms trapped in different regions of the microtrap, and is only possible due to the very low initial temperature of the atoms in the nMOT.

To test this theory, we performed a ramped microtrap experiment where atoms were initially loaded into a shallow microtrap, which negates the possibility of loading into subsidiary maxima, after which the microtrap power was linearly increased.

The microtrap was loaded with an initial microtrap depth of 28 ± 1 µK. The MOT atoms were allowed to fall away under gravity, after which the microtrap power was linearly increased to a final microtrap depth of $(5.2 \pm 0.2) \times 10^2$ µK in the absence of any other light, over a period of 300 ms. A ballistic expansion was then performed. The results of the ballistic expansion in the ramped microtrap is shown in figure 5.20(b). This data is consistent with a single linear fit, resulting in $\chi^2_\nu = 2.1$, and a corresponding fitted temperature of 26.8 ± 0.4 µK. This temperature is in agreement with the hotter temperature measured in figure 5.20(a), which supports our interpretation of the data. We believe the cooler atomic temperature is from atoms trapped in shallower regions of the microtrap, where the potential depth is smaller.

5.5.2 Spectroscopic measurements

To further investigate the loading process into deep microtraps, we performed shelving spectroscopy as a function of microtrap power. For microtrap depths greater than ~ 30 µK, we observed broadening of the shelving resonance towards higher frequencies. An example of the broadened spectrum is shown in figure 5.21(a). The solid blue line is a Gaussian fit to the first 16 data points. It is clear that a Gaussian is a good fit to the left hand side of the resonance, but does not fit the data at higher frequencies. This broadening cannot be explained by finite temperature effects, as one would expect to observe the broadening towards lower frequencies. The broadening of the feature to higher frequencies suggests that some atoms experience a greater AC Stark shift than others in the microtrap. Figure 5.21(b) shows the centre frequency of the fitted Gaussian as a function of microtrap power. We initially observe a steep gradient which is consistent with the data shown in figures 5.18 and 5.19(a). However, as the microtrap power is increased, the shift in centre frequency is curtailed and a severe flattening is observed. This is in conjunction with an increase in the width of the resonance feature. This suggests that some atoms do not observe an AC Stark shift as large as one would expect, which supports our interpretation of the data in the previous section.

To further test this theory, we once again performed a ramped microtrap experiment. The microtrap was loaded with an initial microtrap depth of 28 ± 1 µK. The

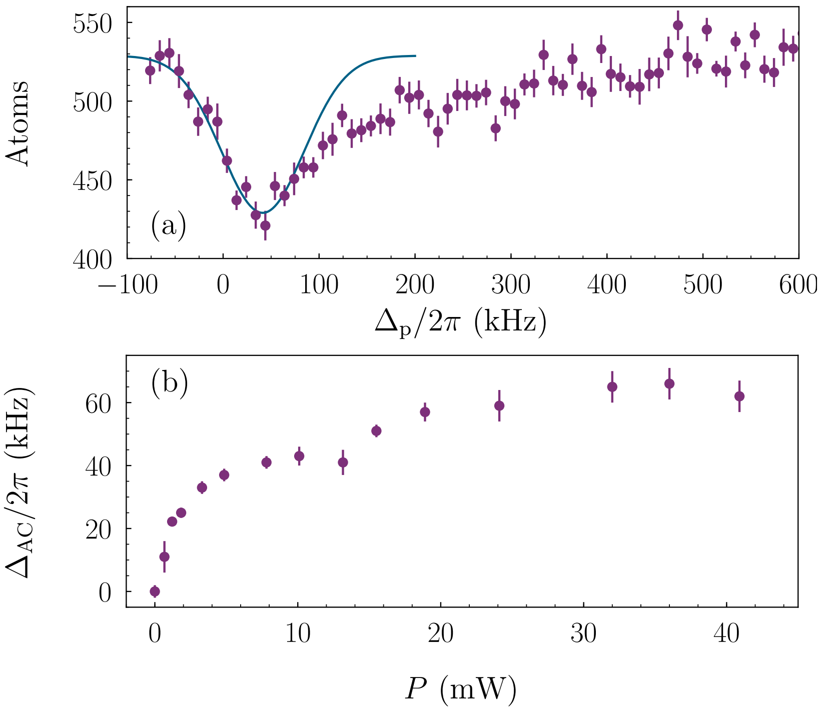

Figure 5.21: (a) Detected atoms (purple circles) as a function of detuning of the 689 nm probe beam with respect to the bare resonance. The solid blue line is a Gaussian fit to the first 16 data points. The microtrap depth is $(5.6 \pm 0.2) \times 10^2$ µK. (b) Centre frequency of the Gaussian fit as a function of microtrap power.

nMOT atoms were allowed to fall away under gravity, after which the microtrap power was increased linearly to a final microtrap depth of $(5.6 \pm 0.2) \times 10^2$ µK in the absence of any other light, over a period of 300 ms. Shelving spectroscopy was then performed following the same method as mentioned above. Figure 5.22 shows that we recover the Gaussian lineshape measured for shallow microtraps, and observe a much greater shift in the centre frequency, as one would expect. This data also supports our interpretation of the data presented in this section.

In conclusion, loading atoms directly from a nMOT directly into a deep microtrap is possible but not useful, due to the large distribution of temperatures and AC Stark shifts of the atoms in the microtrap. We have shown however, that by loading into a shallow microtrap of the order of 30 µK and linearly increasing the microtrap depth, it is possible to trap atoms in a deep microtrap.

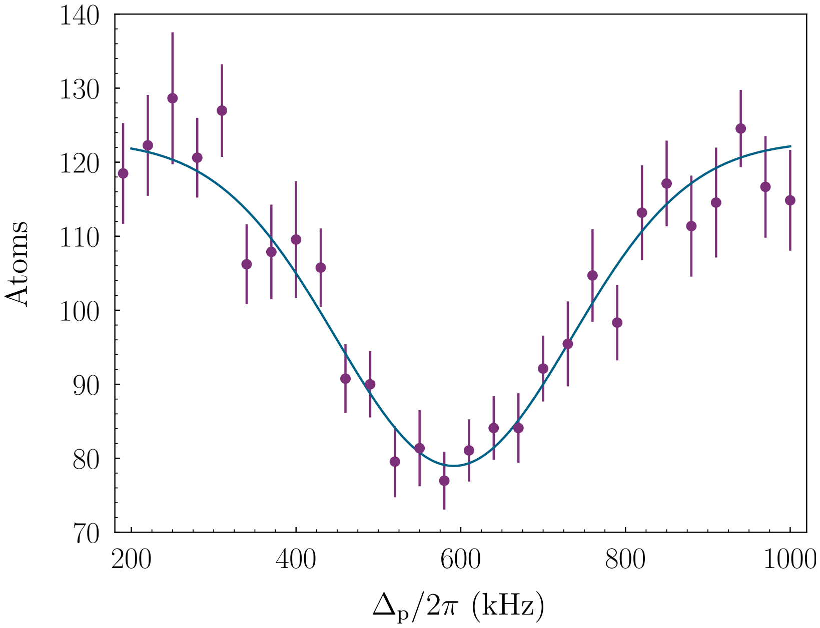

Figure 5.22: Detected atoms (purple circles) as a function of detuning of the 689 nm probe beam with respect to the bare resonance. The solid blue line is a Gaussian fit to the data. The initial and final microtrap depths were 28 ± 1 µK and $(5.2 \pm 0.2) \times 10^2$ µK respectively.

5.6 Summary

In summary, we have demonstrated the first known strontium microtrap, which is loaded directly from a nMOT. We are currently unable to image atoms in the microtrap at the single atom level due to atomic loss associated with the large differential AC Stark shift of the $5s^2\ ^1S_0 \rightarrow 5s5p\ ^1P_1$ transition. We have however proposed several solutions to this problem, and a tunable imaging laser is currently under construction.

We have made the first spectroscopic measurements of the polarisability of the $5s5p\ ^3P_1$ state at 532 nm, which indicates that the predicted magic wavelength at ~ 500 nm is in fact at a larger wavelength. We have also shown that it is not possible to directly load atoms into a deep microtrap from a nMOT, as the combination of low atomic temperature and subsidiary maxima in the trapping potential leads to a non-Gaussian atomic distribution. This problem has been solved by initially loading atoms into a shallow microtrap of the order of < 30 µK and then linearly increasing the microtrap depth. Using this method, we have shown that we are able to achieve atomic temperatures in the microtrap of the order of $k_{\mathrm{B}}T/U_0 \approx 0.01$, which is much smaller than achievable in the alkali-metal atoms. This low atomic temperature should make it relatively simple to cool to the ground state of the microtrap, which will aid in the formation of a spin-squeezed state.

Part II

Probing interactions of thermal Sr Rydberg atoms using simultaneous optical and ion detection

Chapter 6

Ionisation mechanisms in a thermal beam of Sr

Since the first observations of Rydberg EIT in a thermal vapour, it has been known that charged particles are produced [127]. There are a variety of possible mechanisms which are responsible for the apparent spontaneous ionisation of Rydberg atoms [128]. An important step forward to understanding these mechanisms was provided by Barredo *et al.* [129], who combined Rydberg EIT with the detection of ions using electrodes placed in a Rb vapour cell.

Due to the creation of Rydberg atoms in the strontium microtrap, understanding these ionisation and interaction mechanisms may be of significant importance in future work. To study these ionisation mechanisms, A. Bounds created a strontium beam apparatus which facilitates the simultaneous detection of optical and electrical signals produced from a thermal beam of strontium atoms. By using a model based on the Doppler-averaged optical Bloch equations (see section 2.3) we are able to quantitatively connect the optical and electrical signals, which allows us to deduce the origin of the spontaneous ionisation process.

The results in this chapter are based upon the publication:

R. K. Hanley, A. D. Bounds, P. Huillery, N. C. Keegan, R. Faoro, E. M. Bridge, K. J. Weatherill and M. P. A. Jones (2017). *Probing interactions of thermal Sr Rydberg atoms using simultaneous optical and ion detection*, Journal of Physics B: Atomic, Molecular and Optical Physics, **50** 115002, DOI:10.1088/1361-6455/aa6e79.

6.1 Experimental Design

A. Bounds designed and constructed a compact strontium beam apparatus adapted from [132] with the addition of electrodes that enable the simultaneous application of electric fields and detection of charged particles. Figure 6.1(a) shows the interrogation and detection regions of the beam apparatus. A weakly divergent atomic beam of Sr atoms is produced using a resistively heated dispenser [132]. The atomic beam diameter at the interrogation region is $\approx 30\,\mathrm{mm}$. Optical access to the atomic beam is provided orthogonally by two fused silica viewports. Rydberg atoms or ions can be excited using the energy level scheme shown in figure 6.1(b). A pair of electrodes (electrodes 1 and 2) which are orthogonal to both the atomic beam and the laser beams, are made from stainless steel mesh and facilitate the application of electric fields in the interrogation region. The mesh design also enables the collection of emitted fluorescence. The separation between the electrodes is 21 mm. Beyond the interrogation region, the atomic beam is incident on an additional electrode (electrode 4), which functions as a Faraday cup [133]. Charges present in the beam are neutralised at this electrode, causing a current I to flow in an external $1.3\,\mathrm{M\Omega}$ sense resistor. A further ring electrode (electrode 3) is provided in front of the Faraday cup to provide extra control of the charge detection.

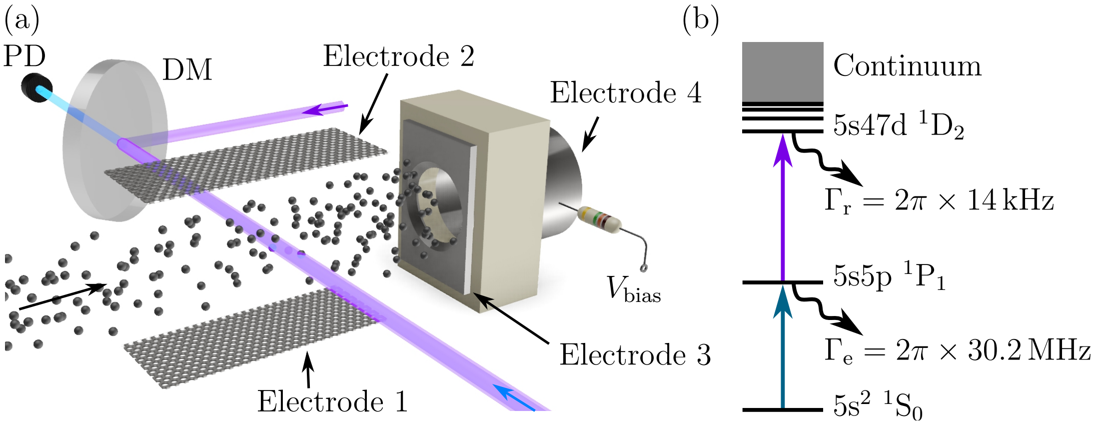

Figure 6.1: (a) Experimental schematic of the interrogation and detection regions of the beam apparatus. PD and DM refer to photodiode and dichroic mirror respectively. (b) Energy level diagram showing the excitation scheme [130, 131].

The probe beam[1] was locked resonantly to the $5s^2\ ^1S_0 \rightarrow 5s5p\ ^1P_1$ transition at 461 nm using polarisation spectroscopy [134] in the same beam apparatus. The probe beam was focused to a $1/e^2$ radius of $w_x \approx w_y = 115 \pm 1\,\mu\text{m}$ at the centre of the interrogation region and overlapped with a tunable, counter-propagating coupling beam[2] at 413 nm using a dichroic mirror. The coupling beam was focused to a measured waist of $w_x \approx w_y = 166 \pm 1\,\mu\text{m}$ at the centre of the cell. Both laser beams were circularly polarised in order to drive the strongest transitions; $|m_j| = 0 \rightarrow |m_j| = 1 \rightarrow |m_j| = 2$. The coupling beam was amplitude modulated using an optical chopper at a frequency of 2 kHz and lock-in detection used to improve the signal-to-noise ratio on both the probe transmission and the current I.

6.1.1 Faraday Cup Calibration

The Faraday cup (electrode 4) detects charges created in the Sr atomic beam. A bias voltage V_{bias} can be applied to the Faraday cup in order to attract or repel positive or negative charges. Since the cup is conductive, charges arriving on the cup are neutralised by a current that flows through the external resistor. The sign of the measured current depends on the sign of the incident charges. In this thesis, we use the convention that positive (negative) current correspond to the detection of negative (positive) charges. In all of the experiments discussed here, the cell body and ring electrode were grounded.

In order to characterise the charge detection system, charges were created in the strontium beam using resonant two-photon photo-ionisation (figure 6.1(b)), by tuning the coupling laser 5 GHz above the ionisation threshold. As long as the probability of photo-ionisation is far from saturated, the ionisation rate is directly proportional to the coupling beam power. Therefore, measuring the dependence of the current on the coupling laser beam power provides a test of the linearity of the detection system. Figure 6.2 shows the measured current I as a function of coupling laser power for a variety of V_{bias}. A linear fit to the data yields a reduced chi-squared

---

[1] MOGLabs ECDL laser.

[2] Toptica SHG system.

statistic [76] of $\chi^2_\nu < 1.5$ for all values of V_{bias}, and in each case the fit passes through the origin within the error bar. Our charge detector is therefore linear for currents $|I| < 2\,\text{nA}$.

The effect of varying V_{bias} at constant coupling laser power is shown in figure 6.3. There are two clear regions. The first is about the origin, where a small change in V_{bias} results in a large change in current. We attribute this variation to the attraction or repulsion of charges in the atomic beam. The average kinetic energy of the beam is estimated to be $\sim 0.1\,\text{eV}$ by spectroscopically measuring the atomic flux and inferring the thermal distribution. As the kinetic energy is $\sim 0.1\,\text{eV}$, only a relatively small voltage is required to modify the trajectory of charges in the beam such that they do or do not hit the detector. The effect of V_{bias} is greater for electrons than for ions due to their much lower mass. This asymmetry is apparent in figure 6.3(b). A negative current (corresponding to the detection of ions) is visible even for $V_{\text{bias}} = 0\,\text{V}$.

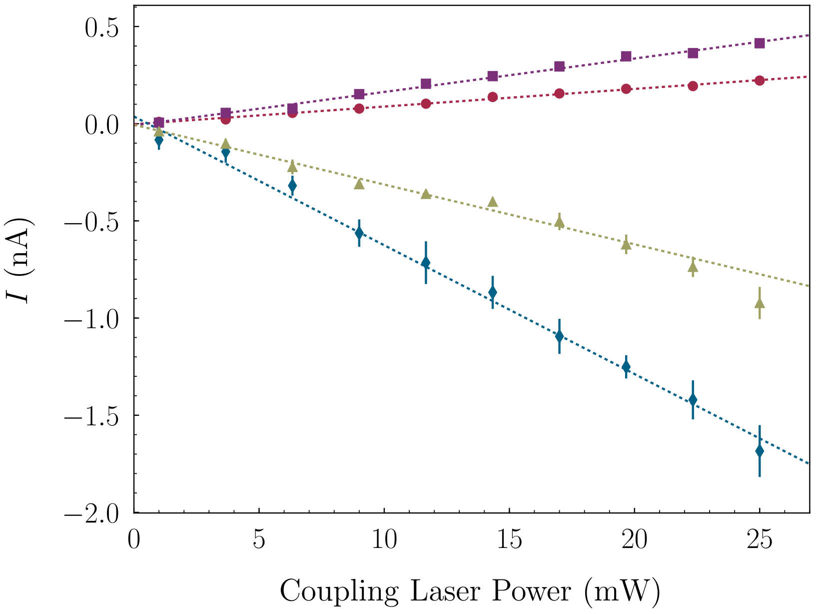

Figure 6.2: Measured current as a function of coupling laser power. The four curves (top to bottom) correspond to $V_{\text{bias}} = +5\,\text{V}$ (purple squares), $+1.5\,\text{V}$ (red circles), $-1.5\,\text{V}$ (green triangles) and $-5\,\text{V}$ (blue diamonds). The dotted lines are a linear fit to each data set.

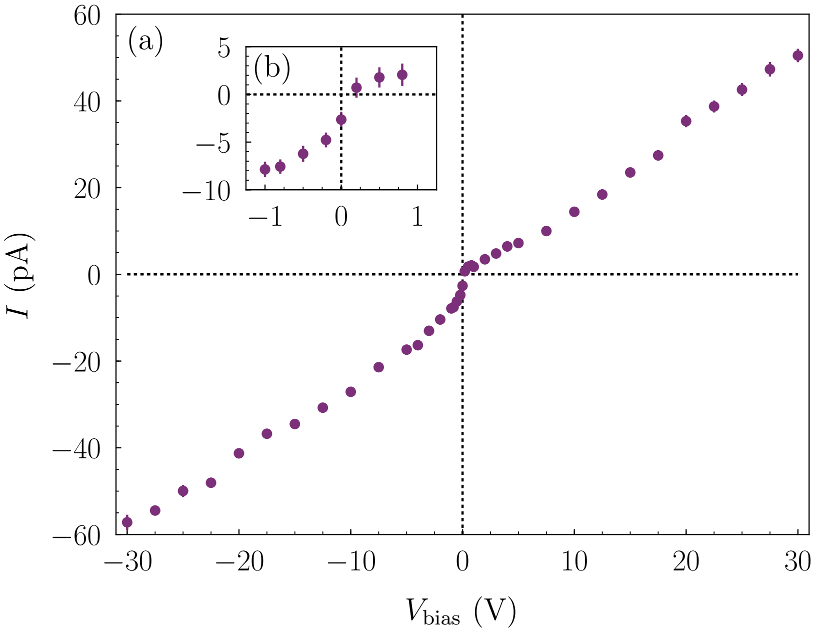

Figure 6.3: (a) Current as a function of V_{bias}. The probe and coupling powers were 3.5 mW and 33.5 mW respectively. (b) shows a zoom about the origin.

At larger voltages ($|V_{\text{bias}}| \gtrapprox 1\,\text{V}$) the magnitude of the current increases linearly with the magnitude of V_{bias}. We attribute this increase to secondary ionisation processes [135, 136]. Incoming charges with energies greater than the work function of the target material can release a charge from the surface which is either re-captured or ejected from the Faraday cup depending on the value of V_{bias}. This can lead to an effective gain of the detector.

6.2 Rydberg spectroscopy using EIT

In order to perform Rydberg spectroscopy in the cell, the coupling laser was tuned close to resonance with the 5s5p $^1\text{P}_1 \rightarrow$ 5s47d $^1\text{D}_2$ transition. Figure 6.4(a) shows the transmission of the probe beam as a function of the probe laser frequency relative to the 5s^2 $^1\text{S}_0 \rightarrow$ 5s5p $^1\text{P}_1$ transition. When the resonance condition for both lasers shown in figure 6.1 is met, an EIT feature is observed within the Doppler-broadened absorption profile. Note that the Doppler-broadened background is not symmetric about zero detuning. This is due to a baffle in the beam apparatus altering the

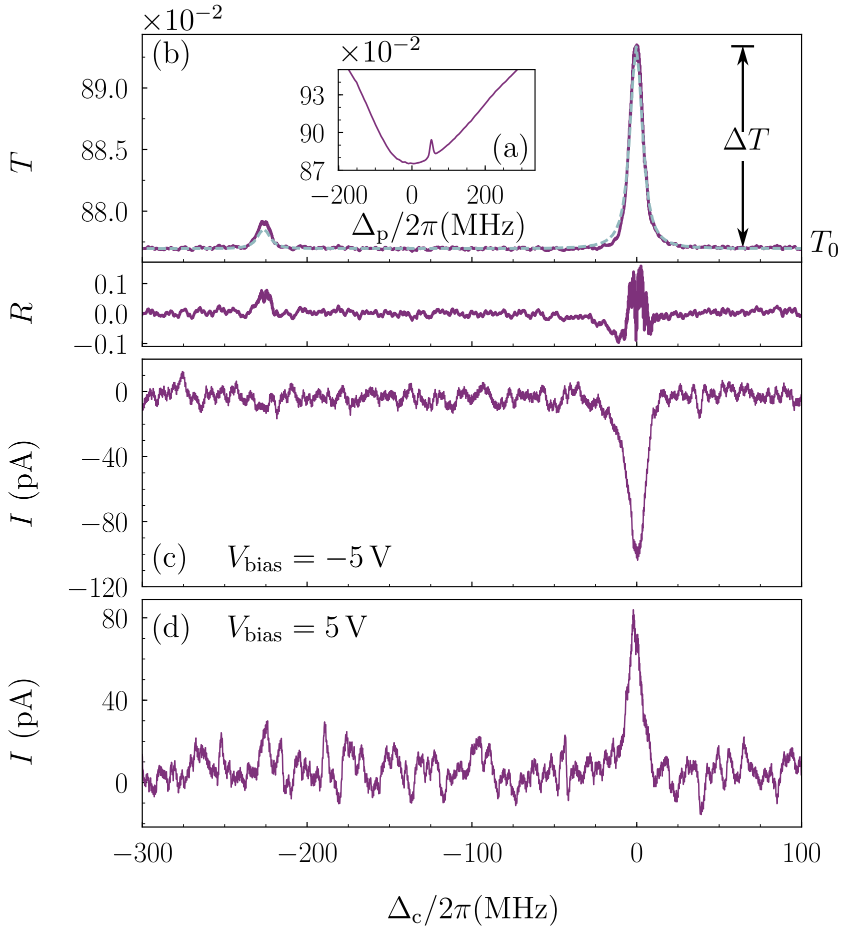

Figure 6.4: (a) Probe transmission T as a function of the probe detuning Δ_p for a fixed coupling beam detuning Δ_c. (b) Probe transmission as a function of coupling beam detuning for fitted coupling Rabi frequency of $\Omega_c/2\pi = 3.1 \pm 0.2\,\text{MHz}$ and coupling laser linewidth $\Gamma_c/2\pi = 0.6 \pm 0.1\,\text{MHz}$. The blue dashed line is the theoretical model and the residuals are shown below. ΔT is the change in transmission of the probe beam at the EIT resonance. T_0 is the transmission of the probe away from EIT resonance. (c) and (d) are the corresponding ion and electron signals.

transverse velocity distribution of the strontium beam [132].

A Doppler-free spectrum was obtained by locking the probe laser on resonance, and scanning the coupling laser. The background probe absorption signal was removed completely by demodulating the probe transmission signal using the lock-in amplifier. The resulting EIT spectrum is shown in figure 6.4(b). The largest peak in the EIT signal is attributed to the ^{88}Sr isotope and the smaller peak is attributed to the ^{86}Sr isotope. A peak from the ^{87}Sr isotope is observable at positive detunings but is not shown in this plot. The full-width at half-maximum (FWHM) of the ^{88}Sr EIT feature is $11 \pm 1\,$MHz, which is significantly smaller than the natural linewidth of the probe transition $\Gamma_{\rm e}/2\pi = 30.2\,$MHz.

The splitting between the EIT features for each isotope provides a measurement of the isotope shift of the 5s47d ^{1}D$_2$ state [137]. The splitting between the two lines was measured to be $\Delta\omega_c = 2\pi \times 227 \pm 4\,$MHz by calibrating the frequency axis in figure 6.4(b) using a high-precision wavemeter[3]. However, due to the wavelength mismatch between the probe and coupling lasers, the measured splitting is not the absolute isotope shift [137]. The probe laser frequency in the atomic rest frame is given by

$$\omega_{\rm p} = \omega_{\rm p0} + \Delta\omega_2 + k_{\rm p} v \ , \tag{6.2.1}$$

where $\omega_{\rm p0}$ is the probe laser frequency and $\Delta\omega_2$ is the isotope shift of the 5s5p ^{1}P$_1$ state between the ^{88}Sr and ^{86}Sr isotopes. The coupling laser frequency in the atomic rest frame is given by

$$\omega_{\rm c} = \omega_{\rm c0} + \Delta\omega_3 - \Delta\omega_2 - k_{\rm c} v \ , \tag{6.2.2}$$

where $\omega_{\rm c0}$ is the probe laser frequency $\Delta\omega_3$ is the isotope shift of the 5s47d ^{1}D$_2$ state. As the probe beam is locked on resonance with the ^{88}Sr atoms, the ^{86}Sr atoms which interact with the probe laser must have a velocity

$$v = -\frac{1}{k_{\rm p}}\Delta\omega_2 \ . \tag{6.2.3}$$

Substituting this back into 6.2.2, we arrive at

$$\omega_{\rm c} - \omega_{\rm c0} = \Delta\omega_3 + \left(\frac{\lambda_{\rm p}}{\lambda_{\rm c}} - 1\right)\Delta\omega_2 \ , \tag{6.2.4}$$

where $\lambda_{\rm p}$ and $\lambda_{\rm c}$ are the wavelengths of the probe and coupling lasers respectively. This yields a value of $\Delta\omega_3 = 2\pi \times 213 \pm 4\,$MHz. This value is in agreement with the trend observed by Lorenzen *et al.* [138].

We solve the OBE's detailed in section 2.3 to produce a quantitative model of the EIT lineshape. Here we use the time-dependent solution since the timescale

---

[3] HighFinesse WS7

for the evolution of the coherences and the populations is longer than the average time taken for an atom to cross the laser beams ($\approx 0.4\,\mu$s). In order to simulate the measured lineshape, the Doppler shift is included in the probe and coupling detunings, and a weighted average is performed over a 1D Boltzmann distribution. The transverse temperature of $T \approx 60\,$K was obtained from the width of the Doppler broadened absorption profile shown in figure 6.4(a). Each isotope was also weighted by its natural abundance.

The results of the model are shown in figure 6.4. The probe laser Rabi frequency ($\Omega_{\mathrm{p}}/2\pi = 13.1 \pm 0.1\,$MHz) was calculated from measurements of the power and beam size as the saturation intensity of the $5\mathrm{s}^2\ {}^1\mathrm{S}_0 \rightarrow 5\mathrm{s}5\mathrm{p}\ {}^1\mathrm{P}_1$ transition is well known [98]. The linewidth ($\Gamma_{\mathrm{p}}/2\pi = 0.7 \pm 0.1\,$MHz) was constrained by measurements of the rms deviation of the in-loop error signal of the polarisation-spectroscopy lock. The only fit parameters were the coupling Rabi frequency $\Omega_{\mathrm{c}}/2\pi = 3.1 \pm 0.2\,$MHz and the coupling laser linewidth $\Gamma_{\mathrm{c}}/2\pi = 0.6 \pm 0.1\,$MHz. The model is in good agreement with the data, although the residuals show that the theory slightly underestimates the width of the feature. This is due to the small amount of asymmetric broadening of the feature caused by the time response of the lock-in amplifier.

6.3 Observation of spontaneous ionisation

Figure 6.4(c) and (d) shows that the creation of the EIT feature also produces a current. Either ions (c) or electrons (d) can be observed simultaneously with the optical signals, using two separate lock-in amplifiers. The signal-to-noise ratio of the current under the conditions of figure 6.4 is ≥ 4 (for the ^{88}Sr isotope), allowing us to clearly resolve features and see a direct correspondence between the EIT and electrical signals. We note that the optical and electrical signals have similar widths. In contrast, previous experiments with alkali atoms observed significant broadening of the electrical signal under EIT conditions [129].

In order to confirm that the detected charges were not simply created by other mechanisms such as field ionisation close to the Faraday cup, we applied a static deflection electric field across the interrogation region. A voltage was applied to

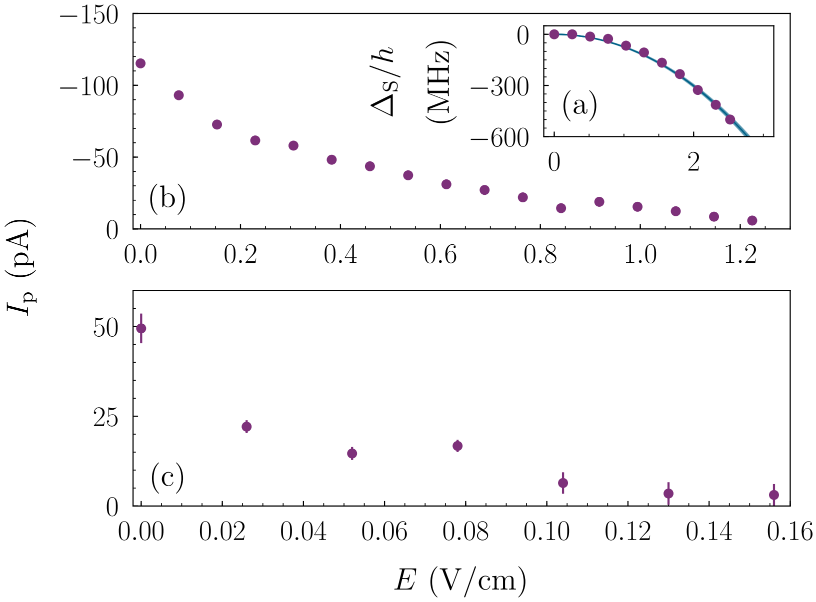

Figure 6.5: (a) Measured DC Stark shift Δ_S of the EIT feature (purple circles) along the with theoretical prediction (blue solid line) as a function of applied electric field E. (b-c) I_p as a function of applied electric field for $V_{\text{bias}} = -1.5\,\text{V}$ and $V_{\text{bias}} = 1.5\,\text{V}$ respectively.

electrodes 1 and 2, and the magnitude of the resulting electric field E was calibrated by scanning the coupling laser and measuring the DC Stark shift of the EIT resonance. For reference, the electric field required to field ionise the Rydberg atoms is $\approx 66\,\text{V/cm}$ [128]. The resulting Stark map is shown in 6.5(a). Due to the laser polarisation, we couple most strongly to the $m_j = 0$ state, since the electric field is perpendicular to the propagation direction. The data are compared to a calculated Stark map, which has two constituent parts. Firstly, the expected spatial distribution of the electric field in the interrogation region is calculated using a finite element analysis method (Autodesk Inventor Simulation Mechanical package). Subsequently, the electric field is converted into a predicted line shift by evaluating the Stark shift in the single electron approximation [75], using the method of [139]. Stark maps are calculated by numerical integration of the Stark Hamiltonian, with the necessary quantum defects obtained from [34]. The resulting prediction for the Stark shift is in very good agreement with the data, as shown in figure 6.5(a), with no adjustable parameters.

The corresponding peak values of the ion (electron) current I_{p} obtained at the Stark-shifted resonance are shown in figure 6.5. As the applied electric field is increased from 0 V/cm, we see a decrease in the both the electron and ion signal, which is eventually suppressed to the noise floor of our detection system. The electron signal diminishes at much lower fields than the ion signal, as one would expect given the large mass difference of the two particles. These data clearly show that the measured current originates in the interrogation region, and not at the detector.

6.4 Origin of the spontaneous ionisation

There are a variety of mechanisms which can ionise Rydberg atoms [128]. We classify these as either one-body or two-body. One-body ionisation may occur via black-body photo-ionisation, or ionising collisions with background contaminants in the beam apparatus. Two-body ionisation can occur due to Rydberg-Rydberg collisions, or due to collisions between Rydberg atoms and another species present in the atomic beam. In our experiments, the possible collision partners are atoms in the ground or intermediate states, as well as ions or electrons. In this section, we show that we can determine the dominant ionisation mechanism by combining the simultaneous measurement of optical and electrical signals with quantitative modelling of the optical response. Here we only consider the ion signal due to the larger signal-to-noise ratio at lower probe absorptions.

Firstly, we varied the population of the Rydberg state at constant ground state density by varying the power of the excitation lasers. The probe and coupling lasers were investigated independently, as shown in figure 6.6. A comparison between these experiments is sensitive to any processes that involve the intermediate state, as changes in the the probe laser power also changes the population of the intermediate state while varying the coupling laser does not.

The dashed lines in figure 6.6 are a theoretical prediction of the measured current. This is derived from the OBE model, by assuming that the measured current is

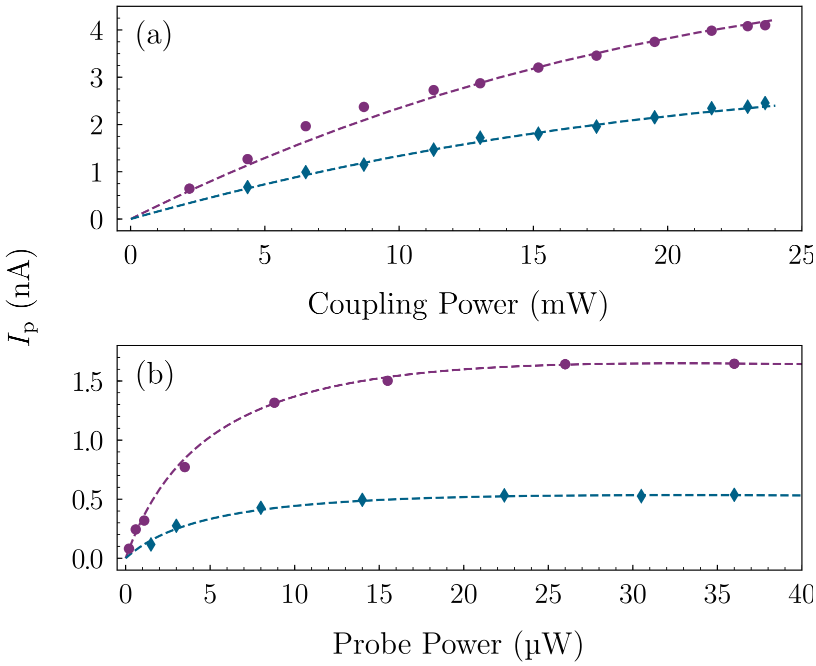

Figure 6.6: Current as a function of coupling beam power for $\Omega_p/2\pi = 17.0 \pm 0.3\,\mathrm{MHz}$ (a) and probe beam power for $\Omega_c/2\pi = 2.7 \pm 0.2\,\mathrm{MHz}$ (b). The blue diamond and purple circle points correspond to 27 % and 32 % percentage absorption in the absence of the coupling beam respectively. The dashed lines are the theoretical fit to the data.

dependent on the Rydberg state population, via a combination of one-body and two-body terms: $I_p \propto a_1 N_{\mathrm{Ryd}} + a_2 N_{\mathrm{Ryd}}^2$ where N_{Ryd} is the number of Rydberg atoms. We find excellent agreement between theory and experiment when the quadratic term is neglected (i.e. $a_2 = 0$), with $\chi_\nu^2 \leq 2.2$ for all curves. This indicates that two-body Rydberg-Rydberg processes do not play an observable role in the measured ionisation process. The current therefore provides a direct measurement of the Rydberg state population. In addition, the agreement between theory and experiment shown in figure 6.6(b) suggests that ionisation mechanisms involving the intermediate state atoms do not play a significant role.

We also studied the density dependence of the current by varying the flux of the atomic beam at constant laser power. The dependence of the optical response and the current on probe beam absorption, $A_p = 1 - T_0$, is shown in figure 6.7. At low density, the optical response is proportional to the probe absorption as expected, before exhibiting a roll-off due to propagation effects. The roll-off is caused by absorption of the probe beam as it propagates through the atomic beam, which leads to a different optical response in different regions of the atomic beam. At high density, this effect becomes significant. To take this into account in our model, we divide the atomic beam into segments along the probe beam propagation direction, following the procedure described in [102]. The OBE model is solved independently in successive segments, with the absorption coefficient in the preceding segment used to set the probe beam intensity in the next. The result is shown in figure 6.7(a) and is in good agreement with the measured probe transmission. In contrast, the current is non-linear in the probe absorption even at low density, strongly indicating that the ionisation mechanism is dependent on the ground state density.

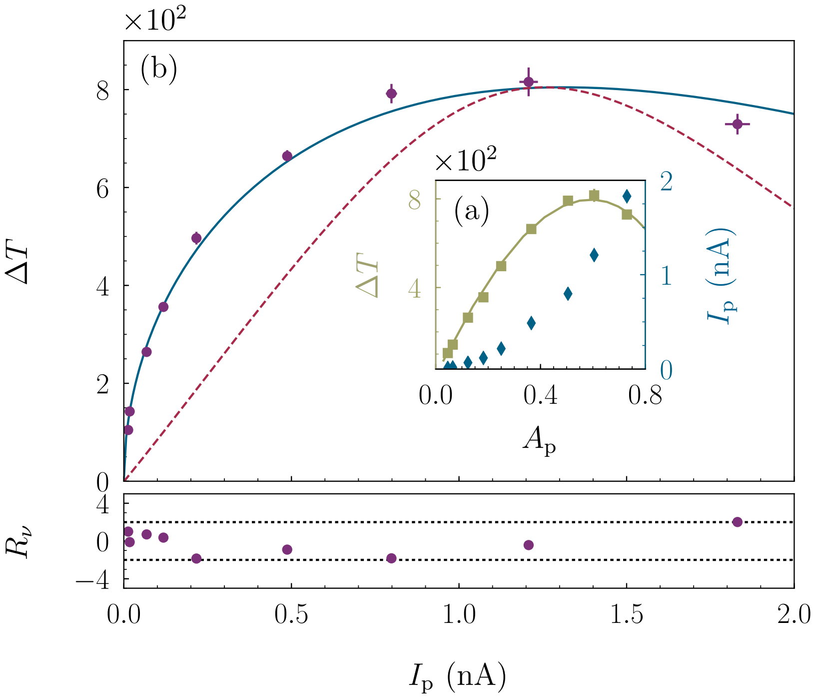

Figure 6.7: (a) ΔT (green squares) and I_p (blue diamonds) as a function of A_p. (b) ΔT as a function of I_p (purple circles). The dashed red curve shows the theoretical model for $I \propto N_\mathrm{Ryd}$. The solid blue curve shows the theoretical model for $I_\mathrm{p} \propto b_1 N_\mathrm{Ryd} + b_2 N_\mathrm{Ryd} N_\mathrm{Gnd}$. The residuals between the data and the blue curve are normalised to the error bar of each point and are shown below the main figure. The dotted lines show $R_\nu = \pm 2$.

Figure 6.7(b) shows the optical response ΔT, defined in figure 6.4 as the maximum change in transmission of the probe beam whilst the coupling laser is scanned across the EIT resonance, as a function of the peak current I_p. By plotting the data in this manner, we are able to directly connect both the optical and electrical signals. We assume that the Rydberg population calculated by the propagation model is related to the current by a sum of one-body and two-body (Rydberg-ground state) terms: $I_\mathrm{p} \propto b_1 N_\mathrm{Ryd} + b_2 N_\mathrm{Ryd} N_\mathrm{Gnd}$ where b_1 and b_2 are fit parameters and N_Gnd is the number of ground state atoms. Here we do not include any two-body terms associated with Rydberg-Rydberg interactions or the intermediate state as these process have previously been excluded (see figure 6.6). The solid black curve shows a fit with b_1 and b_2 as adjustable parameters. The best fit is obtained for $b_1 = 0$, yielding $\chi^2_\nu = 1.9$. This result strongly indicates that the spontaneous ionisation process is not dominated by any of the one-body processes described above. Further emphasis is provided by the lack of agreement between theory and experiment for the dashed red curve which represents $I_\mathrm{p} \propto N_\mathrm{Ryd}$. Furthermore, we note that the absence of a significant one-body ionisation rate in addition to a negligible two-body ionisation rate in figure 6.6 also eliminates the possibility of collisions between ions and Rydberg atoms. The ionisation that we observe is therefore dominated by collisions between ground and Rydberg state atoms, in agreement with [29], and the proposals of [129, 140]. The most likely cause is Penning ionisation, with the necessary extra energy coming from the kinetic energy of the atoms [141]. Other processes such as ion pair formation [142] cannot be excluded, but are expected to be less likely [29].

Using a rate equation approach and making a series of approximations, it is possible to estimate the ionisation cross section σ of this process. We assume that $\dot{I}_\mathrm{Ion} = \bar{n}\sigma\bar{v}_\mathrm{rel}$. Here the dot denotes the time derivative, $\bar{v}_\mathrm{rel}$ is the relative velocity between the ground and Rydberg state atoms and $\bar{n}$ is an average density. The relative velocity of the atoms in an effusive atomic beam differs from that of a random 3D gas and is given by [143]

$$\bar{v}_\mathrm{rel} = 2\sqrt{\frac{2k_\mathrm{B}T}{\pi M}}\left(\frac{7\sqrt{2}-8}{4}\right) , \qquad (6.4.5)$$

where M is the mass and $T \approx 800\,\mathrm{K}$ is the temperature of the strontium atoms respectively. The average density is defined as

$$\bar{n} = \int n_G n_R \, \mathrm{d}^3 r = n_G n_R A \int \mathrm{e}^{-\Gamma_\mathrm{r} z/\bar{v}} \, \mathrm{d}z \ , \tag{6.4.6}$$

where n_G and n_R are the ground and Rydberg state densities respectively and the integral is performed over the interaction volume. The assumption of the interaction volume is the dominant source of error. Here we assume that the interaction volume is constrained by the the area of the intersection between the probe and atomic beams A, and the distance from the probe beam to the Faraday cup. We integrate over an exponentially decreasing Rydberg distribution due to spontaneous emission. We also assume that the atoms travel with an average velocity $\bar{v} = 390\,\mathrm{m\,s^{-1}}$ towards the Faraday cup. Here, $n_G = 5 \times 10^{14}\,\mathrm{m^{-3}}$ is determined from the absorption of the probe beam. Using the OBE model, we estimate that the Rydberg population is $n_R = 0.03\ n_G$. $A = 6.9 \times 10^{-6}\,\mathrm{m^2}$ is calculated form the $1/e^2$ diameter of the probe beam and the width of the atomic beam. The distance between the excitation beams and the Faraday cup is $\approx 30\,\mathrm{mm}$. Using the peak ion signal shown in figure 6.4 and taking into account the gain of the Faraday cup, $\dot{I}_\mathrm{Ion} = 1 \times 10^9\,\mathrm{s^{-1}}$. Using these numbers, we measure the ionisation cross section to be $\sigma = 0.6 \pm 0.2\ \sigma_\mathrm{geo}$ where $\sigma_\mathrm{geo} = \pi \left(n^*\right)^4 a_0^2$ is the geometric area of the Rydberg atom and n^* is the effective quantum number [130]. To first approximation, one would expect that the cross section is the order of σ_geo [128], and therefore our value appears reasonable.

We return to the evolution of the width of the optical and electrical features with ground state number density. Previous studies have observed significant broadening of the optical and/or electrical response due to pressure broadening [129] or interactions [140, 144, 145]. Figure 6.8 shows the measured full-width at half-maximum (FWHM) of the EIT and current lineshapes as a function of ground state number density. It is clear that we do not observe any significant broadening over the range of densities we have studied. The measured width of the optical and electrical features are close to those predicted by the optical Bloch equation model, 8.9 MHz and 11.5 MHz respectively. In particular the model correctly reproduces the difference in width between the two signals. The small amount of extra broadening ≈ 0.7 MHz that we observe is caused by the time response of the lock-in amplifier.

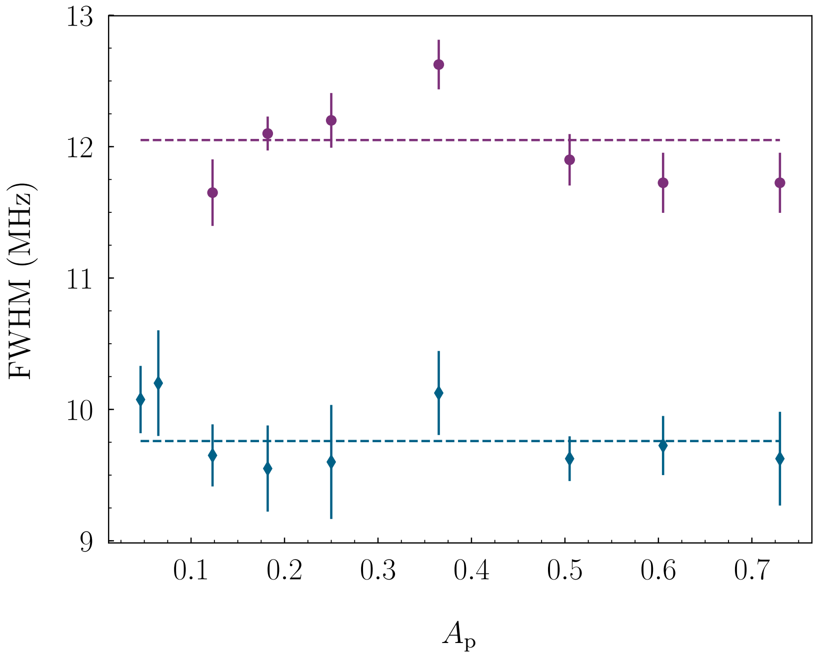

Figure 6.8: Full-width at half-maximum of the EIT feature (blue diamonds) and the current feature (pruple cirlces) as a function of A_p. The dashed lines are fits to the data where the gradient has been constrained to be zero.

6.5 Outlook

When the atomic density is sufficiently high, interactions can play a significant role and lead to non-linear effects. A case where interactions do appear to play a decisive role is the observation of Rydberg-mediated optical bistability [144, 145], which has lead to the observation of non-equilibrium phase transitions as well as detection methods for terahertz radiation [146]. However, while theory has shown that an effective mean-field description of the system leads to quantitative agreement with the experiments [81, 147], the microscopic nature of this effective interaction remains unclear. In particular, the relative importance of dipole-dipole processes (including e.g. superradiance) and charged particles is an open question [140, 145]. The ability to detect both optical and electrical signals in our experimental apparatus offers an opportunity to shed more light on this process.

The detection of charged particles in the atomic beam is facilitated by the use of lock-in detection. As this method requires amplitude modulation of the coupling

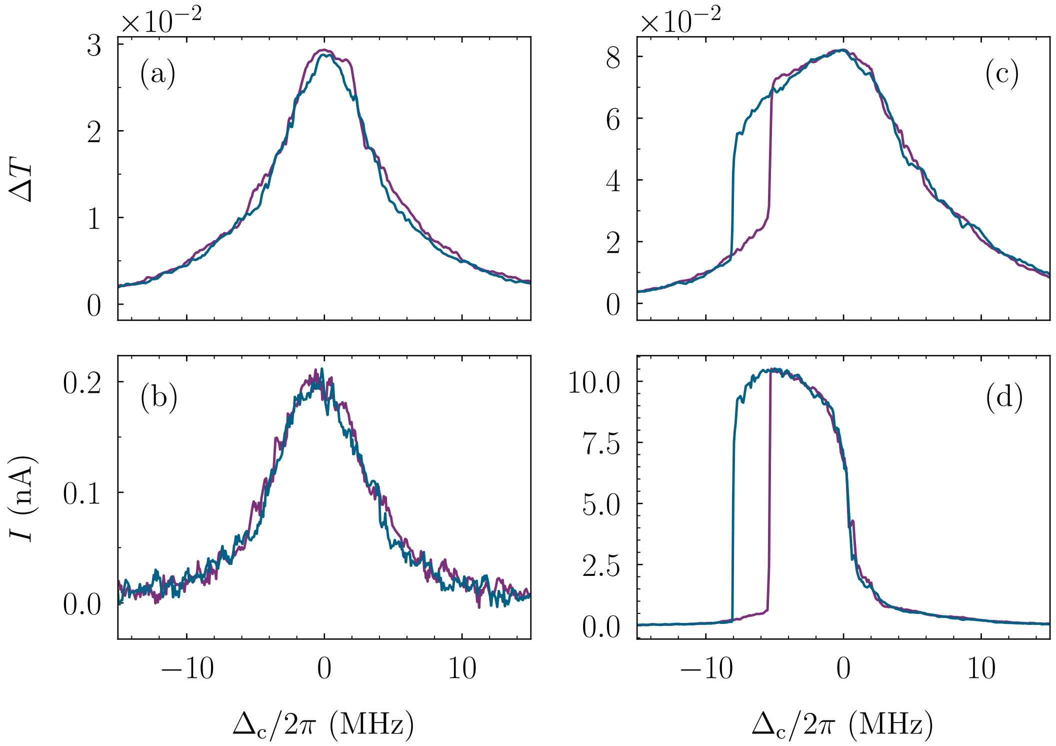

Figure 6.9: Optical and ion signals as a function of coupling beam detuning. The purple and blue lines correspond to scanning up and down in frequency respectively. (a-b) and (c-d) correspond to $T_0 = 0.86$ and 0.37 respectively.

beam, it is not possible to observe a bistable signal. We therefore replace the lock-in detection with a low-noise current amplifier[4], which allows us to measure the current flowing through the Faraday cup and hence detect the charged particles without the need for modulation. To enter a regime where the Rydberg density is large, both the probe and coupling beam powers were increased to 70 µW and 54 mW respectively. Figure 6.9 shows the optical and ion signals at low (a-b) and high atomic flux (c-d). At low atomic flux, we observe a symmetric optical and ion signal, similar to that detailed previously in the chapter. However as the atomic flux is increased, we are able to observe simultaneous bistability in both the optical and ion signals, which is the first observation of electrical bistability in an atomic vapour. This indicates that charged particles play a role in the formation of optical bistability, and support

---

[4] Femto DPLCA-200

the interpretation of [140]. The ability to observe and connect the bistability in both the optical and electrical signals may shed further insight into this mechanism, however this is beyond the scope of this work.

6.6 Summary

In this chapter, we have shown that the measurement of Rydberg EIT leads to the production of charged particles which can be measured with a simple Faraday cup. By quantitatively connecting the optical and electrical signals, we were able to deduce the origin of the spontaneous ionisation process. This is dominated by Rydberg-ground state collisions, with a measured cross section of $\sigma = 0.6 \pm 0.2\ \sigma_{\mathrm{geo}}$. We have also shown that when the atomic density is sufficiently large, we are able to observe simultaneous optical and electrical bistability. This is the first observation of electrical bistability in an atomic vapour, and the ability to link both the optical and electrical signals may shed further light on the mechanism behind bistability in atomic vapours.

Part III

Conclusions and Outlook

Chapter 7

Conclusions

In this thesis, we have developed the pre-requisite experimental tools to create a spin-squeezed atomic clock [7] based upon an array of single strontium atoms. We have demonstrated the admixture of a Rydberg state into the narrow intercombination transitions of strontium, from both an experimental and theoretical basis. We have also detailed the first known observation of a strontium microtrap, a crucial tool to creating arrays of single strontium atoms.

In chapter 3, we demonstrated the coherent admixture of a Rydberg state into the narrow intercombination transitions in strontium. To fully understand this process, we developed a quantitative model of a nMOT operating on the narrow $5\mathrm{s}^2\ {}^1\mathrm{S}_0 \rightarrow 5\mathrm{s}5\mathrm{p}\ {}^3\mathrm{P}_1$ transition, by combining a quantum treatment of the light scattering process with a Monte-Carlo simulation of the atomic motion. We have shown that the model does not only reproduce the steady-state dynamics of the nMOT, such as position and temperature, but the model is also able to quantitatively reproduce transient dynamics. This quantitative understanding is a critical foundation for understanding effects beyond the physics of a nMOT, such as Rydberg dressing.

The observation of Rydberg-dressed interactions in our experiment is limited by the dressing laser power and shape, as well as radiation pressure forces [46]. A clear direction for this work is to upgrade the 319 nm laser system to increase the available power, as well as using beam shaping optics to create a dressing beam with a uniform intensity profile. With these experimental improvements, it should be possible to observe clear signatures of Rydberg-dressed interactions in a nMOT. With the additon of high NA in-vacuo lenses, this may lead to observations of exciting phases of matter such as the formation of Rydberg supersolids [48, 148].

Chapter 4 details the design and construction of the new experimental apparatus used to create a microtrap of strontium. We considered the optimum wavelengths and loading conditions of a strontium microtrap by calculating the dynamic polarisability for all states relevant to laser cooling of strontium. We have shown that the most efficient loading mechanism is direct loading from a nMOT. The new experimental innards has seen a number of upgrades, the most significant of which is the pair of in-vacuo aspheric lenses which facilitates the creation of a microtrap. We have also performed major upgrades to the laser systems used in the experiment, in particular the 689 nm laser system, observing marked improvements in laser stability.

We showed in chapter 5 the first known observations of a microtrap of strontium, directly loaded from a nMOT. We are currently not able to reach the regime of single atom distinguishability as the atoms are rapidly lost form the microtrap. The reason for this is due to the large differential AC Stark shift of the $5s^2\ ^1S_0 \rightarrow 5s5p\ ^1P_1$ transition and the lack of sub-Doppler cooling. Sub-Doppler cooling in the alkali-metal atoms facilitates off-resonance imaging of atoms in a microtrap without appreciable heating. However, due to the lack of hyperfine structure in ^{88}Sr, the temperature of the atoms is limited by Doppler theory which results in a rapid heating fo the atoms in the microtrap. It is therefore not possible to enter a regime where the microtrap depth is significantly larger than the atomic temperature. This in turn limits the amount of detected photons per atom before the atom is lost from the microtrap. We have proposed a number of solutions to this problem, such as imaging using a tunable imaging laser, imaging on the $5s5p\ ^3P_1 \rightarrow 5s6s\ ^3S_1$ transition, or using ^{87}Sr where sub-Doppler cooling is achievable. These proposals should increase the atomic lifetime in the microtrap during imaging, allowing us to enter the regime of single atom distinguishability, which is critical for the creation of an array of single strontium atoms. Following the detection of single strontium atoms, the next is goal is to create an array of microtraps using an spatial-lightmodulator.

We have characterised the microtrap by a series of measurements of the trap frequency, temperature and lifetime. We have explored the pitfalls of these measurements, and shown in particular that the microtrap depth must be much greater than the atomic temperature when measuring microtrap frequencies to ensure that the harmonic approximation to the trapping potential is valid. We have also shown that it is not possible to load directly into a deep microtrap directly from a nMOT, via thermal and spectroscopic measurements of the atoms in the microtrap. This is because it is possible to load atoms into subsidiary maxima in the trapping potential, which is only feasible due to the low initial temperature of the atoms in the nMOT ($\sim 1\,\mu$K). We have also performed shelving spectroscopy of the atoms in the microtrap, leading to the first measurements of the polarisability of the 5s5p ^{3}P$_1$ state at 532 nm. This data indicates that the theoretical polarisabilities are inconsistent with the experimental data, and that the predicted magic wavelength at 500 nm is in fact at a higher wavelength. This discrepancy between theory and experiment is most likely due to inaccuracies in the measurement of the relevant transition rates.

Another direction which is of particular interest is optically trapping both ground and Rydberg state atoms in the same microtrap. One of the challenges of this experiment is the experimental evidence of Rydberg trapping, given the relatively short lifetime of the Rydberg states. We propose to excite a single atom in a deep microtrap to a high n Rydberg state, where the microtrap oscillation period is much greater than the Rydberg state lifetime. A pulse at 408 nm would be overlapped with the microtrap to ionise the Rydberg atom, after which the ion can be detected on the MCP. By performing this measurement as a function of time, it should be possible to determine whether the Rydberg atom is optically trapped in the microtrap. This would result would have a large impact in the field of quantum simulation, as the ability to trap both ground and Rydberg state atoms in a common optical trap is a pre-requisite for many quantum state manipulations involving Rydberg states [22, 23].

Presented finally in chapter 6 is the demonstration of a novel method for probing interaction effects in a thermal beam of strontium atoms using simultaneous measurements of Rydberg EIT and spontaneously created ions or electrons. Due to the creation of Rydberg atoms in the strontium microtrap, understanding these ionisation and interaction mechanisms may be of significant importance in future work. By quantitatively connecting the optical and electrical signals, we were able to deduce the origin of the spontaneous ionisation mechanism. We have also shown that by sufficiently increasing the Rydberg density, it is possible to observe non-linear effects such as bistability. We have demonstrated the first known observation of electrical bistability, and the simultaneity of the measurements of both the optical and electrical signals may shed further light onto the debated mechanism behind this process [140, 144, 145].

Bibliography

[1] C. Guerlin, P. Delva, and P. Wolf. Some fundamental physics experiments using atomic clocks and sensors. *C. R. Phys.*, 16(5):565–575, 2015.

[2] M. S. Safronova, S. G. Porsev, C. Sanner, and J. Ye. Two clock transitions in neutral Yb for the highest sensitivity to variations of the fine-structure constant. *Phys. Rev. Lett.*, 120(17):173001, 2018.

[3] S Blatt, A. D. Ludlow, G. K. Campbell, J. W. Thomsen, T. Zelevinsky, M. M. Boyd, J. Ye, X. Baillard, M. Fouché, R. Le Targat, et al. New limits on coupling of fundamental constants to gravity using Sr 87 optical lattice clocks. *Phys. Rev. Lett.*, 100(14):140801, 2008.

[4] V. A. Dzuba, V. V. Flambaum, and S. Schiller. Testing physics beyond the standard model through additional clock transitions in neutral ytterbium. *Phys. Rev. A*, 98(2):022501, 2018.

[5] A. Derevianko and M. Pospelov. Hunting for topological dark matter with atomic clocks. *Nat. Phys.*, 10(12):933, 2014.

[6] A. Arvanitaki, J. Huang, and K. Van Tilburg. Searching for dilaton dark matter with atomic clocks. *Phys. Rev. D*, 91(1):015015, 2015.

[7] L. I. R. Gil, R. Mukherjee, E. M. Bridge, M. P. A. Jones, and T. Pohl. Spin squeezing in a Rydberg lattice clock. *Phys. Rev. Lett.*, 112:103601, 2014.

[8] G. E. Marti, R. B. Hutson, A. Goban, S. L. Campbell, N. Poli, and J. Ye. Imaging optical frequencies with 100 μHz precision and 1.1 μm resolution. *Phys. Rev. Lett.*, 120(10):103201, 2018.

[9] W. M. Itano, J. C. Bergquist, J. J. Bollinger, J. M. Gilligan, D. J. Heinzen, F. L. Moore, M. G. Raizen, and D. J. Wineland. Quantum projection noise: Population fluctuations in two-level systems. *Phys. Rev. A*, 47(5):3554, 1993.

[10] V. Giovannetti, S. Lloyd, and L. Maccone. Quantum-enhanced measurements: beating the standard quantum limit. *Science*, 306(5700):1330–1336, 2004.

[11] J. Ma, X. Wang, C. Sun, and F. Nori. Quantum spin squeezing. *Phys. Rep.*, 509(2-3):89–165, 2011.

[12] M. Kitagawa and M. Ueda. Squeezed spin states. *Phys. Rev. A*, 47(6):5138, 1993.

[13] A. Louchet-Chauvet, J. Appel, J. J. Renema, D. Oblak, N. Kjaergaard, and E. S. Polzik. Entanglement-assisted atomic clock beyond the projection noise limit. *New. J. Phys.*, 12(6):065032, 2010.

[14] I. D. Leroux, M. H. Schleier-Smith, and V. Vuletić. Orientation-dependent entanglement lifetime in a squeezed atomic clock. *Phys. Rev. Lett.*, 104(25):250801, 2010.

[15] L. Pezzè, A. Smerzi, M. K. Oberthaler, R. Schmied, and P. Treutlein. Quantum metrology with nonclassical states of atomic ensembles. *Rev. Mod. Phys.*, 90(3):035005, 2018.

[16] A. Traverso, R. Chakraborty, Y. N. M. De Escobar, P. G. Mickelson, S. B. Nagel, M. Yan, and T. C. Killian. Inelastic and elastic collision rates for triplet states of ultracold strontium. *Phys. Rev. A*, 79(6):060702, 2009.

[17] W. Bowden, R. Hobson, P. Huillery, P. Gill, M. P. A. Jones, and I. R. Hill. Rydberg electrometry for optical lattice clocks. *Phys. Rev. A*, 96(2):023419, 2017.

[18] D. Frese, B. Ueberholz, S. Kuhr, W. Alt, D. Schrader, V. Gomer, and D. Meschede. Single atoms in an optical dipole trap: Towards a deterministic source of cold atoms. *Phys. Rev. Lett.*, 85(18):3777, 2000.

[19] S. Kuhr, W. Alt, D. Schrader, M. Müller, V. Gomer, and D. Meschede. Deterministic delivery of a single atom. *Science*, 293(5528):278–280, 2001.

[20] N. Schlosser. *Étude et réalisation de micro-pièges dipolaires optiques pour atomes neutres*. PhD thesis, Université Paris XI, 2001.

[21] D. Barredo, V. Lienhard, S. de Léséleuc, T. Lahaye, and A. Browaeys. Synthetic three-dimensional atomic structures assembled atom by atom. *Nature*, 561(7721):79, 2018.

[22] L. Isenhower, E. Urban, X. L. Zhang, A. T. Gill, T. Henage, T. A. Johnson, T. G. Walker, and M. Saffman. Demonstration of a neutral atom controlled-NOT quantum gate. *Phys. Rev. Lett.*, 104:010503, 2010.

[23] M. Saffman, T. G. Walker, and K. Mølmer. Quantum information with Rydberg atoms. *Rev. Mod. Phys.*, 82:2313–2363, 2010.

[24] S. D. Hogan and F. Merkt. Demonstration of three-dimensional electrostatic trapping of state-selected Rydberg atoms. *Phys. Rev. Lett*, 100(4):043001, 2008.

[25] T. Pohl, H. R. Sadeghpour, and P. Schmelcher. Cold and ultracold Rydberg atoms in strong magnetic fields. *Phys. Rep.*, 484(6):181–229, 2009.

[26] K. C. Younge, B. Knuffman, S. E. Anderson, and G. Raithel. State-dependent energy shifts of Rydberg atoms in a ponderomotive optical lattice. *Phys. Rev. Lett.*, 104(17):173001, 2010.

[27] R. Mukherjee, J. Millen, R. Nath, M. P. A. Jones, and T. Pohl. Many-body physics with alkaline-earth Rydberg lattices. *J. Phys. B: At., Mol. Opt. Phys.*, 44(18):184010, 2011.

[28] K. Niemax. Spectroscopy using thermionic diode detectors. *Appl. Phys. B*, 38(3):147–157, 1985.

[29] E. F. Worden, J. G. Conway, and J. A. Paisner. Associative ionization of laser-excited Rydberg states in strontium vapor. *Opt. Lett.*, 3(4):156–158, 1978.

[30] J. P. Hermann and J. J. Wynne. Ionization studies in laser-excited alkaline-earth vapors. *Opt. Lett.*, 5(6):236–238, 1980.

[31] S. Ye, X. Zhang, T. C. Killian, F. B. Dunning, M. Hiller, S. Yoshida, S. Nagele, and J. Burgdörfer. Production of very-high-n strontium Rydberg atoms. *Phys. Rev. A*, 88:043430, 2013.

[32] M. M. Boyd. *High Precision Spectroscopy of Strontium in an Optical Lattice: Towards a New Standard for Frequency and Time.* PhD thesis, University of Colorado, 2007.

[33] D. Boddy. *First observations of Rydberg blockade in a frozen gas of divalent atoms.* PhD thesis, Durham University, 2014.

[34] C. L. Vaillant, M. P. A. Jones, and R. M. Potvliege. Long-range Rydberg–Rydberg interactions in calcium, strontium and ytterbium. *J. Phys. B: At., Mol. Opt. Phys.*, 45(13):135004, 2012.

[35] G. Lochead, D. Boddy, D. P. Sadler, C. S. Adams, and M. P. A. Jones. Number-resolved imaging of excited-state atoms using a scanning autoionization microscope. *Phys. Rev. A*, 87:053409, 2013.

[36] P McQuillen, X Zhang, T Strickler, F. B. Dunning, and T. C. Killian. Imaging the evolution of an ultracold strontium Rydberg gas. *Phys. Rev. A*, 87(1):013407, 2013.

[37] C. Cohen-Tannoudji, J. Dupont-Roc, and G. Grynberg. *Atom-Photon Interactions.* A Wiley-Interscience publication. Wiley, 1998.

[38] C. J. Foot. *Atomic Physics.* Oxford Master Series in Physics. OUP Oxford, 2004.

[39] T. W. Hänsch and A. L. Schawlow. Cooling of gases by laser radiation. *Opt. Comm.*, 13(1):68–69, 1975.

[40] E. L. Raab, M Prentiss, A. Cable, S. Chu, and D. E. Pritchard. Trapping of neutral sodium atoms with radiation pressure. *Phys. Rev. Lett.*, 59(23):2631, 1987.

[41] A. D. Ludlow. *The Strontium Optical Lattice Clock: Optical Spectroscopy with Sub-Hertz Accuracy.* PhD thesis, University of Colorado, 2008.

[42] D. M. Brink and G. R. Satchler. *Angular Momentum.* Oxford science publications. Clarendon Press, 1993.

[43] M. Auzinsh, D. Budker, and S. Rochester. *Optically Polarized Atoms: Understanding Light-atom Interactions.* OUP Oxford, 2010.

[44] X. Zhou, X. Xu, X. Chen, and J. Chen. Magic wavelengths for terahertz clock transitions. *Phys. Rev. A.*, 81(1):012115, 2010.

[45] A. D. Bounds. *A Rydberg-dressed Magneto Optical Trap.* PhD thesis, Durham University, 2018.

[46] N. C. Jackson. *Rydberg spectroscopy and dressing in an ultracold strontium gas.* PhD thesis, Durham University, 2018.

[47] J. E. Johnson and S. L. Rolston. Interactions between Rydberg-dressed atoms. *Phys. Rev. A*, 82:033412, Sep 2010.

[48] N. Henkel, R. Nath, and T. Pohl. Three-dimensional roton excitations and supersolid formation in Rydberg-excited Bose-Einstein condensates. *Phys. Rev. Lett.*, 104(19):195302, 2010.

[49] G. Pupillo, A. Micheli, M. Boninsegni, I. Lesanovsky, and P. Zoller. Strongly correlated gases of Rydberg-dressed atoms: quantum and classical dynamics. *Phys. Rev. Lett.*, 104(22):223002, 2010.

[50] K. J. Boller, A. Imamoğlu, and S. E. Harris. Observation of electromagnetically induced transparency. *Phys. Rev. Lett.*, 66:2593–2596, 1991.

[51] S. E. Harris, J. E. Field, and A. Imamoğlu. Nonlinear optical processes using electromagnetically induced transparency. *Phys. Rev. Lett.*, 64:1107–1110, 1990.

[52] M. Fleischhauer, A. Imamoglu, and J. P. Marangos. Electromagnetically induced transparency: Optics in coherent media. *Rev. Mod. Phys.*, 77:633–673, 2005.

[53] J. D. Jackson. *Classical Electrodynamics.* John Wiley, 1975.

[54] J. Gea-Banacloche, Y. Li, S. Jin, and M. Xiao. Electromagnetically induced transparency in ladder-type inhomogeneously broadened media: Theory and experiment. *Phys. Rev. A*, 51(1):576, 1995.

[55] Y.-Y. Jau, A. M. Hankin, T. Keating, I. H. Deutsch, and G. W. Biedermann. Entangling atomic spins with a Rydberg-dressed spin-flip blockade. *Nat. Phys.*, 12:71, 2015.

[56] J. Zeiher, R. van Bijnen, P. Schauß, S. Hild, J.-Y. Choi, T. Pohl, I. Bloch, and C. Gross. Many-body interferometry of a Rydberg-dressed spin lattice. *Nat. Phys.*, 12:1095–1099, December 2016.

[57] J. Zeiher, J. Choi, A. Rubio-Abadal, T. Pohl, R. van Bijnen, I. Bloch, and C. Gross. Coherent many-body spin dynamics in a long-range interacting ising chain. *Phys. Rev. X*, 7(4):041063, 2017.

[58] J. A. Aman, B. J. DeSalvo, F. B. Dunning, T. C. Killian, S. Yoshida, and J. Burgdörfer. Trap losses induced by near-resonant Rydberg dressing of cold atomic gases. *Phys. Rev. A*, 93:043425, Apr 2016.

[59] E. A. Goldschmidt, T. Boulier, R. C. Brown, S. B. Koller, J. T. Young, A. V. Gorshkov, S. L. Rolston, and J. V. Porto. Anomalous broadening in driven dissipative Rydberg systems. *Phys. Rev. Lett.*, 116:113001, Mar 2016.

[60] S. Helmrich, A. Arias, and S. Whitlock. Uncovering the nonequilibrium phase structure of an open quantum spin system. *Phys. Rev. A*, 98(2):022109, 2018.

[61] T. Boulier, E. Magnan, C. Bracamontes, J. Maslek, E. A. Goldschmidt, J. T. Young, A. V. Gorshkov, S. L. Rolston, and J. V. Porto. Spontaneous avalanche dephasing in large Rydberg ensembles. *Phys. Rev. A*, 96(5):053409, 2017.

[62] E. M. Bridge, N. C. Keegan, A. D. Bounds, D. Boddy, D. P. Sadler, and M. P. A. Jones. Tunable cw UV laser with <35 kHz absolute frequency instability for precision spectroscopy of Sr Rydberg states. *Opt. Express*, 24(3):2281–2292, 2016.

[63] Y. Castin, H. Wallis, and J. Dalibard. Limit of Doppler cooling. *JOSA B*, 6(11):2046–2057, 1989.

[64] T. H. Loftus, T. Ido, M. M. Boyd, A. D. Ludlow, and J. Ye. Narrow line cooling and momentum-space crystals. *Phys. Rev. A*, 70(6):063413, 2004.

[65] F. James. Monte carlo theory and practice. *Rep. Prog. Phys.*, 43(9):1145, 1980.

[66] W. Wohlleben, F. Chevy, K. Madison, and J. Dalibard. An atom faucet. *Eur. Phys. D.*, 15(2):237–244, 2001.

[67] S. Chaudhuri, S. Roy, and C. S. Unnikrishnan. Realization of an intense cold Rb atomic beam based on a two-dimensional magneto-optical trap: Experiments and comparison with simulations. *Phys. Rev. A*, 74:023406, 2006.

[68] R. W. Mu, Z. L. Wang, Y. L. Li, X. M. Ji, and J. P. Yin. A controllable double-well optical trap for cold atoms (or molecules) using a binary π-phase plate: experimental demonstration and Monte Carlo simulation. *Eur. Phys. D.*, 59(2):291–300, 2010.

[69] M. Chalony, A. Kastberg, B. Klappauf, and D. Wilkowski. Doppler cooling to the quantum limit. *Phys. Rev. Lett.*, 107(24):243002, 2011.

[70] S. N. Atutov, V. Biancalana, A. Burchianti, R. Calabrese, S. Gozzini, V. Guidi, P. Lenisa, C. Marinelli, E. Mariotti, L. Moi, et al. Sodium MOT collection efficiency as a function of the trapping and repumping laser frequencies and intensities. *Eur. Phys. D*, 13(1):71–82, 2001.

[71] D. Comparat. Molecular cooling via Sisyphus processes. *Phys. Rev. A*, 89(4):043410, 2014.

[72] M. R. Tarbutt. Magneto-optical trapping forces for atoms and molecules with complex level structures. *New J. Phys.*, 17(1):015007, 2015.

[73] J. Millen. *A cold strontium Rydberg gas.* PhD thesis, Durham University, 2011.

[74] G. Lochead. *Excited state spatial distributions in a cold strontium gas.* PhD thesis, Durham University, 2012.

[75] J. Millen, G. Lochead, G. R. Corbett, R. M. Potvliege, and M. P. A Jones. Spectroscopy of a cold strontium Rydberg gas. *J. Phys. B: At., Mol. Opt. Phys.*, 44(18):184001, 2011.

[76] I. Hughes and T. Hase. *Measurements and Their Uncertainties: A Practical Guide to Modern Error Analysis.* OUP Oxford, 2010.

[77] T. Macrì and T. Pohl. Rydberg dressing of atoms in optical lattices. *Phys. Rev. A*, 89:011402, Jan 2014.

[78] M. Genkin, S. Wüster, S. Möbius, A. Eisfeld, and J. M. Rost. Dipole–dipole induced global motion of Rydberg-dressed atom clouds. *J. Phys. B: At. Mol. Opt. Phys.*, 47(9):095003, 2014.

[79] L. F. Buchmann, K. Mølmer, and D. Petrosyan. Creation and transfer of nonclassical states of motion using Rydberg dressing of atoms in a lattice. *Phys. Rev. A*, 95:013403, Jan 2017.

[80] N. Malossi, M. M. Valado, S. Scotto, P. Huillery, P. Pillet, D. Ciampini, E. Arimondo, and O. Morsch. Full counting statistics and phase diagram of a dissipative Rydberg gas. *Phys. Rev. Lett.*, 113:023006, Jul 2014.

[81] M. Marcuzzi, E. Levi, S. Diehl, J. P. Garrahan, and I. Lesanovsky. Universal non-equilibrium properties of dissipative Rydberg gases. *Phys. Rev. Lett.*, 113:210401, 2014.

[82] H. Weimer, M. Müller, I. Lesanovsky, P. Zoller, and H. P. Büchler. A Rydberg quantum simulator. *Nat. Phys.*, 6(5):382–388, 2010.

[83] I. Bouchoule and K. Mølmer. Spin squeezing of atoms by the dipole interaction in virtually excited Rydberg states. *Phys. Rev. A*, 65(4):041803, April 2002.

[84] J. B. Balewski, A. T. Krupp, A. Gaj, S. Hofferberth, R. Löw, and T. Pfau. Rydberg dressing: understanding of collective many-body effects and implications for experiments. *New J. Phys.*, 16(6):063012, 2014.

[85] A. D. Bounds, N. C. Jackson, R. K. Hanley, R. Faoro, E. M. Bridge, P Huillery, and M. P. A Jones. Rydberg-dressed magneto-optical trap. *Phys. Rev. Lett.*, 120(18):183401, 2018.

[86] S. L. Cornish, N. R. Claussen, J. L. Roberts, E. A. Cornell, and C. E. Wieman. Stable ^{85}Rb Bose-Einstein condensates with widely tunable interactions. *Phys. Rev. Lett.*, 85:1795–1798, Aug 2000.

[87] T. Lahaye, T. Koch, M. Fattori, J. Mettz, A. Griesmaier, S. Giovanazzi, and T. Pfau. Strong dipolar effects in a quantum ferrofluid. *Nature*, 448:672, Jun 2007.

[88] T. Ido, Y. Isoya, and H. Katori. Optical-dipole trapping of Sr atoms at a high phase-space density. *Phys. Rev. A*, 61(6):061403, 2000.

[89] N. Schlosser, G. Reymond, and P. Grangier. Collisional blockade in microscopic optical dipole traps. *Phys. Rev. Lett.*, 89(2):023005, 2002.

[90] Timothy P Dinneen, Kurt R Vogel, Ennio Arimondo, John L Hall, and Alan Gallagher. Cold collisions of Sr*- Sr in a magneto-optical trap. *Phys. Rev. A*, 59(2):1216, 1999.

[91] A Fuhrmanek, R Bourgain, Yvan R. P. Sortais, and A. Browaeys. Light-assisted collisions between a few cold atoms in a microscopic dipole trap. *Phys. Rev. A*, 85(6):062708, 2012.

[92] Y. R. P. Sortais, H. Marion, C. Tuchendler, A. M. Lance, M. Lamare, P. Fournet, C. Armellin, R. Mercier, G. Messin, A. Browaeys, and P. Grangier. Diffraction-limited optics for single-atom manipulation. *Phys. Rev. A.*, 75(1):013406, 2007.

[93] M. Takamoto, F. Hong, R. Higashi, and H. Katori. An optical lattice clock. *Nature*, 435(7040):321, 2005.

[94] T. Ido and H. Katori. Recoil-free spectroscopy of neutral Sr atoms in the Lamb-Dicke regime. *Phys. Rev. Lett.*, 91(5):053001, 2003.

[95] J. E. Sansonetti and G. Nave. Wavelengths, transition probabilities, and energy levels for the spectrum of neutral strontium (Sr I). *J. Phys. Chem. Ref. Data*, 39(3):033103, 2010.

[96] J. R. Rubbmark and S. A. Borgström. Rydberg series in strontium found in absorption by selectively laser-excited atoms. *Phys. Scr.*, 18(4):196, 1978.

[97] H. G. C. Werij, C. H. Greene, C. E. Theodosiou, and A. Gallagher. Oscillator strengths and radiative branching ratios in atomic Sr. *Phys. Rev. A*, 46(3):1248, 1992.

[98] M. Yasuda, T. Kishimoto, M. Takamoto, and H. Katori. Photoassociation spectroscopy of Sr 88: Reconstruction of the wave function near the last node. *Phys. Rev. A*, 73(1):011403, 2006.

[99] S. Stellmer, M. K. Tey, B. Huang, R. Grimm, and F. Schreck. Bose-Einstein condensation of strontium. *Phys. Rev. Lett.*, 103(20):200401, 2009.

[100] T. Grünzweig, A. Hilliard, M. McGovern, and M. F. Andersen. Near-deterministic preparation of a single atom in an optical microtrap. *Nat. Phys.*, 6(12):951, 2010.

[101] L. Beguin. *Measurement of the van der Waals interaction between two Rydberg atoms.* PhD thesis, Institut d'Optique Graduate School, 2014.

[102] D. Sadler. *Many-Body Interactions in a Dissipative Frozen strontium Rydberg Gas*. PhD thesis, Durham University, 2016.

[103] X. Xu, T. H. Loftus, J. W. Dunn, C. H. Greene, J. L. Hall, A. Gallagher, and J. Ye. Single-stage sub-Doppler cooling of alkaline earth atoms. *Phys. Rev. Lett.*, 90(19):193002, 2003.

[104] R. W. P. Drever, J. L. Hall, F. V. Kowalski, J. Hough, G. M. Ford, A. J. Munley, and H Ward. Laser phase and frequency stabilization using an optical resonator. *Appl. Phys. B*, 31(2):97–105, 1983.

[105] E. D. Black. An introduction to Pound-Drever-Hall laser frequency stabilization. *Am. J. Phys.*, 69(1):79–87, 2001.

[106] E. C. Cook, P. J. Martin, T. L. Brown-Heft, J. C. Garman, and D. A. Steck. High passive-stability diode-laser design for use in atomic-physics experiments. *Rev. Sci. Inst.*, 83(4):043101, 2012.

[107] R. Boddy and G. Smith. *Statistical Methods in Practice: For Scientists and Technologists*. Wiley, 2009.

[108] N. Ismail, C. C. Kores, D. Geskus, and M. Pollnau. Fabry-pérot resonator: spectral line shapes, generic and related Airy distributions, linewidths, finesses, and performance at low or frequency-dependent reflectivity. *Opt. Exp.*, 24(15):16366–16389, 2016.

[109] Practical flatness. `https://www.semrock.com/Data/Sites/1/semrockpdfs/idx2395-smkpractical-flatnesstechnote-fin.pdf`. Accessed: 30-07-2018.

[110] D. Bronzi, F. Villa, S. Tisa, A. Tosi, F. Zappa, D. Durini, S. Weyers, and W. Brockherde. 100 000 frames/s 64× 32 single-photon detector array for 2-D imaging and 3-D ranging. *IEEE J. Sel. Top. Quantum Electron.*, 20(6):354–363, 2014.

---

[111] N. Poli, R. E. Drullinger, G. Ferrari, J. Léonard, F. Sorrentino, and G. M. Tino. Cooling and trapping of ultracold strontium isotopic mixtures. *Phys. Rev. A*, 71(6):061403, 2005.

[112] A. Cooper, J. P. Covey, I. S. Madjarov, S. G. Porsev, M. S. Safronova, and M. Endres. Alkaline earth atoms in optical tweezers. *arXiv preprint arXiv:1810.06537*, 2018.

[113] M. A. Norcia, A. W. Young, and A. M. Kaufman. Microscopic control and detection of ultracold strontium in optical-tweezer arrays. *arXiv preprint arXiv:1810.06626*, 2018.

[114] P. D. Lett, W. D. Phillips, S. L. Rolston, C. E. Tanner, R. N. Watts, and C. I. Westbrook. Optical molasses. *JOSA B*, 6(11):2084–2107, 1989.

[115] R. Chang, A. L. Hoendervanger, Q. Bouton, Y. Fang, T. Klafka, K. Audo, A. Aspect, C. I. Westbrook, and D. Clément. Three-dimensional laser cooling at the Doppler limit. *Phys. Rev. A*, 90(6):063407, 2014.

[116] N. R. Hutzler, L. R. Liu, Y. Yu, and K. Ni. Eliminating light shifts for single atom trapping. *New. J. Phys.*, 19(2):023007, 2017.

[117] U. Schünemann, H. Engler, R. Grimm, M. Weidemüller, and M. Zielonkowski. Simple scheme for tunable frequency offset locking of two lasers. *Rev. Sci. Instrum.*, 70(1):242–243, 1999.

[118] J. Appel, A. MacRae, and A. I. Lvovsky. A versatile digital GHz phase lock for external cavity diode lasers. *Meas. Sci. Technol.*, 20(5):055302, 2009.

[119] T. Mukaiyama, H. Katori, T. Ido, Y. Li, and M. Kuwata-Gonokami. Recoil-limited laser cooling of Sr 87 atoms near the Fermi temperature. *Phys. Rev. Lett.*, 90(11):113002, 2003.

[120] S. Friebel, C. D'andrea, J. Walz, M. Weitz, and T. W. Hänsch. Co_2-laser optical lattice with cold rubidium atoms. *Phys. Rev. A.*, 57(1):R20, 1998.

[121] H. Engler, T. Weber, M. Mudrich, R. Grimm, and M. Weidemüller. Very long storage times and evaporative cooling of cesium atoms in a quasielectrostatic dipole trap. *Phys. Rev. A*, 62(3):031402, 2000.

[122] B. Darquié. *Manipulation d'atomes dans des pièges dipolaires microscopiques et émission contrôlée de photons par un atom unique.* PhD thesis, Université Paris XI, 2005.

[123] B. C. Platt and R. Shack. History and principles of Shack-Hartmann wavefront sensing. *J. Refract. Surg.*, 17(5):S573–S577, 2001.

[124] F. Zernike. Beugungstheorie des schneidenver-fahrens und seiner verbesserten form, der phasenkontrastmethode. *Physica*, 1(7-12):689–704, 1934.

[125] M. Born and E. Wolf. *Principles of Optics: Electromagnetic Theory of Propagation, Interference and Diffraction of Light.* Cambridge University Press, 1999.

[126] C. Tuchendler, A. M. Lance, A. Browaeys, Y. R. P. Sortais, and P. Grangier. Energy distribution and cooling of a single atom in an optical tweezer. *Phys. Rev. A*, 78(3):033425, 2008.

[127] A. K. Mohapatra, T. R. Jackson, and C. S. Adams. Coherent optical detection of highly excited Rydberg states using electromagnetically induced transparency. *Phys. Rev. Lett.*, 98(11):113003, 2007.

[128] T. F. Gallagher. *Rydberg Atoms.* Cambridge Monographs on Atomic, Molecular and Chemical Physics. Cambridge University Press, 1994.

[129] D. Barredo, H. Kübler, R. Daschner, R. Löw, and T. Pfau. Electrical readout for coherent phenomena involving Rydberg atoms in thermal vapor cells. *Phys. Rev. Lett.*, 110:123002, 2013.

[130] R. Beigang, K. Lücke, A. Timmermann, P. J. West, and D. Frölich. Determination of absolute level energies of 5sns $^1S_0$ and 5snd $^1D_2$ Rydberg series of Sr. *Opt. Comm.*, 42(1):19–24, 1982.

[131] S-U. Haq, S. Mahmood, M. A. Kalyar, M. Rafiq, R. Ali, and M. A. Baig. Photoionization cross section and oscillator strength distribution in the near-threshold region of strontium. *Eur. Phys. D*, 44(3):439–447, 2007.

[132] E. M. Bridge, J. Millen, C. S. Adams, and M. P. A. Jones. A vapor cell based on dispensers for laser spectroscopy. *Rev. Sci. Instrum.*, 80(1):013101, 2009.

[133] G. Scoles. *Atomic and Molecular Beam Methods*. Number v. 1 in Atomic and Molecular Beam Methods. Oxford University Press, 1988.

[134] C. Javaux, I. G. Hughes, G. Lochead, J. Millen, and M. P. A. Jones. Modulation-free pump-probe spectroscopy of strontium atoms. *Eur. Phys. D*, 57(2):151–154, 2010.

[135] G. Lakits, F. Aumayr, and H. Winter. Statistics of ion-induced electron emission from a clean metal surface. *Rev. Sci. Instrum.*, 60(10):3151–3159, 1989.

[136] K. Ohya and J. Kawata. Direct Monte Carlo simulation of ion-induced kinetic electron emission statistics. *Jpn. J. Appl. Phys.*, 32(4R):1803, 1993.

[137] S. Mauger, J. Millen, and M. P. A. Jones. Spectroscopy of strontium Rydberg states using electromagnetically induced transparency. *J. Phys. B: At., Mol. Opt. Phys.*, 40(22):F319, 2007.

[138] C. J. Lorenzen, K. Niemax, and L. R. Pendrill. Isotope shifts of energy levels in the naturally abundant isotopes of strontium and calcium. *Phys. Rev. A*, 28(4):2051, 1983.

[139] M. L. Zimmerman, M. G. Littman, M. M. Kash, and D. Kleppner. Stark structure of the Rydberg states of alkali-metal atoms. *Phys. Rev. A*, 20(6):2251, 1979.

[140] D. Weller, A. Urvoy, A. Rico, R. Löw, and H. Kübler. Charge-induced optical bistability in thermal Rydberg vapor. *Phys. Rev. A*, 94:063820, 2016.

[141] A. Ben-Amar, G. Erez, S. Fastig, and R. Shuker. Observation of Penning ionization in Sr/Ne discharge by the optogalvanic effect. *App. Opt.*, 23(24):4529–4531, 1984.

[142] I. I. Fabrikant and V. S. Lebedev. Quenching of Rydberg states by atoms with small electron affinities. *J. Phys. B: At., Mol. Opt. Phys.*, 33(8):1521, 2000.

[143] D. M. Lubman, C. T. Rettner, and R. N. Zare. How isolated are molecules in a molecular beam? *J. Phys. Chem.*, 86(7):1129–1135, 1982.

[144] C. Carr, R. Ritter, C. G. Wade, C. S. Adams, and K. J. Weatherill. Nonequilibrium phase transition in a dilute Rydberg ensemble. *Phys. Rev. Lett.*, 111(11):113901, 2013.

[145] D. S. Din, C. S. Adams, B. S. Shi, and G. C. Guo. Non-equilibrium phase-transitions in multi-component Rydberg gases. *arXiv preprint arXiv:1606.08791*, 2016.

[146] C. G. Wade, N. Šibalić, N. R. de Melo, J . M. Kondo, C. S. Adams, and K. J. Weatherill. Real-time near-field terahertz imaging with atomic optical fluorescence. *Nat. Photon.*, 11:40–43, 2016.

[147] N. Šibalić, C. G. Wade, C. S. Adams, K. J. Weatherill, and T. Pohl. Driven-dissipative many-body systems with mixed power-law interactions: Bistabilities and temperature-driven non-equilibrium phase transitions. *Phys. Rev. A*, 94:011401, 2016.

[148] F. Cinti, P. Jain, M. Boninsegni, A. Micheli, P. Zoller, and G. Pupillo. Supersolid droplet crystal in a dipole-blockaded gas. *Phys. Rev. Lett.*, 105(13):135301, 2010.

Appendix A

Experimental apparatus

A.1 MCP wiring

Figure A.1 shows the internal connections to the MCP (left), as well as the connections to the feedthrough on top of the chamber (right). Note that the images were taken when the chamber was inverted.

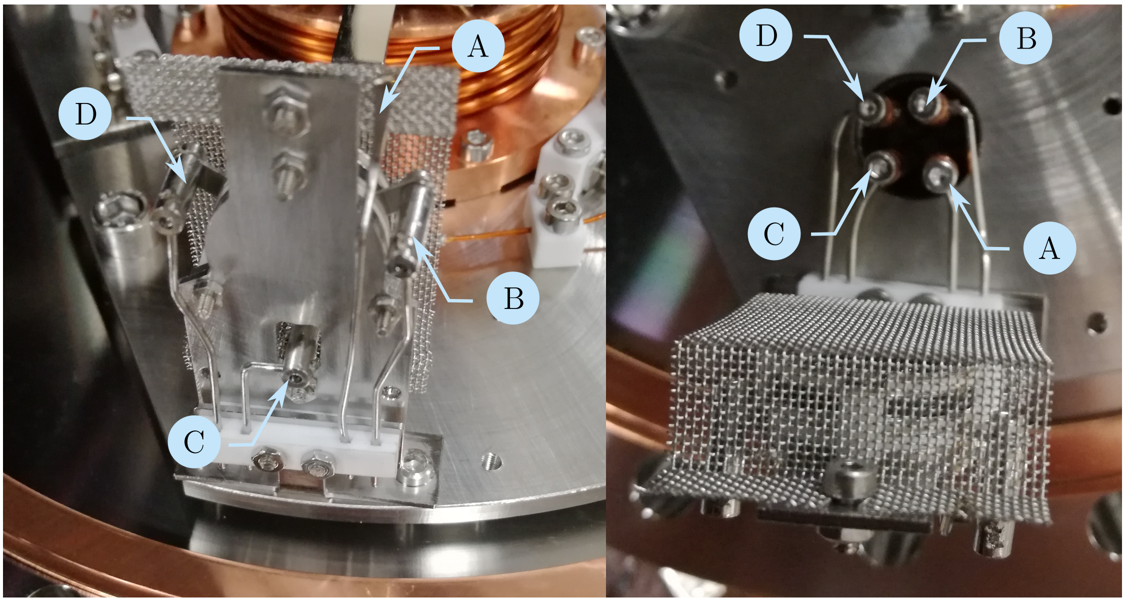

Figure A.1: Wiring of the MCP in the vacuum chamber. The labelling is as follows: A - Mesh, B - Anode, C - MCP In, D - MCP Out.

A.2 Electrode wiring

The electrodes are connected to a multi-pin feedthrough which is alphabetically labelled. Figure A.2 shows the electrical connections to the electrodes on top (left) and bottom (right) of the experimental chamber. Table A.1 shows the connections of vertically opposed electrode pairs in the vacuum chamber.

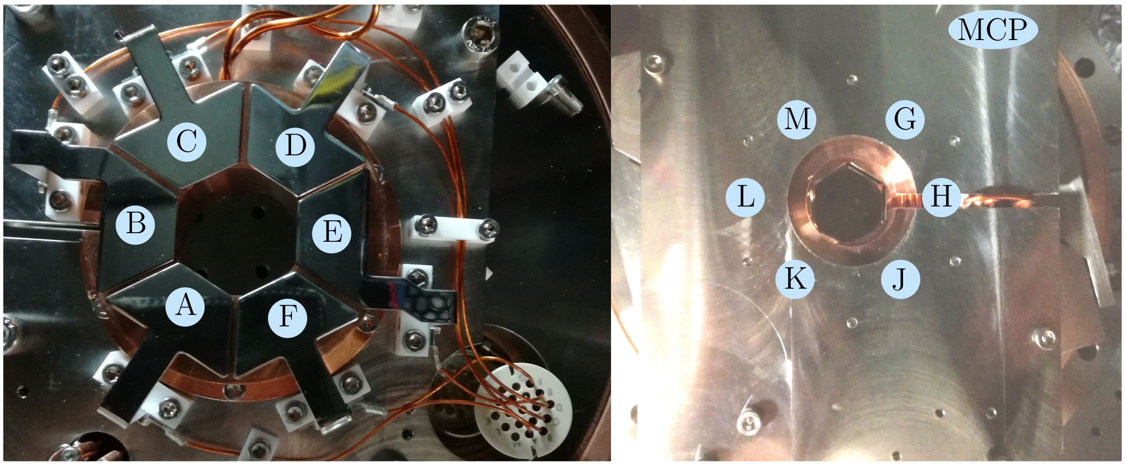

Figure A.2: Wiring of electrodes in the vacuum chamber. The top and bottom electrodes are shown in the left and right image respectively. The alphabetical labelling refers to the labelling of the feedthrough connector.

Top	**Bottom**
A	G
B	H
C	J
D	K
E	L
F	M

Table A.1: The table shows the vertically opposed electrode pairs in the vacuum chamber.

A.3 Viewports

Here we detail the viewports of the main chamber and their respective anti-reflection coatings. These are detailed in figure A.3. The viewports on the vertical axis are not shown on this diagram. These are anti-reflection coated for 461 and 689 nm.

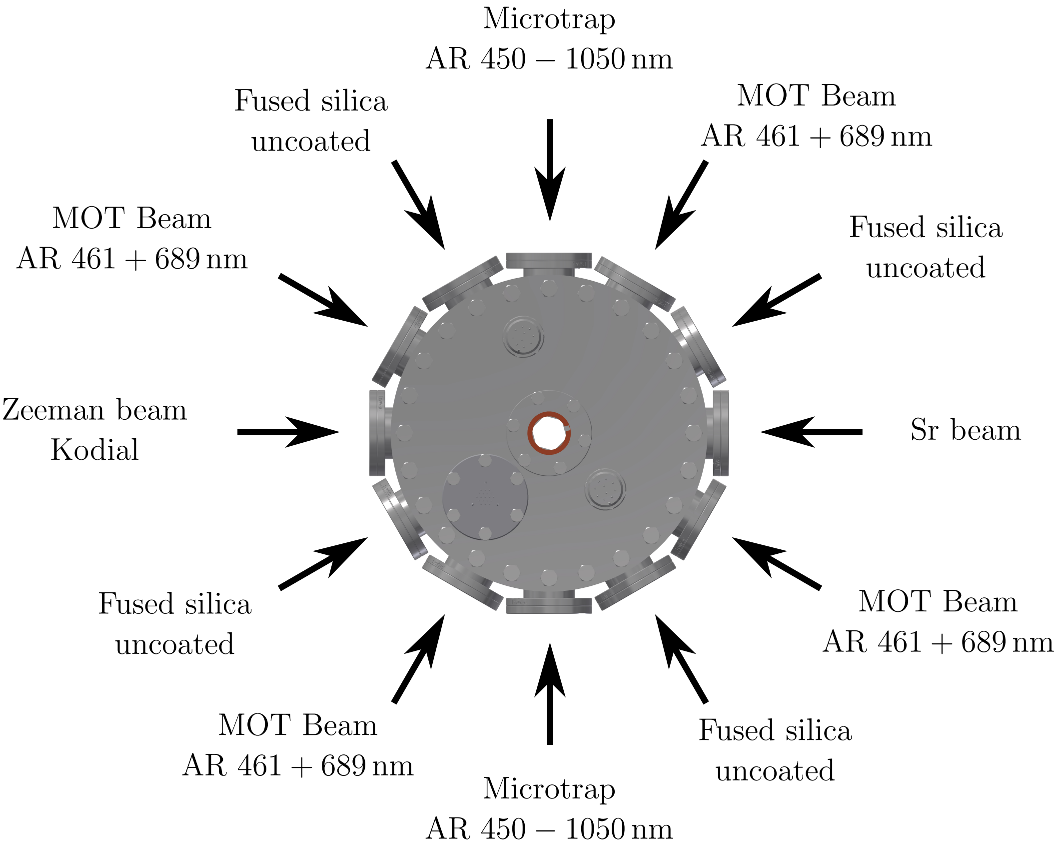

Figure A.3: Diagram indicating the viewports on each flange of the main chamber. The vertical axis has AR 461 + 689 nm coated.

.

Appendix B

MOT coil relay circuit

The circuit consists of two non-latching relays[1] controlled via an external TTL gate voltage. This is shown in figure B.1. A diode is placed across each relay in order to protect the FET from back-EMFs produced by the switching of the relays. The circuit is designed to be switched when there is no current flow in the coils, however upon switching there is a large voltage spike from the current supply to the coils. In order to protect the servo circuit, a 12 V Zener diode is connected across the drain and source pins of the MOSFET.

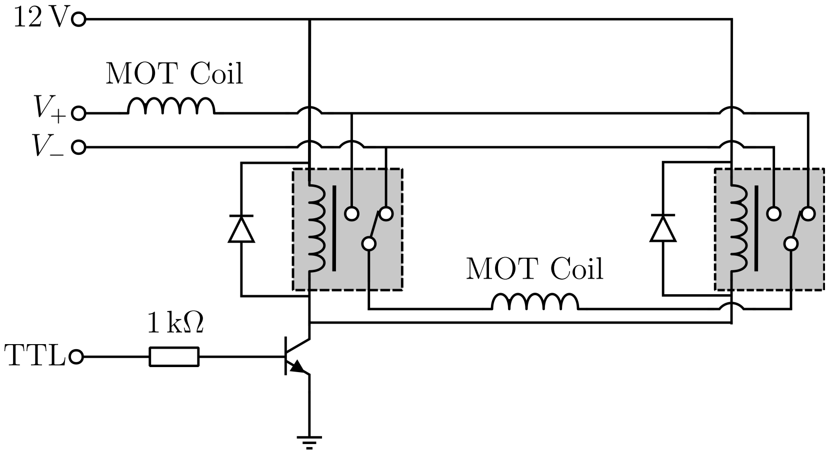

Figure B.1: Circuit diagram of the relay used to switch from anti-Helmholtz to Helmholtz coil configuration. The grey shaded boxes define the relays.

---

[1] TE Connectivity SPDT Non-Latching Relay PCB Mount, 12 V DC Coil, 5 A, RS 718-1752